Technical Physics, Vol. 45, No. 11, 2000, pp. 1375–1382. Translated from Zhurnal Tekhnicheskoĭ Fiziki, Vol. 70, No. 11, 2000, pp. 1–8.

Correlation Effects in the Diffusion and Electrical Conductivity of an Interacting Lattice Gas

G. S. Bokun*, Ya. G. Groda*, C. Uebing, and V. S. Vikhrenko***

** Belarussian State University of Technology, Minsk, 220050 Belarus*

*** Max-Planck-Institut für Eisenforschung GmbH, Düsseldorf, D-40237 Germany*

Received January 26, 2000

Abstract—A simple and effective self-consistent scheme is proposed for the determination of the average potentials which allows thermodynamic functions and other characteristics of lattice systems in equilibrium to be calculated with high accuracy and short computing time. This scheme has been used for analysis of the expressions for the coefficients of diffusion and electrical conductivity obtained on the basis of the modern statistical theory of nonequilibrium processes. Results of the simulations are correlated with the data of Monte Carlo simulations obtained using parallel vector algorithms on a Cray TZE computer of the Max Plank Society (Germany). *© 2000 MAIK "Nauka/Interperiodica".*

INTRODUCTION

Mass transfer and the associated electrical conductivity in crystals and at their surfaces plays a crucial role in numerous phenomena, examples of which are ionic conductivity, chemical reactions, crystal growth, intercalation, phase transitions in nonequilibrium conditions, etc. [1–9]. However, a theoretical description of the mass transfer processes in solids meets with essential difficulties associated with the very different characteristic time scales. The lattice models turn out to be useful for studying phenomena at time scales considerably exceeding the oscillation period of particles near their stationary sites.

For the description of the equilibrium properties of the lattice systems, different mean-field approximations are widely used [10, 11]; however, they are able, at best, to provide semiquantitative results. The more complex mean-field versions [12] and the Kikuchi approximation [13], while being more accurate compared with the molecular field method (or quasi-chemical approximation), nevertheless are not accurate enough and are considerably more complicated in applications [14].

The mass transfer processes in lattice systems were considered mainly as applied to two-dimensional systems [4, 6, 14–17]. Zhdanov [18] was able to express the coefficient of chemical diffusion through equilibrium characteristics of the lattice system, namely, the chemical potential and the probability that two neighboring sites of the two-dimensional lattice would not be occupied by particles. However, the accuracy and application limits were unknown.

SELF-CONSISTENT DIAGRAMMATICAL APPROXIMATION

Consider a system of n particles distributed over $N \geq n$ lattice sites. The state of the system is given by a set of occupation numbers n_i ($i = 1, 2, \ldots, N$), which take the value of 1, if the site i is occupied by a particle, and 0 otherwise. Occupation of a site by more than one particle is forbidden, so the normalization condition is fulfilled:

$$\sum_{i=1}^{N} n_i = n. \tag{1}$$

The energy of the system is determined in the pair interaction approximation

$$U_N = \sum_{i=1}^{N} \sum_{j=i+1}^{N} \Phi_{ij} n_i n_j, \tag{2}$$

where Φ_{ij} is the interaction energy of the particles occupying sites i and j.

The number of independent interaction constants can be considerably reduced if the symmetry of the lattice is taken into account and the notation $J_k = \Phi_{ij}$ is introduced for the sites i and j, which are neighbors of the kth order; that is, they belong to the kth coordination sphere with respect to each other.

Consider also the basic system described by the potentials $\varphi_j(n_i)$ of interaction between a particle ($n_i = 1$) or a vacancy ($n_i = 0$) located at the ith site and the jth site of the lattice. Its energy is

$$U_N^{(0)} = \sum_{i=1, j=1}^{N} \sum \varphi_j(n_i). \tag{3}$$

1063-7842/00/4511-1375$20.00 © 2000 MAIK "Nauka/Interperiodica"

These potentials are in fact average ones, since they are independent of the state of site j; that is, it can be said that the averaging is done over these states. It is supposed that there is no interaction between a particle or vacancy and its own site, $\varphi_j(n_i) = 0$.

The equilibrium properties of the system are determined by its free energy per site

$$F = -(k_B T/N)\ln Q_N, \tag{4}$$

where T is the temperature, k_B is the Boltzmann constant, and Q_N is the partition function.

The latter can be written as

$$\begin{aligned} Q_N &= Sp_{\{n_1, \ldots, n_N\}}\{\exp(-\beta U_N)\} \\ &= Q_N^{(0)}\langle \exp[-\beta(U_N - U_N^{(0)})]\rangle_0, \end{aligned} \tag{5}$$

where $\beta = (k_B T)^{-1}$, $Sp_{\{n_1, \ldots, n_N\}}$ denotes summation over all possible sets of the occupation numbers corresponding to normalization condition (1); the angle brackets $\langle \ldots \rangle_0$ denote averaging over the states of the basic system, while the partition function of the latter can be easily factorized due to the single-particle character of its potential energy (3):

$$\begin{aligned} Q_N^{(0)} &= Sp_{\{n_1, \ldots, n_N\}}\{\exp(-\beta U_N^0)\} \\ &= Sp_{\{n_1, \ldots, n_N\}}\left\{\prod_{i=1}^{N}\exp\left[-\beta\sum_{j=1, j\neq i}^{N}\varphi_j(n_i)\right]\right\} \\ &= \left[\prod_{l=0}^{1}(Q_l/\Theta_l)^N\Theta_l\right]^N, \end{aligned} \tag{6}$$

$$\Theta_0 = (N-n)/N, \quad \Theta_1 = n/N. \tag{7}$$

The partition function per lattice site

$$Q_{n_i} = \exp\left[-\beta\left(\sum_{j=1, j\neq i}^{N}\varphi_j(n_i)\right)\right] \tag{8}$$

is determined for two site states ($n_i = 0$ or 1).

Introducing renormalized Meier functions

$$\begin{aligned} &f_{ij}(n_i, n_j) \\ &= \exp\{-\beta[\Phi_{ij} n_i n_j - \varphi_j(n_i) - \varphi_i(n_j)]\} - 1, \end{aligned} \tag{9}$$

we represent the partition function of the starting system in the form

$$Q_N = Q_N^{(0)}\left\langle \prod_{i=1}^{N}\prod_{j=i+1}^{N}(1 + f_{ij})\right\rangle_0. \tag{10}$$

Relationship (10) enables the free energy of the system to be written in a diagrammatical form,

$$\begin{aligned} F &= -k_B T\left(\Theta_0 \ln\frac{Q_0}{\Theta_0} + \Theta_1 \ln\frac{Q_1}{\Theta_1}\right) \\ &\quad -\frac{k_B T}{2}(b_2 + b_3 + b_4 + \ldots), \end{aligned} \tag{11}$$

where b_j depict a set of diagrams specified at jth sites of the lattice. In particular,

$$\begin{aligned} b_2 &= \sum_{k=1}^{k_{\max}}\sum_{i,j=0}^{1} f_{ij}^{(k)}\Theta_i\Theta_j z_k, \\ b_3 &= \sum_{k=1}^{k_{\max}}\sum_{l=1}^{k_{\max}}\sum_{i,j,m=0}^{1} f_{ij}^{(k)} f_{jm}^{(l)}\Theta_i\Theta_j\Theta_m z_k z_l'. \end{aligned} \tag{12}$$

The summation over k and l is done up to a certain limiting value $k_{\max}$, which is determined by the assumed interaction radius of the particles, while the averaging over the states of the basic system can to a first approximation, be reduced to multiplying by the concentrations of the particles and vacancies (Θ_0 and Θ_1) and summation over these site states.

If all terms of the expansion are taken into account, expression (11) is identical to relationship (4) for an arbitrary form of the potentials $\varphi_j(n_i)$. Therefore, the principle of self-consistent determination of the latter can be formulated by requiring that the sum of a number of first terms in (11), which is considered as an approximate value of the free energy, also be independent of the choice of average potentials. This requirement is tantamount to the condition that the held part of the series be extremal with respect to average potential variation.

Hereafter, we consider only the interaction between nearest neighbors. Taking into consideration only two-site diagrams, we obtain the usual quasi-chemical approximation, in which the average potentials are nonzero only for the nearest neighbor sites. They are defined by the equations

$$X_i = \sum_{j=0}^{1}\frac{W_{ij}\Theta_j}{X_j}; \quad i = 0, 1, \tag{13}$$

$$W_{ij} = \exp(-\beta\Phi_{ij} n_i n_j), \quad X_i = \exp(-\beta\varphi(i)). \tag{14}$$

Here, a shorthand system of notations is introduced, in which indices i and j denote both site indices and indices denoting the state of these sites (0 or 1). Therefore, if the interaction between nearest neighbors is taken into account, then $\Phi_{00} = \Phi_{01} = 0$, $\Phi_{11} = J$, where J is the potential of the nearest neighbor interaction. The poten-

tials $\varphi(0)$ and φ_1 are also defined for the nearest neighbors. Equation (13) is tantamount to the expression

$$\sum_{j=0}^{1} f_{ij}\Theta_j = 0, \tag{15}$$

which means that the renormalized Meier function averaged over the states of one of the sites is equal to zero. As a result, we obtain a new interpretation of the quasi-chemical approximation; namely, for self-consistent choice of the average potentials, according to Eqs. (13) and (14), all diagrams occurring in expansion (11) and having at least one peak from which only one bond emerges go to zero. In other words, the quasi-chemical approximation, through self-consistent conditions, takes into account a wide range of diagrams in the free energy expansion in terms of the Meier functions.

In the quasi-chemical approximation, the radii of action of the average and starting potentials coincide. Therefore, in the nearest neighbor interaction, the average potentials are nonzero only for nearest neighbors as well.

In the next step, diagrams plotted on three and four sites are taken into account. The average potentials for neighboring sites can conveniently be taken equal to their quasi-chemical values determined according to Eqs. (13) and (14), while for the average potentials $\varphi^{(2)}(i)$ of the second neighbors, we obtain a system of equations similar to the quasi-chemical approximation:

$$X_i^{(2)} = \sum_{j=0}^{1} \frac{K_{ij}^2\Theta_j}{X_j^{(2)}}, \tag{16}$$

where

$$K_{ij} = \sum_{k=0}^{1} \frac{W_{ik}W_{jk}\Theta_k}{X_iX_jX_k^2}, \quad X_i^{(2)} = \exp(-\beta\varphi^{(2)}(i)). \tag{17}$$

The solution of the system of Eqs. (16), (17) takes the form

$$X_1^{(2)} = X_0^{(2)}\eta_2, \tag{18}$$

$$X_0^{(2)} = \sqrt{V_{00}\Theta_0 + (V_{01}\Theta_1/\eta_2)}, \tag{19}$$

$$\eta_2 = \frac{-V_{01}(\Theta_1-\Theta_0) + \sqrt{V_{01}^2(\Theta_1-\Theta_0)^2 + 4V_{00}V_{11}\Theta_0\Theta_1}}{2V_{00}\Theta_0}, \tag{20}$$

$$V_{ij} = K_{ij}^2, \tag{21}$$

which is applicable to the quasi-chemical approximation as well if η_2 is replaced by η_1 at $V_{00} = V_{01} = 1$ and $V_{11} = W = \exp(-\beta J)$.

After calculation of the average potentials of interaction with the nearest $\varphi(i)$ and the next-nearest $\varphi^{(2)}(i)$ neighbor sites, the contribution to the free energy (11) of the unaccounted diagrams can be evaluated and the following expression will be obtained:

$$F = k_BT\sum_{i=0}^{1}\Theta_i\ln\Theta_i + \sum_{i=0}^{1}\Theta_i(z_1\varphi(i) + z_2\varphi^{(2)}(i)) + 0.25\sum_{i=0}^{1}\sum_{j=0}(K_{ij}-1)^2\Theta_i\Theta_j. \tag{22}$$

The probability that two nearest neighbor lattice sites are occupied by particles can be determined by differentiating the free energy with respect to the interaction parameter:

$$F(1,1) = \frac{\partial F}{\partial J}. \tag{23}$$

The probabilities that these sites are occupied by a particle and a vacancy ($F(1, 0)$) or by two vacancies ($F(1, 0)$) can be found using the normalization condition

$$F(1,0) = \Theta_1 - F(1,1), \quad F(0,0) = \Theta_0 - F(0,1). \tag{24}$$

Using relationships (13), (14) and (16)–(24), both the thermodynamic properties of a lattice gas of arbitrary density and its correlation properties described by the distribution functions of particles and vacancies $F(i, j)$ can be studied.

ELECTRICAL CONDUCTIVITY AND DIFFUSION COEFFICIENTS

To consider processes associated with the migration of the lattice gas particles (diffusion and electrical conductivity), we take as a dynamic variable a set of the occupation numbers n_i of the lattice sites, which determine the charge distribution in the system as if it were supposed that every particle had a charge q. The electric neutrality of the system is provided by the uniformly distributed lattice charge.

In a weak electric field E_i, the dynamics of small deviations δn_i of the particle density from its equilibrium value $\Theta = \Theta_1$ is described by a linear equation, which, using the method of nonequlibrium statistical ensembles proposed by Zubarev [19, 20], can be written in the form

$$\frac{d\delta n_i}{dt} - \beta\Theta\sum_j \Omega_{ij}(\delta\mu_j - qE_i) + \beta\Theta\sum_j\int_0^\infty \Theta_{ij}(\tau)[\delta\mu_j(t-\tau) - qE_j(t-\tau)]d\tau = 0, \tag{25}$$

where $\delta\mu_j$ is the chemical potential deviation at the jth site from its equilibrium value μ, Ω_{ij} and $\Theta_{ij}(\tau)$ are the

static correlation matrix and the memory matrix, respectively, defined as

$$\Omega_{ij} = \Theta^{-1}\langle \dot{n}_i n_j \rangle, \quad (26)$$

$$\Theta_{ij}(\tau) = \Theta^{-1}\langle Q\delta\dot{n}_i(0) Q\delta\dot{n}_j(\tau)\rangle. \quad (27)$$

The angle brackets $\langle \ldots \rangle$ denote averaging over the equilibrium distribution, dots above the symbols denote time derivatives, and the operator Q corresponds to projection onto the space orthogonal to the basic dynamic variable n_i. Equation (25) takes into account effects of memory (due to the integral over time) and spatial dispersion (due to summation over lattice sites).

Unlike the Hamiltonian systems usually considered in statistical mechanics, the dynamics of a lattice gas is described by an irreversible basic equation [5, 6, and 14–18]

$$\frac{dn_i}{dt} = \sum_j^z [w_{ij} n_j (1 - n_j) - w_{ij} n_i (1 - n_j)], \quad (28)$$

where w_{ij} is the probability of particle transition from site j to site i in a unit time (the transition frequency) and the summation is carried out over z nearest neighbors of the site i; the transition probabilities satisfy the detailed balance principle.

The chemical potential and the electric field appear in the expression of the particle density evolution symmetrically. This means that the particle flux density is proportional to the thermodynamic force (the gradient of the chemical potential) and to the gradient of the electric field, with equal proportionality factors in both cases. In the first Fick's law for the particle flux density, either the coefficient of chemical diffusion multiplied by the concentration gradient or the kinetic diffusion coefficient D_k multiplied by the gradient of the chemical potential appear [4–6, 14, 17, 18]. In terms of the latter, the electrical conductivity coefficient is expressed as

$$\sigma(\omega, \mathbf{k}) = \frac{q^2}{kT} D_k(\omega, \mathbf{k})\rho, \quad (29)$$

where ρ is the particle density and ω and $\mathbf{k}$ are the frequency and wave vector, respectively.

It is seen from (25) that relationship (29) is valid for arbitrary values of the frequency and the wave vector and, thus, represents an extension of Einstein's relationship, which relates electrical conductivity to particle mobility.

To calculate the diffusion coefficient, we exclude the external electric field from Eq. (25) by setting it equal to zero and, after Laplace and Fourier transforms, write the solution as

$$\delta n_{\mathbf{k}}(\omega, \mathbf{k}) = \frac{\delta n_{\mathbf{k}}(0)}{i\omega - \Omega_{\mathbf{k}}\chi_{\mathbf{k}} + \Theta_{\mathbf{k}}(\omega)\chi_{\mathbf{k}}}, \quad (30)$$

where $\chi_{\mathbf{k}}$ is determined by the Fourier transform of the reverse matrix of the density fluctuations

$$\chi_{ij}^{-1} = \Theta^{-1}\langle \delta n_i \delta n_j \rangle \quad (31)$$

and emerges as a result of the transition from the chemical potential to density in the second and third terms of Eq. (25).

The memory matrix Θ_{ij} has a fairly complex structure. In the first approximation, its contribution can be neglected. Then, from (30), an expression for the low frequency limit of the kinetic diffusion coefficient follows, which depends on the wave vector:

$$D_k(\mathbf{k}) = -\Omega_{\mathbf{k}}/k^2, \quad k = |\mathbf{k}|, \quad (32)$$

$$\Omega_{\mathbf{k}} = \sum_{j=1}^{N} \Omega_{ij} e^{i\mathbf{k}\mathbf{r}_{ij}}. \quad (33)$$

Here $\mathbf{r}_{ij}$ is a vector connecting sites i and j. Using the known diffusion coefficient $D_k(\mathbf{k})$, the electrical conductivity coefficient $\sigma(\mathbf{k})$ can be calculated. Let us dwell on the calculation of the matrix Ω_k. Substituting (28) into (26) and using the detailed balance principle and symmetry properties, we obtain

$$\Omega_{\mathbf{k}} = -w\sum_j^z (1 - \cos\mathbf{k}\mathbf{r}_{ij}), \quad (34)$$

where

$$w = \Theta^{-1}\langle w_{li} n_i (1 - n_l)\rangle \quad (35)$$

is the average frequency of the particle hops.

Assuming a value corresponding to the trap model for the hopping frequency,

$$w_{li} = w_0 \exp(\beta\varepsilon_i), \quad \varepsilon_i = \sum_{j=1}^{N} \Phi_{ij} n_j, \quad (36)$$

where w_0 is the hopping frequency of the particle not interacting with other particles and ε_i is the energy of its interaction with the surroundings.

In this case, the averaging in (35) results in the relationship

$$w = w_0 \exp(\beta\mu) F(0, 0)/\Theta. \quad (37)$$

In the hydrodynamic (long-wavelength) limit ($k \longrightarrow 0$), we obtain

$$D_k = D_0 \exp(\beta\mu) F(0, 0)/\Theta, \quad (38)$$

$$D_0 = (za^2/2d)\omega_0, \quad (39)$$

where D_0 is the coefficient of chemical diffusion of the Langmuir (noninteracting) lattice gas, a is the lattice constant, and d is the space dimension.

Relationship (38) represents Zhdanov's formula [6, 18]. Thus, it can be suggested that this formula ignores memory effects resulting from the collective

behavior of the particles. Therefore, it is important to find out how accurately this relationship describes the diffusion in lattice systems.

CORRELATION FACTORS

In investigations of the diffusion and electrical conductivity in the lattice systems, various correlation factors are often introduced and relationships between them are discussed. In particular, the Haven ratio f_H [21–23] is often identified with the self-diffusion correlation factor f^*. The expressions obtained for different diffusion coefficients and the electrical conductivity coefficient enable the relationship between correlation factors of this sort to be unambiguously determined.

For the kinetic diffusion coefficient and the self-diffusion coefficient D^*, expressions of the Kubo–Green type formulas can be written in terms of displacements of the system particles [4, 5]:

$$D_k = \lim_{n,t\to\infty} \frac{1}{ntd}\left\langle \sum_{i=1}^{N}\Delta\mathbf{r}_i \sum_{j=1}^{N}\Delta\mathbf{r}_j \right\rangle, \quad (40)$$

$$D^* = \lim_{n,t\to\infty} \frac{1}{ntd}\left\langle \sum_{i=1}^{N}(\Delta\mathbf{r}_i)^2 \right\rangle, \quad (41)$$

where $\Delta\mathbf{r}_i$ determines the displacement of the ith particle in a time t.

Expression (40) differs from (41) by nondiagonal terms, which are of a two-particle character, i.e., directly accounting for correlations between particles. Let us introduce the many-particle correlation factor f_m, which also accounts for the correlations

$$D_k = f_m D^*. \quad (42)$$

The self-diffusion correlation factor [24] accounts for an enhanced probability of the repeated exchange of places between a given particle and a vacancy in the course of particle migration by the vacancy mechanism. This correlation factor can be determined from the relationship

$$D^* = f^* D_0(1-\Theta). \quad (43)$$

In the general case, there is no direct relationship between f^* and f_m but for the Langmuir gas, it can be shown that

$$f_m = f^*. \quad (44)$$

The Haven ratios [21–23]

$$f_H = D^* q/\xi k_B T \quad (45)$$

are determined from the relationship between the self-diffusion coefficient and the particle mobility ξ that is related to the electrical conductivity as

$$\xi = \sigma/\rho q. \quad (46)$$

Using relationship (29) between the diffusion and electrical conductivity coefficients, we obtain

$$f_H = D^*/D_k = f_m. \quad (47)$$

Therefore, the coefficient f_H is directly related to the many-particle correlation factor rather than to f^*.

RESULTS OF THE CALCULATIONS AND MONTE CARLO SIMULATIONS

Relationships for the chemical potential and distribution functions obtained using the self-consistent diagrammatical approximation (SDA) are only slightly more involved than similar relationships in the quasi-

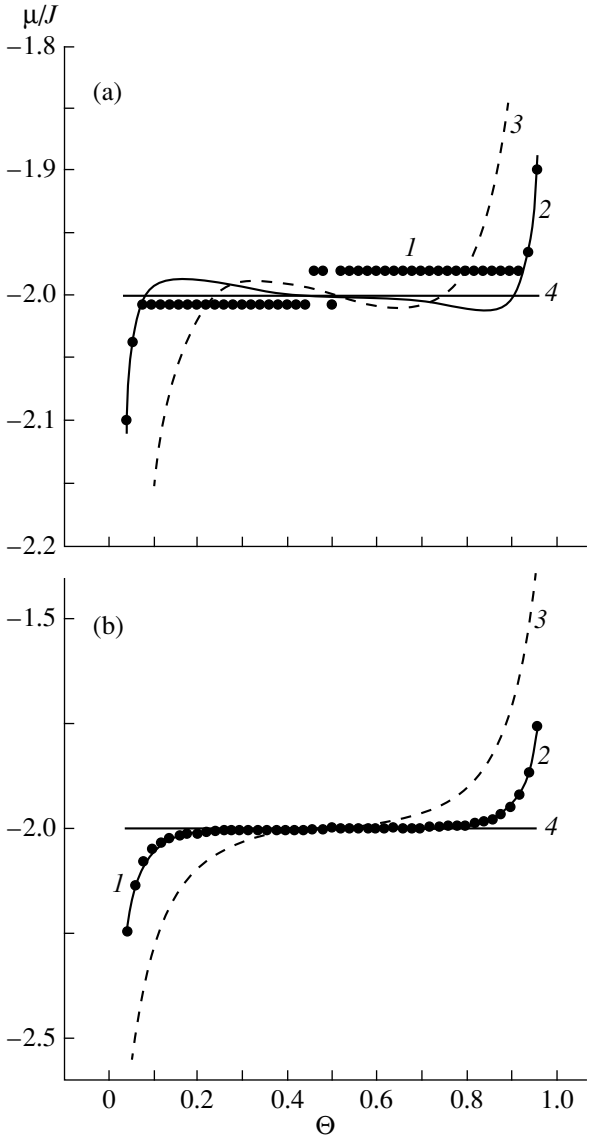

Fig. 1. Dependence of the chemical potential on concentration. T/T_c: (a) 0.95 and (b) 1.05; (*1*) results of Monte Carlo simulation, (*2*) SDA, (*3*) QCA, and (*4*) $\mu = -2J$ line.

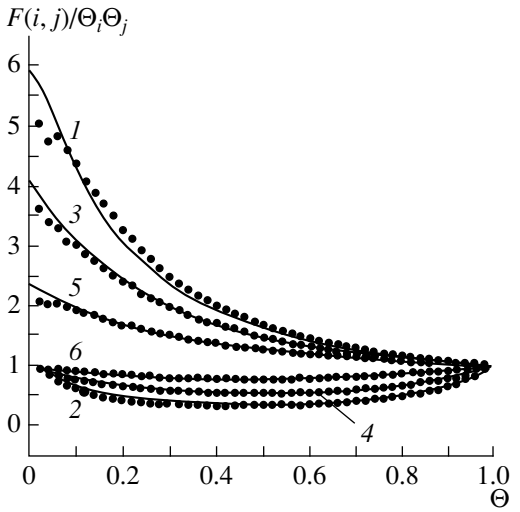

Fig. 2. The distribution functions. (*1*–*3*) $F(1, 1)/\Theta^2$; (*2*, *4*, *6*) $F(1, 0)/\Theta(1 - \Theta)$; T/T_c: (*1*, *2*) 0.95; (*3*, *4*) 1.2; (*5*, *6*) 2.0.

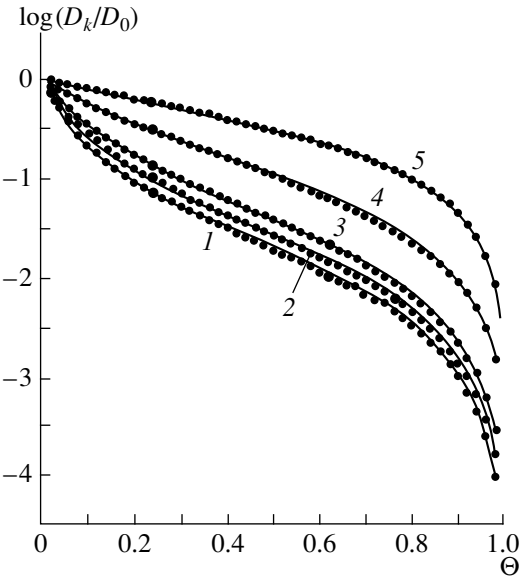

Fig. 3. Dependence of the kinetic diffusion coefficient on concentration. T/T_c: (*1*) 0.95, (*2*) 1.05, (*3*) 1.20, (*4*) 2.00, and (*5*) 6.00.

chemical approximation (QCA) and can easily be calculated on a personal computer in minimal time.

To check the accuracy of the suggested approach, a Monte Carlo simulation of the lattice systems was carried out. The methodology of the simulation was described in [25, 26].

In Fig. 1, the chemical potential isotherms are presented as functions of the particle density obtained using different techniques for a system of particles in a planar two-dimensional square lattice with the nearest-neighbor attraction. This figure demonstrates that SDA, as opposed to QCA, reproduces the data of Monte Carlo simulations with the same accuracy. It should be emphasized that, to compare these data, normalized temperatures T/T_c were used. For the Ising model, the exact value of the critical temperature $k_BT_c = 0.567J$ is known [10, 11] (here a rounded-off value is given), which should be compared with the value $0.565J$ obtained using SDA and $0.721J$ by QCA. It is seen that, in absolute temperature units, the QCA results in substantial errors.

According to the Maxwell rule, at $T < T_c$ the intersection of the chemical potential isotherm with the horizontal line $\mu = -2J$ determines the points of the lattice gas–lattice liquid phase transition. The proposed approximation reproduces the line of phase transition to within 2–3%, while QCA gives a considerably more narrow coexistence region of the two phases.

Figure 2 shows that SDA also reproduces the correlation properties of the lattice gas described by the distribution functions with a high accuracy. In this figure, ratios of the distribution functions to their values $(\Theta_i\Theta_j)$ for the noninteracting gas are given that underline the high accuracy of SDA, since the distribution functions themselves are close to zero in the low concentration range.

The dependence of the kinetic diffusion coefficient on concentration along several isotherms is shown in Fig. 3. The curves represent the results of calculations using relationship (38), with SDA used for the calculation of thermodynamic characteristics. It can be stated that Zhdanov's relationship reproduces the results of Monte Carlo simulations well in a wide range of thermodynamic parameter variation.

Attraction between the particles increases the depth of the traps, which results in a considerable decrease in the diffusion coefficient with increasing particle concentration. Since the model is based on the activation mechanism of particle transfer, the temperature decrease results in a decrease in the diffusion coefficient.

In the logarithmic scale in Fig. 3, small distinctions between the data of Monte Carlo simulations and the results of calculations using Zhdanov's formula are not evident. These distinctions are analyzed in Fig. 4, which shows the ratios of the diffusion coefficient D_{Zh} as calculated by (38) with the use of Monte Carlo computations of the chemical potential and the distribution function $F(0,0)$ and the diffusion coefficient D_{KG}, which was also obtained from computer simulations, but with the use of Eq. (40).

For systems with attraction (Fig. 4a), the error of Eq. (38) does not exceed 20% even in the range of low temperatures and high concentrations. In comparison with the variation by 3–4 orders of magnitude of the diffusion coefficient (Fig. 3), this error should be considered insignificant.

For systems with nearest neighbor repulsion (Fig. 4b) in the existence range of the ordered 2×2

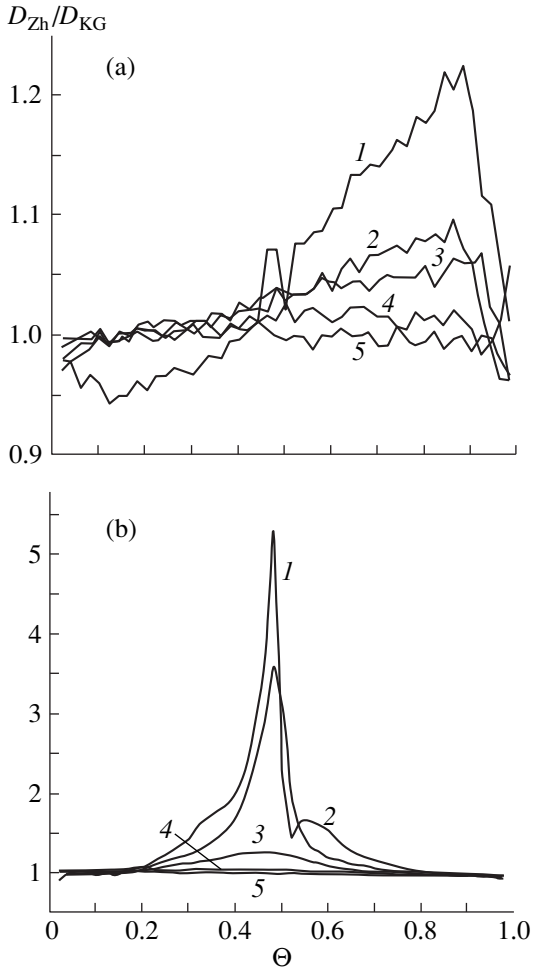

Fig. 4. Results of the simulations using Zhdanov's formula (D_{Zh}) and the Kubo–Green relationship (D_{KG}) of the kinetic diffusion coefficient of the lattice gas with attraction (a) and repulsion (b) of the nearest neighbors. (a) T/T_c: (*1*) 0.95, (*2*) 1.05, (*3*) 1.20, (*4*) 2.00, and (*5*) 6.00; (b) T/T_c: (*1*) 0.50, (*2*) 0.80, (*3*) 1.20, (*4*) 2.00, and (*5*) 6.00.

phase ($T < T_c$, $\Theta \approx 0.5$), the above ratio of the diffusion coefficients can reach a few units, increasing with decreasing temperatures. This means that, in this range, relationship (38) cannot be used. Since Zhdanov's expression follows from the exact relationships for the diffusion coefficient, neglecting the memory effects, it can be stated that the role of these effects in the ordered phase is essential.

CONCLUSION

From the general equation of the particle density evolution written in the framework of the method of nonequilibrium ensembles proposed by D.N. Zubarev, rigorous expressions have been obtained for the coefficients of diffusion and electrical conductivity of lattice systems, which take into account the effects of spatial dispersion and memory. It has been found that, in the general case, the electrical conductivity coefficient is proportional to the kinetic diffusion coefficient.

In the hydrodynamic limit (long wavelengths, low frequencies) ignoring the memory effects, it has been shown that, from the general expression for the diffusion coefficient, Zhdanov's relationship follows, which expresses the diffusion coefficient using equilibrium characteristics of the lattice system.

To calculate thermodynamic characteristics and distribution functions, the self-consistent diagrammatical approximation has been proposed. It provides simple expressions for the average potentials similar to those of the quasi-chemical approximation, while, in contrast to the latter, ensuring that the system with the nearest-neighbor attraction has an accuracy of thermodynamic calculations within the error of Monte Carlo simulations. The use of equilibrium values obtained by SDA in Zhdanov's relationship makes it possible to reproduce with good accuracy the kinetic diffusion coefficient values obtained by computer simulations. It has been shown that for a lattice gas with the nearest neighbor interaction, the Zhdanov's relationship reproduces the kinetic diffusion coefficient well throughout the range of thermodynamic variables, with the exception of the region of the ordered phase of the system with repulsion.

The relationship between the correlation factors of the self-diffusion, many-particle, and Haven factors is discussed.

ACKNOWLEDGMENTS

This work was supported by INTAS (Project no. 96-0533).

REFERENCES

1. M. V. Perfil'ev, A. K. Demin, B. I. Kuzin, and A. S. Lipilin, *High-Temperature Electrolysis of Gases* (Nauka, Moscow, 1988).
2. C. A. Angell, Chem. Rev. **90**, 523 (1990).
3. J. P. Clerc, G. Giraund, J. M. Laugier, and J. M. Luch, Adv. Phys. **39** (3), 191 (1990).
4. R. Gomer, Rep. Prog. Phys. **53**, 917 (1990).
5. A. R. Allnatt and A. R. Lidiard, *Atomic Transport in Crystals* (Cambridge Univ. Press, Cambridge, 1993).
6. V. P. Zhdanov, *Elementary Physicochemical Processes on Solid Surfaces* (Plenum, New York, 1991).
7. K. Funke, Prog. Solid State Chem. **22**, 111 (1993).
8. R. Nassif, Y. Boughaleb, A. Hekkouri, *et al.*, Eur. Phys. J. B **1,** 453 (1998).
9. N. V. Nikonorov and G. T. Petrovskiĭ, Fiz. Khim. Stekla **25** (1), 21 (1999).
10. M. E. Fisher, *The Nature of Critical Points* (Univ. of Colorado Press, Boulder, 1965; Mir, Moscow, 1968).
11. K. Huang, *Statistical Mechanics* (Wiley, New York, 1963; Mir, Moscow, 1966).
12. G. S. Bokun, C. Uebing, V. S. Vikhrenko, and V. A. Zhuk, Solid State Ionics **119**, 331 (1999).

13. R. Kikuchi, Prog. Theor. Phys. Suppl. **115**, 1 (1994).
14. A. Danani, R. Ferrando, E. Scalas, and M. Torri, Int. J. Mod. Phys. **11**, 2211 (1997).
15. L. P. Kadanoff and J. Swift, Phys. Rev. **165**, 310 (1968).
16. A. A. Tarasenko and A. A. Chumak, Fiz. Tverd. Tela (Leningrad) **22**, 2939 (1980) [Sov. Phys. Solid State **22**, 1716 (1980)].
17. D. A. Redd, Surf. Sci. **102**, 588 (1981).
18. V. P. Zhdanov, Surf. Sci. **149** (1), L13 (1985).
19. D. N. Zubarev, *Nonequilibrium Statistical Thermodynamics* (Nauka, Moscow, 1971; Consultants Bureau, New York, 1974).
20. D. Zubarev, V. Morozov, and G. Repke, in *Statistical Mechanics of Nonequilibrium Processes* (Akademic, Berlin, 1997), Vol. 2.
21. K. Compaan and T. Haven, Trans. Faraday Soc. **52**, 786 (1956).
22. H. Okazaki, J. Phys. Soc. Jpn. **23**, 355 (1967).
23. G. E. Murch, Solid State Ionics **7**, 177 (1982).
24. R. A. Tahir-Kheli, Phys. Rev. B **35** (11), 5503 (1987).
25. C. Uebing and R. A. Gomer, J. Chem. Phys. **95**, 7626 (1991).
26. C. Uebing and R. Gomer, J. Chem. Phys. **100**, 7759 (1994).

Translated by M. Lebedev

Technical Physics, Vol. 45, No. 11, 2000, pp. 1383–1389. Translated from Zhurnal Tekhnicheskoĭ Fiziki, Vol. 70, No. 11, 2000, pp. 9–14.

Calculation of the Heat Transfer between Coaxial Cylinders for Arbitrary Knudsen Numbers

S. A. Savkov and A. A. Yushkanov

Orel State University, Orel, 302015 Russia

Received March 4, 1999; in final form, December 6, 1999

Abstract—The problem of calculating the heat flux between coaxial cylinders is considered. A procedure that is analogous to the method of half-spatial moments is applied to solving the kinetic equation. The calculation results for the Bhatnagar–Gross–Krook model (BGK) of the collision integral for the case of purely diffuse reflection are presented. © *2000 MAIK "Nauka/Interperiodica".*

The description of gas properties for arbitrary Knudsen numbers is one of the classic problems in the kinetic theory of gases. A sufficiently complete review of publications on this problem is given in [1, 2]. It should be noted that most of the experimental data and results of numerical solution are presented as a ratio in comparison with the corresponding data from the gas-dynamic solution. In the case of a rarefied gas, the results being compared differ appreciably from each other, which indicates that the range of intermediate and large Knudsen numbers is far from being studied. The analytical results known at present were obtained using the Lees method [1]. The authors here confine themselves to a consideration of only the simplest function, which does not give a correct description of the distribution of the gas molecules as the distance from the inner cylinder increases and does not allow one to correctly formulate the boundary conditions at the surface of the outer cylinder.

Thus, let us consider two coaxial cylinders of radii $R_1 < R_2$ between which a constant temperature difference $\Delta T = T_1 - T_2$ is maintained. The temperature difference is assumed to be small enough to linearize the problem.

Let us introduce a cylindrical coordinate system with the z-axis coinciding with the cylinder axis. The gas state between the cylinders is described by the Boltzmann kinetic equations (see, for instance, [3]). Confining ourselves to the BGK model of the collision integral [4] and taking into account the linearity and axial symmetry of the problem, let us write

$$C_r\frac{\partial\Phi}{\partial r}+\frac{C_\varphi^2}{r}\frac{\partial\Phi}{\partial C_r} = \nu\left(\frac{\delta n}{n_0}+(C^2-3/2)\frac{\Delta T}{T_0}+2\mathbf{C}\mathbf{G}-\Phi\right). \quad (1)$$

Here,

$$\frac{\delta n}{n_0} = \pi^{-3/2}\int\Phi\exp(-C^2)d\mathbf{C},$$

$$\frac{\delta T}{T_0} = \pi^{-3/2}\int\Phi\left(\frac{2}{3}C^2-1\right)\exp(-C^2)d\mathbf{C},$$

$$\mathbf{G} = \pi^{-3/2}\int\Phi\mathbf{C}\exp(-C^2)d\mathbf{C}, \quad (2)$$

$$\nu = \frac{\sqrt{\pi}}{3\lambda} = \frac{5n}{\kappa}\sqrt{\frac{k^2T_0}{8m}},$$

where Φ is a correction to the equilibrium distribution function; $\mathbf{C} = \mathbf{V}\sqrt{m/2kT_0}$ is the nondimensional velocity of the gas molecules; λ is the mean free path length of the gas molecules; κ is the thermal conductivity of the gas; T_0 and n_0 are certain values of the gas temperature and the concentration of the gas molecules, respectively, that are assumed to be equilibrium values that, without loss of generality, can be taken to be equal to the temperature and the concentration of the molecules reflected from the surface of the outer cylinder.

The correction sought for must satisfy the boundary conditions for the interaction between the gas molecules and the surfaces of both the inner and outer cylinders. These boundary conditions, in the very general form (see, for instance, [3]), can be written as follows:

$$\Phi_k^r = \Omega_k\Phi_k^i \quad \text{at} \quad r = R_k (k = 1, 2), \quad (3)$$

where Φ_k^i and Φ_k^r are functions describing the velocity distributions of the molecules incident on, and reflected from, the surface of the corresponding cylinder and Ω_k is the integral operator governed by the character of the gas–surface interaction.

In the conventional approach [1], the two-stream distribution function is used, one stream being that of molecules with velocity vectors inside the wedgelike

1063-7842/00/4511-1383$20.00

area affected by the inner cylinder and the other stream being that of molecules with velocity vectors outside this area, so that the boundary condition at $r = R_1$ can be satisfied. To satisfy the boundary conditions at the surface of the outer cylinder, let us distinguish the molecules with positive and negative velocity projections C_r; that is, represent and write the distribution function sought for in the form

$$\Phi = \Phi_1 H_1 + \Phi_2 H_2 + \Phi_3 H_3, \tag{4}$$

where

$$H_1 = H(C_r - C_p\sqrt{1 - R_1^2/r^2}),$$
$$H_2 = H(C_r) - H_1, \quad H_3 = H(-C_r),$$

$$C_p = \sqrt{C^2 - C_z^2}, \quad H(x) = \begin{cases} 1 & \text{at } x > 0 \\ 0 & \text{at } x < 0 \end{cases}$$

is the conventional Heaviside function.

The use of such a distribution function allows one to write conditions (3) in the form

$$\Phi_1 = \Omega_1 \Phi_3 \quad \text{at} \quad r = R_1 \quad \text{and}$$
$$\Phi_3 = \Omega_2(\Phi_1 H_1 + \Phi_2 H_2) \quad \text{at} \quad r = R_2. \tag{5}$$

We shall seek function Φ_i in a form which is analogous to the Chapman–Enskog distribution

$$\Phi_i = a_1^i + a_2^i(3/2 - C^2) + a_3^i C_r + a_4^i C_r(5/2 - C^2). \tag{6}$$

Let us note that, in the conventional approach, only the moments defining the temperature field and the concentration of the gas molecules are considered. The moments describing the heat and mass fluxes are not taken into account, which prevents one (in the case $R_2 - R_1 \gg \lambda$) from obtaining the correct description of the gas state within the gas-dynamic region, that is, at sufficiently large distances from the cylinder surfaces in comparison with the free path length.

Coefficients a_j^i, which depend only on r, are determined from the solution of the moment equations. To derive the moment equations, let us multiply kinetic Eq. (1) with distribution functions (4), (6) successively by $\exp(-C^2)H_j$, $C^2\exp(-C^2)H_j$, $C_r\exp(-C^2)H_j$, and $C_r(5/2 - C^2)\exp(-C^2)H_j$ and integrate with regard to the velocity. Introducing a new variable $x = r/R_1$, we obtain

$$\frac{\pi}{4x}\frac{d}{dx}(2a_1^1 - a_2^1) + \frac{\sqrt{\pi}}{2}\left(\phi + \frac{\gamma}{x}\right)\frac{da_3^1}{dx} + \frac{\sqrt{\pi}}{2}\left(\phi - \frac{\gamma}{x}\right)\frac{a_3^1}{x}$$
$$= R_1\nu\left\{\sqrt{\pi}\left(\frac{1}{2x^2} + \frac{\phi^2}{\pi} - \phi\right)a_1^1 - \frac{\sqrt{\pi}}{4x^2}a_2^1\right.$$
$$+ \left(\frac{\gamma}{x} + 2\phi - \pi\right)\frac{a_3^1}{2x} + (\phi - \pi)\frac{a_4^1}{4x}$$
$$+ \frac{\sqrt{\pi}}{2}\left(\phi - \frac{2}{\pi}\phi^2 + \frac{x-1}{x^2}\right)a_1^2 - \frac{\sqrt{\pi}}{4}\frac{x-1}{x^2}a_2^2$$
$$+ \left(\frac{\pi}{2x} + \phi\frac{x-2}{x} - \frac{\gamma}{x^2}\right)\frac{a_3^2}{2} + \frac{\phi}{4}\frac{x-1}{x}a_4^2$$
$$\left. + \frac{\sqrt{\pi}}{2}\left(\phi - \frac{1}{x}\right)a_1^3 + \frac{\sqrt{\pi}}{4x}a_2^3 + \left(\frac{\pi}{4x} - \frac{\phi}{2}\right)a_3^3 - \frac{\phi}{4}a_4^3\right\}, \tag{7}$$

$$\frac{\pi}{2x}\frac{d}{dx}(2a_1^1 - 3a_2^1) + \frac{5\sqrt{\pi}}{4}\left(\phi + \frac{\gamma}{x}\right)\frac{d}{dx}(a_3^1 - a_4^1)$$
$$+ \frac{5\sqrt{\pi}}{4}\left(\phi - \frac{\gamma}{x}\right)\frac{a_3^1 - a_4^1}{x}$$
$$= R_1\nu\left\{\frac{\sqrt{\pi}}{2}\left(\frac{2}{x^2} + \frac{3\phi^2}{\pi} - 3\phi\right)a_1^1\right.$$
$$- \frac{\sqrt{\pi}}{2}\left(\frac{1}{x^2} + \frac{3\phi^3}{\pi} - 3\phi\right)a_2^1 + \left(\frac{\gamma}{x} + 3\phi - \pi\right)\frac{a_3^1}{x}$$
$$+ \frac{\pi - \phi}{2x}a_4^1 + \sqrt{\pi}\left(\frac{3\phi}{4} - \frac{3\phi^2}{2\pi} + \frac{x-1}{x^2}\right)a_1^2 \tag{8}$$
$$- \sqrt{\pi}\left(\frac{3\phi}{4} - \frac{3\phi^2}{2\pi} + \frac{x-1}{2x^2}\right)a_2^2$$
$$+ \left(\frac{\pi}{2x} - \frac{\gamma}{x^2} + \phi\frac{x-2}{x}\right)a_3^2 - \frac{\phi}{2}\frac{x-1}{x}a_4^2$$
$$+ \sqrt{\pi}\left(\frac{3}{4}\phi - \frac{1}{x}\right)a_1^3 + \frac{\sqrt{\pi}}{4}\left(\frac{2}{x} - 3\phi\right)a_2^3$$
$$\left. + \left(\frac{\pi}{2x} - \phi\right)a_3^3 + \frac{\phi}{2}a_4^3\right\},$$

$$\frac{\sqrt{\pi}}{2}\left(\phi + \frac{\gamma}{x}\right)\frac{d(a_1^1 - a_2^1)}{dx}$$
$$+ \pi\frac{3x^2 - 1}{8x^3}\frac{d(2a_3^1 - a_4^1)}{dx} + \pi\frac{2a_3^1 - a_4^1}{8x^4}$$
$$= R_1\nu\left\{\left(\frac{\gamma}{x} + 2\phi - \pi\right)\frac{2a_1^1 - a_2^1}{4x}\right.$$
$$+ \frac{\sqrt{\pi}}{2}\left(\frac{2\gamma\phi}{\pi x} - \frac{\gamma}{x} - \phi + \frac{\phi^2}{\pi} + \frac{x^2 - 1}{\pi x^4} + \frac{7}{12x^2}\right)a_3^1 \tag{9}$$
$$\left. - \frac{\sqrt{\pi}a_4^1}{48x^2} + \left(\gamma - \frac{\gamma}{x} + \phi x - 2\phi + \frac{\pi}{2}\right)\frac{2a_1^2 - a_2^2}{4x}\right.$$

$$+\sqrt{\pi}\left(\frac{\gamma}{4x}-\frac{\gamma\phi}{\pi x}+\frac{\phi}{4}-\frac{\phi^2}{2\pi}-\frac{x^2-1}{2\pi x^4}+\frac{7(x-1)}{24x^2}\right)a_3^2$$

$$-\sqrt{\pi}\frac{x-1}{48x^2}a_4^2+\left(\frac{\pi}{2x}-\frac{\gamma}{x}-\phi\right)\frac{2a_1^3-a_2^3}{4}$$

$$+\sqrt{\pi}\left(\frac{\gamma}{4x}+\frac{\phi}{2}-\frac{7}{24x}\right)a_3^3+\frac{a_4^3\sqrt{\pi}}{48x}\Bigg\},$$

$$\frac{5\sqrt{\pi}}{4}\left(\phi+\frac{\gamma}{x}\right)\frac{da_2^1}{dx}-\pi\frac{3x^2-1}{16x^3}\frac{d(2a_3^1-13a_4^1)}{dx}$$

$$-\pi\frac{2a_3^1-13a_4^1}{16x^4}=R_1\nu\Bigg\{\frac{\phi-\pi}{8x}(2a_1^1+7a_2^1)$$

$$-\frac{a_3^1\sqrt{\pi}}{48x^2}+\frac{5\sqrt{x}}{4}\left(\frac{11}{24x^2}-\frac{\gamma}{x}-\phi\right)a_4^1 \qquad (10)$$

$$+\frac{\pi-2\phi}{16x}(2a_1^2+7a_2^2)-\sqrt{\pi}\frac{x-1}{96x^2}(2a_3^2-55a_4^2)$$

$$+\pi\frac{2a_1^3+7a_2^3}{16x}+\sqrt{\pi}\frac{2a_3^3-55a_4^3}{96x}\Bigg\},$$

$$\pi\frac{x-1}{4x}\frac{d}{dx}(2a_1^2-a_2^2)+\frac{\sqrt{\pi}}{2}\left(\frac{\pi}{2}-\phi-\frac{\gamma}{x}\right)\frac{da_3^2}{dx}$$

$$+\frac{\sqrt{\pi}}{2}\left(\frac{\pi}{2}-\phi+\frac{\gamma}{x}\right)\frac{a_3^2}{x}+\frac{\pi}{8x}(2a_1^2-a_2^2-2a_1^3+a_2^3)$$

$$=R_1\nu\Bigg\{\frac{\sqrt{\pi}}{2}\left(\phi-\frac{2\phi^2}{\pi}+\frac{x-1}{x^2}\right)a_1^1-\frac{\sqrt{\pi}(x-1)}{4x^2}a_2^1$$

$$+\left(\gamma-\frac{\gamma}{x}+\frac{\pi}{2}+\phi x-2\phi\right)\frac{a_3^1}{2x}+(\pi-2\phi)\frac{a_4^1}{8x}$$

$$+\frac{\sqrt{\pi}}{2}\left(\frac{2\phi^2}{\pi}-\frac{\pi}{2}+\frac{(x-1)^2}{x^2}\right)a_1^2-\frac{\sqrt{\pi}}{4}\frac{(x-1)^2}{x^2}a_2^2 \qquad (11)$$

$$-\left(\frac{\gamma}{2x}+\phi\right)\frac{x-1}{x}a_3^2-(2\phi+\pi)\frac{x-1}{8x}a_4^2$$

$$+\frac{\sqrt{\pi}}{2}\left(\frac{\pi}{2}-\phi-1+\frac{1}{x}\right)a_1^3+\sqrt{\pi}\frac{x-1}{4x}a_3^2$$

$$+\frac{2\phi x-\pi}{4x}a_3^3+\frac{2\phi-\pi}{8}a_4^3\Bigg\},$$

$$\pi\frac{x-1}{2x}\frac{d}{dx}(2a_1^2-3a_2^2)+\frac{5\sqrt{\pi}}{4}\left(\frac{\pi}{2}-\phi-\frac{\gamma}{x}\right)\frac{d}{dx}(a_3^2-a_4^2)$$

$$+\frac{5\sqrt{\pi}}{4}\left(\frac{\pi}{2}-\phi+\frac{\gamma}{x}\right)\frac{a_3^2-a_4^2}{x}+\frac{\pi}{4x}(2a_1^2-3a_2^2$$

$$-2a_1^3+3a_2^3)=R_1\nu\Bigg\{\sqrt{\pi}\left(3\phi\frac{\pi-2\phi}{4\pi}+\frac{x-1}{x^2}\right)a_1^1$$

$$-\sqrt{\pi}\left(3\phi\frac{\pi-2\phi}{4\pi}+\frac{x-1}{2x^2}\right)a_2^1$$

$$+\left(\gamma-\frac{\gamma}{x}+\frac{\pi}{2}+\phi x-2\phi\right)\frac{a_3^1}{x}+(2\phi-\pi)\frac{a_4^1}{4x} \qquad (12)$$

$$+\sqrt{\pi}\left(\frac{3\phi^2}{2\pi}-\frac{3\pi}{8}+\frac{(x-1)^2}{x^2}\right)a_1^2$$

$$+\sqrt{\pi}\left(\frac{3\pi}{8}-\frac{(x-1)^2}{2x^2}-\frac{3\phi^2}{2\pi}\right)a_2^2-\left(\frac{\gamma}{x}+2\phi\right)\frac{x-1}{x}a_3^2$$

$$+(2\phi+\pi)\frac{x-1}{4x}a_4^2+\sqrt{\pi}\left(\frac{3}{8}(\pi-2\phi)-1+\frac{1}{x}\right)a_1^3$$

$$+\sqrt{\pi}\left(\frac{3}{8}(2\phi-\pi)+\frac{x-1}{2x}\right)a_2^3$$

$$-\left(\frac{\pi}{2x}-\phi\right)a_3^3-\left(\frac{\phi}{2}-\frac{\pi}{4}\right)a_4^3\Bigg\},$$

$$\frac{\sqrt{\pi}}{2}\left(\frac{\pi}{2}-\phi-\frac{\gamma}{x}\right)\frac{d(a_1^2-a_2^2)}{dx}+\frac{\pi}{8}\left(2-\frac{3}{x}+\frac{1}{x^3}\right)$$

$$\times\frac{d(2a_3^2-a_4^2)}{dx}+\pi\frac{x^3-1}{8x^4}(2a_3^2-a_4^2)$$

$$=R_1\nu\Bigg\{\left(x\phi-2\phi+\frac{\pi}{2}-\frac{\gamma}{x}\right)\frac{2a_1^1-a_2^1}{4x}$$

$$+\sqrt{\pi}\left(\frac{\phi}{4}-\frac{\phi^2}{2\pi}-\frac{\gamma\phi}{\pi x}+\frac{\gamma}{4x}+\frac{x^2-1}{2\pi x^4}+\frac{7(x-1)}{24x^2}\right)a_3^1 \qquad (13)$$

$$-\sqrt{\pi}\frac{x-1}{48x^2}a_4^1-\left(\frac{\gamma}{2x}+\phi\right)\frac{x-1}{2x}(2a_1^2-a_2^2)$$

$$+\sqrt{\pi}\left(\frac{\gamma\phi}{\pi x}+\frac{\phi^2}{2\pi}-\frac{\pi}{8}+\frac{x^2-1}{2\pi x^4}+\frac{7(x-1)^2}{24x^2}\right)a_3^2$$

$$-\frac{\sqrt{\pi}}{48x^2}(x-1)^2a_4^2+\left(\frac{\gamma}{x}+\phi-\frac{\pi}{2x}\right)\frac{2a_1^3-a_2^3}{4}$$

$$+\sqrt{\pi}\left(\frac{\pi}{8}-\frac{\gamma}{4x}-\frac{\phi}{4}-\frac{7(x-1)}{24x}\right)a_3^3+\sqrt{\pi}\frac{x-1}{48x}a_4^3\Bigg\},$$

$$\sqrt{\pi}\frac{5}{4}\left(\frac{\pi}{2}-\phi-\frac{\gamma}{x}\right)\frac{da_2^2}{dx}+\frac{\pi}{16}\left(\frac{3}{x}-2-\frac{1}{x^3}\right)$$
$$\times\frac{d(2a_3^2-13a_4^2)}{dx}-\pi\frac{x^3-1}{16x^4}(2a_3^2-13a_4^2)$$
$$=R_1\nu\left\{\left(\phi\frac{x-1}{8x}(2a_1^1+7a_2^1\right)-\sqrt{\pi}\frac{x-1}{96x^2}(2a_3^1-55a_4^1)\right. \quad (14)$$
$$-\frac{x-1}{16x}(2\phi+\pi)(2a_1^2+7a_2^2)-\sqrt{\pi}\frac{(x-1)^2}{48x^2}a_3^2$$
$$+\sqrt{\pi}\frac{5}{4}\left(\frac{\gamma}{x}+\phi-\frac{\pi}{2}+\frac{11(x-1)^2}{24x^2}\right)a_4^2$$
$$\left.+\pi\frac{x-1}{16x}(2a_1^3+7a_2^3)+\sqrt{\pi}\frac{x-1}{96x}(2a_3^3-55a_4^3)\right\},$$

$$\frac{\pi}{4}\frac{d}{dx}(a_2^3-2a_1^3)+\frac{\pi}{8x}(2a_1^2-a_2^2-2a_1^3+a_2^3)$$
$$+\frac{\pi^{3/2}}{4}\frac{da_3^3}{dx}+\frac{\pi^{3/2}}{4x}a_3^3$$
$$=R_1\nu\left\{\sqrt{\pi}\frac{\phi x-1}{2x}a_1^1+\frac{\sqrt{\pi}}{4x}a_2^1+\left(\frac{\pi}{2x}-\frac{\gamma}{x}-\phi\right)\frac{a_3^1}{2}\right. \quad (15)$$
$$+\frac{\pi a_4^1}{8x}+\sqrt{\pi}\left(\frac{\pi}{2}-\phi-1+\frac{1}{x}\right)\frac{a_1^2}{2}+\sqrt{\pi}\frac{x-1}{4x}a_2^2$$
$$+\left(\phi-\frac{\pi}{2x}+\frac{\gamma}{x}\right)\frac{a_3^2}{2}+\frac{\pi}{8}\frac{x-1}{x}a_4^2$$
$$\left.+\sqrt{\pi}\frac{2-\pi}{4}a_1^3+-\sqrt{\pi}\frac{a_2^3}{4}+\frac{a_4^3\pi}{8}\right\},$$

$$\frac{\pi}{2}\frac{d}{dx}(3a_2^3-2a_1^3)+\frac{\pi}{4x}(2a_1^2-3a_2^2-2a_1^3+3a_2^3)$$
$$+\frac{5\pi^{3/2}}{8}\frac{d(a_3^3-a_4^3)}{dx}+\frac{5\pi^{3/2}}{8x}(a_3^3-a_4^3)$$
$$=R_1\nu\left\{\sqrt{\pi}\frac{3\phi x-4}{4x}a_1^1+\sqrt{\pi}\frac{2-3\phi x}{4x}a_2^1+\left(\frac{\pi}{2x}-\frac{\gamma}{x}-\phi\right)a_3^1\right. \quad (16)$$
$$-\frac{\pi a_4^1}{4x}+\sqrt{\pi}\left(\frac{3\pi-6\phi}{8}-1+\frac{1}{x}\right)a_1^2$$
$$+\sqrt{\pi}\left(\frac{6\phi-3\pi}{8}+\frac{x-1}{2x}\right)a_2^2+\left(\phi+\frac{\gamma}{x}-\frac{\pi}{2x}\right)a_3^2$$
$$\left.-\frac{\pi(x-1)}{4x}a_4^2+\sqrt{\pi}\frac{8-3\pi}{8}a_1^3+\sqrt{\pi}\frac{3\pi-4}{8}a_2^3-\frac{a_4^3\pi}{4}\right\},$$

$$\frac{\pi^{3/2}}{4}\frac{d}{dx}(a_1^3-a_2^3)-\frac{\pi}{4}\frac{d(2a_3^3-a_4^3)}{dx}-\frac{\pi}{8x}(2a_3^3-a_4^3)$$
$$=R_1\nu\left\{\frac{\pi-2\phi x}{8x}(2a_1^1-a_2^1)+\sqrt{\pi}\left(\phi x+\gamma-\frac{7}{6}\right)\frac{a_3^1}{4x}\right.$$
$$+\frac{\sqrt{\pi}}{48x}a_4^1+\frac{2\phi x-\pi}{8x}(2a_1^2-a_2^2) \quad (17)$$
$$+\sqrt{\pi}\left(\pi x-2\phi x-2\gamma-\frac{7}{3}(x-1)\right)\frac{a_3^2}{8x}$$
$$\left.+\sqrt{\pi}\frac{x-1}{48x}a_4^2+\sqrt{\pi}\frac{7-3\pi}{24}a_3^3-\frac{\sqrt{\pi}}{48}a_4^3\right\},$$

$$\frac{5\pi^{3/2}}{8}\frac{da_2^3}{dx}+\frac{\pi}{8}\frac{d(2a_3^3-13a_4^3)}{dx}+\frac{\pi}{16x}(2a_3^3-13a_4^3)$$
$$=R_1\nu\left\{-\frac{\phi}{8}(2a_1^1+7a_2^1)+\frac{\sqrt{\pi}}{96x}(2a_3^1-55a_4^1)\right. \quad (18)$$
$$+\frac{2\phi-\pi}{16}(2a_1^2+7a_2^2)+\sqrt{\pi}\frac{x-1}{96x}(2a_3^2-55a_4^2)$$
$$\left.+\frac{\pi}{16}(2a_1^3+7a_2^3)-\sqrt{\pi}\frac{a_3^3}{48}+\sqrt{\pi}\frac{55-60\pi}{96}a_4^3\right\},$$

where $\phi=\arcsin x^{-1}$ and $\gamma=\cos\phi=\sqrt{1-x^{-2}}$.

Summing up Eqs. (7), (11), and (15), as well as (8), (12), and (16), we obtain the mass and energy conservation laws

$$\frac{d}{dx}Jx=0 \quad \text{and} \quad \frac{d}{dx}Qx=0,$$

respectively, which can be integrated in explicit form. Here,

$$J=\pi^{-3/2}\int\Phi C_r\exp(-C^2)d\mathbf{C}$$
$$+\frac{2a_1^1-a_2^1}{4x\sqrt{\pi}}+\left(\frac{\gamma}{x}+\phi\right)\frac{a_3^1}{2\pi}+\frac{x-1}{4\sqrt{\pi}x}(2a_1^2-a_2^2) \quad (19)$$
$$+\left(\frac{\pi}{2}-\frac{\gamma}{x}-\phi\right)\frac{a_3^2}{2\pi}-\frac{2a_1^3-a_2^3}{4\sqrt{\pi}}+\frac{a_3^3}{4}$$

and

$$Q=\pi^{-3/2}\int\Phi C^2C_r\exp(-C^2)d\mathbf{C}$$

$$= \frac{2a_1^1 - 3_2^1}{2x\sqrt{\pi}} + \frac{5}{4\pi}\left(\frac{\gamma}{x} + \phi\right)(a_3^1 - a_4^1)$$
$$+ \frac{x-1}{2\sqrt{\pi}x}(2a_1^2 - 3a_2^2) + \frac{5}{4\pi}\left(\frac{\pi}{2} - \frac{\gamma}{x} - \phi\right)(a_3^2 - a_4^2) \quad (20)$$
$$- \frac{2a_1^3 - 3a_2^3}{2\sqrt{\pi}} + \frac{5}{8}(a_3^2 - a_4^2)$$

are the nondimensional mass and heat fluxes, respectively. In a similar way, the summation of Eqs. (9), (13), and (17) gives the momentum conservation law.

The solution of Eqs. (7)–(18) must satisfy conditions (5). The suggested approach being proposed allows one to use arbitrary forms of the reflection law (see, for instance, [5]). For a concrete numerical analysis, let us confine ourselves to a model of purely diffuse reflection; that is, we shall assume a Maxwellian distribution for the molecules reflected from the surfaces of each of the cylinders according to the Maxwell distribution function corresponding to their surface characteristics. Assuming that the distribution function for the molecules reflected from the outer cylinder is at equilibrium, we write

$$\Phi_1 = \frac{\Delta n}{n_2} + \left(C^2 - \frac{3}{2}\right)\frac{\Delta T}{T_2} \quad \text{at } x = 1 \quad \text{and}$$
$$\Phi_3 = 0 \quad \text{at } x = \frac{R_2}{R_1}. \quad (21)$$

Comparing (21) with (6), we obtain

$$a_1^1 = \frac{\Delta n}{n_2}, \quad a_2^1 = -\frac{\Delta T}{T_2}, \quad a_3^1 = a_4^1 = 0 \quad \text{at} \quad x = 1 \quad (22)$$

and

$$a_1^3 = a_2^3 = a_3^3 = a_4^3 = 0 \quad \text{at} \quad x = R_2/R_1. \quad (23)$$

In this case, the concentration difference $\Delta n = n_1 - n_2$ of the gas molecules should be determined from the conditions of zero mass flux between the cylinders ($J = 0$). Therefore, instead of the first conditions in (22), it is necessary to use the equality

$$2a_1^1 - a_2^1 - 2a_1^3 + a_2^3 + \sqrt{\pi}a_3^3 = 0 \quad (24)$$

following from (19) at $x = 1$.

Moreover, it is necessary to take into account that the set of moment equations has a singularity at the surface of the inner cylinder, conditioned by the region due to the collapse of an area in the velocity space, which corresponds to function Φ_2. Expanding the sought for solution into a series in powers of $\xi = x - 1$ and allowing for the requirement that the distribution function should be finite, we obtain four more conditions:

$$A_1 = A_2 = A_3 = A_4 = 0 \quad \text{at} \quad x = 1. \quad (25)$$

Here, $A_{1,2} = (x-1)a_{1,2}^2$ and $A_{3,4} = (\pi/2 - \phi x - \gamma/x)a_{3,4}^2$.

Thus, the boundary conditions are determined by the distribution functions of the molecules reflected from the surfaces of the inner and outer cylinders, i.e., by the values of Φ_1 at $r = R_1$ and Φ_3 at $r = R_2$, respectively, as well as by the requirement that function Φ_2 be finite at $r = R_2$.

The results of numerical solution of the set of equations (7)–(18) under conditions (22)–(25) may be represented in the form

$$Q = \frac{\Delta T}{T_2}\frac{R_1}{r}\left(\frac{4}{5}R_1\nu\ln(R_2/R_1) + \alpha\right)^{-1}. \quad (26)$$

Parameter α describes the difference of the heat flux from that obtained in the gas-dynamic solution. Figures 1–3 show the variation of this parameter with changing ratio of the radii of the cylinders, as well as with the degree of gas rarefaction.

It should be noted that the linear character of the dependence of α on the ratio R_1/R_2 is observed in Fig. 1 when the distance between the cylinders is much greater than the mean path length of the gas molecules, i.e., at $(R_2 - R_1) \gg 1$. In this case, expression (26) can be written in the form

$$Q = \frac{\Delta T}{T_2}\frac{R_1}{r}\left(\frac{4}{5}R_1\nu\ln(R_2/R_1) + \alpha^*(1 + R_1/R_2)\right)^{-1}, \quad (27)$$

where $\alpha^* = \lim_{R_2 \to \infty} \alpha$.

The variation of α^* with $R_1\nu$ is approximated by the expression

$$\alpha^* = \frac{\sqrt{\pi} + 2.4624(R_1\nu)^{0.9}}{1 + 2.3474(R_1\nu)^{0.9}}$$

to an accuracy of up to 0.3%.

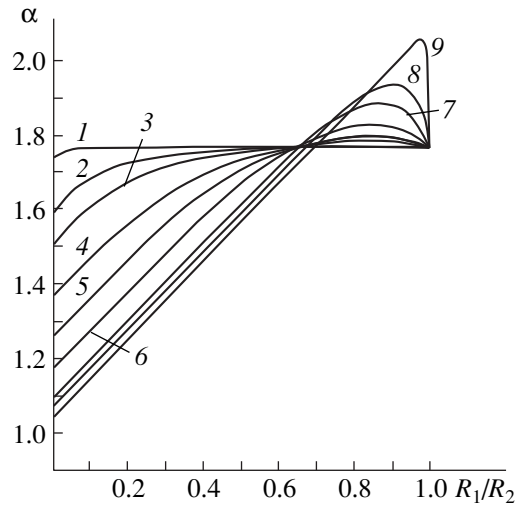

Fig. 1. Variation of parameter α with ratio R_1/R_2 at various $R_1\nu$: (*1*) 0.01, (*2*) 0.1, (*3*) 0.2, (*4*) 0.5, (*5*) 1, (*6*) 2, (*7*) 5, (*8*) 10, and (*9*) 100.

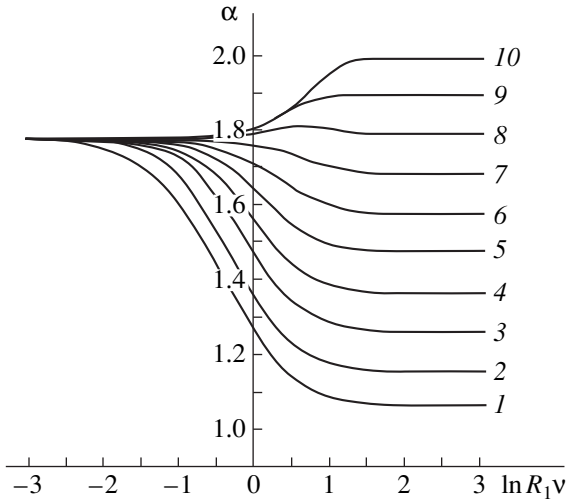

Fig. 2. Variation of parameter α with R_1ν at various ratios R_1/R_2: (*1*) 0.01. (*2*) 0.1, (*3*) 0.2, (*4*) 0.3, (*5*) 0.4, (*6*) 0.5, (*7*) 0.6, (*8*) 0.7, (*9*) 0.8, and (*10*) 0.9.

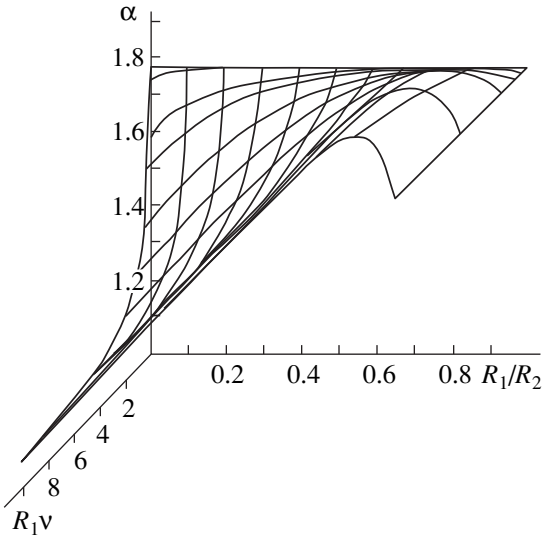

Fig. 3. The total profile of parameter α vs. the ratio between the radii of the cylinders and the degree of gas rarefaction.

It is obvious that the plot of function $\alpha^*(R_1\nu)$ practically coincides with curves *1* ($R_1/R_2 = 0.01$) in Figs. 2 and 3.

The consideration of cylinders of relatively large radii, when $R_1\nu \gg 1$ and $(R_2 - R_1)\nu \gg 1$, is of particular interest. In this case, α* ceases to depend on the degree of gas rarefaction and tends to the value

$$\alpha_\infty = 1.0489. \tag{28}$$

On the other hand, the set of moment equations permits an analytical solution in the limit considered, and the heat flux, to an accuracy up to the terms which are linear in the Knudsen number ($Kn_i = \lambda/R_i$), can be presented in the form

$$q = n(2k^3T^3/m)^{1/2}Q = \frac{\kappa}{r}\Delta T(\ln(R_2/R_1) + C_t(Kn_1 + Kn_2))^{-1}, \tag{29}$$

where C_t is the temperature change ramp coefficient.

Comparing (27) and (29) with allowance for (28) and the definition of ν in (2), we find

$$C_t = \frac{5\alpha_\infty}{4\nu\lambda} = 2.2193,$$

which differs by less than 1% from $C_t = 2.2049$, which was the value obtained by a numerical method in paper [6].

Note also the case $R_2/R_1 \longrightarrow 1$, when, in the velocity space, the region determining the contribution of the function Φ_2 is absent. As is seen from the plots presented, the value of parameter α in the regime considered varies from $2\alpha_\infty = 2.0978$ at $(R_2 - R_1)\nu \gg 1$, which corresponds to expression (29), to $\sqrt{\pi}$ at $(R_2 - R_1)\nu \ll 1$. This is explained by the fact that the gas molecules travel the distance between the cylinders practically without collisions. Consequently, the function Φ_3 remains equal to zero throughout the gas volume. Therefore, as is seen from conditions (22) and (24) and relation (20),

$$2a_1^1 = a_2^1 = -\frac{\Delta T}{T_2}, \quad Q = \frac{\Delta T}{T_2}\frac{R_1}{r}\frac{1}{\sqrt{\pi}}.$$

A similar situation also takes place at $R_1\nu \ll 1$. In this case, one can neglect the influence of the inner cylinder and assume that the distribution function coincides with the distribution of the molecules reflected from the surface of the outer cylinder. The difference between functions Φ_3 and Φ_2 thus vanishes (i.e., $a_i^2 = a_i^3 = 0$) and parameter α is equal to $\sqrt{\pi}$.

The conventional Lees method leads to an analogous relation

$$Q_s = \frac{\Delta T}{T_2}\frac{R_1}{r}\left(\frac{4}{5}R_1\nu\ln(R_2/R_1) + \sqrt{\pi}\right)^{-1}, \tag{30}$$

where the part of the parameter corresponding to α is assigned to $\sqrt{\pi}$, which is independent of the system characteristics.

The coincidence of expressions (26) and (30) takes place only in a collisionless regime when the radius of the inner cylinder or the distance between the cylinders is negligible in comparison with the free path length of the gas molecules. It has been shown that in these cases, the heat flux is exclusively governed by the conservation laws and the problem can be solved by simple qualitative reasoning.

The formal coincidence of the results is also observed in the gas-dynamic regime. However, in this case, the conventional Lees method gives a correction to the gas-dynamic solution that does not depend on the ratio of the cylinder radii and, in the limiting case when $R_2 \gg R_1$, corresponds to the greatly overvalued temperature change coefficient $C_t = 3.75$.

In an intermediate range of the ratio between the radii of the cylinders and the free path length of the gas molecules, parameter α varies in quite a wide interval, changing almost twofold. The value of α turns out to be close to the conventional one at the ratio R_1/R_2, which is about 0.7. In the case of $R_2 > 1.5R_1$, the conventional Lees method underestimates the heat flux. The maximum difference between Q and Q_s reaches 15% in the range $R_1\nu \sim 1$ at $R_2 \sim 10R_1$. When the gap between the cylinders is less than $0.5R_1$, the conventional method gives an overvalued result. In that case, the maximum difference between Q an Q_s reaches 10% in the region of the maxima of the curves in Fig. 1; i.e., at $R_1\nu \gg 1$ and R_2 it changes from approximately $1.1R_1$ to $1.2R_1$.

REFERENCES

1. L. Lees and Liu Chung-Yen, Phys. Fluids **5**, 1137 (1962).
2. Yu. G. Semyonov, S. F. Borisov, and P. E. Suetin, Int. J. Heat Mass Transfer **27**, 1789 (1984).
3. M. N. Kogan, *Dynamics of Rarefied Gas* (Nauka, Moscow, 1967).
4. P. L. Bhatnagar, E. P. Gross, and M. A. Krook, Phys. Rev. **94**, 511 (1954).
5. S. A. Savkov and A. A. Yushkanov, Mekh. Zhidk. Gaza, No. 5, 149 (1986).
6. Y. Sone and K. Aoki, Mem. Fac. Eng., Kyoto Univ. **49**, 237 (1987).

Translated by N. Mende

Technical Physics, Vol. 45, No. 11, 2000, pp. 1390–1398. Translated from Zhurnal Tekhnicheskoĭ Fiziki, Vol. 70, No. 11, 2000, pp. 15–23.

Capillary Vibrations of a Viscoelastic Medium under the Action of a Constant External Force

D. F. Belonozhko and A. I. Grigor'ev

Demidov State University, Sovetskaya ul. 14, Yaroslavl, 150000 Russia

E-mail: grig@uniyar.ac.ru

Received November 15, 1999.

Abstract—A layer of a viscoelastic liquid was found to exhibit two types of instabilities, aperiodic and vibrational, when its free surface was subjected to an external force. For the aperiodic instability, the critical condition and increment value were derived analytically. If the angle between the force direction and external normal to the free surface of the liquid is smaller than 45 degrees, only the vibrational instability sets up in the system; if the angle is larger, the aperiodic one alone is observed. © *2000 MAIK "Nauka/Interperiodica".*

INTRODUCTION

It is known that, when a very viscous medium is subjected to an external force that generates both normal and tangential stresses, a wavy relief forms on the its initially planar surface. Such effects take place during percussion (explosion) welding or when a silicon solid surface is irradiated by a high-energy atomic beam (see [1, 2] and refs. therein). There are still no appropriate theoretical explanations of these experimental data; therefore, the problem stated below is of interest.

(1) Consider a plane liquid film with a density ρ, kinematic viscosity ν_0, viscosity relaxation time τ, and thickness d on a solid substrate. The system is under the gravity field $\mathbf{g}$. Let the momentum flux of a material beam falling at an angle to the normal to the film exert a constant force action on the film surface. The spectrum of capillary motions in the liquid layer is to be determined.

Let $\Pi_{jk} = \delta V_j V_k$ be the momentum flux density tensor of the external force in a domain over the liquid surface (V_j are the beam velocity components, and δ is the beam density) [3]. For the sake of simplicity, we will solve the two-dimensional problem in the Cartesian coordinate system XOZ with the OZ-axis directed vertically up ($\mathbf{n}_z \| -\mathbf{g}$). The equations for the perturbed and unperturbed free surfaces of the liquid have the form $z = \xi(x, t)$ and $z = 0$, respectively, and the solid bottom is situated at $z = -d$. The matter flux into the liquid is neglected. In the small-amplitude-wave approximation, the full mathematical statement of the problem is given by

$$\frac{\partial \mathbf{U}}{\partial t} + [\nabla \times \mathbf{U}] \times \mathbf{U} = -\frac{1}{\rho}\left(P + \frac{U^2}{2}\right) + \nu \Delta \mathbf{U} + \mathbf{g}, \quad (1)$$

$$\mathrm{div}\mathbf{U} = 0, \quad (2)$$

$$z = \xi: \frac{\partial \xi}{\partial t} = U_z - U_x \frac{\partial \xi}{\partial x}, \quad (3)$$

$$\sigma_{jk} n_k^* + \Pi_{jk} n_k = P_\gamma n_j, \quad (4)$$

$$P_\gamma = -\gamma \frac{\partial^2 \xi}{\partial x^2}, \quad n_j = \begin{bmatrix} -\dfrac{\partial \xi}{\partial x} \\ 1 \end{bmatrix}, \quad n_j^* = \begin{bmatrix} \dfrac{\partial \xi}{\partial x} \\ -1 \end{bmatrix},$$

$$\Pi_{jk} = \begin{bmatrix} \delta V_x^2 & \delta V_x V_z \\ \delta V_x V_z & \delta V_z^2 \end{bmatrix},$$

$$\sigma_{jk} = \begin{bmatrix} \rho U_x^2 + P - 2\rho\nu \dfrac{\partial U_x}{\partial x} & \rho U_x U_z - \rho\nu\left(\dfrac{\partial U_x}{\partial z} + \dfrac{\partial U_z}{\partial x}\right) \\ \rho U_x U_z - \rho\nu\left(\dfrac{\partial U_x}{\partial z} + \dfrac{\partial U_z}{\partial x}\right) & \rho U_z^2 + P - 2\rho\nu \dfrac{\partial U_z}{\partial z} \end{bmatrix},$$

$$z = -d: \mathbf{U} = 0, \quad (5)$$

$$\xi = \xi_0 \exp(st - ikx), \quad (6)$$

$$\nu = \frac{\nu_0}{1 + s\tau}, \quad (7)$$

where

$$P_\gamma = -\gamma \frac{\partial^2 \xi}{\partial x^2}$$

1063-7842/00/4511-1390$20.00

is the Laplacian pressure under the perturbed free surface of the liquid [3, 4], γ is the surface tension coefficient, n_j is the column of the outer normal coordinates, and n_j^* is the column vector of the inner normal. The square matrices Π_{jk} and σ_{jk} contain the components of the momentum flux density tensor over and under the perturbed surface [3], respectively. Let a perturbation of the initially planar surface be traveling wave (6) with the wave number $k = 2\pi/\lambda$ and complex frequency s. As in [5], we assume that the viscosity ν depends on frequency according to Maxwell's formula (7).

(2) Problem (1)–(7) will be solved by expanding in the small amplitude ξ_0 of the wave perturbation. We assume that, for a given force, the velocity field in the liquid has only the horizontal component in the zero-order approximation and both the horizontal and vertical components in higher order approximations. Under this assumption, by applying the standard linearization procedure to (1)–(5), we obtain the problems of the zero- and first-order approximations with respect to ξ_0.

To find the zero-order approximation for the stationary component $p = p_0(z)$ of the pressure inside the liquid and for the horizontal component $u_0 = u_0(z)$ of the velocity, we have to solve the problem given by

$$\frac{d}{dz}\left(\frac{p_0}{\rho} + gz\right) = 0, \quad \frac{d^2u_0}{dz^2} = 0,$$

$$z = 0: -\delta V_x V_z - \rho\nu\frac{du_0}{dz} = 0,$$

$$-\delta V_z^2 + p_0 = 0,$$

$$z = -d: u_0 = 0.$$

The solution is easily obtained as

$$u_0 = U_0\left(1 + \frac{z}{d}\right), \quad U_0 = -\frac{\delta V_x V_z}{\rho\nu}d, \tag{8}$$

$$P = -\rho gz + \delta V_z^2. \tag{9}$$

The additions of the first order of smallness to the pressure $p = p(x, z, t)$ and velocity field $\mathbf{u} = u_x\mathbf{n}_x + u_z\mathbf{n}_z$, where $u_x = u_x(x, z, t)$ and $u_z = u_z(x, z, t)$, are given by the equations

$$\frac{\partial\mathbf{u}}{\partial t} + [\nabla \times u_0\mathbf{n}_x] \times \mathbf{u} + [\nabla \times \mathbf{u}] \times u_0\mathbf{n}_x$$

$$= -\nabla\left(\frac{p}{\rho} + u_0u_x\right) + \nu\Delta\mathbf{u},$$

$$\mathrm{div}(\mathbf{u}) = 0,$$

$$z = 0: u_z = \frac{\partial\xi}{\partial t} + u_0\frac{\partial\xi}{\partial x},$$

$$\frac{\partial\xi}{\partial x}(\delta V_x^2 - \delta V_z^2) + \rho u_0\frac{\partial\xi}{\partial t} = \rho\nu\left(\frac{\partial u_x}{\partial z} + \frac{\partial u_z}{\partial x}\right),$$

$$p + \rho g\xi - 2\rho\nu\frac{\partial u_z}{\partial z} = -\gamma\frac{\partial^2\xi}{\partial x^2},$$

$$z = -d: \mathbf{u} = 0.$$

With the Helmholtz theorem on the decomposition of an arbitrary vector field into the potential and rotational components, the first-order problem can be formulated in the scalar form

$$\hat{\mathbf{N}}_1 \equiv \frac{\partial}{\partial x}\mathbf{n}_x + \frac{\partial}{\partial z}\mathbf{n}_z, \quad \hat{\mathbf{N}}_2 \equiv -\frac{\partial}{\partial z}\mathbf{n}_x + \frac{\partial}{\partial x}\mathbf{n}_z,$$
$$\Delta \equiv \frac{\partial^2}{\partial x^2} + \frac{\partial^2}{\partial z^2}, \tag{10}$$

$$\mathbf{u} = \hat{\mathbf{N}}_1\varphi + \hat{\mathbf{N}}_2\psi, \tag{11}$$

$$\Delta\left(\frac{\partial\psi}{\partial t} - \nu\Delta\psi\right) + u_0\Delta\left(\frac{\partial\psi}{\partial x}\right) = 0, \tag{12}$$

$$\hat{\mathbf{N}}_2\left(\frac{\partial\psi}{\partial t} - \nu\Delta\psi - \frac{du_0}{dz}\varphi\right) + u_0\Delta\psi\mathbf{n}_z$$
$$= \hat{\mathbf{N}}_1\left(\frac{p}{\rho} + \frac{\partial\varphi}{\partial t} + u_0\left(\frac{\partial\varphi}{\partial x} - \frac{\partial\psi}{\partial z}\right) - \psi\frac{du_0}{dz}\right) = 0, \tag{13}$$

$$\Delta\varphi = 0, \tag{14}$$

$$z = 0: \frac{\partial\varphi}{\partial z} + \frac{\partial\psi}{\partial x} = \frac{\partial\xi}{\partial t} + u_0\frac{\partial\xi}{\partial x}, \tag{15}$$

$$\frac{\partial\xi}{\partial x}W + \rho u_0\frac{\partial\xi}{\partial t} = \rho\nu\left(2\frac{\partial^2\varphi}{\partial x\partial z} + \frac{\partial^2\psi}{\partial x^2} - \frac{\partial^2\psi}{\partial z^2}\right),$$

$$W = \delta(V_x^2 - V_z^2), \tag{16}$$

$$p - \rho g\xi - 2\rho\nu\left(\frac{\partial^2\varphi}{\partial x^2} + \frac{\partial^2\psi}{\partial x\partial z}\right) = -\gamma\frac{\partial^2\xi}{\partial x^2}, \tag{17}$$

$$z = -d: \frac{\partial\varphi}{\partial x} - \frac{\partial\psi}{\partial z} = 0, \tag{18}$$

$$\frac{\partial\varphi}{\partial z} + \frac{\partial\psi}{\partial x} = 0. \tag{19}$$

The solution to (10)–(19) is sought in the form

$$\varphi = Z(z)\exp(st - ikx), \tag{20}$$

$$\psi = \Lambda(z)\exp(st - ikx). \tag{21}$$

It immediately follows from Laplace equation (14) that

$$\varphi = (A\cosh(kz) + B\sinh(kz))\exp(st - ikx); \quad A, B - \text{const}. \tag{22}$$

It is shown in Appendix A that Eq. (15) can be transformed to the following system of two ordinary differential equations for the unknown function $\Lambda(z)$:

$$\left(D^2 - q^2 - i\frac{U_0}{\nu}\left(1 + \frac{z}{d}\right)\right)F(z) = 0, \quad q^2 = k^2 + \frac{s}{\nu},$$
$$(D^2 - k^2)\Lambda(z) = F(z), \quad D^2 = \frac{d^2}{dz^2}. \tag{23}$$

(3) The problem under study becomes simpler if the speed u_0 of the stationary flow along the horizontal axis is much smaller than, or comparable to, that of liquid wave motions. According to (8), the related condition can be written as follows:

$$U_0 = \frac{\delta|V_x V_z|}{\rho\nu}d = \frac{\delta}{\rho}\frac{V^2|\sin(2\beta)|}{2\nu|s|}kd \lesssim |u_k|,$$
$$\frac{\delta}{\rho}\frac{V^2|\sin(2\beta)|}{2\nu|s|}kd = \frac{\delta}{\rho}\frac{V^2}{|u_k u_\nu|}\frac{|\sin(2\beta)|}{2}$$
$$= \frac{\delta}{\rho}\frac{V^2|\sin(2\beta)|}{2|u_k|^2}kd|\alpha| \lesssim 1,$$

or

$$u_k = \frac{s}{k}, \quad u_\nu = \frac{\nu}{d}, \quad \alpha = \frac{s}{\nu k^2}, \tag{24}$$

where β is the angle between the external force direction and the normal to the free surface. We will seek solutions to (10)–(19) that satisfy condition (24). This means that the terms either containing φ, ψ, ξ, p, and u or proportional to u_0 or du_0/dz can be omitted in all the equations and boundary conditions, because they have orders of smallness higher than one. Then, condition (13) takes the integrable form

$$\nabla\left(\frac{p}{\rho} + \frac{\partial\varphi}{\partial t}\right) = 0, \quad \nabla \equiv \mathbf{N}_1 \equiv \frac{\partial}{\partial x}\mathbf{n}_x + \frac{\partial z}{\partial z}\mathbf{n}_z.$$

It follows from the second equation of system (23) that the function $F(z)$ has the first order of smallness with respect to ξ_0. Therefore, the action of the part of the operator proportional to U_0 in the first equation in (23) on $F(z)$ results in a term of the second order of smallness. Thus, (23) transforms to a system of second-order differential equations with constant coefficients:

$$(D^2 - q^2)F = 0, \quad (D^2 - k^2)\Lambda = F, \quad q^2 = k^2 + \frac{s}{\nu}, \quad D^2 = \frac{d^2}{dz}. \tag{25}$$

The general solution of (25) is considered in Appendix B. It is also shown there that, in view of (22) and (11), the integration constants in the general expressions for φ and ψ may be redefined so that the scalar problem for the first-order terms takes the form

$$\varphi = (A\cosh(kz) + B\sinh(kz))\exp(st - ikx),$$
$$\psi = (a\cosh(qz) + b\sinh(qz))\exp(st - ikx), \tag{26}$$

$$p = -\rho\frac{\partial\varphi}{\partial t}, \tag{27}$$

$$z = 0: \frac{\partial\varphi}{\partial z} + \frac{\partial\psi}{\partial x} = \frac{\partial\xi}{\partial t}, \tag{28}$$

$$\frac{\partial\xi}{\partial x}W = \rho\nu\left(2\frac{\partial^2\varphi}{\partial x\partial z} + \frac{\partial^2\psi}{\partial x^2} - \frac{\partial^2\psi}{\partial z^2}\right),$$
$$W \equiv \delta(V_x^2 - V_z^2), \tag{29}$$

$$p - \rho g\xi - 2\rho\nu\left(\frac{\partial^2\varphi}{\partial z^2} + \frac{\partial^2\psi}{\partial x\partial z}\right) = -\gamma\frac{\partial^2\xi}{\partial x^2}, \tag{30}$$

$$z = -d: \frac{\partial\varphi}{\partial x} - \frac{\partial\psi}{\partial z} = 0, \tag{31}$$

$$\frac{\partial\varphi}{\partial z} + \frac{\partial\psi}{\partial x} = 0. \tag{32}$$

(4) It is easy to transform (26)–(32) to the following system of four homogeneous linear equations for constants a, b, A, and B:

$$s\nu(k^2 + q^2)A + \omega_0^2 B - i\omega_0^2 a - i2\nu kqb = 0,$$
$$ik^2(2\rho\nu s - W)B + (\rho\nu s(k^2 + q^2) - k^2 W)a = 0,$$
$$-ik\cosh(kd)A + ik\sinh(kd)B$$
$$+ q\sinh(qd)a - q\cosh(qd)b = 0,$$
$$-\sinh(kd)A + \cosh(kd)B$$
$$- i\cosh(qd)a + i\sinh(qd)b = 0.$$

This system has a unique solution only if the determinant of the matrix containing the coefficients multiplying the unknown variables equals zero. This condition specifies the dispersion equation for the problem subject to approximation (24). Introducing dimensionless variables by setting $\rho = \gamma = g = 1$ and taking the following characteristic scales for k, s, ν, and d,

$$k_* \equiv \sqrt{\rho g/\gamma}, \quad s_* \equiv \sqrt[4]{\rho g^3/\gamma}, \quad \nu_{0*} = \sqrt[4]{\gamma^3/(g\rho^3)},$$
$$d_* = \sqrt{\gamma/\rho g}, \quad \tau = \sqrt[4]{\gamma/\rho g^3},$$
$$k^2 q\left(4s(k^2 + q^2) - (3k + q)\frac{W}{\nu}\right)$$
$$+ \frac{s\omega_0^2}{\nu^2}(k\cosh(kd)\sinh(qd) - q\sinh(kd)\cosh(qd))$$

$$-2k^3q\left(2s-\frac{W}{\nu}\right)(k\cosh(kd)\cosh(qd)$$

$$-q\sinh(kd)\sinh(qd))+(k^2+q^2)\left(s(k^2+q^2)-k^2\frac{W}{\nu}\right)$$

$$\times(k\sinh(kd)\sinh(dq)-q\cosh(kd)\cosh(qd))\;=\;0,$$

$$\omega_0^2\equiv k(1+k^2),\quad \nu\equiv\frac{\nu_0}{1+s\tau},$$

we obtain the dispersion equation in the form

$$W\equiv(\delta/\rho)\sqrt{\rho/(g\gamma)}(V_x^2-V_z^2)$$
$$\equiv-(\delta/\rho)\sqrt{\rho/(g\gamma)}V^2\cos(2\beta). \qquad (33)$$

The function ω_0 represents the frequency of gravitational capillary waves for an infinitely thick layer of perfect liquid. The dimensionless parameter W depends on the dimensionless momentum flux density in the beam and angle of incidence β.

(5) Consider an inelastic medium with $\tau = 0$. The general solutions to the dispersion equation are shown in Fig. 1, where the real and imaginary parts of the frequency s are plotted as functions of the dimensionless parameter W for $k = 1$, $kd = 1$, and $\nu = 0.5$.

The most interesting curves (*1–3*) of Eq. (33) have common branching point. The coordinates of this point are $s \approx -1.2$ and $W \approx -0.8$. Curve *2*, associated with capillary wave motions, goes to the left of the branching point, i.e., to the domain of negative W values. The wave frequency increases as W decreases. Two curves of aperiodic motion go to the right of the branching point: curve *1* increases with W, and curve *3* decreases as W grows. Curve *3* and the part of curve *1* where $\mathrm{Re}\,s < 0$ describe exponentially damped motions. At $W \approx 1.6$, curve *1* enters into the domain where $\mathrm{Re}\,s > 0$, i.e., where the motion is unstable.

Also shown in Fig. 1 are curve *4* of wave motions and curves *5–8*, which describe aperiodically damped motions. The extension of the domain of calculation with respect to the magnitude of s revealed other real curves that are similar to curves *5–8* and lie below them. It was also shown that Eq. (33) has an infinite number of aperiodically damped solutions related to the reflection of the moving liquid from the bottom (for details, see [6]). Curve *4* of wave motions appears as a result of interaction between curves *3* and *5*. It is interesting that the frequency of wave motion *4* increases with W.

In analysis which follows, we will consider the first three solutions of the dispersion equation, which emerge from the branching point (*1–3*). This point is a starting point of unstable curves. The curves with numbers larger than *3* are not of interest (when $\tau = 0$) for studying free surface stability and are discarded. The viscosity dependence of the increment of the aperiodic instability associated with curve *1* is shown in Fig. 2.

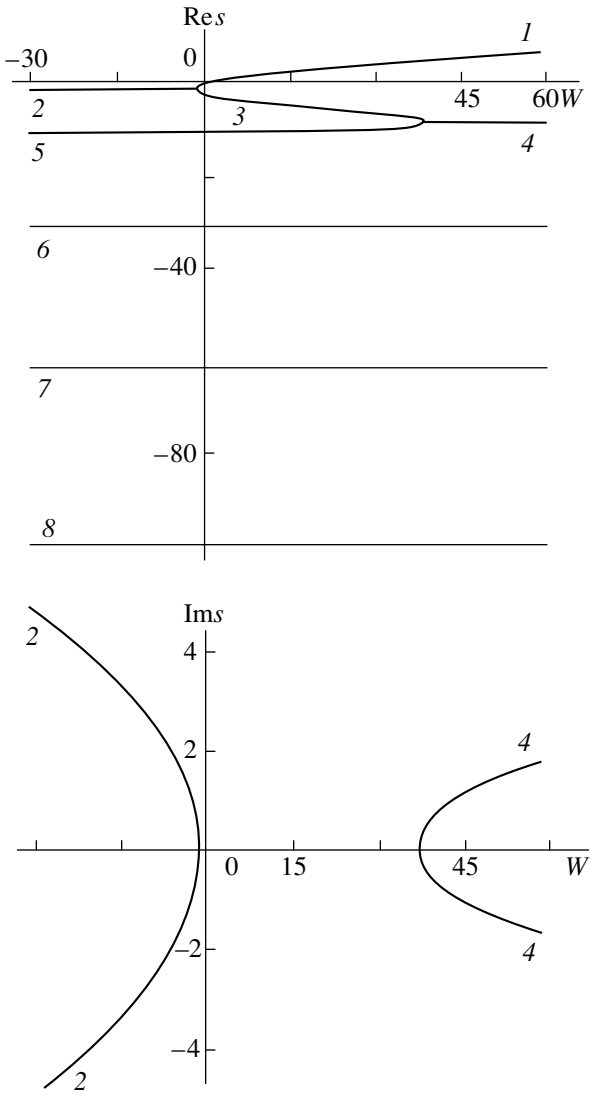

Fig. 1. Real and imaginary parts of the complex frequency s as functions of W for $k = 1$, $\nu = 0.5$, $kd = 1$, and $\tau = 0$.

For larger wave numbers, the patterns are qualitatively similar but both the branching point (*1–3*) and the critical value of $W \equiv W_c$ at which instability occurs shift to the right. For example, at $k = 10$, the branching point coordinates are $s \approx -1.4$ and $W \approx -0.7$ and the critical W value increases to $W_c \approx 8.2$. The instability increment is shown in Fig. 3 as a function of W for $k = 10$ and various viscosity values.

(a) According to [4], the highly viscous liquid approximation is defined by the condition

$$|\alpha| \ll 1,\quad \alpha\equiv\frac{s}{\nu k^2}. \qquad (34)$$

It is clear that condition (24) remains valid in this case. Moreover, it follows from [4] that inequality $|s|^2 > \omega_0^2$ holds when the viscosity is high, so that (24) trans-

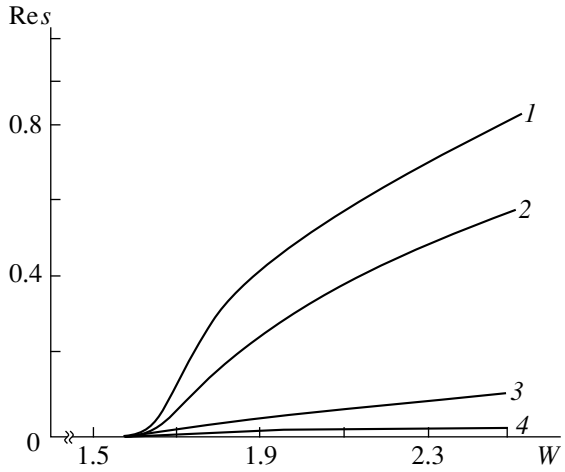

Fig. 2. Real part of the complex frequency (increment of aperiodic instability) as a function of W in the domain $\mathrm{Re}\, s > 0$ for $k = 1$, $kd = 1$, $\tau = 0$, and $\nu = (1)$ 0.01, (2) 0.1, (3) 1, and (4) 10.

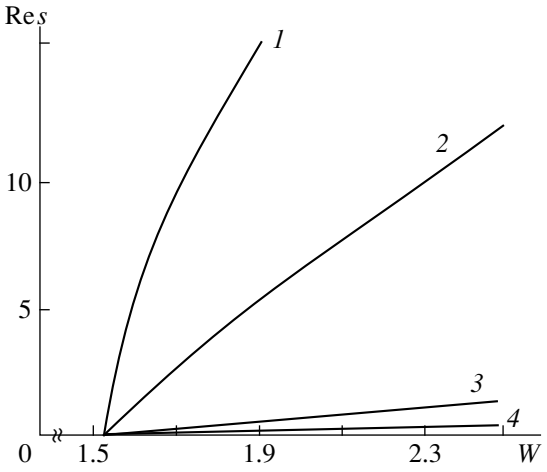

Fig. 3. The same as in Fig. 2 for $k = 10$.

forms to the strict inequality

$$\frac{\delta}{\rho}\frac{V^2|\sin(2\beta)|}{2U_k^2}kd|\alpha| < 1, \quad U_k = \frac{\omega_0^2}{k^2}, \qquad \omega_0^2 = k(1+k^2), \tag{35}$$

where U_k is the phase velocity of a gravitational capillary wave. It can be shown that a nontrivial asymptotic approximation of the dispersion equation at $\alpha \longrightarrow 0$ can be obtained by expanding the functions involved in (33) in integral powers of α and omitting the terms of order $O(\alpha^4)$ or higher. The result is the approximate dispersion equation for a high-viscosity liquid,

$$\begin{gathered}\eta s^2 + \kappa s + (\mu - k^2(kd)^2 W) = 0,\\ \eta \equiv (kd)^2 + \sinh(kd)\cosh(kd)kd - \cosh^2(kd),\\ \kappa \equiv 2\nu k^2(\cosh^2(kd) - (kd)^2),\\ \mu \equiv \omega_0^2(\sinh(kd)\cosh(kd) - kd),\end{gathered} \tag{36}$$

which is valid only for small values of the variable kd.

This quadratic equation has an instability-related root with a positive real part only if

$$W > \left(k + \frac{1}{k}\right)\left(\frac{\sinh(kd)\cosh(kd)}{(kd)^2} - \frac{1}{kd}\right). \tag{37}$$

This formula represents the critical condition for instability occurrence. When (37) holds, the positive root of (36), which defines the instability increment, satisfies condition (34) and has the form

$$s = \frac{1}{2\eta}(\sqrt{\kappa^2 - 4\eta(\mu - k^2(kd)^2 W)} - \kappa). \tag{38}$$

When the condition

$$\frac{4\mu\eta - \kappa^2}{4\eta} < k(kd)^2 W < \mu + \nu k^2(\kappa + \eta\nu k^2), \qquad kd < 10 \tag{39}$$

is valid, $|\alpha| < 1$ and (38) adequately describes at least one solution to (33); this solution represents the aperiodic instability increment if condition (37) holds or the aperiodic damping decrement otherwise.

The aforesaid is illustrated in Fig. 4, where curve *1* has the same meaning as before, while curve *1a* was calculated from (38). The vertical dashed lines separate out the domain of W values that satisfy (39). Here, curve *1a* approximates curve *1* of dispersion Eq. (33) well. The accuracy of this approximation improves as the domain shrinks to the threshold value $W = W_c$, which is the point of tangency of curves *1* and *1a*. It is seen that W_c does not depend on viscosity.

Note that the above reasoning is valid only for a thin liquid layer, because the expansion of Eq. (33) in powers of a small parameter implies the power series expansion of the hyperbolic functions whose argument $kdO(\alpha)$ has the first order of smallness with respect to α.

It follows from (37) that a wave with $k = 1$ is the most unstable and the critical W value for it is

$$W_c = 2\left(\frac{\sinh(kd)\cosh(kd)}{(kd)^2} - \frac{1}{kd}\right) \quad (k = 1). \tag{40}$$

The critical W values are positive due to $kd > 0$, which takes place only if the angle of incidence is greater than $\pi/4$.

(b) Consider the approximation of a very thin highly viscous layer without taking into account the disjoining pressure [7]. With possible fluctuation forces neglected,

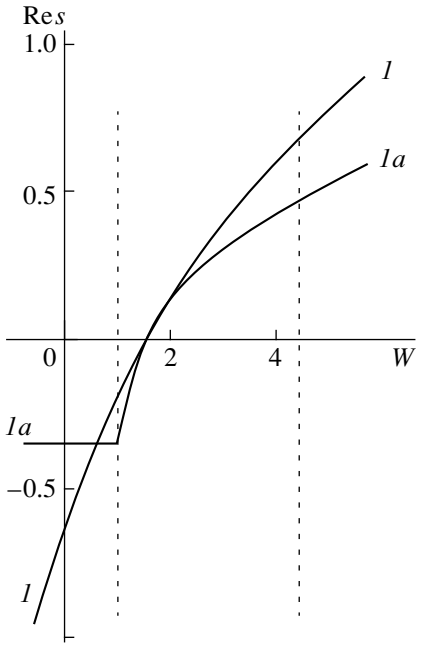

Fig. 4. Real parts of the solutions to (*1*) full dispersion Eq. (33) and (*1a*) asymptotic dispersion Eq. (36) for aperiodic instability at $k = 1$, $kd = 1$, and $\nu = 0.5$.

expressions (37) and (40) take the following forms in the limit of small *kd*:

$$W > (2/3)kd(k + 1/k), \quad (kd \ll 1), \tag{41}$$

$$W_c = (4/3)kd \quad (kd \ll 1, k = 1). \tag{42}$$

When $kd \longrightarrow 0$, W_c tends to zero on the side of positive values and the critical angle of incidence tends to $\pi/4$ on the side of larger angles.

To conclude this section, we note that, physically, the aperiodic instability may arise when the energy of tangential stresses on the free surface of the layer is transferred to that of normal stresses.

(6) Let us return to the viscoelastic liquid. Curves similar to those given in Fig. 1 but calculated for the nonzero viscosity relaxation time are shown in Figs. 5 and 6. The curves that are not associated with the branching points (*1–3*) and (*3–5*) from Fig. 1 change slightly. For this reason, they are not shown in Figs. 5 and 6, and the scale is chosen in such a way as to make clearer the behavior of curves *1–5* and new curves *6–8*. The latter are related to liquid elasticity and have nothing in common with the identically numbered curves in Fig. 1.

Comparing Fig. 1 with Figs. 5 and 6, we can conclude that, if the liquid is elastic, the branching points (*1–3*) and (*3–5*) merge together, curve *3* disappears, and a single branching point (*1–2–4–5*) arises. Curves *1* and *2* change only slightly. In particular, the condition for aperiodic instability (see the previous section) does not change when $\tau \neq 0$ (elastic liquid).

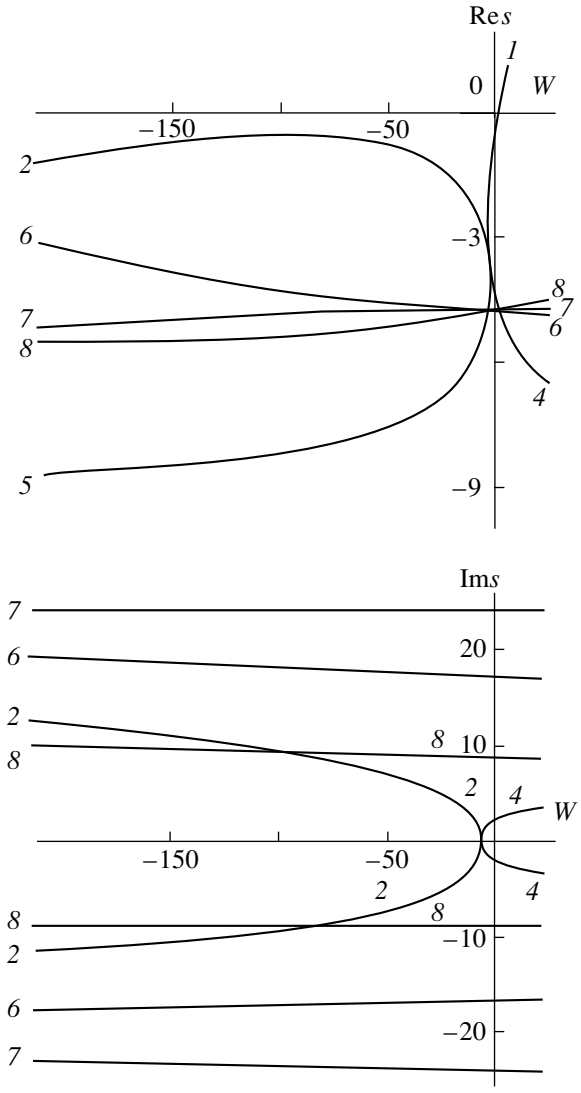

Fig. 5. Real and imaginary parts of the complex frequency as functions of *W* for $k = 1$, $\nu = 0.5$, $kd = 1$, and $\tau = 0.1$.

As τ increases, the curves forming the branching point (*1–2–4–5*) are rearranged so that curves *1* and *5*, associated with aperiodic motions, join. For designations to be consistent, the unstable part of the resulted curve (Re *s* > 0) is marked by number *1* in Fig. 6 and the stable one (Re *s* < 0), by number *5*.

Figures 5 and 6 depict the same curves as in Fig. 1 but for $W < 0$ at $\tau = 0.1$ and 0.4, respectively. It follows from the calculations that, as the dimensionless relaxation time increases to $\tau = 0.3$, the maximum of the real part of curve *2* in Fig. 5 shifts up to the right and touches the horizontal axis. When $\tau = 0.4$, the hump enters into the domain Re *s* > 0 and shifts still further to the right as shown in Fig. 6. At $\tau > 0.3$, there is a set (segment) of negative *W* values at which high-frequency vibrational instability occurs. Nearly at its center, the instability increment peaks. The segment appears when $\tau > 0.3$ and covers the value $W \approx -40$. For

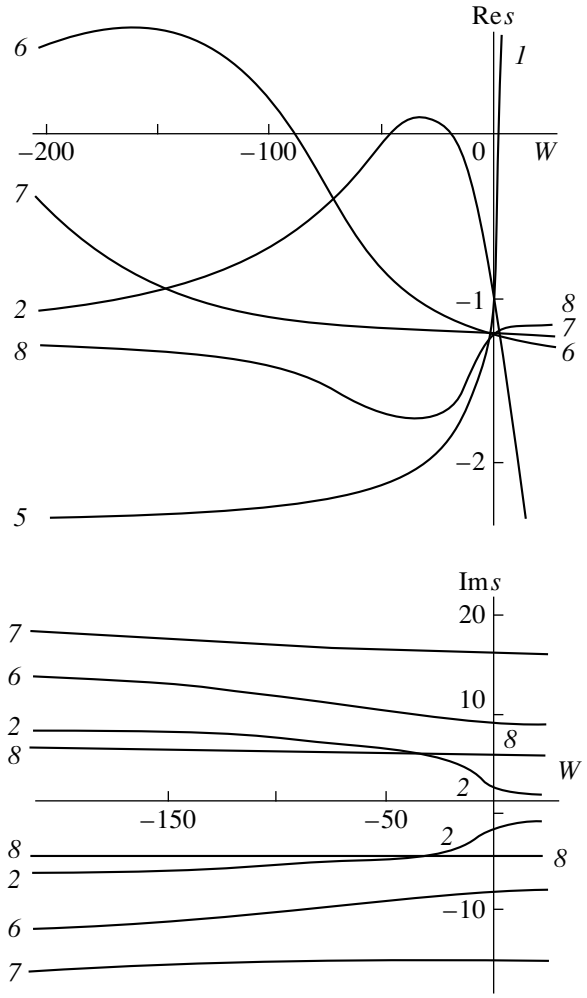

Fig. 6. The same as in Fig. 5 for $\tau = 0.4$.

greater τ's, the center shifts to the right and the segment extends: at $\tau = 0.4$, its width is $\Delta W \approx 20$ and its center is at $W \approx -30$. We believe that this instability is due to capillary waves excited by the elastic waves. When τ and the wave number k grow, the right border of the vibrational instability domain tends to $W = 0$.

A similar analysis can be performed for the evolution of curves *6* and *7*. These curves have the same properties as curve *2*. However, related instabilities exist at negative W values much larger in magnitude; at the same time, they are observed at smaller relaxation times τ. In addition, these curves are associated with viscoelastic wave motions, rather than with capillary ones.

It seems likely that the shift of the W range, associated with the vibrational instability, toward negative values at large viscosity relaxation times is caused by passing alternating stability and vibrational instability domains. The capillary waves are unstable in the instability domain nearest to the point $W = 0$; the viscoelastic waves, in the others. At small relaxation times, only the latter are unstable.

Numerical calculations with $W > 0$ revealed only the instability discussed in the previous section. The critical condition for its occurrence remained unchanged at nonzero τ values, while the increment increased with τ (for details, see [8]).

It is interesting that, in contrast to other capillary instabilities of the liquid free surface, such as the Tonks–Frenkel, Kelvin–Helmholtz, and Rayleigh–Taylor instabilities [9–12], both instabilities observed are generated by the tangent, rather than by normal, component of the dynamic boundary condition.

A possible physical reason for vibrational instability is the mutual exciting of capillary and relaxation waves in the presence of external energy.

CONCLUSIONS

Forces acting constantly on the free surface of a viscoelastic liquid may result in both vibrational and aperiodic instabilities. The vibrational instability occurs only if the liquid is elastic and the double angle between the force direction and external normal to the free surface is smaller than 90°. The condition for aperiodic instability does not depend on the elasticity properties of the liquid. It takes place only when the tangent (to the free surface) component of the momentum flux density exceeds the normal one.

APPENDIX A

Derivation of the Equation for the Stream Function

If the solution to Eq. (13) is sought for in traveling wave form (21), we can write

$$\frac{\partial \psi}{\partial x} = -ik\psi, \quad \frac{\partial \psi}{\partial t} = s\psi,$$

$$\Delta\psi = ((D^2 - k^2)\Lambda(z))\exp(st - ikx),$$

$$\frac{\partial \psi}{\partial t} - \nu\Delta\psi = -\nu((D^2 - (k^2 + s/\nu))\Lambda(z))\exp(st - ikx),$$

$$D^2 \equiv \frac{d^2}{dz^2}.$$

Hence,

$$\Delta\left(\frac{\partial \psi}{\partial t} - \nu\Delta\psi\right)$$

$$= -\nu((D^2 - k^2)(D^2 - (k^2 + s/\nu))\Lambda(z))\exp(st - ikx),$$

$$u_0\Delta\left(\frac{\partial \psi}{\partial x}\right) = -iku_0((D^2 - k^2)\Lambda(z))\exp(st - ikx),$$

where $\Lambda(z)$ is the amplitude of the stream function. Substituting the last two expressions into Eq. (16) and

omitting the preexponential, one obtains the ordinary differential equation for $\Lambda(z)$

$$-\nu(D^2-k^2)(D^2-(k^2+s/\nu))\Lambda - iku_0((D^2-k^2)\Lambda) = 0,$$

$$u_0 = \frac{U_0}{\nu}\left(1+\frac{z}{d}\right).$$

Since the differential operators (D^2-k^2) and $(D^2-(k^2+s/\nu))$ are commutative, this equation can be written as

$$(D^2-(k^2+s/\nu))(D^2-k^2)\Lambda(z) - ik\frac{u_0}{\nu}(D^2-k^2)\Lambda(z) = 0.$$

Taking $(D^2-k^2)\Lambda(z)$ as a new function and using the definition of u_0, we can write the last equation in the form of the system

$$(D^2-q^2)F(z) - i\frac{U_0}{\nu}\left(1+\frac{z}{d}\right)F(z) = 0,$$

$$q^2 = k^2+\frac{s}{\nu},$$

$$(D^2-k^2)\Lambda(z) = F(z).$$

Separating out the differential operator acting on $F(z)$ in the left of the first equation of this system, one comes to system (23).

APPENDIX B

Derivation of the Velocity Field Potential and the Stream Function

(1) General expression for the stream function in (24). In approximation (24), the amplitude value $\Lambda(z)$ of the stream function in the form (21) satisfies system (25), in which the first equation has the solution

$$F = C\exp(qz) + G\exp(-qz); \quad C, G \text{ are constants.}$$

Then, the second equation transforms into the inhomogeneous problem

$$(D^2-k^2)\Lambda = C\exp(qz) + G\exp(-qz). \qquad \text{(B.1)}$$

Excluding the case $s = 0$ ($k = q$), we will arrive at the following particular solution to (B.1):

$$\tilde{\Lambda} = \frac{C\exp(qz)}{q^2-k^2} + \frac{G\exp(qz)}{q^2-k^2} = L\exp(qz) + M\exp(-qz).$$

If L and M are taken as new integration constants, the general solution of (B.1) equals the sum of the particular solution found and the general solution of the related homogeneous equation:

$$\Lambda = L\exp(qz) + M\exp(-qz) + \eta\exp(kz) + \chi\exp(-kz).$$

Redefining the constants and using (21), we can write the general solution for ψ in terms of hyperbolic functions:

$$\begin{gathered}\psi = \psi_1 + \psi_2;\\ \psi_1 = (a\cosh(qz) + b\sinh(qz))\exp(st-ikx);\\ a, b, c, r = \text{const};\\ \psi_2 = (c\cosh(kz) + r\sinh(kz))\exp(st-ikx).\end{gathered} \qquad \text{(B.2)}$$

Note the following properties of ψ_2:

$$\begin{aligned}\hat{\mathbf{N}}_2\psi_2 &= -\frac{\partial\psi_2}{\partial z}\mathbf{n}_x + \frac{\partial\psi_2}{\partial x}\mathbf{n}_z\\ &= -k\psi_2\mathbf{n}_x - ik\psi_2\mathbf{n}_z = -\text{grad}(i\psi_2),\end{aligned} \qquad \text{(B.3)}$$

$$\Delta\psi_2 = \frac{\partial^2\psi_2}{\partial x^2} + \frac{\partial^2\psi_2}{\partial z^2} = -k^2\psi_2 + k^2\psi_2 \equiv 0. \qquad \text{(B.4)}$$

(2) Redefining the potential and the stream function. In view of (B.2) and (B.3), (11) takes the form

$$\begin{gathered}\mathbf{u} = \hat{\mathbf{N}}_1\nabla\Phi + \hat{\mathbf{N}}_2\psi_1, \quad \Phi = \varphi - i\psi_2,\\ \Delta\Phi = 0.\end{gathered} \qquad \text{(B.5)}$$

Property (B.5) of the initial potential φ, which served to scalarize the equations and boundary conditions of the problem, is also valid for the new function Φ. There is no need to perform this procedure again using the new function Φ, since only the name of the potential would change. Therefore, we will keep the same symbol φ for the potential and, according to (22), (B.2), and (B.4), use the following expressions for the general solution to the hydrodynamics equations:

$$\varphi = ((A-ic)\sinh(kz) + (B-ir)\cosh(kz))\exp(st-ikx);$$

$$A, B, c, r = \text{const};$$

$$\psi = (a\cosh(qz) + b\sinh(qz))\exp(st-ikx);$$

$$a, b = \text{const}.$$

For the sake of brevity, we denote the constants $(A-ic)$ and $(B-ir)$ by A and B, respectively, and eventually obtain

$$\begin{gathered}\varphi = (A\sinh(kz) + B\cosh(kz))\exp(st-ikx);\\ A, B = \text{const};\end{gathered} \qquad \text{(B.6)}$$

$$\begin{gathered}\psi = (a\cosh(qz) + b\sinh(qz))\exp(st-ikx);\\ a, b = \text{const}.\end{gathered} \qquad \text{(B.7)}$$

REFERENCES

1. S. K. Aslanov, in *Proceedings of the XVIII Conference of the Commonwealth of Independent States "Disperse Systems," Odessa, 1998*, p. 16.
2. V. K. Smirnov, D. S. Kibalov, S. A. Krivelevich, *et al.*, Nucl. Instrum. Methods Phys. Res. B **147**, 310 (1999).

3. L. D. Landau and E. M. Lifshitz, *Course of Theoretical Physics*, Vol. 6: *Fluid Mechanics* (Nauka, Moscow, 1986; Pergamon, New York, 1987).
4. V. G. Levich, *Physicochemical Hydrodynamics* (Fizmatgiz, Moscow, 1959).
5. L. D. Landau and E. M. Lifshitz, *Course of Theoretical Physics*, Vol. 7: *Theory of Elasticity* (Nauka, Moscow, 1982; Pergamon, New York, 1986).
6. A. I. Grigor'ev, S. O. Shiryaeva, V. A. Koromyslov, and D. F. Belonozhko, Zh. Tekh. Fiz. **67** (8), 27 (1997) [Tech. Phys. **42**, 877 (1997)].
7. D. F. Belonozhko, A. I. Grigor'ev, and M. I. Munichev, Pis'ma Zh. Tekh. Fiz. **23** (19), 66 (1997) [Tech. Phys. Lett. **23**, 763 (1997)].
8. S. O. Shiryaeva and O. A. Grigor'ev, Pis'ma Zh. Tekh. Fiz. **25** (2), 1 (1999) [Tech. Phys. Lett. **25**, 41 (1999)].
9. A. I. Grigor'ev, O. A. Grigor'ev, and S. O. Shiryaeva, Zh. Tekh. Fiz. **62** (9), 12 (1992) [Sov. Phys. Tech. Phys. **37**, 904 (1992)].
10. O. A. Grigor'ev and S. O. Shiryaeva, Zh. Tekh. Fiz. **66** (2), 23 (1996) [Tech. Phys. **41**, 124 (1996)].
11. S. O. Shiryaeva, Pis'ma Zh. Tekh. Fiz. **22** (13), 48 (1996) [Tech. Phys. Lett. **22**, 540 (1996)].
12. A. I. Grigor'ev, V. A. Koromyslov, and S. O. Shiryaeva, Zh. Tekh. Fiz. **69** (5), 7 (1999) [Tech. Phys. **44**, 486 (1999)].

Translated by V. Gursky

Technical Physics, Vol. 45, No. 11, 2000, pp. 1399–1405. Translated from Zhurnal Tekhnicheskoĭ Fiziki, Vol. 70, No. 11, 2000, pp. 24–30.

Electronic–Polarization Investigations of the Electron Velocity Distribution Function in an Anisotropic Plasma

A. S. Mustafaev, I. B. Movchan, and A. P. Mezentsev

St. Petersburg State Mining Institute (Engineering University), Vtoraya liniya 21, St. Petersburg, 199026 Russia

Received October 21, 1999; in final form, March 1, 2000

Abstract—The electron velocity distribution function (EVDF) in an anisotropic plasma is investigated using both the probe method and the magnetic–polarization Hanle techniques. In a helium beam–plasma discharge, the moments of the anisotropic EVDF are measured and the rate constant is determined for the disalignment of helium atoms in the 4^1D_2 state due to collisions with charged particles. A new method for investigating anisotropic properties of distant plasma objects unavailable for contact diagnostics is tested experimentally. The EVDF, the cross sections for the alignment of the total angular moments of the excited helium atoms by electron impact, and the degree of the electron pressure anisotropy are measured. An advantage of the method proposed is the possibility of directly measuring the EVDF anisotropy in distant plasma objects, which until now has been estimated only theoretically. *© 2000 MAIK "Nauka/Interperiodica".*

INTRODUCTION

At present, investigations of an anisotropic plasma are stimulated by new areas for its application in modern plasma technologies; power engineering; and designing high-power lasers, novel plasma light sources, and radiation-resistant plasma electronic devices, as well as by the necessity of developing new methods for investigating distant astrophysical and geophysical plasma objects.

In this study, anisotropic electron velocity distribution functions (EVDFs) are measured in various plasma objects using the probe technique [1–13] combined with the polarization spectroscopy method [14–16].

The depolarization of the 4^1D_2–2^1P_1 spectral line of helium atoms is analyzed at a density of charged particles of about 10^{11} cm^{-3}, and the rate constant is determined for the disalignment of helium atoms in the 4^1D_2 state due to collisions with charged particles.

A method for investigating the anisotropic properties of distant plasma objects is proposed. The moments of the anisotropic EVDF, the cross sections for the alignment of the total angular moments of the excited helium atoms by electron impact, and the degree of electron pressure anisotropy are measured.

The EVDF moments describe different ordering degrees of the electron velocity vectors and determine the anisotropic properties of the plasma. Therefore, most attention is paid to measuring the moments of the anisotropic EVDF.

REPRESENTATION OF THE EVDF IN AN ANISOTROPIC PLASMA

An EVDF in an axisymmetric anisotropic plasma in spherical coordinates with an axis oriented along the local axis of plasma symmetry can be expanded in the orthogonal Legendre polynomials [17]:

$$f(\varepsilon, \Theta) = \sum_{j=0}^{\infty} f_j(\varepsilon) L_j(\cos\Theta), \tag{1}$$

where $\varepsilon = m\vartheta^2/2$ is the electron energy, ϑ is the absolute value of the electron velocity, Θ is the polar angle, and $L_j(\cos\Theta)$ is the Legendre polynomial.

The coefficients $f_j(\varepsilon)$ determine a number of the main plasma parameters. The first three expansion coefficients are the most important. Except for a factor, the coefficient f_0 determines the electron distribution in the absolute value of velocity, the plasma density n, and the rate Γ of excitation and ionization of the plasma-forming component

$$\begin{aligned} n &= \frac{4\pi\sqrt{2}}{m^{3/2}} \int_0^{\infty} \sqrt{\varepsilon} f_0(\varepsilon) d\varepsilon, \\ \Gamma &= 4\pi N_a \int_{\varepsilon_{\lim}}^{\infty} \sigma_{ea}^i(\vartheta) f_0(\vartheta) \vartheta^2 d\vartheta. \end{aligned} \tag{2}$$

Here, σ_{ea}^i are the cross sections for the corresponding processes and N_a is the gas atom density. The coefficient f_1 is uniquely related to the electron hydrodynamic velocity and the electron current density

$$j_e = \frac{8\pi e}{3m^2} \int_0^{\infty} \varepsilon f_1(\varepsilon) d\varepsilon. \tag{3}$$

1063-7842/00/4511-1399$20.00

The electron pressure in a plasma is related to the diagonal elements Π_{ij} of the tensor of the electron momentum flux density [18]

$$\Pi_{ij} = m\int[\vartheta_i\vartheta_j f(\boldsymbol{\vartheta})]d\boldsymbol{\vartheta} = \begin{pmatrix} p-\frac{1}{5}p_1 & 0 & 0 \\ 0 & p-\frac{1}{5}p_1 & 0 \\ 0 & 0 & p+\frac{2}{5}p_1 \end{pmatrix}, \quad (4)$$

where the scalar electron pressure p is determined by the isotropic part f_0 of the EVDF:

$$p = \frac{8\pi\sqrt{2}}{3m^{3/2}}\int_0^\infty \varepsilon^{3/2} f_0(\varepsilon)d\varepsilon. \quad (5)$$

The anisotropic part p_1 of the tensor of the electron momentum flux density is determined by the coefficient f_2:

$$p_1 = \frac{8\pi\sqrt{2}}{3m^{3/2}}\int_0^\infty \varepsilon^{3/2} f_2(\varepsilon)d\varepsilon. \quad (6)$$

The remaining EVDF expansion coefficients, together with the first three, determine the angular structure of the EVDF and play an important role in investigating both the populations of the Zeeman atomic sublevels and the diagram of the collisional electron scattering.

INVESTIGATION METHODS

The orthogonal expansion coefficients $f_j(eU)$ of the anisotropic EVDF were determined by the method of a flat single-sided probe from the second derivative $I_U''(eU, \alpha)$ of the probe current density with respect to the probe potential [1, 6, 9, 13] for different orientations of the probe with respect to the plasma symmetry axis (Fig. 1):

$$f_j(eU) = \frac{(2j+1)m^2}{4\pi q^3 S}\int_{-1}^{1}\left[I_U''(eU, x) + \int_{eU}^{\infty} I_U''(\varepsilon, x)R_j(eU, \varepsilon)d\varepsilon\right]L_j(x)dx, \quad (7)$$

where $x = \cos\alpha$, α is the angle between the normal to the probe surface and the plasma symmetry axis, and $R_j(eU, \varepsilon)$ is the known resolvent of the integral equation for the Legendre components of the EVDF [13]

$$R_j = \begin{cases} 0, & j = 0 \\ \frac{1}{2eU}, & j = 1 \\ \frac{3}{2eU}\sqrt{\frac{\varepsilon}{eU}}, & j = 2. \end{cases} \quad (8)$$

Thus, the method of a flat single-sided probe consists in measuring $I_U''(eU, \alpha)$ and subsequent calculations of $f_j(eU)$ (Fig. 2) using expressions (1) and (7). Note that this method does not require any *a priori* information about the shape of the EVDF in a plasma, because the basic relationship (7) is valid for any degree of anisotropy.

Noncontact optical measurements were carried out using a polarization spectroscopy method based on the relation between the polarization of the line emission and the EVDF quadrupole moment $f_2(\vartheta)$ [14, 15, 19, 20]. Polarization measurements were conducted using the magnetic–polarization Hanle technique [16], which is based on examining the dependence of the polarization of spontaneous emission from the atom ensemble on the magnetic field H applied to the discharge. The magnetic field was chosen to be low enough for the kinetic characteristics of particles in the discharge plasma to remain unchanged. However, it was sufficiently high to disalign the transverse components of the atomic levels. As a result, in the line emission spectrum, the Hanle effect manifested itself as a characteristic dependence of the degree of polarization of spontaneous emission along the external magnetic field on the magnetic field strength (Fig. 3). The shape of the Hanle signal provides information about the anisotropic properties of a plasma object [14–16].

INVESTIGATIONS OF DEPOLARIZATION OF THE HELIUM 4^1D_2 ATOMIC STATE BY CHARGED PARTICLES: PROBE MEASUREMENTS

The depolarization of excited helium atoms due to collisions with charged particles was studied in a helium beam–plasma discharge (BPD) excited between two plane circular electrodes. The distance between the electrodes was varied from 0.1 to 2 cm [1, 11]. The cathode was a 0.15-cm-thick porous tungsten tablet impregnated with barium–calcium aluminate. The cathode temperature was varied from 1000 to 1500 K (to within an accuracy of ±10 K). The plasma column in the discharge gap was axisymmetric and had the shape of a 1.1-cm-diameter cylinder. The preliminary thermal and vacuum treatment of the device provided 10^{-9}-torr residual pressure. The helium pressure was varied from 10^{-1} to 1 torr. The cathode emission current was maintained at a level of 10^{-2}–5×10^{-1} A.

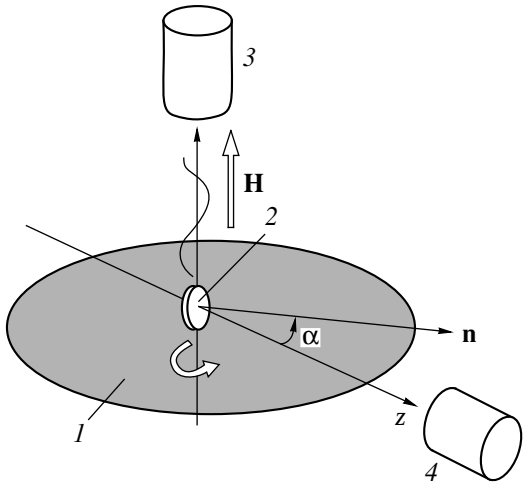

Fig. 1. Schematic of measurements in a BPD: (*1*) discharge plasma, (*2*) rotating flat single-sided probe, (*3*) Hanle polarization spectrometer, and (*4*) EVDF detector. The *z*-axis is directed from the cathode to the anode; *n* is the normal to the probe surface.

Investigations of the anisotropic plasma were carried out using the method of a flat single-sided probe and the magnetic–polarization Hanle technique [16]. A plane single-sided probe was inserted into the device through its side wall. The probe was installed on a three-coordinate micrometer positioning system, which enabled us to place the probe at a chosen point between the electrodes to within an accuracy of about 0.05 mm. EVDF anisotropy was investigated not only along the axis, but also at different angles to the axis (from 0° to 180° to within an accuracy of ±0.5°). Simultaneously with the probe measurements, the degree of polarization of spontaneous emission from excited helium atoms was recorded at the same discharge point (Fig. 1). The line of sight coincided with the direction of the external magnetic field **H**, whose strength determined the polarization of the observed emission.

The range of helium pressures under study corresponded to the collisionless regime of a BPD: $l_0 > d$, where l_0 is the mean free path of the beam electrons and d is the distance between the electrodes. In this regime, at low discharge currents, the beam electrons do not have enough time to relax, either in momentum or in energy, due to pair collisions [10]. As a result, the EVDF is substantially nonequilibrium and is characterized by strong anisotropy, due to which the plasma is unstable against the excitation of plasma oscillations [5, 10–12]. The function $f_0(\varepsilon)$ (Fig. 4) has maxima at both low (2 eV) and high (30 eV) energies. These maxima correspond to two separate groups of electrons. One group consists of slow electrons with the density n_1 and an almost isotropic distribution function. The second group consists of fast beam electrons with the den-

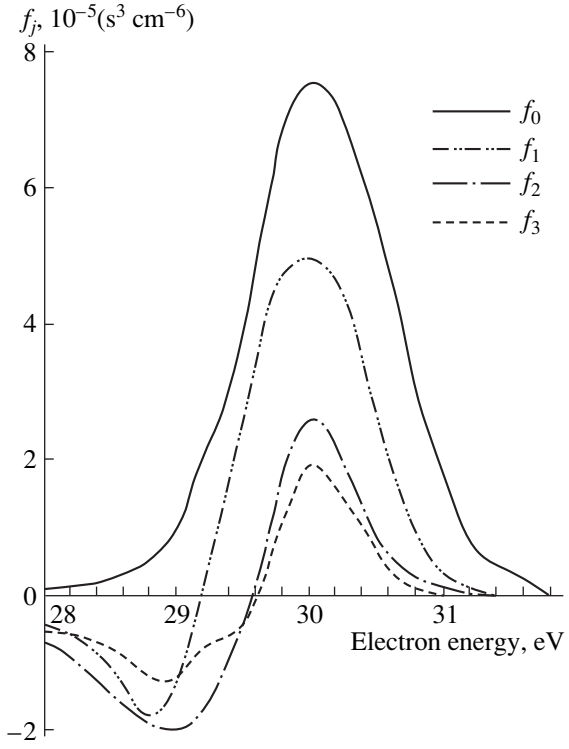

Fig. 2. The EVDF Legendre coefficients vs. the electron energy for the discharge parameters I_p = 0.1 A and p_{He} = 0.25 torr.

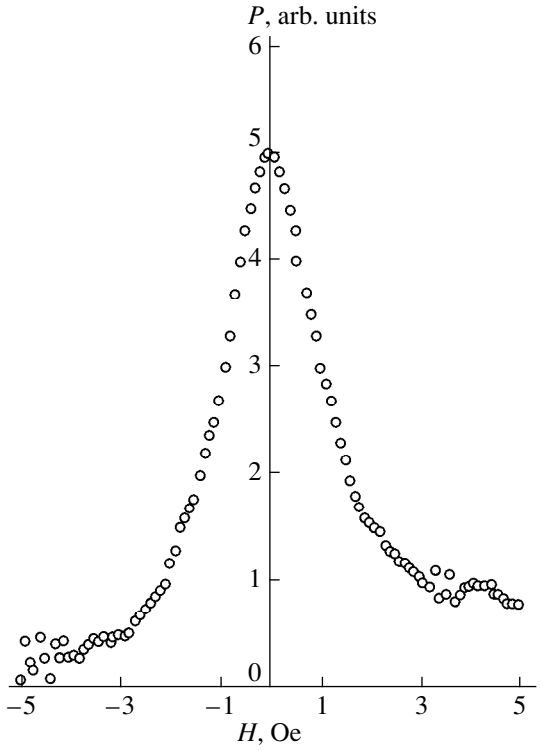

Fig. 3. The contour of the Hanle signal for the He 4922-Å line in a BPD at the charged particle density $n_{ch} = 1.6 \times 10^{11}$ cm^{-3} and the pressure p_{He} = 0.25 torr.

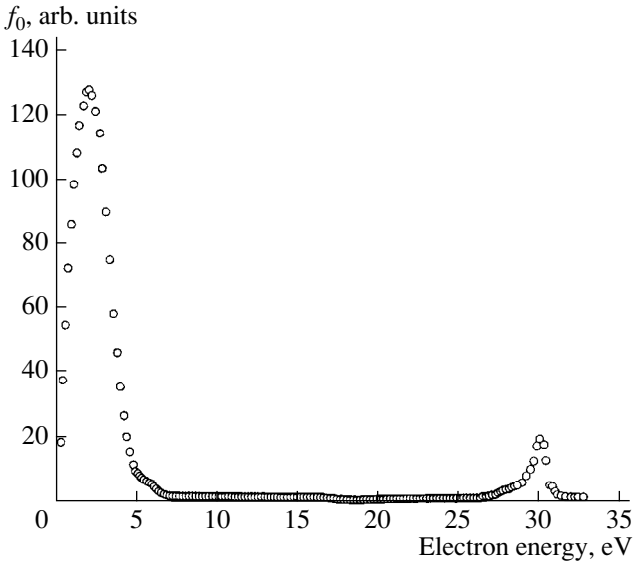

Fig. 4. Electron distribution function f_0 in the BPD for p_{He} = 0.25 torr and I_p = 0.1 A.

sity n_2; these electrons move from the cathode toward the anode and excite helium atoms, simultaneously aligning their angular moments. In a collisionless helium BPD, the beam electrons have a low energy dispersion and their density is usually on the order of the density of slow electrons [10]. Figure 5 displays the diagrams of the electron distributions in velocity directions for the above groups of electrons.

Probe measurements demonstrate that, in the collisionless regime, mechanisms for the relaxation of an anisotropic EVDF have a wave nature and come into play when the discharge current reaches the threshold value. There are two stages in EVDF relaxation. In the first stage, EVDF isotropization is accompanied by an insignificant electron energy loss at small distances from the cathode $z \ll l_0$ (Fig. 6). In the second stage, the weakly anisotropic beam does not reach the anode, rapidly relaxes in energy, and approaches the state with the plateau-shaped EVDF at distances $z < d$.

MAGNETIC–POLARIZATION MEASUREMENTS

Measurements of the contours of Hanle signals for the helium lines λ_R = 4922 Å and λ_T = 6678 Å demonstrate their relative broadening as the discharge current and, correspondingly, the charged particle density, increase. Both the contribution of charged particles to the collisional depolarization and the width of the Hanle signal increase with the density. This width is related to the alignment constant γ_2, which mainly depends on the emission lifetime of a given atomic state and the frequency of pair collisions. There are two types of these collisions: electron–atom (n) and electron–electron (ch). Hence, we have

$$\gamma_2 = \gamma_0 + \gamma_n + \gamma_{ch}. \quad (9)$$

Here, γ_0 is the natural decay constant related to the depopulation of the helium 4^1D_2 state and [16]

$$\gamma_{ch} = n_{ch}\langle \tilde{v}\sigma_{ch}(\tilde{v})\rangle, \quad (10)$$

where $\tilde{v}$ is the relative velocity of colliding particles, $\sigma_{ch}(\tilde{v})$ is the effective cross section for collisional depolarization, and n_{ch} is the total charged particle density in a quasineutral plasma

$$n_{ch} = 2n_e = 2(n_1 + n_2), \quad (11)$$

n_e being the electron density.

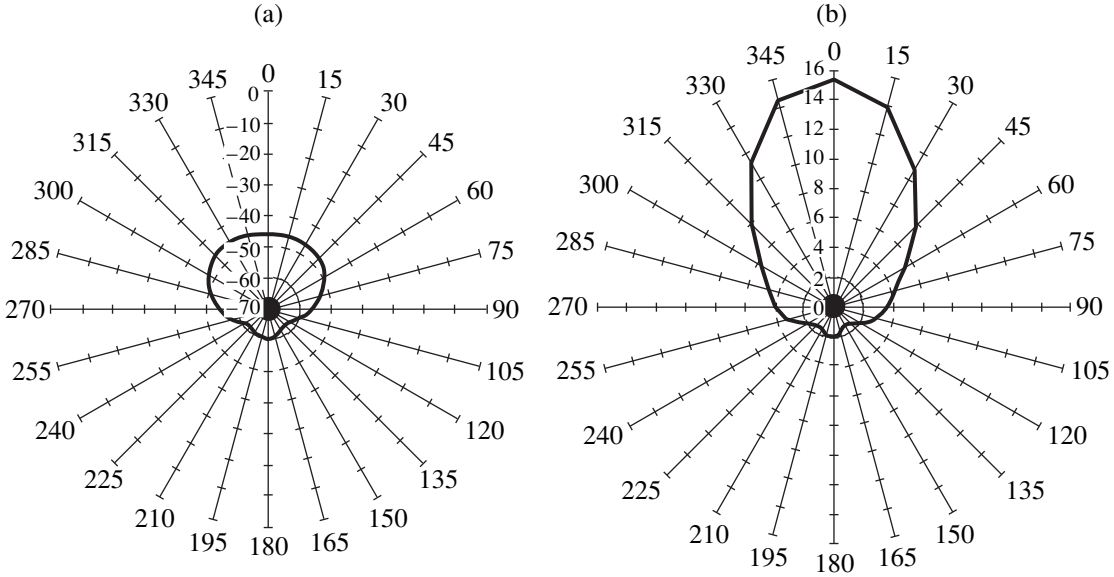

Fig. 5. Diagrams of the electron distribution in velocity directions for I_p = 0.1 A and p_{He} = 0.25 torr: (a) slow electrons (ε = 2 eV) and (b) beam electrons (ε = 30 eV). Zero angle corresponds to the probe normal oriented from the cathode to the anode.

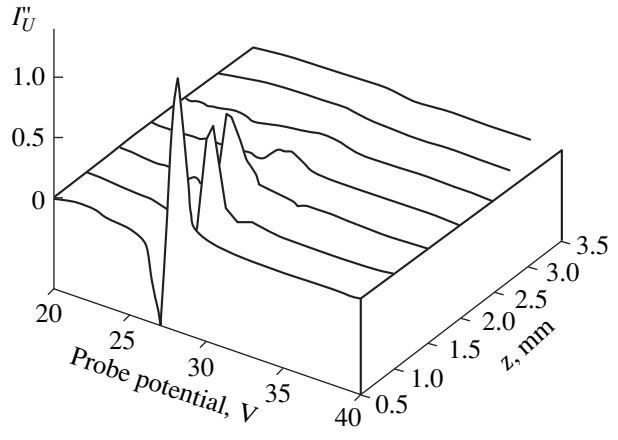

Fig. 6. Profiles of the second derivative of the probe current vs. the probe potential in a BPD for $\alpha = 0$, $p_{He} = 0.25$ torr, $l_0 = 2.0$ cm, $d = 1.2$ cm, $I_p = 0.5$ A, $n_1 = 2.8 \times 10^{11}$ cm^{-3}, and $n_2 = 6 \times 10^{10}$ cm^{-3}.

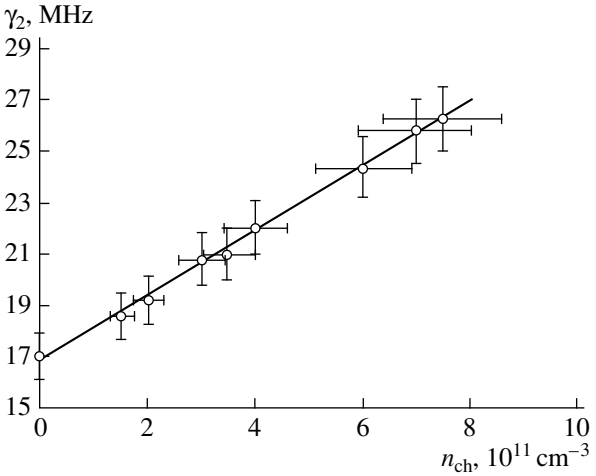

Fig. 7. The width of the Hanle signal vs. the total density of charged particles in a BPD for $\lambda = 4922$ Å.

Relationship (10) shows that, by extrapolating the width of the Hanle signal as a function of n_{ch} to $n_{ch} = 0$, one can find the component $(\gamma_0 + \gamma_n)$ of the alignment relaxation constant (Fig. 7). In the BPD regimes under study, the depolarization rate constant for the helium 4^1D_2 atomic state is found to be $\langle \tilde{v}\, \sigma_{ch}(\tilde{v}) \rangle = \gamma_{ch}/n_{ch} = (1.27 \pm 0.38) \times 10^{-5}$ cm^3 s^{-1}, which, within the measurement accuracy, is in good agreement with estimates [16] obtained from the theory of collisional relaxation of atom polarization moments, assuming that the trajectories of charged particles are straight and the collision process is isotropic.

A METHOD FOR RECONSTRUCTING THE EVDF AND ANISOTROPIC PARAMETERS OF DISTANT PLASMA OBJECTS

According to [19, 20], the degree of linear polarization of a spectral line P corresponding to a local group of atoms is a function of the population ρ_0 of the main level and the determinant ρ_2 of the alignment tensor:

$$P = f\left(\frac{\rho_2}{\rho_0}\right). \tag{12}$$

The tensor components characterize the anisotropy of electron-impact excitation of an atom from the main level. The quantity ρ_2 is determined by the anisotropic part f_2 of the EVDF [15]:

$$\rho_2 = \frac{N_a n_e}{\gamma_2} \int_{\varepsilon_{lim}}^{\infty} \varepsilon Q_2(\varepsilon, \varepsilon_{lim}) f_2(\varepsilon) d\varepsilon, \tag{13}$$

where γ_2 is the alignment relaxation constant determined by relationships (9) and (10), ε_{lim} is the threshold energy for the excitation of a given spectral line, Q_2 is the alignment cross section, and f_2 is the quadrupole Legendre coefficient of the EVDF determined by expression (7).

The population of the main level is related to the EVDF by a relationship similar to expression (13):

$$\rho_0 = \frac{N_a n_e}{\gamma_0} \int_{\varepsilon_{lim}}^{\infty} \varepsilon Q_0(\varepsilon, \varepsilon_{lim}) f_0(\varepsilon) d\varepsilon, \tag{14}$$

where Q_0 is the excitation cross section and γ_0 is the natural decay constant [see (9)].

If f_0 and f_2 are known and the degree of polarization of the Rth and Tth spectral lines is $P \approx \rho_2/\rho_0$, then, for a plasma object with a certain atomic composition, we obtain the set of equations

$$\begin{aligned} P_R \int_{\varepsilon_{th}^2}^{\infty} \varepsilon Q_0(\varepsilon, \varepsilon_{lim}^{(R)}) f_0(\varepsilon) d\varepsilon &= \int_{\varepsilon_{th}^2}^{\infty} \varepsilon Q_2(\varepsilon, \varepsilon_{lim}^{(R)}) f_2(\varepsilon) d\varepsilon, \\ P_T \int_{\varepsilon_{th}^T}^{\infty} \varepsilon Q_0(\varepsilon, \varepsilon_{lim}^{(T)}) f_0(\varepsilon) d\varepsilon &= \int_{\varepsilon_{th}^T}^{\infty} \varepsilon Q_2(\varepsilon, \varepsilon_{lim}^{(T)}) f_2(\varepsilon) d\varepsilon. \end{aligned} \tag{15}$$

Solving this system yields the atomic constants Q_0 and Q_2, which are invariant with respect to the conditions under which the plasma is produced.

In order to analyze the EVDF in a distant plasma object with identical atomic composition, it is necessary to measure the degrees of polarization P_R and P_T of spontaneous emission and, using the invariant atomic constants Q_0 and Q_2, find the isotropic (f_0) and anisotropic (f_2) parts of the EVDF from Eqs. (15). Thus, the method proposed for determining the EVDF and the electron pressure anisotropy in distant plasma objects consists in the following. Under laboratory conditions,

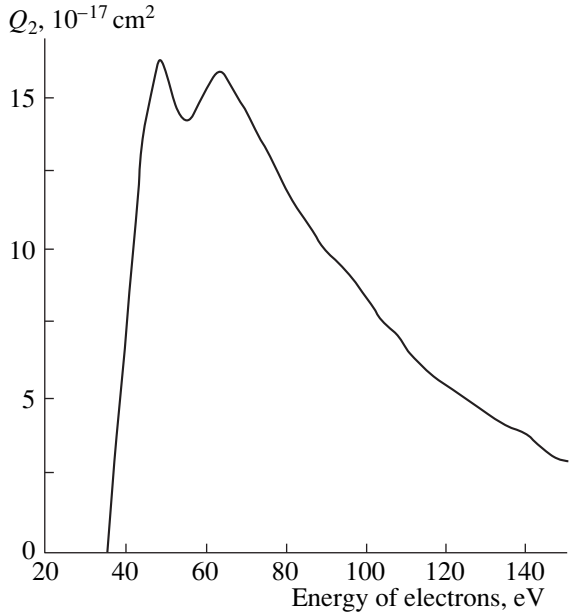

Fig. 8. Energy dependence of the cross section for the alignment of the total angular moments of the excited electrons by electron impact for $\lambda = 4922$ Å.

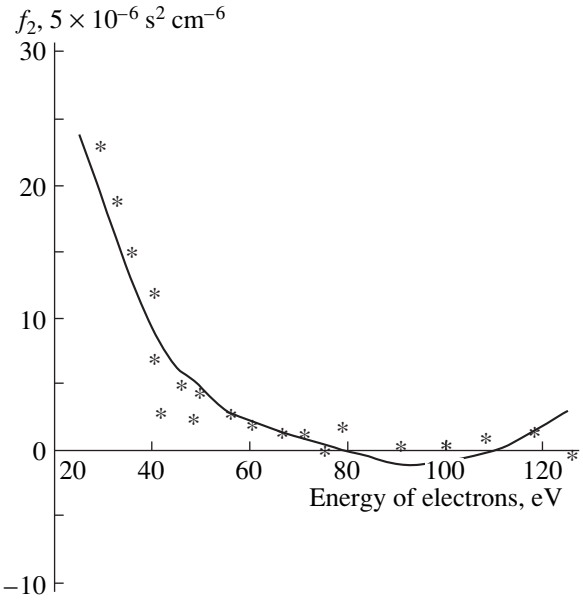

Fig. 9. Energy dependence of the EVDF quadrupole moment f_2 for the plasma of a positive column at $p_{He} = 2 \times 10^{-2}$ torr and $I_p = 0.4$ A. The solid line shows the data obtained by the proposed method, and the asterisks present the results of independent probe measurements.

a model plasma object is created that contains atoms of the same chemical element as in a distant object. The moments f_0 and f_2 and the degrees of polarization of two lines of spontaneous emission are measured simultaneously. Solving Eqs. (15), the alignment (Q_2) and excitation (Q_0) cross sections are calculated. Then, the degrees of linear polarization of these two spectral lines of the atoms contained in the distant plasma object are substituted into Eqs. (15). Finally, from the known values of Q_0 and Q_2, one can calculate f_0, f_2, and the relative anisotropy of the electron pressure in the distant plasma object.

The method proposed was tested experimentally. In the laboratory, we created a low-pressure helium BPD as a model object. In this discharge, we measured the EVDF moments f_0 and f_2 using the method of a flat single-sided probe. Simultaneously, we carried out spectroscopic measurements of the degrees of polarization of the He lines described above. As a result, we reconstructed the energy dependence of the cross section for the alignment of the total angular moments of the excited helium atoms by electron impact (Fig. 8).

In our experiment, a distant plasma object was modeled by a positive column of a helium electric discharge, whose EVDF differed significantly from the EVDF in a BPD. The degree of polarization of spontaneous emission from the plasma object was measured. The EVDF in the plasma object was determined using Q_0 and Q_2 (Fig. 9).

The reliability of the experimental results obtained by the proposed method was confirmed by independent probe measurements.

Finally, the relative anisotropy of the electron pressure in the "distant" plasma object was found to be $p_1/p = 2.74 \times 10^{-2}$.

CONCLUSION

A hybrid electronic–polarization method is proposed for analyzing anisotropic EVDFs in distant plasma objects.

The moments of the anisotropic EVDF are measured. The depolarization of the helium 4^1D_2–2^1P_1 atomic spectral line is investigated for a charged particle density of about 10^{11} cm^{-3}. The rate constant of the disalignment of helium atoms in the 4^1D_2 state due to collisions with charged particles is determined. The cross sections for the alignment of the total angular moments of helium atoms by electron impact and the degree of electron pressure anisotropy are measured.

An important advantage of the proposed method is the possibility of direct measurements of an anisotropic EVDF in distant plasma objects in the case when a priori information about the EVDF anisotropy is lacking.

ACKNOWLEDGMENTS

We are grateful to G.A. Dyuzhev for support and fruitful discussions.

REFERENCES

1. A. S. Mustafaev, A. P. Mezentsev, *et al.*, Zh. Tekh. Fiz. **54**, 2153 (1984) [Sov. Phys. Tech. Phys. **29**, 1263 (1984)].
2. A. S. Mustafaev, V. I. Demidov, and A. P. Mezentsev, Pis'ma Zh. Tekh. Fiz. **11**, 693 (1985) [Sov. Tech. Phys. Lett. **11**, 289 (1985)].
3. A. P. Mezentsev, A. S. Mustafaev, and V. L. Fedorov, Zh. Tekh. Fiz. **55**, 544 (1985) [Sov. Phys. Tech. Phys. **30**, 322 (1985)].
4. V. L. Fedorov, Zh. Tekh. Fiz. **55**, 926 (1985) [Sov. Phys. Tech. Phys. **30**, 554 (1985)].
5. A. S. Mustafaev and A. P. Mezentsev, J. Phys. D **19**, L69 (1986).
6. A. P. Mezentsev, A. S. Mustafaev, V. F. Lapshin, and V. L. Fedorov, J. Phys. B **20**, L723 (1987).
7. V. L. Fedorov and A. P. Mezentsev, Zh. Tekh. Fiz. **57**, 595 (1987) [Sov. Phys. Tech. Phys. **32**, 363 (1987)].
8. A. P. Mezentsev, A. S. Mustafaev, and V. L. Fedorov, J. Phys. D **21**, 1464 (1988).
9. V. F. Larshin and A. S. Mustafaev, Zh. Tekh. Fiz. **59** (2), 35 (1989) [Sov. Phys. Tech. Phys. **34**, 150 (1989)].
10. V. F. Lapshin, A. P. Mezentsev, and A. S. Mustafaev, J. Phys. D **22**, 857 (1989).
11. F. G. Baksht, V. F. Lapshin, and A. S. Mustafaev, J. Phys. D **28**, 689 (1995).
12. F. G. Baksht, V. F. Lapshin, and A. S. Mustafaev, J. Phys. D **28**, 694 (1995).
13. A. S. Mustafaev, A. P. Mezentsev, and V. L. Fedorov, NATO ASI Ser., Ser. B **367**, 531 (1998).
14. S. A. Kazantsev, Usp. Fiz. Nauk **139**, 621 (1983) [Sov. Phys. Usp. **26**, 328 (1983)].
15. S. A. Kazantsev, Pis'ma Zh. Éksp. Teor. Fiz. **37**, 131 (1983) [JETP Lett. **37**, 158 (1983)].
16. S. A. Kazantsev, A. S. Mustafaev, *et al.*, Opt. Spektrosk. **76**, 909 (1994) [Opt. Spectrosc. **76**, 809 (1994)].
17. L. Huksley and R. Crompton, *Diffusion and Drift of Electrons in Gases* (New York, 1974).
18. V. E. Golant, A. P. Zhilinskii, and S. A. Sakharov, *Fundamentals of Plasma Physics* (Atomizdat, Moscow, 1977; Wiley, New York, 1980).
19. L. Ya. Margolin, N. Ya. Polynovskaya, *et al.*, Teplofiz. Vys. Temp. **22**, 193 (1984).
20. S. A. Kazantsev, N. Ya. Polynovskaya, *et al.*, Usp. Fiz. Nauk **156**, 3 (1988) [Sov. Phys. Usp. **31**, 785 (1988)].

Translated by I. Efimova

Technical Physics, Vol. 45, No. 11, 2000, pp. 1406–1410. Translated from Zhurnal Tekhnicheskoĭ Fiziki, Vol. 70, No. 11, 2000, pp. 31–35.

Threshold for a Cumulative Resonant Microwave Streamer Discharge in a High-Pressure Gas

V. S. Barashenkov*, L. P. Grachev, I. I. Esakov**, B. F. Kostenko*, K. V. Khodataev**, and M. Z. Yur'ev**

** Joint Institute for Nuclear Research, Dubna, Moscow oblast, 141980 Russia*

*** Moscow Radiotechnical Institute, Russian Academy of Sciences, Varshavskoe sh. 132, Moscow, 113519 Russia*

E-mail: esakov@dataforce.net

Received December 2, 1999

Abstract—Results are reported from experiments aimed at investigating how the structure of a microwave streamer discharge depends on the gas pressure. The formation of a bright core in the streamer channel is shown to be of a threshold nature: in discharges initiated in the field of a standing electromagnetic wave of an open two-mirror cavity, a bright core forms in air and hydrogen in the pressure ranges $p_0 \geq 540 \pm 50$ torr and $p_0 \geq 740 \pm 70$ torr, respectively. Estimates are presented, according to which the appearance of a bright core can be attributed to the onset of a local microwave pinch effect. © *2000 MAIK "Nauka/Interperiodica".*

INTRODUCTION

In a gas at a high pressure p_0 and at the natural level of initial ionization, an electrodeless discharge in a linearly polarized electromagnetic (EM) microwave field of a TEM wave originates from an individual background electron and rapidly evolves into a thin plasma channel (streamer) stretched out in both directions along the vector of the electric component E_0 of the EM field. As the streamer length $2L$ approaches its maximum (resonant) value, the effective absorption cross section of the discharge channel becomes several orders of magnitude larger than the area of the visible transverse (with respect to the propagation direction of the EM wave) cross section of the discharge and the electric current in the streamer channel rapidly increases. In a gas at a comparatively low pressure, this phenomenon is observed as a bright flash extending almost over the entire streamer, which indicates that the microwave energy is absorbed essentially uniformly over the streamer length. As the gas pressure increases, the streamer starts to behave in a radically different manner: a very bright core appears in the central region of the streamer, and the microwave energy is largely deposited in this core [1, 2].

Figure 1 illustrates the pressure ranges in which these states of a resonant microwave streamer discharge in an EM field with the angular frequency $\omega \cong 2 \times 10^{10}$ cm^{-1} are observed in air and hydrogen [1, 2]. On the pressure scales, the ranges in which the discharge can be initiated at a fixed amplitude E_0 = 6.5 kV/cm of the field of a running wave are hatched [2]. At E_0 = 30 kV/cm, a discharge in air at the pressure p_0 = 760 torr was excited in the field of a standing wave of an open two-mirror cavity [1]. The pressure ranges in which discharges with a bright core (cumulative discharges) were observed in experiments are marked with arrows.

The data illustrated in Fig. 1 indicate that, in the pressure range $130 < p_0 < 760$ torr, the structure of discharges in air does not change in time, so that it remains unclear whether the evolution of a discharge into a cumulative state is continuous or threshold in nature. Continuous evolution implies that, at low pressures, the microwave energy is deposited relatively uniformly over the streamer length. As the gas pressure increases, the region where the microwave energy is absorbed becomes progressively shorter; at very high pressures, the microwave energy is deposited in an extremely short (pointlike) region. A threshold nature of the discharge evolution implies that the core in the streamer channel can only form when certain experimental conditions are met, the first of these being certain ratios of the microwave field amplitude E_0 to the gas pressure p_0. According to Fig. 1, these conditions are satisfied in streamer discharges in hydrogen: at a fixed amplitude E_0 = 6.5 kV/cm, the EM energy is deposited in the streamer core in the pressure range $p_0 \geq 250$ torr.

Grachev *et al.* [2] supposed that the bright core peculiar to cumulative streamer discharges stems from the local microwave pinch effect—plasma compression under the action of the magnetic field of the microwave current in the channel region where this current is the highest. It is clear that the pinch effect in electrodeless microwave discharges is a new physical phenomenon that requires further investigation.

In this paper, we report the results of experiments with microwave streamer discharges in air and hydrogen. We studied the evolution of discharges initiated in

1063-7842/00/4511-1406$20.00

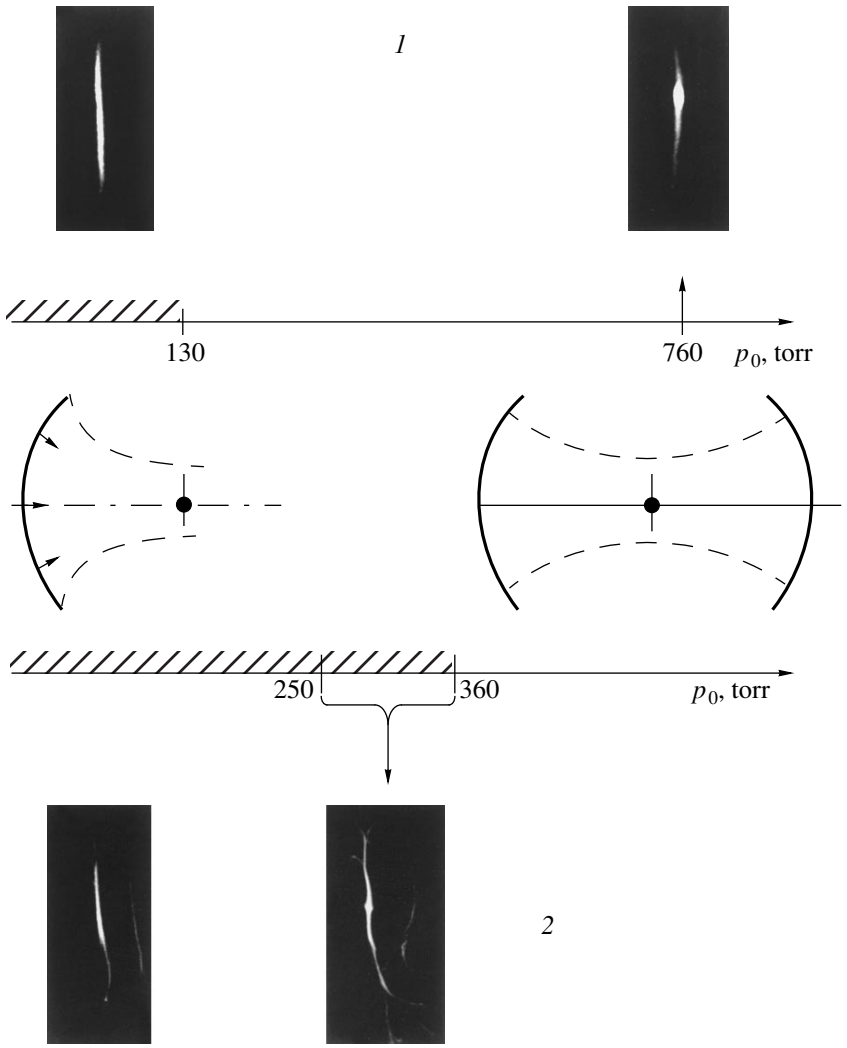

Fig. 1. Ranges of (*1*) air and (*2*) hydrogen pressures in which electrodeless microwave discharges with different structures can be excited (according to the experimental data of [1, 2]).

the focal region of a high-quality open two-mirror cavity by gradually changing the initial gas pressure p_0.

It is well known [3] that the pinch effect occurs when the magnetic-field pressure p_m (which is proportional to the squared ratio of the electric current I_0 in the channel to the channel diameter $2a$) at the surface of the current channel becomes higher than the gas-kinetic pressure p inside the channel. In experiments with an open cavity, regardless of the sort of gas, the electric current I_0 flowing in the central region of the streamer increases with p_0, because it is proportional to the initial field strength E_0, which cannot be lower than the breakdown field E_{br}, which in turn increases with p_0. On the other hand, the higher the pressure p_0, the smaller the diameter $2a$ of the streamer. Additionally, if the streamer current rapidly increases, then, by the time the "constriction" develops, the gas-kinetic pressure p in the channel can exceed the initial pressure p_0 only slightly. These considerations show that, in a streamer discharge in an open cavity, the higher the pressure p_0, the more favorable the conditions for the onset of the microwave pinch effect. Consequently, we can conclude that there exists a threshold pressure p_{0th} above which a streamer discharge should evolve into the cumulative state. Our experimental investigations were aimed precisely at determining the pressure thresholds p_{0th} for cumulative streamer discharges in air and hydrogen.

EXPERIMENTAL DEVICE

A schematic of the experimental setup is shown in Fig. 2. A microwave oscillator is capable of producing rectangular microwave pulses with the duration t_{pul} = 40 μs and a power of several megawatts, the angular frequency of the EM field being $\omega \cong 2 \times 10^{10}\ s^{-1}$. A specially designed matching transmission line feeds

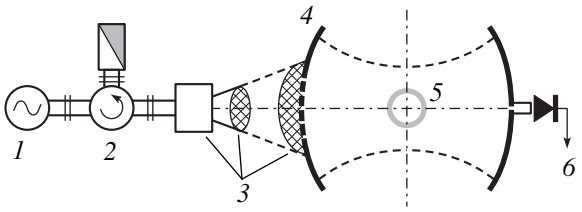

Fig. 2. Schematic of the experimental device for investigating microwave streamer discharges in an open two-mirror cavity: (*1*) microwave oscillator, (*2*) circulator, (*3*) matching transmission line, (*4*) open two-mirror cavity with spherical mirrors, (*5*) gas-filled cell, and (*6*) connection to an oscillograph.

microwave pulses from the oscillator into a high-quality open two-mirror cavity formed by two coaxial spherical concave mirrors 55 cm in diameter, with a radius of curvature of 35 cm. One of the mirrors is fixed and serves to couple pulses from the oscillator to the cavity, the power coupling coefficient being $\alpha_{con} \cong 10^{-3}$.

In the cavity, a microwave-transparent cell—a 50-cm-long quartz tube with an inner diameter of 8 cm and a 0.5-cm-thick wall—is installed. The cell is positioned symmetrically with respect to the center of the cavity and is oriented perpendicular to the cavity axis. The cell ends are sealed hermetically with 2-cm-thick plane glass. The cell is preevacuated to pressures $p < 1$ torr and then filled with the required gas at the desired pressure p_0. Note that, in experiments, the pressure in the cell was varied from 300 torr (at which pressure the streamer structure of a discharge was already pronounced [1]) to a maximum pressure above which we failed to achieve gas breakdown. The remaining volume of the cavity is filled with air at atmospheric pressure.

The cell–cavity system is tuned to resonance by gradually moving the cell and one of the mirrors in the axial direction. A small hole at the center of the fixed mirror serves to transmit the control signal to the oscillograph input through a linear amplitude detector. The cell–cavity system is tuned until the control signal becomes most intense. Calibrating the measurement line makes it possible to determine the amplitude E_0 of the EM field at the center of the cell by the amplitude of the control signal on the oscillograph screen.

The discharges can be photographed through the end glasses of the cell with an exposure time longer than the discharge duration.

EXPERIMENTAL RESULTS

Increasing the distance $2H$ between the mirrors from 45 to 61 cm along the cavity axis, we found that the amplitude E_0 of the EM field focused at the center of the cavity (and, accordingly, of the cell) was maximum for $2H = 50.4$ cm. Along the cavity axis, the EM field has the form of a linearly polarized standing TEM wave. The maximum of the wave occurs at the cavity center, the distance between the nodes being $\lambda_{res}/2 = 4.7$ cm. The vector of the electric component E_0 is perpendicular to the cavity axis. In the directions transverse to the cavity axis, the EM field is azimuthally symmetric and obeys a nearly Gaussian distribution function, which decreases by a factor of e on the characteristic spatial scale $F = 6$ cm.

After the microwave pulse is switched on, the total microwave energy W_{res} is fed into the cavity during a characteristic period of several microseconds. On this time scale, the field amplitude at the cell center reaches its maximum value $E_{0max} = 30$ kV/cm. In our experiments, the highest air pressure at which the breakdown can occur in such a field was $p_{0max} = 1$ atm and the relevant hydrogen pressure was $p_{0max} = 1.2$ atm.

When the cell is initially filled with a gas at a pressure $p_0 < p_{0max}$, then the field amplitude E_0 does not reach its maximum value: a field E_0 stronger than the breakdown field E_{br} produces gas breakdown and gives rise to a microwave streamer. After a significant fraction of the microwave energy has been deposited in the streamer channel, the coupling between the microwave oscillator and the cavity is violated and, according to the oscilloscope trace of the control signal, the microwave energy is no longer fed into the cavity.

Discharges initiated in gases at different pressures p_0 were observed to evolve into plasma channels (streamers) stretched out in both directions along the vector of the electric component E_0 of the EM field. Regardless of the shape of the discharge, the visible diameter of the plasma channels in both air and nitrogen was about $2a \cong 0.07$ cm, the channel length being $2L = 2.5 \pm 0.3$ cm. These discharge parameters were found to depend weakly on p_0.

The experimentally established pressure thresholds for cumulative streamer discharges are as follows: $p_{0th} = 540 \pm 50$ torr for cumulative discharges in air at $E_0 = 22$ kV/cm and $p_{0th} = 740 \pm 70$ torr for cumulative discharges in hydrogen at $E_0 = 21$ kV/cm. The streamers in air have, as a rule, one bright core in the central part, while those in hydrogen have two cores (sometimes, for p_0 close to p_{0max}, we observed one core at the center of a streamer in hydrogen, as is the case with streamers in air).

As an example, Fig. 3 shows photographs of discharges in air at the pressures $p_0 = 480$ torr $< p_{0th}$ and $p_0 = 760$ torr $> p_{0th}$. Figure 4 displays photographs of discharges in hydrogen at $p_0 = 480$ and 1000 torr. We can see that, for $p_0 < p_{0th}$, the brightness of discharges in both air and hydrogen is comparatively uniform along the streamer channel, whereas, for $p_0 > p_{0th}$, the discharges are seen to have bright cores in the central regions.

DISCUSSION

The energy flux P_{res} through the central cross section of the cavity per unit time just before the breakdown can be estimated from the geometric dimensions of the cavity and the parameters of the EM field:

$$P_{res} = \frac{E_0^2}{2Z_0}\frac{\pi F^2}{2}, \quad (1)$$

where $Z_0 = 120\pi\Omega$ is the wave impedance of free space. The estimate for the microwave energy stored in the cavity just before the breakdown can be obtained in a similar way:

$$W_{res} = P_{res}(2H/c), \quad (2)$$

where c is the speed of light and $2H/c$ is the shortest time after which the microwave energy is no longer fed into the cavity.

For example, at $E_0 = E_{0max}$, we have $P_{res} \cong 7 \times 10^7$ W (which is higher than the power of the supply microwave oscillator by a factor of several tens), $W_{res} \cong 0.12$ J, and $2H/c \cong 1.7$ ns.

Under the condition $\nu_c \gg \omega$ (where $\nu_c = 4 \times 10^9 p$ [torr] s^{-1} is the rate of collisions between plasma electrons and air molecules), which is satisfied in our experiments, the amplitude of a spatially uniform, quasi-continuous, microwave breakdown field can be estimated from the formula $E_{br} = 40\ p$ [torr] V/cm [4]. For example, for $p_{0max} = 1$ atm, we have $E_{br} = 30$ kV/cm, and, at the threshold pressure p_{0th}, we obtain $E_{br} \sim 22$ kV/cm. These field amplitudes coincide with the experimentally measured amplitudes. Thus, we can conclude that, in our experiments, the spatial nonuniformity of the microwave field and its unsteady nature do not affect air breakdown.

For hydrogen, for which we have $\nu_c = 5 \times 10^9 p$ [torr] s^{-1}, the breakdown field amplitude under the same experimental conditions is calculated to be $E_{br} = 14p$ [torr] V/cm [4]. Consequently, at the maximum field amplitude E_{0max}, the breakdown in nitrogen should occur at a pressure of 3 atm. However, the experimentally obtained value is equal to $p_{0max} = 2.1$ atm, which corresponds to the ratio $E_{br}/p = 19$ V/(cm torr); at the threshold pressure p_{0th}, this ratio is even higher at 30 V/(cm torr). Hence, experiments on breakdown in hydrogen should be prepared with allowance for the spatial nonuniformity and unsteady nature of the microwave field in the breakdown region. The experimentally observed increase in the ratio E_{br}/p with decreasing p_0 provides evidence that the breakdown process can be affected by electron diffusion, because a similar dependence of E_{br}/p on p_0 was also revealed in experiments reported in [5], in which the amplitude of the microwave field remained unchanged after the microwave field was switched on.

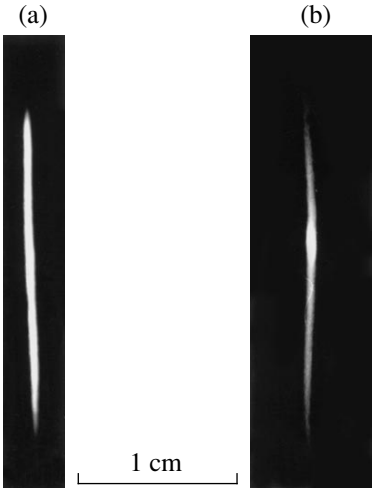

Fig. 3. Electrodeless microwave discharges in air at p_0 = (a) 480 and (b) 760 torr.

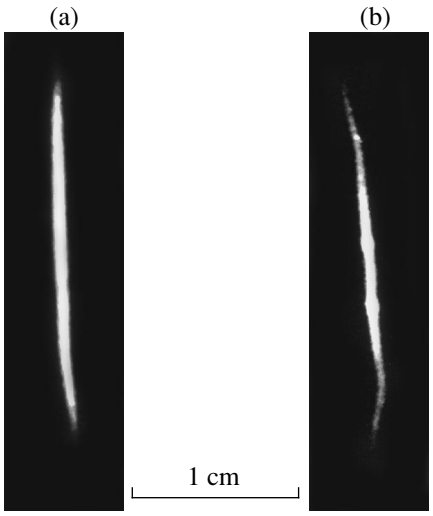

Fig. 4. Electrodeless microwave discharges in hydrogen at p_0 = (a) 480 and (b) 1000 torr.

Our experiments provide clear evidence that the structure of the microwave streamer changes only when the initial gas pressure becomes higher than a certain threshold pressure. Let us show that the conditions in a resonant streamer can be favorable for the onset of the pinch effect, which may be responsible for such an evolution of the streamer discharge.

Recall that the pinch effect occurs when the magnetic-field pressure at the surface of the current channel is higher than the gas-kinetic pressure inside the channel, i.e., $p_m > p$. To estimate the ratio of magnetic-field to gas-kinetic pressure in the range $p_0 \geq p_{0th}$, we assume that an experimentally observed streamer with the maximum length $2L$ behaves as a resonant vibrator, i.e., that its equivalent reactance is equal to zero and the main

contribution to its equivalent resistance comes from the radiation resistance R_Σ.

We consider a discharge in air at the pressure $p_0 = p_{0\text{th}}$. Along the entire streamer, the current flowing in the central region has the form

$$I_0 = E_0 L/R_\Sigma \cong 1.4 \times 10^3 \text{ A}, \quad (3)$$

where $R_\Sigma \cong 20\ \Omega$ for the maximum streamer length $2L$ [6].

In this case, the magnetic-field pressure is equal to

$$p_m = \frac{\mu_0 I_0^2}{(2\pi a)^2} = 5 \times 10^5 \text{ N/m}^2 = 5 \text{ atm}, \quad (4)$$

where $\mu_0 = 4\pi \times 10^{-7}$ H/m.

We can see that p_m is higher than p_0 by a factor of 7, so that the pinch effect is likely to occur. Such a high magnetic-field pressure p_m (in comparison with the initial gas pressure p_0) at the threshold for cumulative streamer discharges may stem from the fact that the estimates were made without consideration of the resistance of the plasma channel (in which case the actual electric current I_0 may turn out to be lower) and of the intense deposition of the microwave energy in the plasma (in which case the plasma pressure inside the channel increases).

In [2], the time scale on which the length of a streamer in air approaches its maximum (resonant) value was estimated to be several tens of nanoseconds. From the experimentally observed maximum streamer length $2L \cong 2.5$ cm, we can estimate the mean rate at which the streamer develops and the mean rise time of the microwave current as 10^7 cm/s and $\partial I_0/\partial t > 10^{10}$ A/s, respectively. The latter estimate usually refers to conventional dynamic pinches [3].

Similar estimates for a streamer in hydrogen (at the relevant threshold pressure $p_{0\text{th}}$ give $I_0 = 1.3 \times 10^3$ A and $p_m = 4.5 \times 10^5$ N/m^2 = 4.5 atm. In this case, the magnetic-field pressure also exceeds the initial gas-kinetic pressure; however, the estimated ratio $p_m/p_{0\text{th}} = 4.5$ is somewhat smaller than that obtained for air.

Finally, we emphasize that the experimentally observed significant difference between the threshold pressures $p_{0\text{th}}$ for streamers in the fields of standing and running waves in hydrogen (Fig. 1) requires a separate analysis [1].

CONCLUSION

Our experiments provide direct evidence for the existence of a pressure threshold for electrodeless cumulative resonant microwave streamer discharges in both hydrogen and air. To answer the question of whether the threshold nature of cumulative streamer discharges can be explained as being due to a local microwave pinch effect requires further experimental and theoretical investigations.

ACKNOWLEDGMENTS

We are grateful to K.V. Aleksandrov for help in carrying out the experiments.

REFERENCES

1. L. P. Grachev, I. I. Esakov, G. I. Mishin, and K. V. Khodataev, Zh. Tekh. Fiz. **66** (7), 32 (1996) [Tech. Phys. **41**, 652 (1996)].
2. L. P. Grachev, I. I. Esakov, G. I. Mishin, and K. V. Khodataev, Zh. Tekh. Fiz. **64** (2), 26 (1994) [Tech. Phys. **39**, 130 (1994)].
3. K. D. Sinel'nikov and B. N. Rutkevich, *Lectures on Plasma Physics* (Kharkov Gos. Univ., Kharkov, 1964).
4. A. D. MacDonald, *Microwave Breakdown in Gases* (Wiley, New York, 1966; Mir, Moscow, 1969).
5. L. P. Grachev, I. I. Esakov, and K. V. Khodataev, Zh. Tekh. Fiz. **68** (4), 33 (1998) [Tech. Phys. **43**, 378 (1998)].
6. G. T. Markov and D. M. Sazonov, *Antennas* (Énergiya, Moscow, 1975).

Translated by G. Shepekina

Technical Physics, Vol. 45, No. 11, 2000, pp. 1411–1416. Translated from Zhurnal Tekhnicheskoĭ Fiziki, Vol. 70, No. 11, 2000, pp. 36–41.

The Repetitive Microwave Discharge as a Catalyst for a Chemical Reaction

A. I. Babaritskiĭ, E. N. Gerasimov, S. A. Demkin, V. K. Zhivotov, A. A. Knizhnik, B. V. Potapkin, V. D. Rusanov, E. I. Ryazantsev, R. V. Smirnov, and G. V. Sholin

Russian Research Centre Kurchatov Institute, pl. Kurchatova 1, Moscow, 123182 Russia

Received January 17, 2000

Abstract—Results are presented from studies on plasma catalysis of the decomposition of methane into hydrogen and carbon in a repetitive microwave discharge. The dependence of the propagation velocity of a plasma channel on the sort of gas is determined; from this dependence, a preliminary conclusion can be drawn about both the mechanism for the development of the discharge and the ion composition of the discharge plasma. The measurements of the electron temperature in the discharge show that the rate at which active particles are produced is high enough to explain the acceleration of a chemical reaction by chain processes with the participation of these particles. © *2000 MAIK "Nauka/Interperiodica".*

Electric discharges are widely used to accelerate chemical processes. The energy of an equilibrium discharge is used, in particular, to efficiently heat the plasma, thus stimulating a chemical reaction due to the high temperature of the reagents. The energy of a nonequilibrium discharge can be used more selectively; however, in any case, a significant portion of the electromagnetic-field energy is converted into useless heat.

This seemingly inevitable loss of electric power can be reduced, e.g., by acting on preliminarily heated (in some ordinary way) reagents with a low-power electric discharge. In this case, the heat content of the reagents is chosen to be high enough for the chemical process to occur; however, because of kinetic limitations, the reaction rate is low. In such a situation, the electric discharge acts as a catalyst for the endoergic chemical process, whereas the energy necessary for this process is taken from the heat storage.

This paper is devoted to the study of the chemical decomposition of methane into hydrogen and carbon

$$CH_4 \longrightarrow 2H_2 + C_T, \qquad (1)$$

when a plasma produced by a repetitive microwave pseudocorona discharge at atmospheric pressure acts on preliminarily heated methane.

Figure 1 shows a schematic of the experimental device [1, 2]. The device consisted of a methane heater and a plasmocatalytic reactor, which included a discharge chamber and a system for the input of microwave power. The duration of the microwave pulses could be varied within the range 0.1–1 μs at a repetition rate of 1kHz. A modulator allowed us to obtain different regimes of magnetron operation (with a pulse power of up to 50 kW). Microwave pulses with a frequency of 9.04 GHz were launched into a 20-mm-diameter cylindrical discharge chamber through a ferrite circulator and mode converter, which converted microwaves into the H_{11} mode of a circular waveguide. A short-circuited piston with small-diameter holes was mounted in front of a quartz window at the end of the discharge chamber; this allowed us to observe visible emission from the discharge and prevented microwaves from leaving the chamber. At a distance of one-fourth of the microwave wavelength from the piston, a tungsten needle could be inserted into the chamber. The electric field near the needle point was higher than the breakdown field. When the needle was removed from the chamber, breakdown did not occur and the microwave power was completely reflected from the piston into a matched load, which enabled calorimetric measurements of the magnetron radiation power. The difference between the calorimeter data in the presence and absence of a discharge gave the average microwave power W_{av} absorbed in the discharge.

The parameters of the electron component in a hydrogen discharge were measured from the relative intensities of the H_α, H_β, and H_γ spectral lines. The line spectrum was obtained with an ISP-51 prism spectrograph and recorded with two photomultipliers. Signals from the multipliers were fed through pulsed amplifiers to a two-channel fast analog-to-digital converter (8 bit, 50 MHz) and were processed by a computer. With this diagnostic module, we could simultaneously measure the time dependences of two spectral lines with a 20-ns time step.

Visually, microwave pseudocorona discharges at atmospheric pressure in different gases (air, methane, hydrogen carbon dioxide, or argon) seem to be identical. The discharge is seen as a bunch of thin plasma filaments emerging from the needle point. Up to ten such filaments can exist in each pulse. Figure 2 shows the photos of individual pulsed discharges for different

1063-7842/00/4511-1411$20.00 © 2000 MAIK "Nauka/Interperiodica"

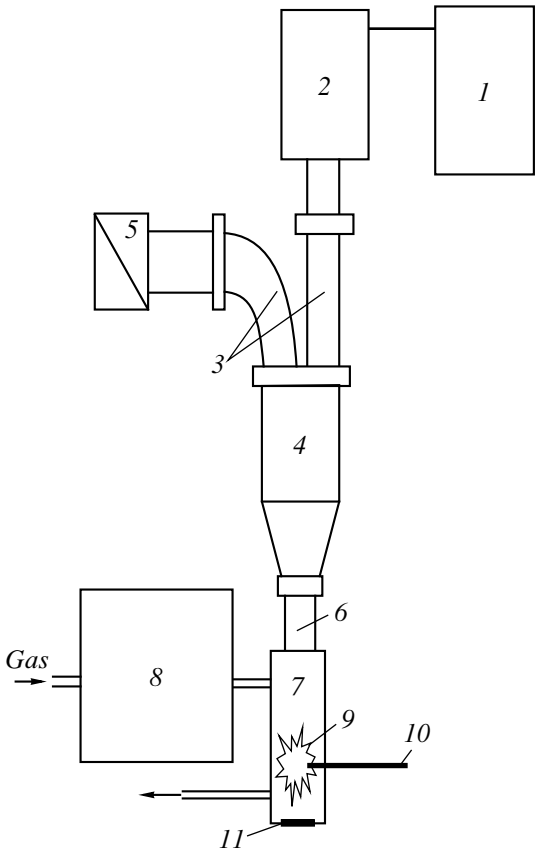

Fig. 1. Schematic of the device: (*1*) modulator, (*2*) magnetron, (*3*) waveguides, (*4*) ferrite circulator, (*5*) matched load, (*6*) mode converter, (*7*) discharge chamber, (*8*) heater, (*9*) discharge, (*10*) tungsten needle, and (*11*) quartz window.

magnetron powers and pulse durations; the photos illustrate the spatiotemporal dynamics of the nonsteady-state discharge plasma.

At the same time, the propagation velocity of the head of the plasma channel is different for gases with different molecular weights. This velocity was measured by recording the front of the pulsed radiation emitted from a small (0.1 mm in diameter) discharge region selected with the help of a diaphragm. The discharge emission was recorded with a photomultiplier and digital oscillograph with 20-ns resolution; the oscillograph was synchronized to the modulator pulses. First, we chose the tungsten-needle point for the observation region and determined the instant at which the leading edge of the emission pulse appeared; then, the observation region was displaced by a certain distance along the propagation direction of the plasma channels. In this case, the leading edge of the emission pulse (which corresponded to the instant at which the channel head reached the observation region) appeared with a delay. The propagation velocity was calculated from the ratio of the distance of the observation region from the needle to the delay time. Results of the velocity measurements in hydrogen, air, carbon dioxide, and methane discharges are presented in Fig. 3. An analysis of the dependence of the propagation velocity of the plasma channel on the sort of gas allows us to draw a preliminary conclusion about both the mechanism for the development of the discharge and the ion composition of the discharge plasma.

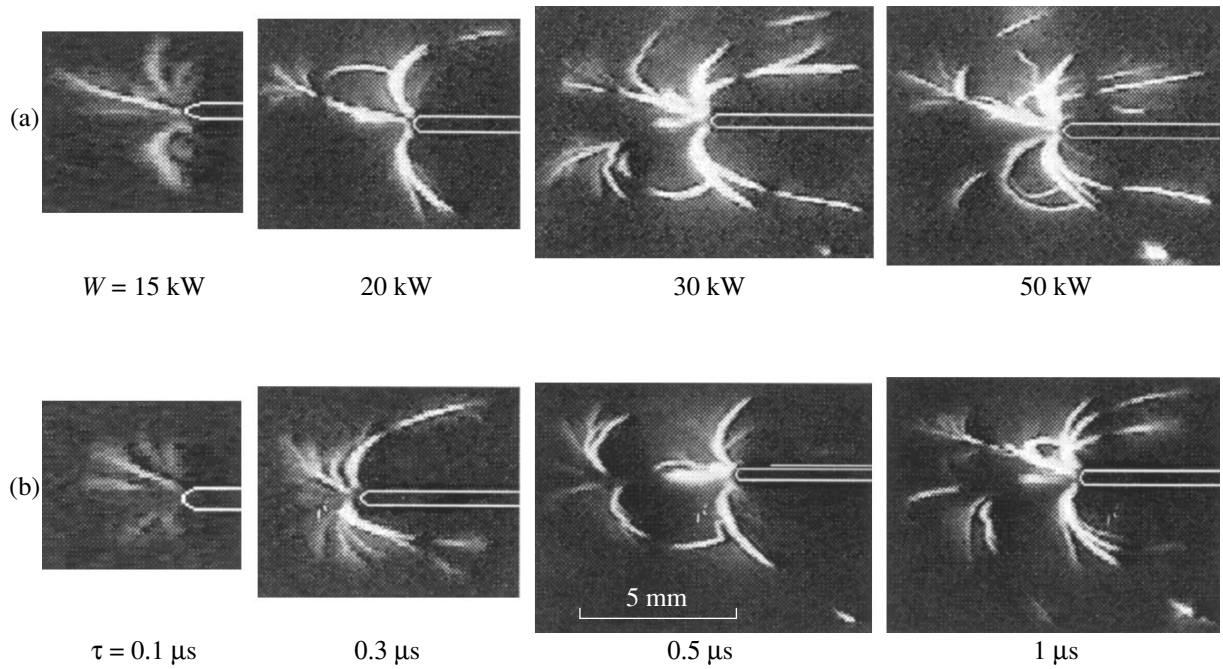

Fig. 2. Photos of a discharge in air (a) for different pulse powers W and a constant pulse duration $\tau = 1$ μs and (b) for different pulse durations τ and a constant pulse power $W = 50$ kW. The spatial scale is shown in Fig. 2b for a duration of 0.5 μs. The position of the needle point is schematically depicted.

Near the needle point, where the microwave electric field can attain a value of $E \approx 10^5$ V/cm, seed plasma regions arise. Electrons of this plasma efficiently absorb the field energy; as a result, the average electron kinetic energy T reaches a value on the order of the ionization energy I_0 (see Fig. 5 and its discussion). Since the formation of streamers is impossible because of the high frequency of the microwave field, the ionization front propagates along the force lines of the charge-separation field E_p maintained by the pressure gradient ∇p_e of the electrons heated by microwaves to the temperature $T_e \approx I_0$. The relations between the main field and plasma parameters can be written in the form

$$en_eE \approx \nabla p_e \approx I_0 \nabla n_e. \quad (2)$$

Under the action of the field E_p, the plasma ions at the discharge boundary acquire a drift velocity, which governs the propagation of the ionization front. It is important, however, that the electric field generated by the electron-pressure gradient is so high that the ion drift can be described by the relation [3]

$$M_i V_{\text{ion}}^2 = \frac{eE}{N_0 \sigma_{\text{ia}}}, \quad (3)$$

where M_i is the ion mass, V_{ion} is the ionization-front velocity, N_0 is the neutral density, and σ_{ia} is the ion–neutral collision cross section.

Substituting expression (2) for the electric field E_p into relation (3) and taking into account that the plasma density increases along the ionization length $l_i \approx (N_0\sigma_{\text{ion}})^{-1}$ (with σ_{ion} being the ionization cross section), we obtain the front velocity

$$V_{\text{ion}} = \sqrt{\frac{I_0}{M_i}} \sqrt{\frac{\sigma_{\text{ion}}}{\sigma_{\text{ia}}} \ln \frac{n_e}{n_{e0}}}, \quad (4)$$

where n_{e0} is the electron density outside the ionization region.

The ratio of the cross sections σ_{ion} and σ_{ia} in the region where $T_e \approx I_0$ is about 10^{-1}–10^{-2}; we also have $\ln(n_e/n_{e0}) \approx 20$–$40$. Hence, to a high accuracy, the propagation velocity of the discharge is

$$V_{\text{ion}} \approx \sqrt{\frac{I_{\text{ion}}}{M_i}}, \quad (5)$$

which coincides with the critical Alfvén velocity.

An analysis of heating and ionization processes in the microwave field shows that singly ionized ions prevail at the head of the plasma channel. As for the mass composition of positive ions at the head of the plasma channel, a consideration of the kinetics of ion–molecule reactions at atmospheric pressure reveals a stable tendency toward the formation of heavy ion complexes in both bimolecular and trimolecular processes [4]:

$$N_2^+ + 2N_2 \longrightarrow N_4^+ + N_2, \quad (6)$$

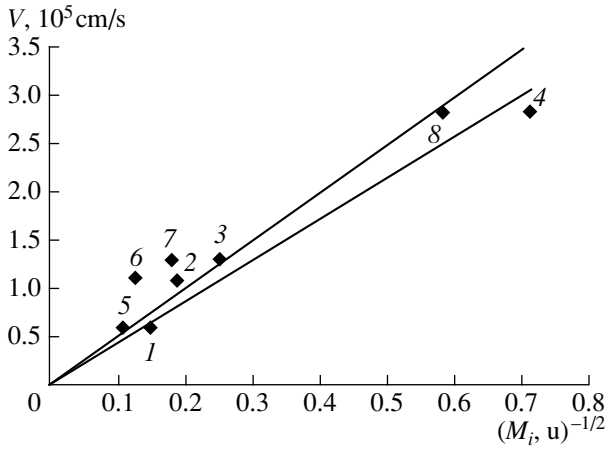

Fig. 3. Dependence of the propagation velocity of the plasma channels V on the ion molecular weight M_i. Each experimentally measured velocity value is presented by two points corresponding to different possible ion compositions: (*1*, *5*) discharge in CO_2, (*1*) CO_2^+, and (*5*) $C_2O_4^+$; (*2*, *6*) discharge in air, (*2*) N_2^+, and (*6*) N_4^+; (*3*, *7*) discharge in CH_4, (*3*) CH_4^+, and (*7*) $C_2H_6^+$; and (*4*, *8*) discharge in H_2, (*4*) H_2^+, and (*8*) H_3^+.

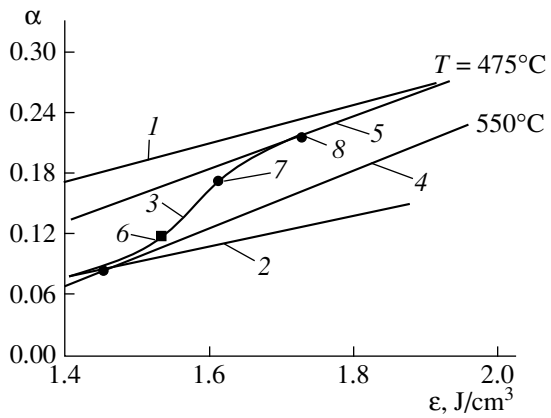

Fig. 4. Results of experiments and calculations in degree of conversion–energy input coordinates: (*1*) thermodynamic calculation, (*2*) experiment with the heat energy input, (*3*) experiment with the combined energy input, and (*4*, *5*) calculated straight lines of the parametric set $\alpha(\varepsilon_T)$ for $T = 550$ and 475°C. Experimental points *6*–*8* correspond to $W_{\text{av}} = 10$, 20, and 30 W, respectively.

$$CO_2^+ + 2CO_2 \longrightarrow C_2O_4^+ + CO_2, \quad (7)$$

$$H_2^+ + H_2 \longrightarrow H_3^+ + H. \quad (8)$$

Hence, we can expect that, at atmospheric pressure and a microwave pulse duration of ~1 μs, the most abundant positive ions in air will be N_4^+ ions. In carbon dioxide, these are $C_2O_4^+$ ions; and, in hydrogen, these are H_3^+ ions.

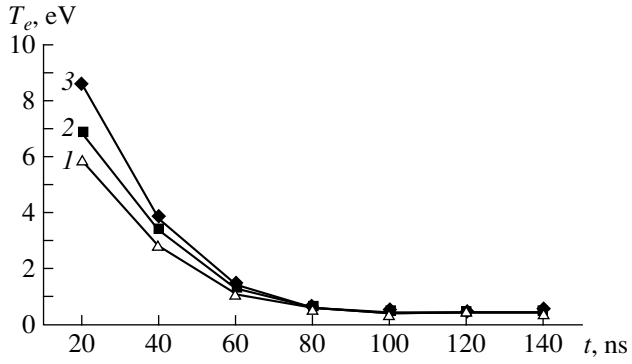

Fig. 5. Time dependences of the average electron energy T_e for different values of the microwave power W: (*1*) 10, (*2*) 20, and (*3*) 30 W.

When analyzing the propagation of the plasma channels in methane, one should take into account the formation of complex hydrocarbons like ethane ions,

$$CH_4^+ + CH_4 \longrightarrow C_2H_6^+ + H_2, \quad (9)$$

which can form ethylene molecules in the recombination reaction

$$C_2H_6^+ + e \longrightarrow C_2H_4 + H_2, \quad (10)$$

and also propane ions in the trimolecular process

$$CH_4^+ + 2CH_4 \longrightarrow C_3H_8^+ + 2H_2. \quad (11)$$

The propane ions form cyclopropane in the recombination reaction

$$C_3H_8^+ + e \longrightarrow C_3H_6 + H_2. \quad (12)$$

However, the rates of these reactions may be insufficiently high because of the complicated conversion of the molecular orbitals in them and the number of heavy $C_2H_6^+$ and $C_3H_8^+$ ions may be small. At the same time, at electron energies of $T_e \geq 15$ eV, the dissociative ionization in methane

$$CH_4 + e \longrightarrow CH_2^+ + H_2, \quad (13)$$

in which lighter ions are produced, begins to play an important role.

The presence of a significant amount of N^+, CO^+, O^+, and CH_2^+ ions at the ionization front might be evidence that the contribution from vibrational kinetics to the chemical processes at the ionization front is substantial, which is typical of steady-state conditions.

The measured dependences of the propagation velocity of the plasma channel shows that heavy ions prevail for hydrogen and carbon dioxide (points *2*, *3*, *5*, and *8* in Fig. 3 are more closely fitted by a straight line than points *1–4*), which agrees with the data on the rates and directions of the ion–molecule reactions at the gas pressures and degrees of ionization under study. For air and methane, the contribution from vibrational kinetics to the chemical processes presumably provides a much more varied ion composition at the front of the ionization region.

The time evolution of the discharge (Fig. 2b) allows us to distinguish two characteristic phases. At $t <$ 100 ns, the discharge is seen as a weakly luminous, fan-like quasicorona structure. At $t >$ 100 ns, a series of bright plasma channels grows from the initial plasma structure. As will be shown below (Fig. 5), the parameters of the electron component in these two different spatiotemporal phases of the discharge are also different.

Before proceeding to the experiments on determining the electron temperature T_e, we cite one result from studies of the effect of plasma catalysis [1, 2], which then will be compared with the results of T_e measurements.

Experiments on the decomposition of preliminarily heated methane under the action of a pulsed microwave discharge were conducted in the following way. Methane was heated to 400–600°C in a heater (Fig. 1) and injected at atmospheric pressure into a discharge chamber with the flow rate Q = 30–250 cm^3/s. The methane temperature T was measured in the discharge chamber with the help of a movable thermocouple. In the discharge, the gas acquired an additional energy ε_P, which was no more than 15% of the thermal energy ε_T acquired in the heater.

With the help of a chromatograph, we analyzed the gas-fraction composition at the outlet of the device in the presence and absence of a discharge and determined how the degree of methane conversion α increased under the action of the discharge. The experimental and calculated data are shown in Fig. 4. The degree of methane conversion α into hydrogen and carbon via reaction (1) is plotted on the ordinate. The specific energy deposition into methane ε is plotted on the abscissa. It consists of the thermal energy ε_T acquired in the heater plus the energy contributed by the discharge ε_P (in the presence of a discharge):

$$\varepsilon = \varepsilon_T + \varepsilon_P. \quad (14)$$

Here, $\varepsilon_P = W_{av}/Q$, W_{av} is the average microwave power, and the energy ε_T is a function of the temperature T and the degree of methane conversion α [1, 2]:

$$\varepsilon_T = (1-\alpha)\varepsilon_m(T) + \alpha\Sigma\varepsilon_r(T) + \alpha H(T_0). \quad (15)$$

The first term in expression (15) is the heat energy needed to heat an unreacted portion of methane from the room temperature T_0 to the temperature T, the second term describes the energy needed to heat the reaction products from T_0 to T, and the third term describes the heat effect from converting methane into the reaction products at a given degree of conversion α.

Curve *1* in Fig. 4 shows the result of equilibrium thermodynamic calculations in α and ε_T coordinates,

and curve *2* shows the experimental results obtained in the absence of a discharge (with only heat energy input into the system). The zero point corresponds to a heating temperature of 550°C and heating power of 190 W. Curve *3* describes the experiment with the preliminary heating of methane to 550°C and different discharge powers W [the input energy ε was determined according to relation (14)]. A comparison of curves *1–3* clearly demonstrates the effect of plasma catalysis, which manifests itself in the fact that the degree of methane conversion approaches the equilibrium value (curve *1*).

Note that curve *4* in Fig. 4 corresponds to the case of a conventional thermocatalytic endoergic process at a constant temperature (T = 550°C in this case). This curve was obtained by inverting dependence (15) with respect to the quantity α: $\alpha = F(\varepsilon_T, T)$, where the degree of conversion α depends on the input energy ε_T and the temperature T plays the role of a fixed parameter. Curve *5* in Fig. 4 presents the same dependence, but for the temperature T = 475°C. An analysis of the data in Fig. 4 shows that plasma catalysis increases the gas temperature (from 550 to 475°C in the experiment under consideration) due to the energy consumption in endoergic reaction (1). It is important that the decrease in the temperature of the system due to plasma catalysis does not affect the efficiency of catalysis, because the latter depends on the electron temperature, rather than on the gas temperature.

The acceleration of the process of methane conversion (1) may be attributed to the following effects. Either the discharge nonuniformly heats the gas to a high temperature and methane is rapidly decomposed in these hot regions or active particles are generated in the plasma, which favors the decomposition of methane in chain reactions [1, 2]. The first reason should be discarded, because the experimental curve *3* cannot lie over curve *4* in the case of thermal acceleration. Indeed, isotherm *4* is a limiting case for the thermal mechanism, in which all the additional energy that the discharge contributes to the system is used for dissociation only (without additional heating of the gas). Radicals, ions, carbon clusters, or excited particles may be active particles. It is shown in [2] that the effect of plasma catalysis can be explained with a high degree of certainty by the Winchester ion–molecular mechanism. In this mechanism, the role of active particles is played by positive ions that aid the decomposition of methane molecules and, thus, the formation of carbon clusters.

For the experiment to be explained by the processes involving active particles, the rate at which such particles are produced should be rather high. This rate is largely dependent on the electron energy distribution in the discharge. The average electron energy in the discharge was measured from the relative intensity of hydrogen spectral lines emitted from a 1×1-mm region near the needle point. The spectral response of the photomultipliers was calibrated by an incandescent band lamp emitting as a black body at a known temperature. The lamp temperature was measured with a pyrometer. For a given ratio between the intensities of two lines, the excitation temperature T_H of hydrogen atoms was determined from the following relation:

$$\frac{1}{T_H} = \frac{1}{T} - \frac{1}{E_i - E_j}\ln(C_{ij}n), \tag{16}$$

where T is the lamp temperature; E_i and E_j are the energies of the emitting levels; C_{ij} is a constant obtained from calibration, which accounts for the dependences of the spectrograph dispersion and the photomultiplier response on the emission wavelength; and n is the measured ratio of the line intensities.

In order to find the relation between the average energy of free plasma electrons and the experimentally determined excitation temperature of hydrogen atoms, a model of the discharge emission was developed. We solved the set of equations describing the population of excited states,

$$\frac{dn_n}{dt} = \Sigma S_{\text{in}} + \Sigma I_{\text{in}} + \Sigma T_{\text{in}} + R_n - \Sigma S_{\text{ni}} - \Sigma I_{\text{ni}} - \Sigma T_{\text{ni}} = 0, \tag{17}$$

for different values of the average electron density. In Eq. (17), the summands $S_{\text{in}} = n_i n_e \langle \sigma_{\text{in}} V \rangle$ $(i < n)$ account for electron-impact excitation, $I_{\text{in}} = g_{\text{in}} n_i A_{\text{in}}$ $(i > n)$ account for spontaneous emission, $T_{\text{in}} = n_i n_e \langle \sigma^*_{\text{in}} V \rangle$ $(i > n)$ account for the quenching by superelastic collisions, and $R_n = \delta n_e^2 \langle \sigma_n V \rangle$ account for the capture of an electron during recombination emission. Here, g_{in} is the escaping factor [5] introduced to allow for the absorption of radiation in the plasma channel, A_{in} is the Einstein coefficient, and δ is the fraction of H atoms in the discharge. One of the equations in (17) is a dependent equation; hence, the set of equations was supplemented by the equation Σn_n = const.

The electron energy distribution function in the initial phase of the discharge (t < 100 ns) was determined by solving the kinetic Boltzmann equation in the two-term approximation. We used a model similar to the dc discharge model, because the ratio of the electron-energy relaxation rate to the field frequency is much higher than unity over a wide range of electron energies under the given conditions. The necessary cross sections for elementary processes in methane (i.e., for vibrational and electronic excitation, ionization, and dissociation) were taken from [6, 7]; for hydrogen, we used the cross sections from [8]. In the later phase of the discharge, when the plasma in the channel is almost completely thermalized, the electron energy distribution function was assumed to be Maxwellian.

Besides the population level n_n, two additional parameters, namely, the electron density n_e and the hydrogen atom density n_{H}, enter set (17) through δ

and g_{in}. The dependence of n_e on the average electron energy ε (i.e., on the discharge phases with different values of ε) was chosen so as to fit the experimental data on the radiation intensity $I \sim n_e^2 \exp(-\Delta E/\varepsilon)$; the proportionality factor was found from the condition that the maximum density n_e is equal to the critical electron density: $n_{e\max} = n_{cr} = 6 \times 10^{15}$ cm^{-3}. For a given n_e, the n_H density can be determined from the equation describing the electron-impact dissociation of H_2 molecules. For electron energies that are not too high ($\varepsilon \le 10$ eV), a good approximation is $n_H = \text{const} \approx 10^{18}$ cm^{-3} and $\delta \approx 0.04$.

By solving set (17), we determined the populations n_n, which were then used to calculate the intensities of spectral lines and the excitation temperature corresponding to the average electron energy. This also allowed us to solve the inverse problem—to determine the average electron energy from the experimentally measured excitation temperature.

The calculated time dependences of the electron temperature are shown in Fig. 5. The measurements were carried out for three values of the microwave power absorbed in the discharge: 10, 20, and 30 W, which correspond to the experimental points *6–8* in Fig. 4. For all these regimes, the temperature in the second discharge phase (Fig. 2, $t > 100$ ns), in which a set of bright plasma channels is formed, is almost the same and is equal to 0.6 eV. In the first (pseudocorona) phase of the discharge, a detectable discharge emission appears by the end of the leading edge of the microwave pulse (this instant corresponds to the zero time in Fig. 5). In this discharge phase, the temperature is significantly higher and reaches nearly 10 eV at $t = 20$ ns. The excitation temperature T_{ex} at $t = 0$ was determined with a large error due to the low radiation intensity. This fact prevented us from determining the electron temperature with a reasonable accuracy when solving set (17). It may be only suggested that, within the time interval 0–20 ns, the electron temperature exceeds 10 eV. Note that, in all three regimes, the temperatures deduced from the H_β to H_α and H_γ to H_α ratios coincided.

A preliminary analysis shows that the observed high electron temperature in the initial discharge phase ($t <$ 50 ns) can provide high efficiency of the production of positive ions (with a cost of 100 eV). In the early phase of the discharge (before thermalization of the channel, which occurs in a time on the order of 100 ns), while the ion density is relatively low (on the order of 10^{14} cm^{-3}), the ion–molecular mechanism of plasma catalysis [2] can provide methane conversion with an energy cost of nearly 0.1–1 eV. Let us recall that the corresponding energy expenditure in experiment [1] was equal to 0.2 eV. The influence of recombination for a given ion density is still unimportant at this stage. During recombination decay, it might be possible to lower the cited cost of conversion by nearly one order of magnitude. However, thermalization of the plasma channel is accompanied by a substantial increase in the ion density (up to 5×10^{16} cm^{-3}). This, on the one hand, increases the energy deposition during the second (thermalized) discharge phase and, on the other hand, sharply decreases the efficiency of plasma catalysis because of recombination processes. At a sufficiently high temperature, the usual thermal mechanism governs the decomposition of methane inside the channel and the conversion cost approaches the thermal value. However, the ions produced inside the thermalized channel may be used for methane conversion during diffusive decay of the plasma channel after the pulse, when the ion density falls because of diffusion and the contribution from the recombination mechanism is reduced. A preliminary analysis of the discharge afterglow shows that, in principle, the cost of methane conversion may be lowered due to plasma catalysis to a value of about 0.2 eV.

In summary, acceleration of the thermal decomposition of methane under the action of a repetitive microwave discharge has been demonstrated experimentally. The electric power of the discharge is no more than 15% of the heat power expended for preliminary heating of methane. The reaction acceleration results from the production of chemically active particles in the discharge. The electron temperature in the discharge, at least in its initial phase, is high enough to ensure the necessary rate for producing such particles. Theoretical estimates of the possible influence of various active particles on the decomposition of methane can be found in [1, 2].

REFERENCES

1. V. D. Rusanov, K. Étivan, A. I. Babaritskiĭ, *et al.*, Dokl. Akad. Nauk **354**, 213 (1997).
2. A. I. Babaritskiĭ, M. A. Deminskiĭ, S. A. Demkin, *et al.*, Khim. Vys. Énerg. **33** (1), 59 (1999).
3. Yu. P. Raizer, *Gas Discharge Physics* (Nauka, Moscow, 1987; Springer, Berlin, 1991).
4. K. Smith and R. M. Thompson, *Computer Modeling of Gas Lasers* (Plenum, New York, 1978; Mir, Moscow, 1981).
5. R. McWhirter, in *Plasma Diagnostic Techniques*, Ed. by R. H. Huddlestone and S. L. Leonard (Academic, New York, 1965; Mir, Moscow, 1967).
6. D. K. Davies, L. E. Kline, and W. E. Bies, J. Appl. Phys. **65**, 3311 (1989).
7. T. Nakano, H. Toyoda, and H. Sugai, Jpn. J. Appl. Phys. **30** (11A), 2912 (1991).
8. *Joint Institute of Laboratory Astrophysics Transactions*, Ed. by A. V. Phelps *et al.*, 1985.

Translated by N. Larionova

Technical Physics, Vol. 45, No. 11, 2000, pp. 1417–1421. Translated from Zhurnal Tekhnicheskoĭ Fiziki, Vol. 70, No. 11, 2000, pp. 42–47.

SOLIDS

Phase States and Ferroelectric Properties of $Pb(Zr, Sn, Ti)O_3$ Ceramic

V. V. Shvartsman, S. E. Aksenov, and E. D. Politova

Karpov Research Institute of Physical Chemistry (Russian State Scientific Center), ul. Vorontsovo pole 10, Moscow, 103064 Russia

Received December 22, 1999

Abstract—The ferroelectric and dielectric properties of $Pb_{0.99}[(Zr_{1-x}Sn_x)_{1-y}Ti_y]_{0.98}Nb_{0.02}O_3$ ceramic of composition (I) $x = 0.5$, $y = 0.04$–0.12 and (II) $x = 0.4$, $y = 0.06$–0.09 were studied, and the T–x and E–T diagrams were constructed. When zinc is substituted for tin, the range of coexistence of the ferroelectric and antiferroelectric phases extends. The range of the nonpolar phase shrinks when the titanium content is increased. © *2000 MAIK "Nauka/Interperiodica".*

INTRODUCTION

Lead zirconate–based solid solutions are widely used in electronic engineering, instrument building, and other branches of industry. However, the behavior of these oxides near the phase transitions has not been adequately understood. Research in this field continues to be topical from both scientific and applied viewpoints.

At room temperature, $PbZrO_3$ has a rhombic unit cell and antiferroelectric (AFE) properties. At ~510 K, it undergoes the phase transition to the rhombohedral ferroelectric (FE) phase, which exists between 0 and 26°C, and then to the paraelectric (PE) phase [1]. When zirconium is partially replaced by titanium, the stability range of the high-temperature rhombohedral FE phase extends. When the titanium content exceeds 5 at.%, the solid solution exhibits FE properties even at room temperature [2]. The incorporation of tin cations into octahedral sites decreases the distortion of the rhombohedral perovskite cell of the FE phase and bridges the gap between the AFE and FE phase volumes. This makes it possible to vary the temperature and concentration ranges of existence of these phases in wider limits [3]. It has been established that the temperature interval where the free energies of the AFE and FE phases are close extends when tin is incorporated into the composition [4]. With this in mind, one can expect the induced AFE-to-FE state transition at relatively low electric field strengths and in a wide temperature range. At such transitions, the electromechanical and thermodynamic characteristics exhibit steps, which can be used for energy conversion [5], specifically in cryogenic devices. These devices use the so-called electrocaloric effect (ECE): cooling of a working substance by induced passing to the FE state under adiabatic conditions [6]. As follows from thermodynamic considerations, the ECE is the most pronounced at phase transitions [7]. To date, the greatest experimental ECE value has been found to be $\Delta T = 2.6$ K, which is quite sufficient for applications. This value was obtained in the $Pb(Zr, Sn, Ti)O_3$ system at 425 K [8]. Ceramics intended for electrocaloric applications must have compositions that undergo the induced phase transition at electric field strengths $E < 20$ kV/cm, with the transition temperature in an interval of ~50 K around room temperature.

In this work, we studied the phase states, as well as the dielectric and FE properties, of the $Pb_{0.99}[(Zr_{1-x}Sn_x)_{1-y}Ti_y]_{0.98}Nb_{0.02}O_3$ solid solutions with (I) $x = 0.5$, $y = 0.04$–0.12 and (II) $x = 0.4$, $y = 0.06$–0.09. Our aim was to estimate the ECE in these compositions.

EXPERIMENTAL

Sample preparation. Ceramic samples were obtained by solid-phase synthesis from associated oxides and carbonates. Niobium (2 at. %) was introduced in order to raise the resistivity and decrease the coercive field of the samples [9, 10]. Synthesis was carried out at $T_1 = 850$°C for 6 h. The sintering temperatures of the ceramics were $T_2 = 1300$°C (samples I), 1300°C and 1380°C (samples with $y = 0.085$–0.095), and 1380°C (samples II). The sintering duration was 1 h in each of the cases.

Measuring techniques. The phase composition of the samples was studied by X-ray phase analysis (XPA). The dielectric parameters (permittivity ε, conductivity σ, and dielectric loss tangent $\tan\delta$) were measured with an automatic setup at temperatures between 300 and 900 K and frequencies of 100 Hz–100 kHz. Dielectric hysteresis loops were observed with a Soyer–Tower installation between 300 and 600 K. The voltage applied to the samples was up to 2 kV, and the applied field frequency was 50 Hz.

1063-7842/00/4511-1417$20.00

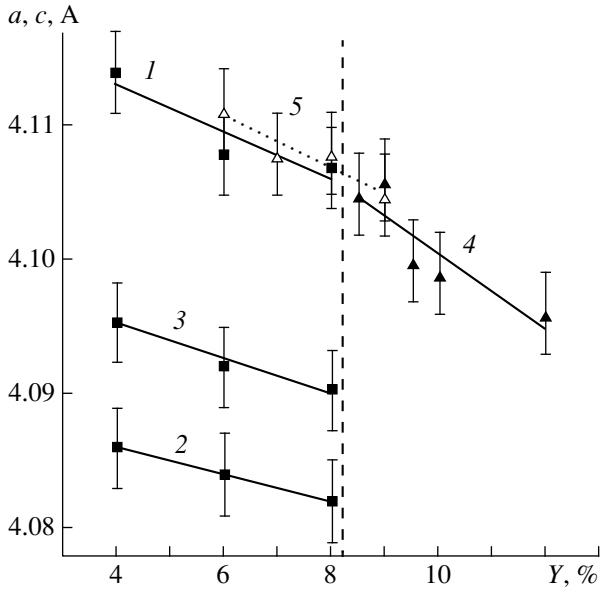

Fig. 1. Concentration dependences of the cell parameters for the $Pb_{0.99}[(Zr_{1-x}Sn_x)_{1-y}Ti_y]_{0.98}Nb_{0.02}O_3$ samples. (*1*) c_t, (*2*) a_t, (*3*) a_t, (*4*) a_{kh} (type-I) and (*5*) a_{kh} (type II).

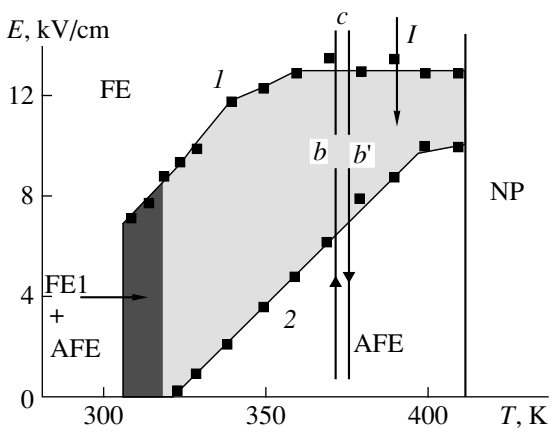

Fig. 2. Temperature–field phase diagram for the $Pb_{0.99}[(Zr_{0.6}Sn_{0.4})_{0.94}Ti_{0.06}]_{0.98}Nb_{0.02}O_3$ sample. (*1*) Temperature dependence of the field $E_1(T)$, which induces the AFE-to-FE transition, and (*2*) temperature dependence of the field $E_2(T)$, at which the reverse transition to the AFE phase takes place.

EXPERIMENTAL RESULTS

In all the samples, the phase with the perovskite-like structure prevails, as follows from XPA data. Diffractograms taken from the samples with $x = 0.5$ have extra lines that indicate the presence of impurity phases in small amounts. Type-I samples with $y \le 0.08$ have a tetragonal unit cell; and those with $y \ge 0.085$, rhombohedral. All type-II samples have a rhombohedral unit cell. As y grows, the unit cell volume decreases in samples of both types (Fig. 1). For type-I samples, the unit cell volume grows stepwise at the concentration morphotropic transition from tetragonal to rhombohedral symmetry.

At room temperature, type-II samples are ferroelectric. The spontaneous polarization P_s determined from the hysteresis loops rises from 7 to 12.5 μC/cm^2 as y grows. The coercive field strength E_c was ~4.5 kV/cm.

Type-I samples obtained at $T_2 = 1300$°C are of low dielectric strength and are inappropriate for dielectric hysteresis loop observation. The phase states in these samples were identified by the second-harmonic-generation (SHG) method [11]. In the tetragonal samples ($y \le 0.08$), the intensity of the SHG signal is low ($q < 5$), which is typical of centrally symmetric materials (AFEs). For the samples with $y \ge 0.085$, $q > 20$, which means that they are centrally asymmetric (FE properties). The observation of saturated hysteresis loops at room temperature for the samples with $y = 0.085$–0.095 obtained at $T_2 = 1380$°C is consistent with the SHG data. For these compositions, the spontaneous polarization rises from 13 ($y = 0.085$) to 15.5 μC/cm^2 ($y = 0.095$) and E_c is ~4.8 kV/cm.

The samples that are ferroelectric at room temperature pass to the AFE state when heated. This state is identified by the occurrence of double hysteresis loops. Between the temperature at which the saturated loops disappear and the one above which the loops are observed, there exist intervals, ~10–25 K for type-II samples and ~20–40 K for type-I ones, where unsaturated FE loops are observed at low field intensities. On a further increase in the field, these loops become distorted, showing a waist, and take the form of double

Room-temperature spontaneous polarizations P_s and coercive fields E_c, fields E_1 inducing the AFE-to-FE transition, and fields E_2 of the reverse (FE-to-AFE) transition

Composition	P, μC/cm^2	E_c, kV/cm	E_1, kV/cm	E_2, kV/cm
$x = 0.5$, $y = 0.085$	12.9	4.8	11 ($T = 390$ K)	8.4 ($T = 390$ K)
$x = 0.5$, $y = 0.09$	13.5	4.8	7.3 ($T = 390$ K)	2.4 ($T = 390$ K)
$x = 0.5$, $y = 0.095$	15.5	4.8	5.8 ($T = 390$ K)	2 ($T = 390$ K)
$x = 0.4$, $y = 0.06$	7.2	4.5	13 ($T = 400$ K)	8 ($T = 400$ K)
$x = 0.4$, $y = 0.08$	10.1	4.6	7 ($T = 400$ K)	3 ($T = 400$ K)
$x = 0.4$, $y = 0.09$	12.5	4.5	4.3 ($T = 400$ K)	0.6 ($T = 400$ K)

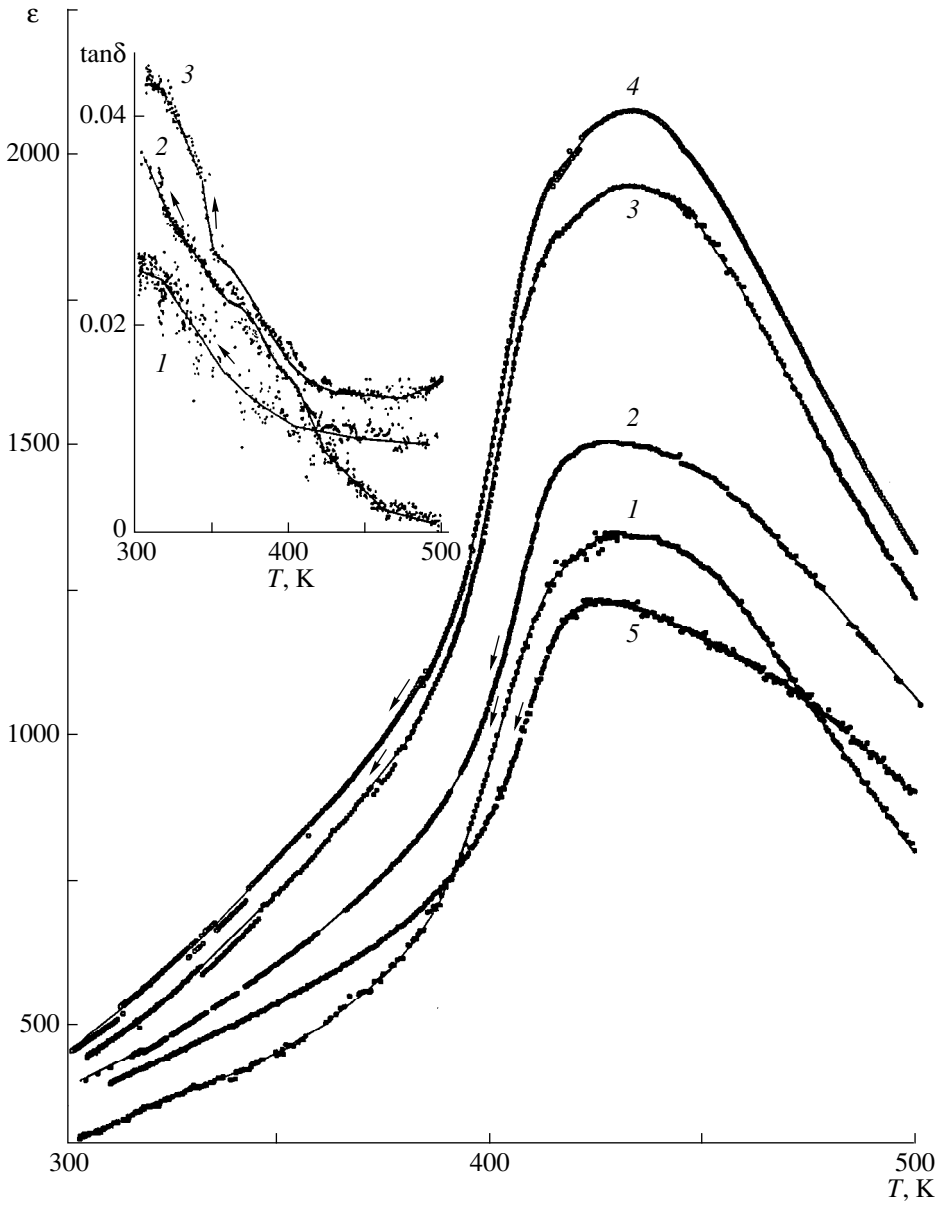

Fig. 3. Permittivity ε and dielectric loss tangent tanδ vs. temperature for $Pb_{0.99}[(Zr_{1-x}Sn_x)_{1-y}Ti_y]_{0.98}Nb_{0.02}O_3$ ceramics. (*1–4*) Samples sintered at T_2 = 1380°C with y = (*1*) 0.085, (*2*) 0.090, (*3*) 0.095 (measuring field frequency f = 100 kHz), and (*4*) 0.095 (f = 1 kHz). (*5*) Type-I sample (T_2 = 1300°C) with y = 0.09.

AFE loops. As y grows, the AFE-to-FE transition temperature determined from the appearance of saturated hysteresis loops upon cooling rises from 300 to 380 K (x = 0.4) and from 320 to 350 K (x = 0.5).

In samples of both types, an increase in y is accompanied by a decrease in the field that induces the AFE-to-FE transition (E_1) and in the field at which the reverse transition takes place (E_2) (see table). For type-I samples, the values of E_1 are greater.

Figure 2 shows the *T–E* diagram for the samples with y = 0.06 (II). When the electric field is switched on and then off, the states change following the phase trajectory a(AFE) ⟶ b(AFE) ⟶ c(FE) ⟶ b'(FE) ⟶ a(AFE). In the shaded region (I), the samples that passed into the FE state when the field was applied retained this state when the field was subsequently decreased to E_2.

Temperature dependences of the permittivity $\varepsilon(T)$ peak at T_m for all the samples (Figs. 3, 4). The temperature of the maximum T_m is 10–30 K (I) and 20–40 K (II) higher than that at which the double hysteresis loops disappear. For the type-II samples, T_m shifts from 446 (y = 0.06) to 420 K (y = 0.09); and for the samples of type I, from 446 (y = 0.06) to 416 K (y = 0.12). For the samples of both types, the $\varepsilon(T)$ curve has a plateau near the peak. The plateau narrows with increasing tita-

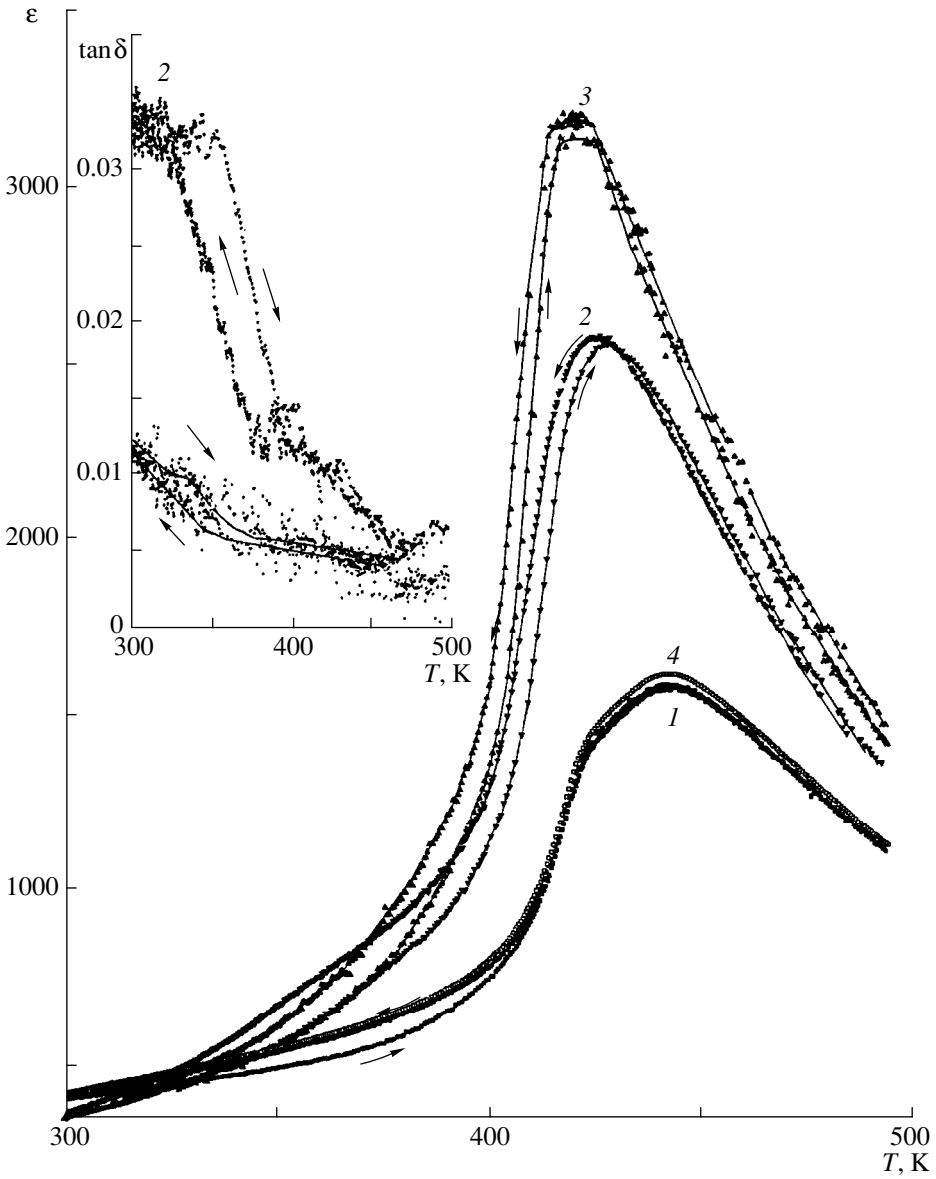

Fig. 4. Permittivity ε and dielectric loss tangent $\tan\delta$ vs. temperature for the type-II samples (T_2 = 1380°C) with y = (*1*) 0.06, (*2*) 0.08, (*3*) 0.09 (measuring field frequency f = 100 kHz), and (*4*) 0.06 (f = 1 kHz).

nium concentration. The peak value of ε, ε_m, grows with y.

The AFE-to-FE transition is accompanied by low-temperature anomalies like steps in the $\tan\delta(T)$, $\log\sigma(T)$, and $1/\varepsilon(T)$ curves. Their smearing increases as y diminishes. The low-temperature anomalies show a hysteresis loop, which tends to shrink with growing y.

For the type-I samples sintered at T_2 = 1300°C, the smearing of the anomalies is greater and the value of ε_m is lower than for those obtained at T_2 = 1380°C.

The temperatures at which the dielectric anomalies are observed do not depend on the frequency of the field at which the measurements are taken.

DISCUSSION

Figure 5 shows a concentration–temperature diagram that is constructed from the data for the dielectric hysteresis loops, temperature dependences of the dielectric characteristics, and SHG signal intensities. A distinct demarcation line between the FE and AFE states is seen to be absent for the composition studied. Instead, an intermediate region where these phases coexist is observed. For the solid solutions of type I, this region is much wider than for those of type II. In the intermediate region, the solid solutions are AFE + FE mixtures. This is corroborated by the form of the hysteresis loops: as the field strength E grows, the unsaturated ferroelectric loop becomes distorted, transforming into a double loop with a broad waist. The

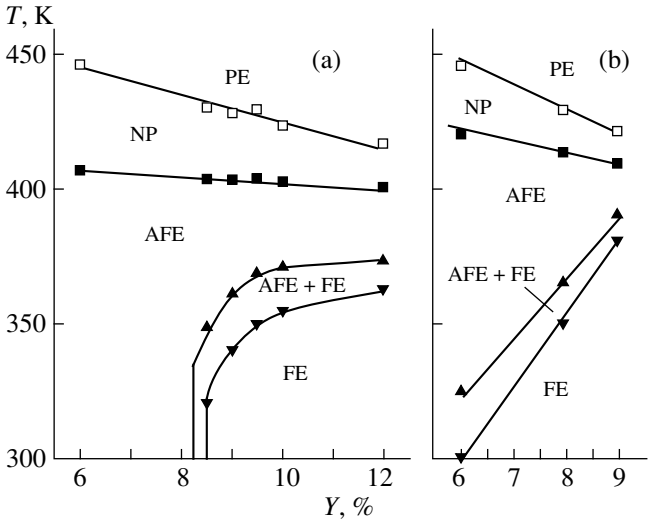

Fig. 5. Composition–temperature phase diagram for the $Pb_{0.99}[(Zr_{1-x}Sn_x)_{1-y}Ti_y]_{0.98}Nb_{0.02}O_3$ samples with x = (a) 0.5 (type I) and (b) 0.4 (type II).

mixed phase composition in the intermediate region also follows from the fact that the smearing of the dielectric anomalies observed at the FE-to-AFE transition changes. As the concentration moves away from the morphotropic boundary between the tetragonal AFE and rhombohedral FE phases, the two-phase region narrows (as follows from the dielectric measurements and hysteresis data).

As was noted, the temperature T_m of the $\varepsilon(T)$ maximum exceeds the one at which the double hysteresis loop disappears. The latter coincides with the temperature at which $d\varepsilon/dT$ peaks. Similar behavior of $\varepsilon(T)$ was also observed in $Pb_{0.99}[(Zr_{1-x}Sn_x)_{1-y}Ti_y]_{0.98}Nb_{0.02}O_3$ [12], (Pb, Sr)ZrO_3 [13], and Pb(Zn, Sn)O_3 [14, 15] solid solutions. It can be explained by the presence of the region where the AFE and FE phases coexist. In [12], such behavior is associated with an intermediate cubic phase having a multiplet unit cell. In [13], the smearing of the $\varepsilon(T)$ peak is attributed to transition nonpolar phases emerging between the tetragonal AFE and PE phases. Such a conclusion was made from anomalies in the temperature dependence of the specific elongation. The nature of these nonpolar phases still remains unclear. The transitions between them were suggested to be treated as "crumpling" transitions rather than transitions between two AFE phases [16]. Our data for the hysteresis loops, as well as the lowering of T_m and narrowing of the transition region when the titanium content increases, are consistent with this treatment.

Thus, in the studied solid solutions, one can induce the AFE-to-FE phase transition by applying electric fields in the range of E = 8–14 kV/cm. This transition is identified by the presence of double dielectric hysteresis loops. In samples of both types, an increase in the titanium content makes the FE state more stable. When the tin content is raised, the range of coexistence of the AFE and FE phases extends; moreover, the AFE phase becomes more stable. The greater the tin concentration, the higher the field inducing the AFE-to-FE transition (provided that the titanium concentration is the same).

To conclude, our data demonstrate that the electrocaloric effect calls for further investigation in samples of type I (y = 0.085–0.095) and type II (y = 0.06–0.08).

ACKNOWLEDGMENTS

This work was financially supported by the Russian Foundation for Basic Research (grant no. 98-03-32848).

REFERENCES

1. F. Jona and G. Shirane, *Ferroelectric Crystals* (Pergamon, Oxford, 1962; Mir, Moscow, 1970).
2. Yu. N. Venevtsev, E. D. Politova, and S. A. Ivanov, *Ferrielectrics and Antiferrielectrics in the Barium Titanate Family* (Khimiya, Moscow, 1985).
3. B. Jaffe, R. S. Roth, and S. Marzullo, J. Res. Natl. Bur. Stand. **55**, 239 (1955).
4. B. Jaffe, Proc. Inst. Radio Eng. **49**, 1264 (1961).
5. W. Pan, Q. Zhang, A. Bhalla, and L. E. Cross, J. Am. Ceram. Soc. **72**, 571 (1989).
6. Y. V. Sinyavsky and V. M. Brodyansky, Ferroelectrics **32**, 321 (1992).
7. E. Kh. Birks, in *Phase Transition and Associated Phenomena in Ferroelectrics* (Riga, 1994), pp. 171–182.
8. B. A. Tuttle and D. A. Payne, Ferroelectrics **37**, 603 (1981).
9. P. D. Thacher, J. Appl. Phys. **39**, 1996 (1968).
10. R. Gerson and H. Jaffe, J. Phys. Chem. Solids **24**, 979 (1963).
11. S. E. Aksenov, E. V. Lovkova, E. D. Politova, and S. Yu. Stefanovich, in *Proceedings of the III International Conference "Crystals: Growth, Properties, Real Structure, Applications," Aleksandrov, 1995*, Vol. 2, p. 364.
12. D. Berlincourt, H. H. A. Krueger, and B. Jaffe, J. Phys. Chem. Solids **25**, 659 (1964).
13. N. N. Kraĭnik, Zh. Tekh. Fiz. **28**, 525 (1958) [Sov. Phys. Tech. Phys. **3**, 493 (1958)].
14. G. A. Smolenskiĭ, A. I. Agranovskaya, A. M. Kalinina, and T. M. Fedotova, Zh. Tekh. Fiz. **25**, 2134 (1955).
15. Yu. N. Venevtsev and G. S. Zhdanov, Izv. Akad. Nauk SSSR, Ser. Fiz. **21**, 411 (1957).
16. G. A. Smolenskiĭ, V. A. Bokov, V. A. Isupov, *et al.*, *Ferroelectrics and Antiferroelectrics* (Nauka, Leningrad, 1971).

Translated by V. Isaakyan

Technical Physics, Vol. 45, No. 11, 2000, pp. 1422–1427. Translated from Zhurnal Tekhnicheskoĭ Fiziki, Vol. 70, No. 11, 2000, pp. 48–53.

SOLIDS

Amorphization of Nanometer Precipitates in Metals

R. E. Voskoboĭnikov, V. A. Borodin, and A. E. Volkov

Kurchatov Institute Russian Research Centre, pl. Kurchatova 1, Moscow, 123182 Russia

Received April 20, 1999; in final form, October 12, 1999

Abstract—According to the theoretical concepts, the set of compositions of amorphizable metal alloys can be extended by increasing the cooling rate. This approach can be tested by quenching nanometer second-phase precipitates in a metal matrix. The precipitates are melted by the action of fast heavy ions or femtosecond laser pulses initiating thermal flares. The cooling rate of the precipitates as a function of their parameters, as well as the parameters of the matrix and thermal flares, was studied. With these parameters optimized, the cooling rate may greatly exceed those typical of conventional techniques for metal glass production. © *2000 MAIK "Nauka/Interperiodica".*

INTRODUCTION

The production and study of disordered metals (metal glasses) are of interest for both applications and fundamental research of metastable materials. Rapid quenching of the melt is widely used in the production of metal glasses. With the cooling rates currently available, the set of compositions of alloys to be amorphized is limited by those close to deep eutectics. However, according to present-day concepts [1], the set of compositions can be greatly extended if the cooling rate is enhanced. Moreover, under conditions of superfast cooling, even pure metals can vitrify, which has not been observed so far.

The time of cooling of molten material by heat removal to the environment depends largely on the sample size; therefore, one could expect superhigh cooling rates for small low-melting metal precipitates. These precipitates are melted by the action of thermal flares of a size comparable to that of the precipitates and are cooled by heat removal to a surrounding cold solid matrix of high heat conductivity.

Today, such experiments are a real possibility, since there exist metallic materials with nanometer second-phase precipitates [2] and various ways of producing a short rapid rise in temperature within regions on the order of 10 nm in size. Examples are irradiation by femtosecond laser pulses [3] or by fast heavy ions [4]. The advantage of these irradiations is the absence of elastic interaction with the ion subsystem of the target. The time of such thermal flares is sufficient for melting the precipitates (they melt within several periods of atomic oscillations). A local rise in temperature may reach several hundred to several thousand degrees (according to various estimates) [5–9]; hence, the flares can melt a variety of chemical compositions. Finally, one more advantage of this technique is that a frozen metastable structure (metal glass) is fairly stable to external effects and can readily be identified.

The melting points for most of materials are well known (corrections due to small precipitate sizes are insignificant and can be directly measured [2]). Therefore, amorphous precipitates can be used for experimentally estimating the thermal spike. In fact, analytic evaluations are currently the single source of information on local heating in thermal spikes [5–9]. In the above ways of producing thermal flares, the energy is first absorbed by the electron subsystem and only a small part of it is then spent on heating the ion subsystem of the matrix. Therefore, predictions are strongly dependent on applied models of electron–ion interaction and may differ by one order of magnitude.

In the nanometer size range, the rate of cooling by heat removal into the cold metal matrix may reach 10^{14}–10^{16} K/s, as follows from estimates. However, the achievement of such values in experiments requires optimization of the precipitate and matrix parameters. In this work, we investigated the solidification kinetics of a molten precipitate in a cold matrix. Also, the effect of the system parameters (matrix and precipitate materials, initial temperature profile, temperature of experiment, etc.) on the solidification time was studied.

STATEMENT OF THE PROBLEM

Consider the solidification of individual precipitates of radius R in a solid infinite matrix. The precipitates are melted by locally heating in the thermal spike. It is assumed that the melting point of the matrix is much higher than that of the precipitates T_m and exceeds the maximum (peak) temperature $T_{\max}$ of the flare. Next, the volume density of the precipitates is assumed to be relatively low in order that cooling of one precipitate can be considered independently of the others. To simplify the calculations, we will assume that the temperature T distribution within the precipitate and in the surrounding matrix is symmetric about the precipitate center, which is taken as the origin.

1063-7842/00/4511-1422$20.00

The solidification kinetics of a completely molten precipitate is represented as follows. The thermal spike heats up the precipitate to a temperatures above T_m. Due to heat removal into the matrix, the precipitate temperature drops with time. At the instant the precipitate surface cools down to the temperature of liquid–solid phase transition, the precipitate starts to solidify. Since we are interested in the solidification process itself, it is convenient to take the time instant when $T(R, 0) = T_m$ for the zero time $t = 0$. If the cooling rate is high, the disordered atomic structure of the melt supercools (below T_m) and is fixed in the amorphous state at some temperature known as the glass-transition temperature T_g [1]. Since the precipitate cools down from the surface, an interface between the supercooled liquid and metastable solid (amorphization front) arises when the surface temperature of the precipitate drops to T_g. Upon subsequent cooling, the interface shifts toward the center of the precipitate. At any time t instant, the position R_s of the amorphization front is defined by the relationship $T(R_s, t) = T_g$. At the time instant t_0 when the front reaches the center of the precipitate [$R_s(t_0) = 0$], the solidification of the precipitate in the amorphous state is complete.

From the above, the mean cooling rate $\dot{T}$ upon quenching to the amorphous state is given by

$$\dot{T} \simeq \frac{T_m - T_g}{t_0}. \qquad (1)$$

Relationship (1) is a conservative estimate of the quenching rate, since the real time of passing the temperature interval $T_m - T_g$ is less than t_0 at any point of the precipitate. Since the melting point and glass-transition temperature are intrinsic characteristics of the precipitate material, t_0 is the only parameter in (1) that can be varied by changing the matrix and precipitate parameters.

In analyzing the solidification kinetics, we subdivide the space into three regions (Fig. 1). The central part of the precipitate (region *I*) contains the melt with a temperature higher than T_g, whereas the outer part of the precipitate (region *II*) and the matrix (region *III*) are solid. Before the amorphization front emerges, region *II* is absent, and at $t = t_0$, region *I* disappears.

The cooling of a precipitate in an infinite matrix is described by the heat conduction equation

$$\frac{\partial T}{\partial t} = a^2 \Delta T, \qquad (2)$$

where the thermal diffusivity a^2 takes the values of a_I^2, a_{II}^2, and a_{III}^2 according to the region number.

In the calculations, we ignore the temperature dependences of a_I^2 and a_{II}^2, since the precipitation temperature changes little during amorphization; therefore,

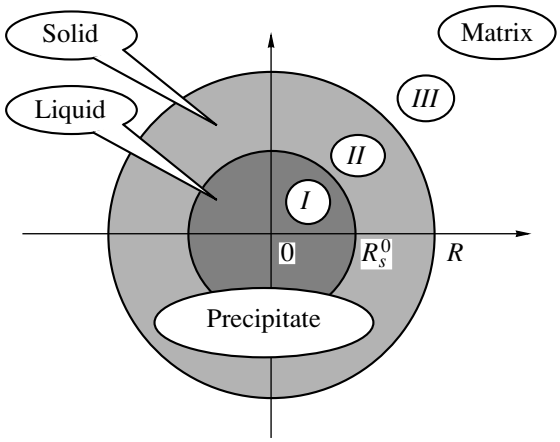

Fig. 1. Geometry of the problem.

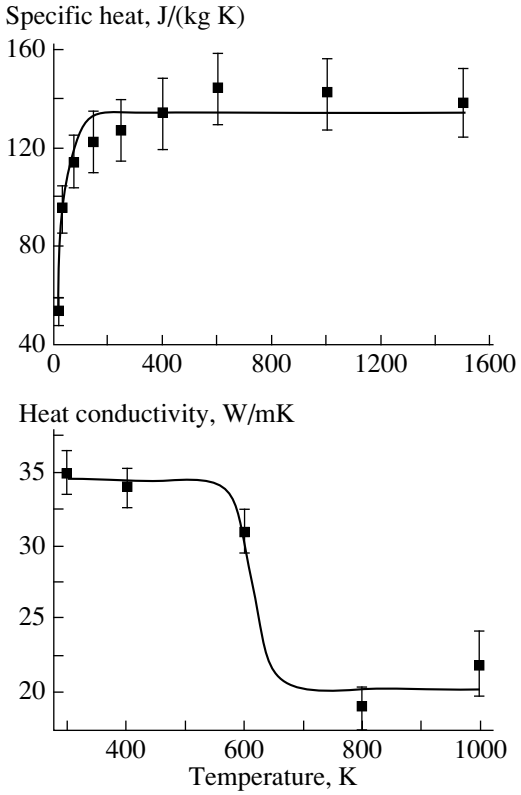

Fig. 2. Specific heat and heat conductivity vs. temperature. Data points for lead are taken from [11].

the temperature dependences of the specific heat and heat conductivity are insignificant (see Fig. 2).

Away from the precipitate, boundary conditions for Eq. (2) depend on the matrix temperature T_∞:

$$T(r \longrightarrow \infty, t) = T_\infty. \qquad (3)$$

At the center of the precipitate, we must put

$$\left.\frac{\partial T}{\partial r}\right|_{r=0} = 0. \qquad (4)$$

because of the spherical symmetry of the problem.

In our case, solidification means the liquid–glass phase transition; therefore, the latent heat of melting is not released [1]. We will also assume that the temperature and flux are continuous at the boundaries between regions *I* and *II* and regions *II* and *III*.

Finally, the spatial temperature distribution at the time instant $t = 0$ has the form

$$T(r, 0) = T_0(r), \tag{5}$$

where T_0 depends on the heating and cooling history of the precipitate and is a variable parameter in our case (with regard for the restriction $T_0(R) = T_m$).

ANALYSIS AND CALCULATION

To analytically find the solidification time t_0, we will proceed from the simplest approximation. In this case, the heat conductivity of the matrix is infinitely large and the initial temperature profile is a step: $T(r \le R, 0) = T_m$ and $T(r > R, 0) = T_\infty$. This corresponds to the case of a uniformly heated precipitate in a cold matrix.

To perform analytic calculations and computer simulations, we introduce the following dimensionless parameters: temperature $\Theta = T/T_m$, melting point $\Theta_m \equiv 1$, glass-transition temperature $\Theta_g = T_g/T_m$, matrix temperature $\Theta_\infty = T_\infty/T_m$, and distance to the precipitate center $\xi = r/R$. The diffusivities of the three regions are normalized by that of region *II*. The dimensionless time τ is given by $\tau = t/t_{II}$, where

$$t_{II} = \frac{R^2}{a_{II}^2} \tag{6}$$

is the characteristic cooling time.

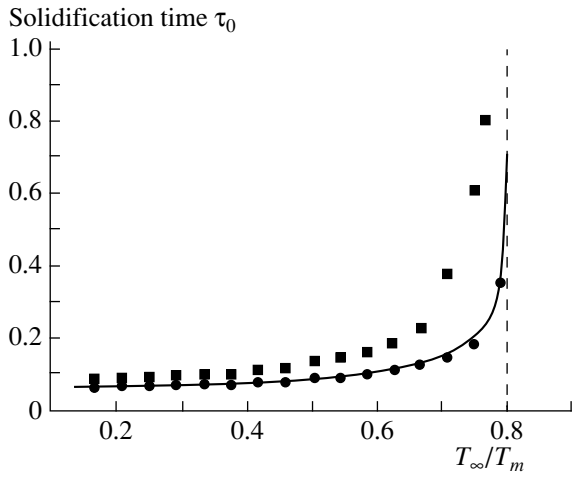

Fig. 3. Solidification time vs. matrix temperature. Computer simulation results for (■) limited and (●) infinitely large thermal diffusivity of the matrix. The curve is an analytic estimate according to (11).

Using the general method for analytically solving heat conduction problems of this class [10], we arrive at the space–time temperature distribution in the precipitate

$$\Theta_l = \Theta_\infty + (1 - \Theta_\infty)\frac{2}{\xi}\sum_{n=1}^{\infty}\frac{\sin\alpha_n\xi}{F'(\alpha_n)}\frac{\exp(-\alpha_n^2\tau)}{\alpha_n}, \tag{7}$$

where

$$F(\alpha) \equiv \sin\alpha\xi_s \sin\frac{a_I}{a_{II}}(1 - \xi_s) \times\left[\cot\alpha\xi_s + \cot\frac{a_I}{a_{II}}(1 - \xi_s) + \frac{1 - a_I/a_{II}}{\alpha\xi_s}\right] \tag{8}$$

and α_n is the nth root in ascending order of the roots of the equation

$$F(\alpha) = 0. \tag{9}$$

The implicit expression for solidification time τ_0 can readily be derived from (7) if one takes into account that the amorphization time reaches the center of the precipitate ($r = 0$) at τ_0:

$$\frac{\Theta_g - \Theta_\infty}{1 - \Theta_\infty} = \frac{2a_{II}}{a_I}\sum_{n=1}^{\infty}(-1)^n\exp(-(\pi n)^2\tau_0). \tag{10}$$

When the first term of the sum on the right of (10) is dominant, we have

$$\tau_0 = -\frac{1}{\pi^2}\ln\frac{a_I}{2a_{II}}\left(\frac{\Theta_g - \Theta_\infty}{1 - \Theta_\infty}\right). \tag{11}$$

To estimate the applicability range of (11), we contrast the dependence of the solidification time on the matrix temperature Θ_∞ with numerical solutions of Eq. (2). In the calculations, the parameters of the problem were [11] $a_I^2 = 1.41 \times 10^5$ (m/s)^2, $a_{II}^2 = 2.30 \times 10^5$ (m/s)^2, $a_{III}^2 = 9.38 \times 10^5$ (m/s)^2, $T_m = 600$ K, and $T_\infty = 150$ K. Hereafter, the same values will be used unless otherwise stated.

A comparison of the τ_0 vs. Θ_∞ dependences obtained by numerically solving Eq. (2) with expression (11) shows that the latter is a good approximation of τ_0 everywhere but in a narrow range of matrix temperatures near the glass-transition temperature Θ_g (Fig. 3).

As follows from Fig. 3, for low temperatures of a matrix with an infinitely large heat conductivity, the solidification rate of a nanometer precipitate reaches ~10^{14} K/s, which is close to the theoretical limit. In this case, the characteristic cooling time becomes comparable to several periods of atomic oscillations. Clearly, the simplifications made in deriving relationship (11) tend to decrease the solidification duration. Therefore, it is of interest to see how much t_0 would increase if the matrix and precipitate properties were more realistic. In

this case, analysis is rather difficult, and we simulated the solidification kinetics by numerically solving the heat conduction problem. Space–time variations of the temperature in the track are demonstrated in Fig. 4.

The calculations show that the solidification time is essentially dependent on the relative glass-transition temperature of the precipitate Θ_g and the temperature of the surrounding matrix. As is seen in Fig. 5, a decrease in Θ_g extends the solidification period, which is especially noticeable when Θ_g approaches the matrix temperature Θ_∞. Conversely, as long as Θ_∞ is much lower than Θ_g, τ_0 varies insignificantly.

The effect of the matrix and precipitate parameters also depends on the difference between Θ_g and Θ_∞. For example, for finite values of the matrix thermal diffusivity, the solidification time grows with decreasing a_{III}^2 (Fig. 3, ■). If, however, Θ_∞ are much less than Θ_g, relationship (11) is a fairly good approximation of τ_0, even if the thermal diffusivities of the matrix and precipitate are comparable to each other (Fig. 6). In contrast, at "high" (comparable to Θ_g) matrix temperatures, the solidification interval remains close to that predicted by (11) only if heat transfer in the matrix proceeds with a relatively high rate. The demarcation line between "low"- and "high"-temperature regions is defined by the ratio a_{III}^2/a_{II}^2. For example, for the case depicted in Fig. 3, relationship (11) reasonably approximates τ_0 if $T_\infty < 0.6T_g$. Similarly, the solidification time is weakly dependent on the thermal diffusivity a_I^2 of the molten precipitate at low matrix temperatures (Fig. 7).

One more factor that significantly influences the solidification time is the initial temperature traverse in the thermal flare. The step profile (Fig. 8), used in the analytic estimations, implies instantaneous heat dissipation in the matrix ($a_{III}^2 \gg a_{II}^2$) and rapid equalizing of the temperature in the melt. We also considered two other initial profiles (Fig. 8), namely, mixed and Gaussian. In the former case, the initial matrix temperature remains constant near the precipitate (T_∞) and follows the Gaussian curve inside the precipitate, with the maximum $T_{\max}$ at its center. The temperature is normalized so that the condition $T(R, 0) = T_m$ is met on the precipitate surface. In the latter case, the Gaussian profile (with the parameters as in the previous case) also covers the matrix (this makes it possible to estimate the effect of limited thermal diffusivity).

Numerical results on the solidification time as a function of the maximum temperature at the precipitate center $\Theta_{\max} = T_{\max}/T_m$ for these profiles are given in Fig. 9. The solidification time depends on the profile shape. For the mixed profile, τ_0 grows with $\Theta_{\max}$ monotonically; this seems to be quite natural, since the amount of heat accumulated in the precipitate also

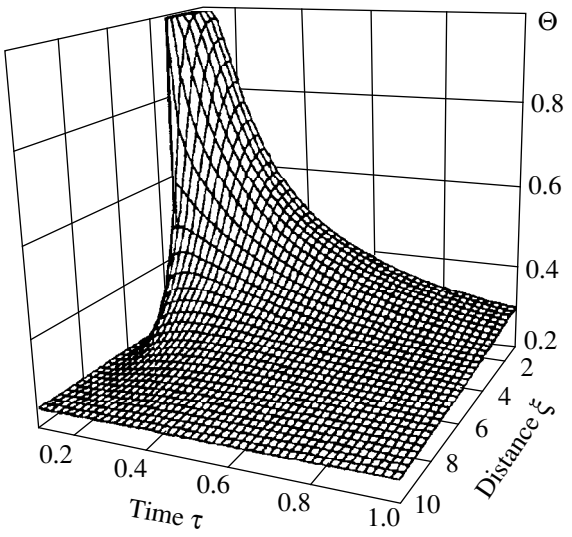

Fig. 4. Temperature vs. time and distance to the precipitate center.

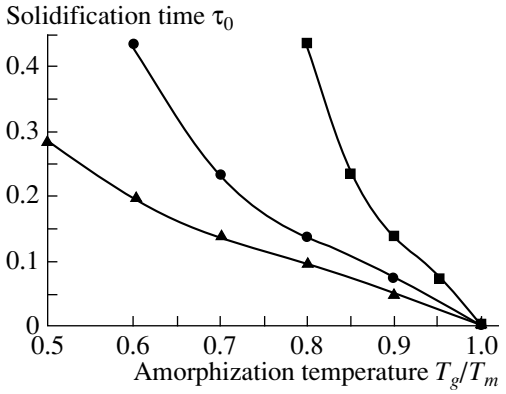

Fig. 5. Solidification time vs. relative glass-transition temperature. T_∞/T_m = (■) 0.25, (●) 0.5, and (▲) 0.75.

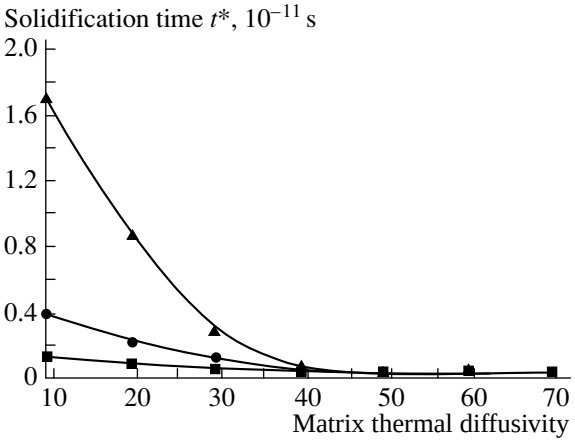

Fig. 6. Solidification time vs. thermal diffusivity of the matrix. (■) 275, (●) 375, and (▲) 475 K.

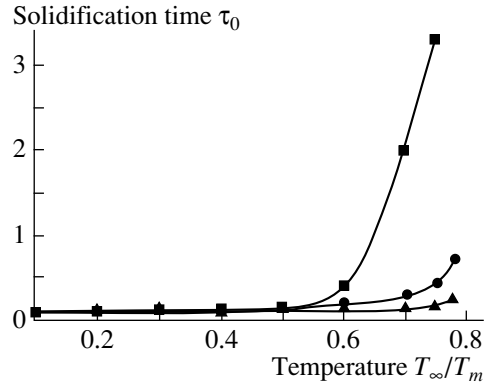

Fig. 7. Solidification time vs. thermal diffusivity of the molten material. a_I/a_{II} = (▲) 5, (●) 1, and (■) 0.1.

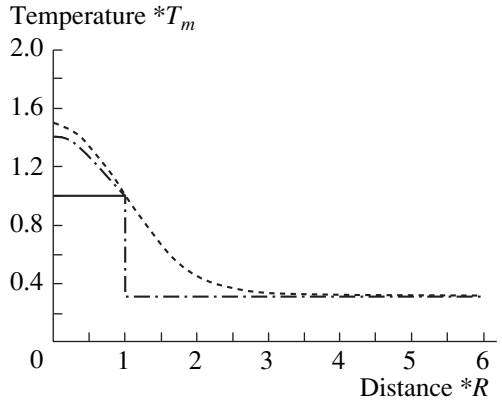

Fig. 8. Initial temperature profile inside and around the precipitate.

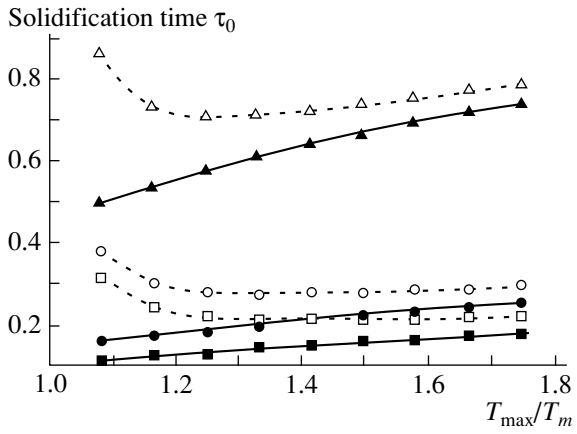

Fig. 9. Solidification time vs. relative maximum temperature of the precipitate for T_∞/T_m = (□, ■) 0.25, (○, ●) 0.5, and (△, ▲) 0.75. Dotted line, Gaussian profile; continuous line, mixed profile.

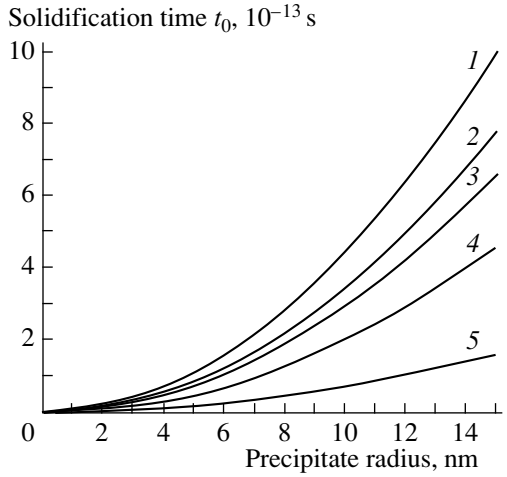

Fig. 10. Solidification time of the precipitates in the aluminum matrix as a function of precipitate radius. (*1*) Pb, (*2*) In, (*3*) Tl, (*4*) Co, and (*5*) Bi.

grows monotonically with Θ_{max}. For the Gaussian profile, the situation is more intricate. At small overheatings, $\Theta_{max} - 1 \ll 1$, the temperature "tail" in the matrix markedly slows down heat transfer from the precipitate and increases τ_0. However, even at $\Theta_{max} \geq 1.5$, the effect of the initial matrix temperature nonuniformity on τ_0 weakens and the solidification time curves tend to those for the mixed profile (Fig. 9).

Thus, it follows from the aforesaid that the dimensionless solidification time can be maintained at a level of 10^{13}–10^{15} K/s by properly choosing the matrix and/or precipitate parameters and process conditions (the use of low matrix temperatures, $\Theta_\infty \ll \Theta_g$, and matrixes with high thermal diffusivity). Since τ_0 and t_0 are related as

$$t_0 = \frac{R^2}{a_{II}^2}\tau_0,$$

one can effectively control the solidification process by varying the radius R and thermal diffusivity of the precipitates (note that τ_0 depends neither on R nor on a_{II}).

Figure 10 demonstrates numerical results on the solidification time for precipitates of different composition (Pb, Bi, In, Tl, and Cd) and size ($0 < R < 15$ nm) in the aluminum matrix. The metals listed are hardly soluble in aluminum, so that their nanometer precipitates can be obtained [2]. The shortest solidification time, $t_0 \approx 0.7 \times 10^{-12}$ s, is observed for lead precipitates; according to (1), this corresponds to the cooling rate $\dot{T} \sim 1.7 \times 10^{14}$ K/s. Such high cooling rates (several orders of magnitude higher than those attainable upon cooling massive amorphous metals) make possible the use of thermal spikes (occurring, for example, when the material is irradiated by fast heavy ions or femtosecond laser pulses) for superfast quenching of precipitates in metals and checking theoretical predictions on pure metal amorphization [12].

One should bear in mind that cooling rate is not the only factor that governs crystallization during solidification. For example, heterogeneous crystallization and/or epitaxial growth that starts from the surface may substantially facilitate bulk crystallization. These undesirable processes must be avoided in experiments on pure metal vitrification through superfast quenching. They can effectively be suppressed by appropriately selecting the matrix and precipitate materials (for example, with various types and parameters of the crystal lattice) [12]. Materials used in [2] are well suited for such experiments.

CONCLUSIONS

We investigated the effect of the precipitate, matrix, and flare parameters on the precipitate solidification time. With the system parameters optimized, a cooling rate close to the theoretical limit (five or six orders of magnitude higher than those typical of conventional techniques for metal glass production) can be attained. Our results indicate that the use of metal matrixes with nanometer precipitates is promising for experimentally checking the possibility of producing pure amorphous metals by quenching from the melt.

ACKNOWLEDGMENTS

This work was partially supported by the Russian Foundation for Basic Research (grant no. 98-02-16216) and grants from the Russian Research Center Kurchatov Institute for young scientists.

REFERENCES

1. F. E. Luborsky, in *Amorphous Metallic Alloys* (Butterworth, London, 1993), p. 640.
2. H. H. Andersen and E. Johnson, Nucl. Instrum. Methods Phys. Res. B **106**, 480 (1995).
3. P. Saeta, J.-K. Wang, Y. Siegal, *et al.*, Phys. Rev. Lett. **67**, 1023 (1991).
4. M. D. Hou, S. Klaumünzer, and G. Schumacher, Phys. Rev. B **41**, 1144 (1990).
5. A. E. Volkov and V. A. Borodin, Nucl. Instrum. Methods Phys. Res. B **146**, 137 (1998).
6. M. Toulemonde, C. Dufour, and R. Paumier, Phys. Rev. B **46**, 14362 (1992).
7. V. L. Ginzburg and V. P. Shabanskiĭ, Dokl. Akad. Nauk SSSR **100**, 445 (1955).
8. M. I. Kaganov, I. M. Livshits, and L. V. Tantarov, Zh. Éksp. Teor. Fiz. **31**, 232 (1956) [Sov. Phys. JETP **4**, 173 (1956)].
9. G. E. Geguzin, M. I. Kaganov, and I. M. Livshits, Fiz. Tverd. Tela (Leningrad) **15**, 2425 (1973) [Sov. Phys. Solid State **15**, 1612 (1973)].
10. H. S. Carslaw, in *Introduction to the Mathematical Theory of the Conduction of Heat in Solids* (Dover, New York, 1945), p. 268.
11. *Physical Quatities: A Handbook*, Ed. by I. S. Grigor'ev and E. Z. Melikhov (Énergoatomizdat, Moscow, 1991).
12. D. M. Herlach, Mater. Sci. Eng., R **12**, 177 (1994).

Translated by V. Isaakyan

Technical Physics, Vol. 45, No. 11, 2000, pp. 1428–1431. Translated from Zhurnal Tekhnicheskoĭ Fiziki, Vol. 70, No. 11, 2000, pp. 54–57.

SOLIDS

Crystallization-Water-Stimulated Dynamic Conductivity

B. M. Gorelov, K. P. Konin, and D. V. Morozovskaya

Institute of Surface Chemistry, National Academy of Sciences of Ukraine, Kiev, 252022 Ukraine

Received July 20, 1999

Abstract—In water-molecule-doped barium peroxide and barium oxide, a step increase in the dynamic conductivity to ~10^{-3} Ω^{-1} cm^{-1} was found. The increase is observed when water molecules are present in two nonequivalent states in the lattice, with concentrations of the molecules n_t of $\geq 2.2 \times 10^{21}$ cm^{-3}. At $n > n_t$, the conductivity does not depend on the number of molecules in the lattice but is temperature-dependent, obeying the law $\sigma(T) = C_1\exp(-E_1/kT) + C_2\exp(-E_2/kT)$. The run of the $\sigma(n, T)$ curve is explained by trapping electrons that result from H_2O dissociation and by two sorts of carrier jumps between localized and delocalized states. © *2000 MAIK "Nauka/Interperiodica".*

INTRODUCTION

Water molecules absorb electromagnetic radiation in a wide frequency range. It is therefore natural to assume that H_2O molecules introduced into the crystal lattice of polar insulators, such as barium peroxide or barium oxide, will encourage the absorption of microwave radiation. Several mechanisms that enhance absorption are known. In one of them, conduction is due to energy absorption by H_2O dipoles localized in the lattice [1],

$$\sigma(\omega) = \frac{n\mathbf{D}^2}{3kT}\frac{1}{1+\exp(W/kT)}\frac{\omega^2\tau}{1+\omega^2\tau^2}, \qquad (1)$$

(where n is the dipole concentration, **D** is the dipole moment, T is temperature, ω is the frequency, τ is the relaxation time, and W is the energy difference for the dipole transition) and grows with dipole concentration. Two other mechanisms are possible if water molecules dissociate in the crystal field of the insulator as

$$H_2O \Leftrightarrow H^+ + OH^- \quad \text{and} \quad 2H_2O \Leftrightarrow H_3O^+ + OH^- \quad (2), (3)$$

to form hydrogen, hydroxyl, and hydroxonium ions. These ions may act as charge carriers and possess, like OH^-, a dipole moment. In this case, microwave absorption can be related to ion transitions both in the lattice and in the ion dipoles. In addition, the formation of donor and acceptor centers in the crystal lattice may lead to the appearance of charge carriers in the electron spectrum if, for example, Ba^{2+} cations capture one or two electrons or O_2^{2-} or O^{2-} anions capture holes. H_2O molecules and products of their dissociation are localized randomly and seem to polarize the lattice. This may cause carrier localization, on the one hand, and polaron formation, on the other. Also, if free or localized carriers appear as a result of H_2O dissociation, insulators may pass to the metal state as the number of water molecules in the lattice grows.

In this work, we studied the water-stimulated dynamic conductivity of barium peroxide and barium oxide. The compounds were doped by water vapor adsorption. In the lattice, H_2O molecules occupy interstices, forming two bound states that may variously add to the conductivity. Therefore, water adsorption and the evolution of the bound states are considered first. Then, temperature and concentration dependences of the conductivity and the effect of the bound states are discussed. Measurements were made by the thermogravimetric (TG) method, differential thermal analysis (DTA), and the method of dynamic conductivity.

SAMPLES AND EXPERIMENT

Samples used were extra-pure-grade powders of barium peroxide and barium oxide with the mean grain size ~10 μm and specific surface area ~10 m^2/g. Prior to water adsorption, BaO_2 and BaO were dehydrated and annealed at a pressure of ~10^{-3} torr at 150–180°C for ~2 h. Adsorption was carried out at 21°C and a saturation pressure of 18.7 torr. The water concentration in the samples depended on adsorption time.

The amount of adsorbed water was measured with a McBain balance, and the concentration of bound H_2O molecules was determined with a Q-1500 derivatograph from water thermal desorption data. The bound states of crystallization water were annealed off by heating the samples to 120 and 145°C at a rate of 5°C/min.

The dynamic conductivity was measured using the method of a short-circuited line at 10 GHz using a Ya2R-67 VSWR indicator [2]. The bulk density of the samples was 1.3–2.1 g/cm^3.

RESULTS AND DISCUSSION

Temperature dependences of the weight loss Δm and DTA signals from the BaO_2 samples exposed to water

vapor are shown in Fig. 1. On the BaO samples, adsorption proceeds in a similar way. Upon heating, dehydrated samples do not change their mass (Fig. 1a). For short adsorption times ($t \le 15$ min), a layer of physically bonded water molecules appears on the grain surface. A decrease in the weight and endothermic DTA signals between 60 and 105°C indicate the evaporation of the polylayer from the grain surface, the heat of desorption of the layer being Q_d = 15–18 kJ/mol (Fig. 1b). The thickness of the polylayer h can be estimated from the relationship

$$h = m(\mu_p s)^{-1}\omega_{H_2O}N_A^{2/3}M^{-2/3}\rho^{-1/3}, \qquad (4)$$

where m, μ_p, and M are the weight of adsorbed water, sample weight, and gram-molecular weight of water, respectively; s is the specific sample surface; ρ is the water density; ω_{H_2O} is the surface area occupied by an H_2O molecule; and N_A is Avogadro's number. If ω_{H_2O} = 10.2 Å [3] and ρ = 1 g/cm^3, $h \simeq 20$ Å.

With increasing adsorption time, H_2O molecules diffuse from the polylayer into the crystal lattice, occupy nonequivalent interstices, and form two bound states. They are observed under desorption in the TG and DTA curves in the intervals T_{d1} = 80–120°C (Q_{d1} = 25 and 21 kJ/mol for BaO_2 and BaO, respectively) and T_{d2} = 125–140°C (Q_{d2} = 18 and 31 kJ/mol for BaO_2 and BaO, respectively) (Fig. 1c). The states are independent of each other, since upon heating to 120°C, the first state is annealed off, with Q_{d2} remaining unchanged (Fig. 1d). At 145°C, the samples are dehydrated. The number of water molecules in each of the states grows with adsorption time (Fig. 2). The molecules are weakly bonded to the atomic environment, since the heats of desorption for physically bonded and crystallization waters diverge insignificantly.

It should be noted that, when H_2O molecules are incorporated into the lattice, the DTA curves exhibit two signals (at ~240 and 360–395°C) that are not accompanied by a weight change (Fig. 1d) and are likely to be associated with structure transformations. Thus, water adsorption on the surface of BaO_2 and BaO grains forms a polylayer of physically bonded water and two nonequivalent states of H_2O molecules in the lattice.

The conductivity of BaO_2 and BaO varies nonmonotonically with adsorbed water amount (Fig. 3). When the amount of the adsorbate reaches the threshold value $m_t \approx 0.8$ and 4 mmol/g for BaO_2 and BaO, respectively, σ increases stepwise, the value of the jump growing with temperature by a factor of ~5×10^2 (BaO_2) and ~33 (BaO) at $T \simeq 70$°C. With a further rise in the amount of adsorbed water ($m > m_t$), σ remains practically unaffected, although the number of molecules in the first, n_1, and second, n_2, states grows (Fig. 2). The threshold amount of the H_2O molecules in the first

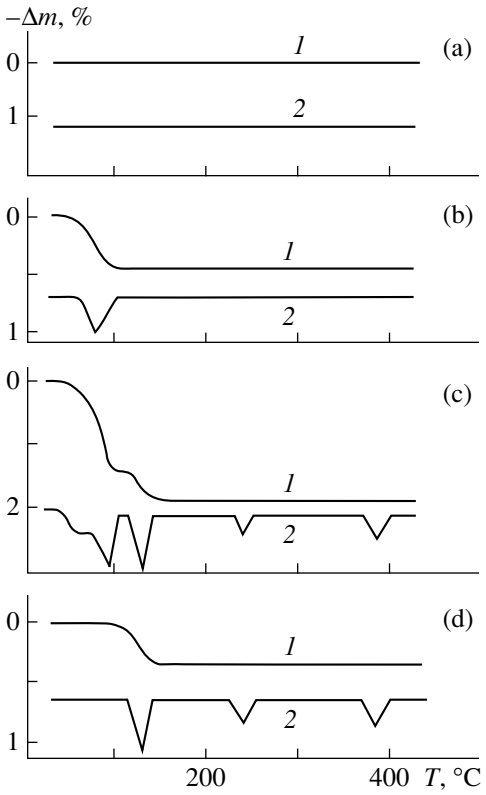

Fig. 1. (*1*) Weight loss vs. temperature and (*2*) DTA curves for the BaO_2 samples (a) before and after water desorption for (b) 10, (c) 60, and (d) 60 min with subsequent heating to 120°C.

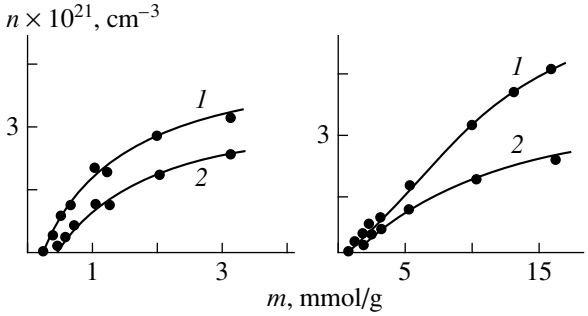

Fig. 2. Number of H_2O molecules in the crystal lattice of (a) BaO_2 and (b) BaO in the two states (*1*, *2*) vs. adsorbed water amount.

bound state, which corresponds to the jump in the $\sigma(m, T)$ curve, was found to be $n_{1t} \simeq 1.4 \times 10^{21}$ cm^{-3}; in the second state, the threshold amount was $n_{2t} \simeq 7.5$–9.0×10^{20} cm^{-3}. This corresponds to the mean distance between the water molecules $t = (n_{1t} + n_{2t})^{-1/3} = 8$ Å, which slightly exceeds the lattice constants (4–5 Å) of BaO_2 and BaO [4].

Figure 4 shows temperature dependences of BaO_2 and BaO conductivities in the dehydrated and doped

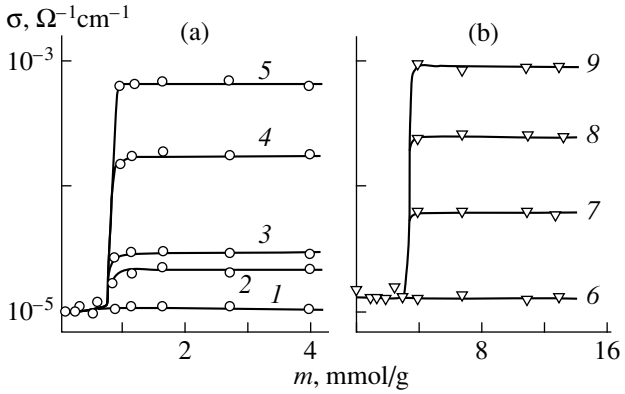

Fig. 3. Concentration dependences of the conductivity of (a) BaO_2 at T = (*1*) 285, (*2*) 292, (*3*) 301, (*4*) 335, and (*5*) 347 K and (b) BaO at T = (*6*) 291, (*7*) 305, (*8*) 319, and (*9*) 328 K.

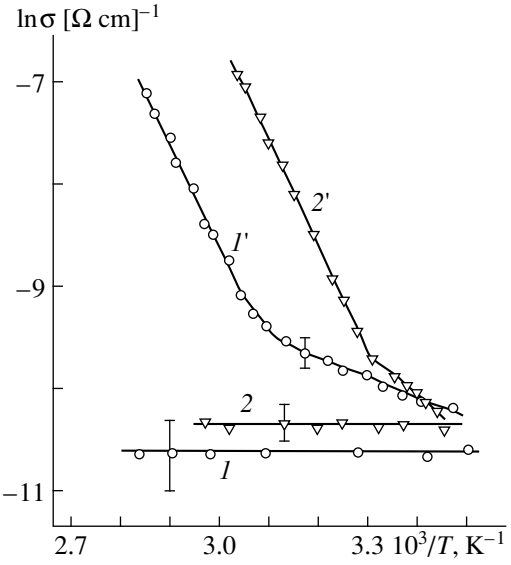

Fig. 4. Temperature dependences of the conductivity of (*1*, *1*') BaO_2 and (*2*, *2*') BaO before and after doping by H_2O molecules.

($m > m_t$) states. In the latter state at $T < T_{d1}$, the conductivity of both compounds obeys the temperature law

$$\sigma(\omega, T) = C_1 \exp(-E_1/kT) + C_2 \exp(-E_2/kT). \quad (5)$$

For BaO_2, E_1 = 1.13 eV, $C_1 = 5.5 \times 10^6\ \Omega^{-1}\ cm^{-1}$ at $T > 325$ K and E_2 = 0.18 eV, $C_2 \simeq 5.5 \times 10^{-2}\ \Omega^{-1}\ cm^{-1}$ at $T < 325$ K; for BaO, E_1 = 1.01 eV, $C_1 \simeq 2.4 \times 10^7\ \Omega^{-1}\ cm^{-1}$ at $T > 303$ K and E_2 = 0.22–0.25 eV, $C_2 \simeq 1.4\ \Omega^{-1}\ cm^{-1}$ at $T < 303$ K. The compounds pass into the conductive state in the temperature range where the first bound state of water molecules exists. If, for example, $T < T_{d1}$, the behavior of $\sigma(T)$ changes reversibly with temperature. If, however, $T_{d1} \le T < T_{d2}$, σ suddenly drops to the value typical of dehydrated samples as the n_1 molecules are annealed off and is independent of the number n_2 of the molecules in the BaO_2 and BaO lattices. In addition to this, at $T < T_{d1}$, σ starts to grow when $T \ge 285$ K for BaO_2 and $T \ge 293$ K for BaO. At lower temperatures, the values of σ in the doped and undoped states are the same.

It should be emphasized that the dynamic conductivities of the dehydrated samples and doped samples that contain water molecules in the second bound state with the concentration $n_2 \ge n_{2t}$ after annealing and do not contain H_2O in the first bound state ($n_1 = 0$) are the same and nearly temperature-independent.

Thus, doping of BaO_2 and BaO by water molecules with a concentration of no less than $\sim 2.2 \times 10^{21}\ cm^{-3}$ causes a step increase in the conductivity. The conductivity is governed by two nonequivalent states of the molecules in the lattice, does not depend on the number of the molecules, and has two components that exponentially depend on temperature.

It is worth noting that the nonmonotonic behavior of $\sigma(m)$ can be related to proton conductivity in the polylayer of physically bonded water. This conductivity is characterized by the threshold dependence on the thickness h, since it becomes noticeable once a continuous water layer has been formed on the grain surface. It is due to proton tunneling through the network of hydrogen bonds [5–7]. The conductivity of proton gas in the polylayer [5] $\sigma_p = \sigma_s/h = (l\mathbf{v}F^2)/3RT$ (where l is the free path, $\mathbf{v}$ is the velocity, F is the Faraday constant, and R is the gas constant) equals $\sim 3 \times 10^{-4}\ (\Omega\ cm)^{-1}$ (provided that the network of hydrogen bonds entirely covers the film and the surface conductivity $\sigma_s \simeq 6 \times 10^{-11}\ \Omega^{-1}$ [7]). This value exceeds σ at $T \le 337$ K in BaO_2 and at $T \le 316$ K in BaO. However, proton conductivity, in our case, is unlikely. When, with increasing m, islands on the grain surface tend to coalesce to produce the continuous polylayer (T = 285 K for BaO_2 and 293 K for BaO), no step of σ_p is observed (Fig. 3; curves *1*, *6*). Consequently, the behavior of $\sigma(m)$ is due to crystallization water.

A step increase in $\sigma(n, T)$ with a growing number of dipoles in the lattice, the independence of σ from n at $n > (n_{1t} + n_{2t})$, and the equality of the conductivities of as-prepared and doped samples [i.e., $\sigma(n, T) = \sigma(0, T)$ at $T \le 285$ K for BaO_2 and $T \le 293$ K for BaO when $n > (n_{1t} + n_{2t})$ and also at $T < T_{d2}$ if $n_1 = 0$ and $n_2 \ge n_t$] exclude microwave losses due to dipole transitions and orientation dipole relaxation. In these cases, an electron may pass over a barrier U when the conductivity has the form [1]

$$\sigma(\omega) \simeq 0.3nN(W)B(U)\mathbf{D}^2kT\omega, \quad (6)$$

where $N(W)$ and $B(U)$ are the energy distributions of the number of dipoles and barriers when $\sigma \sim n$.

Hence, conduction cannot be related to energy losses in H_2O dipoles or OH^- and H_3O^+ ionic dipoles.

Note again that σ lies in the range 10^{-5}–10^{-3} Ω^{-1} cm^{-1} (which is much less than the associated values for metals), obeys the temperature law $\sigma \sim C\exp(-E/kT)$ ($d\sigma/dT > 0$), and at $n > (n_{1t} + n_{2t})$, does not depend on the concentration of H_2O molecules or products of their dissociation (hence, on the charge carrier density). This means the absence of free carriers in the electron spectrum and excludes microwave losses due to OH^-, H^+, or H_3O^+ ion transfer in the lattice.

The run of the $\sigma(m)$ and $\sigma(T)$ curves indicates that conduction is due to absorption of the microwave energy by carriers, which then leave the localized states. The carriers are generated by H_2O dissociation. Since conduction occurs in the presence of the two nonequivalent states of the molecules, two molecules from the different states are involved in the dissociation reaction to form H_3O^+ and OH^- ions. Reaction (3) proceeds at $T \geq 285$–293 K. A possible reason for this is an increase in the dissociation rate. Another reason that seems likely is that the formation of hydroxonium ions is facilitated under conditions of enhanced thermal motion of molecules as T rises (because they are loosely bonded to the atomic environment in the lattice). In this case, electrons trapped by Ba^{2+} ions from OH^- centers and localized near the conduction band bottom can serve as charge carriers. These local levels are produced by the 6*s* orbitals of the Ba atoms. Since Ba^{2+} ions can capture one or two electrons, three types of localized states can exist in the energy spectrum: two-electron and one-electron states, which are separated by the Coulomb gap, at the conduction band tails and free states. The carriers may be localized because of polarization-induced lattice distortions. The polarization may be a result of electron capture or be induced by the random potential of the H_2O molecules and ions produced by dissociation.

Within the model of electrons localized in potential wells, conduction is due to transitions between the localized and delocalized states. The independence of $\sigma(\omega, T)$ of carrier concentration suggests that the behavior of $\sigma(T)$ in the doped state is governed by the temperature dependence of mobility, which rises stepwise in going from the component $C_2\exp(-E_2/kT)$ to $C_1\exp(-E_1/kT)$. Since dependences like $\sigma(\omega, T) \sim C(\omega)\exp(-E/kT)$ are typical of carrier transitions between localized, bound, and delocalized states [8], the components of $\sigma(T)$ can be assigned to a change in transition type with growing T. The transitions with the energy E_2 take place between the localized one-electron states at the Fermi level in the energy gap and free states at the tails of the conduction band or at its bottom. Those with the energy E_1 are associated with electrons that leave the one-electron states for delocalized states in the conduction band. In this case, the mobility of the delocalized electrons sharply increases; hence, a step in the $\sigma(m, T)$ curve (Fig. 3). In this model, the carriers localized on the two-electron states, which are below the Fermi level, do not add to the conductivity. Therefore, when the electrons occupy these states, σ does not depend on n if $n > (n_{t1} + n_{t2})$.

REFERENCES

1. N. F. Mott and E. A. Davis, *Electronic Processes in Non-Crystalline Materials* (Clarendon, Oxford, 1971; Mir, Moscow, 1974).
2. F. J. Tischer, *Mikrowellen-Messtechnik* (Springer, Berlin, 1958; Fizmatgiz, Moscow, 1963).
3. R. N. Meals and F. M. Lemis, *Silicones* (Reinhold, New York, 1963).
4. I. I. Vol'nov, *Peroxidates of Alkaline Earth Metals* (Nauka, Moscow, 1978).
5. V. Ya. Antonchenko, A. S. Davydov, and V. V. Il'in, *Foundations of Water Physics* (Naukova Dumka, Kiev, 1991).
6. V. F. Kiselev, *Surface Effects in Semiconductors and Dielectrics* (Nauka, Moscow, 1970).
7. V. N. Pak and N. G. Ventov, Zh. Tekh. Fiz. **87** (2), 491 (1986).
8. A. Madan and M. Shaw, *The Physics and Applications of Amorphous Semiconductors* (Academic, Boston, 1988; Mir, Moscow, 1991).

Translated by V. Isaakyan

Technical Physics, Vol. 45, No. 11, 2000, pp. 1432–1436. Translated from Zhurnal Tekhnicheskoĭ Fiziki, Vol. 70, No. 11, 2000, pp. 58–62.

SOLIDS

Phase Transitions and Electrical Properties of Solid Solutions of Sodium, Lithium, and Strontium Niobates

L. A. Reznichenko, O. N. Razumovskaya, L. A. Shilkina, A. Ya. Dantsiger, S. I. Dudkina, I. V. Pozdnyakova, and V. A. Servuli

Research Institute of Physics, Rostov State University, pr. Stachki 194, Rostov-on-Don, 344090 Russia

E-mail: larisa@riphys.rnd.su

Received October 19, 1999; in final form, May 5, 2000

Abstract—An additional study of solid solutions in the (Na, Li, $Sr_{0.5}$)NbO_3 ternary system was performed. More detailed information concerning its phase diagram and physical parameters in a wide range of component concentrations is obtained. The compositions obtained are of interest for application in highly sensitive and high-frequency transducers. © *2000 MAIK "Nauka/Interperiodica".*

INTRODUCTION

The phase diagram and main electrical properties of the (Na, Li, $Sr_{0.5}$)NbO_3 system are briefly outlined in [1]. In this study, which continues the phase diagram investigation, new phases and morphotropic regions (MRs) were found. Furthermore, concentration dependences of the electrical parameters of the solid solutions (SS) in the system are studied in detail, and their relation with the structure parameters, specifically, homogeneous strain parameter δ, is revealed [2].

We considered six quasi-binary cross sections where the content of the *z* component of the $Sr_{0.5}NbO_3$ system ranged from 2 to 50 mol %. In each of the cross sections, compositions with 2–15 mol % of $LiNbO_3$ *y* sections were synthesized. Synthesis and sintering conditions are presented in [1].

RESULTS AND DISCUSSION

The studied region of the $NaNbO_3$–$LiNbO_3$–$Sr_{0.5}NbO_3$ phase diagram was adjacent to the $NaNbO_3$ vertex of the Gibbs triangle (Fig. 1). Thin lines depict *y* and *z* sections, and heavy lines represent boundaries between single- and two-phase regions with different symmetry.

The phase diagram of the ternary system was determined by the binary phase diagrams. We found that solid solutions in $(100 - z)NaNbO_3$–$zSr_{0.5}NbO_3$ have rhombic symmetry (similar to $NaNbO_3$) with the unit cell parameter quadrupled along the *b* axis (M_4 phase) in a narrow range of concentrations ($z \le 2$). At $2 < z < 30$, the cell multiplicity decreases: it becomes doubled along *b*-axis (M_2 phase). The range $30 \le z \le 50$ corresponds to SS having cubic symmetry with doubled parameter (K_2 phase). These results differ from earlier data of other authors. Specifically, according to [3], in the ranges $0 < z \le 30$ and $30 \le z \le 50$, SS have monoclinic and tetragonal symmetries, respectively. Phase transitions in the $(100 - y)NaNbO_3$–$yLiNbO_3$ system were investigated in [4] and refined in [5].

Note that the phase diagram under study is less complicated than, for example, that described in [6] for the (Na, Li, $Pb_{0.5}$)NbO_3 system.

In the (Na, Li, $Sr_{0.5}$)NbO_3 system, one can separate the wide MR_1 ($M_2 + Rh$) (*Rh* means rhombic phase) and

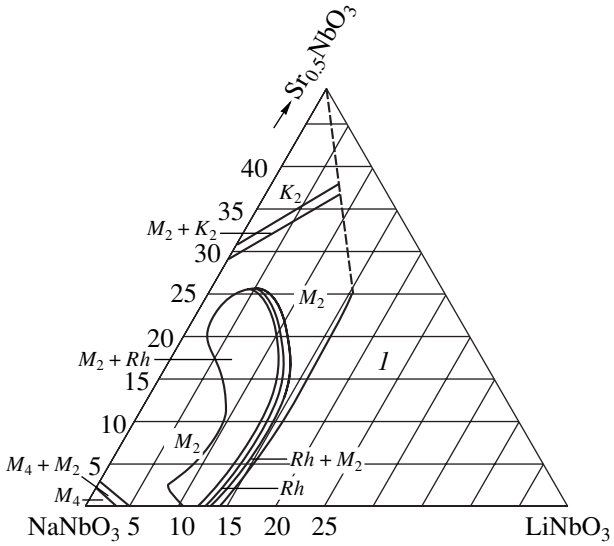

Fig. 1. Phase diagram of the (Na, Li, $Sr_{0.5}$)NbO_3 ternary system (*1*, heterogeneous region).

1063-7842/00/4511-1432$20.00 © 2000 MAIK "Nauka/Interperiodica"

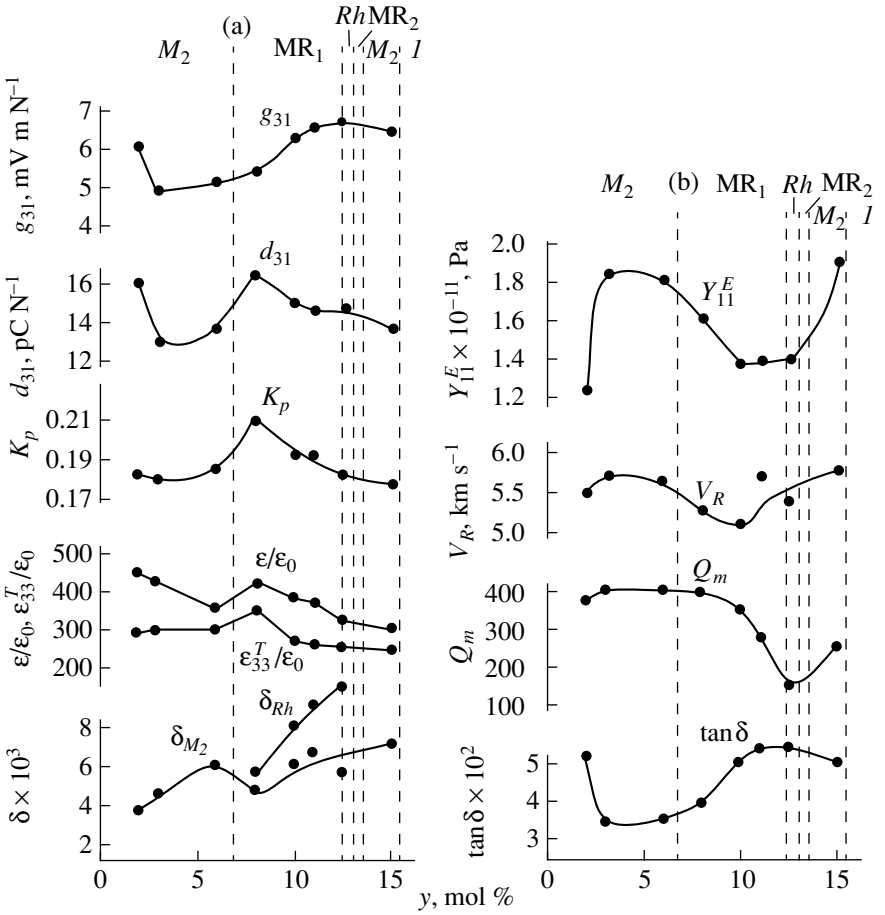

Fig. 2. Structure and electrical parameters of the (Na, Li, $Sr_{0.5}$)NbO_3 solid solutions vs. $LiNbO_3$ content for the section z = 15 mol % of $Sr_{0.5}NbO_3$ (*1*, the same as in Fig. 1).

narrow MR_2 (Rh + M_2) regions, in which neighborhood the extremal structure and electrical parameters can be expected. Other narrow, MR_3 (M_4 + M_2) and MR_4 (K_2 + M_2) regions, are beyond the SS being studied; therefore, their influence is not taken into account.

Let us consider the z and y sections that are most typical of our system. Figure 2 depicts concentration dependences of the structure and electrical parameters for z = 15. δ, $\varepsilon_{33}^T/\varepsilon_0$, $\varepsilon/\varepsilon_0$, K_p, d_{31}, and g_{31} are shown in Fig. 2a; $\tan\delta$, Q_M, V_R, and Y_{11}^E, in Fig. 2b.[1] Dashed lines mark the wide MR_1 and narrow MR_2. The permittivities and parameter g_{31} pass through a maximum near the opposite boundaries of the MR_1, which is typical of ferroelectrics. The peaks of K_p, d_{31}, and $\varepsilon_{33}^T/\varepsilon_0$ coincide. To these peaks, there correspond the minimal δ's within the MR_1. As to the other parameters (Fig. 2b), the run of some of them correlates with changes in the SS ferroelectric elastance. In particular, V_R and Y_{11}^E vary in opposition to $\varepsilon_{33}^T/\varepsilon_0$. However, the behavior of $\tan\delta$ and Q_M cannot be explained through elastance variation. Unlike the other parameters, they exhibit a kink at the MR_1–Rh interface.

In contrast to the considered case, in other z sections, the characteristics are much more irregular, since some of the parameters also have extrema at a distance well away from the above MRs. This irregularity can hardly be attributed to MR location only. The dependences of the parameters for z = 10 are plotted in Fig. 3. It is seen that $\varepsilon_{33}^T/\varepsilon_0$, K_p, d_{31}, and g_{31} have two maxima: the first maximum is in the vicinity of the MR_1 boundary, and the second is far beyond it, at 3–6 mol % of $LiNbO_3$. At approximately the same $LiNbO_3$ concentrations, Raman spectra from the corresponding SS revealed effects associated with the presence of subsystems with different composition ordering of unlike

[1] $\varepsilon_{33}^T/\varepsilon_0$ and $\varepsilon/\varepsilon_0$ are the relative permittivities, K_p is the electromechanical coupling coefficient, d_{31} and g_{31} are the piezoelectric parameters, $\tan\delta$ is the dielectric loss tangent, Q-factor, Q_M is the mechanical Q-factor, V_R is the sound velocity, and Y_{11}^E is Young's modulus.

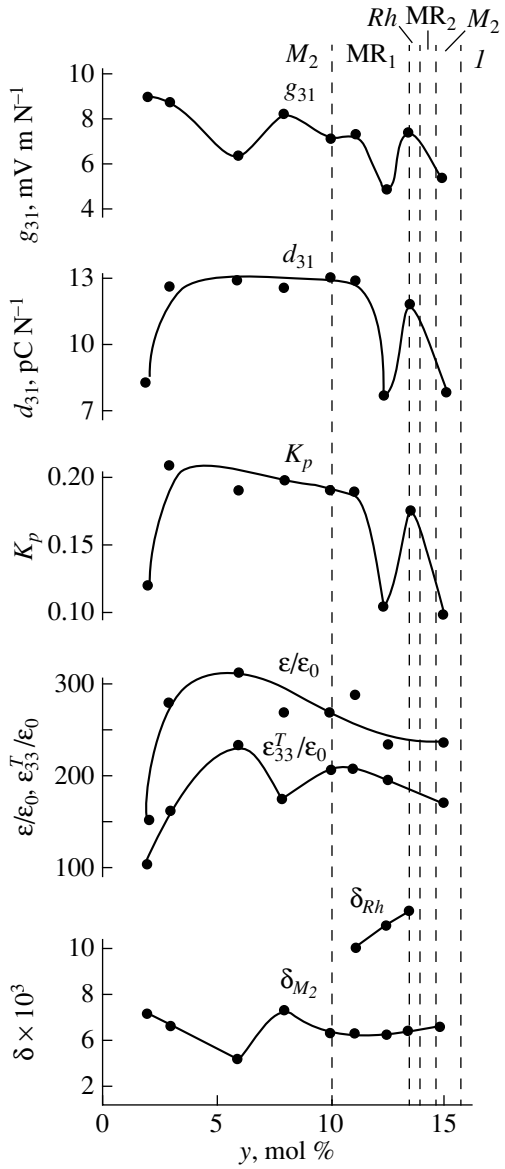

Fig. 3. Structure and electrical parameters of the (Na, Li, $Sr_{0.5}$)NbO_3 solid solutions vs. $LiNbO_3$ content for the section z = 10 mol % of $Sr_{0.5}NbO_3$ (*1*, the same as in Fig. 1).

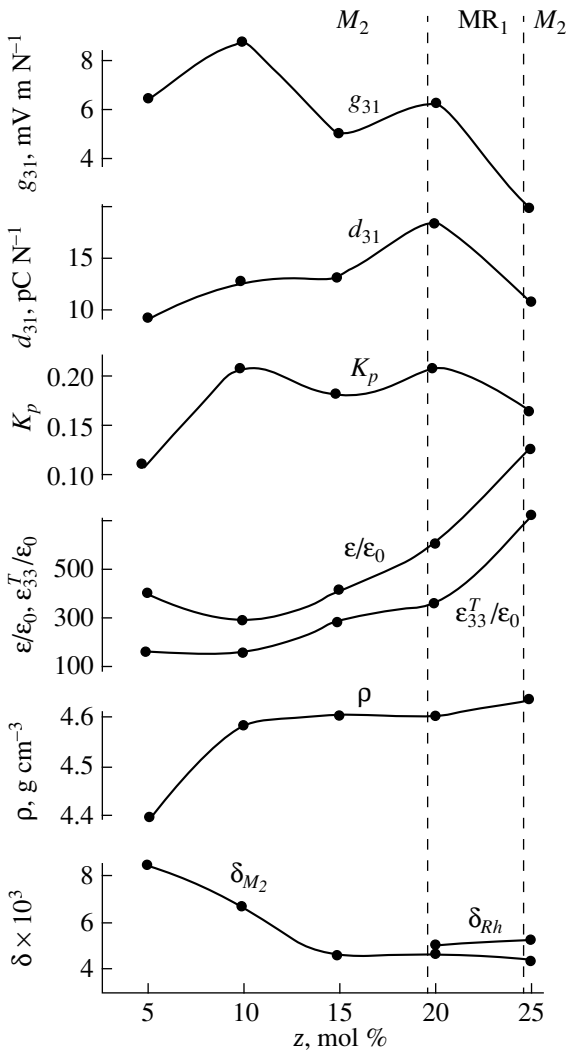

Fig. 4. Structure and electrical parameters of the (Na, Li, $Sr_{0.5}$)NbO_3 solid solutions vs. $Sr_{0.5}NbO_3$ content for the section y = 3 mol % of $LiNbO_3$.

ions in the *A* sublattices. To discover the influence of composition ordering of the ions on the electrical parameters of the SS, we analyzed the reasons [7] for the high permittivity of complex oxides $A(B'_{1/2}B''_{1/2})O_3$ with the disordered structure. According to [7], the free space where the small *B* ions regularly surrounded by the larger ions can move is considerably less in ordered structures than in disordered ones. Therefore, when exposed to an electric field, the disordered structure is more favorable for small ion motion without damaging the oxygen framework than the ordered one. This

Parameters of some (Na, Li, $Sr_{0.5}$)NbO_3 compositions

Composition no.	T_c, °C	$\varepsilon_{33}^T/\varepsilon_0$	K_p	g_{31}, mV m/N	Q_M	V_R, km/s
1	320	127	0.193	10.0	650	5.7
2	338	107	0.215	13.7	40	4.9
3	287	110	0.296	15.8	295	5.4

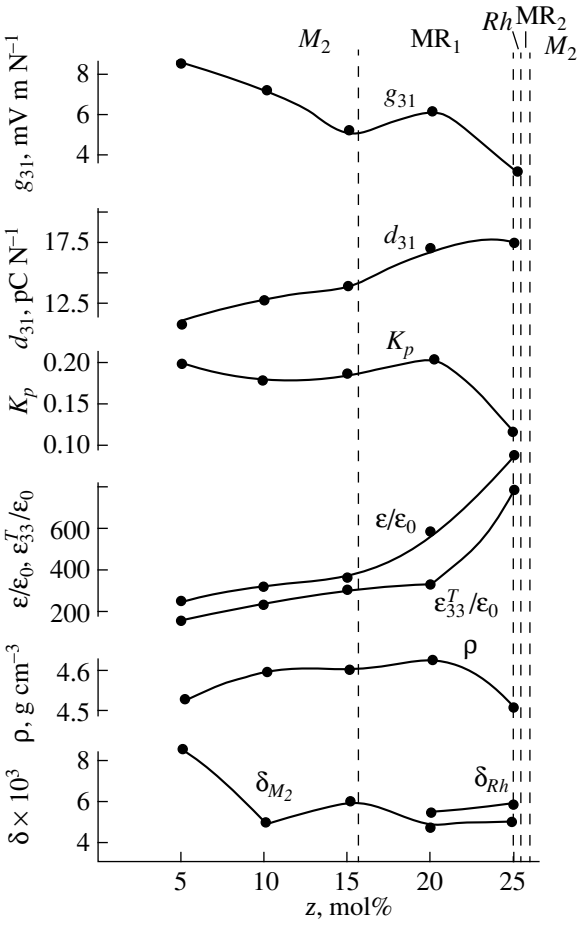

Fig. 5. Structure and electrical parameters of the (Na, Li, $Sr_{0.5}$)NbO_3 solid solutions vs. $Sr_{0.5}NbO_3$ content for the section y = 6 mol % of $LiNbO_3$.

increases the polarization per unit field and, hence, the permittivity. The same growth mechanism of the permittivity and related electrical parameters is likely to be responsible for the above extrema at the interfaces between the subsystems with different degrees of composition ordering.

The y sections can also be subdivided into those with irregular and smoothed dependences of the parameters. An example of the former case is shown in Fig. 4 (y = 3). Here, g_{31}, d_{31}, and K_p peak within the MR_1 (at its left boundary), whereas $\varepsilon_{33}^T/\varepsilon_0$ peaks beyond the right boundary of the MR_1. In addition, away from the MR_1, at about 10 mol % of $LiNbO_3$, there are the second maxima of K_p and g_{31}, which may result from an increase in δ_{M_2} combined with a sharp fall of the density ρ (Fig. 4).

Figure 5 gives an example of smoother dependences of the parameters for y = 6 mol % of $LiNbO_3$. It is seen that the incomplete maximum of $\varepsilon_{33}^T/\varepsilon_0$ is shifted beyond the MR_1 right boundary, while the g_{31} and K_p maxima are approximately at the center of the MR_1, where δ is minimal. A further increase in g_{31} and K_p in the M_2 phase is accompanied by the growth of δ.

One of the most interesting properties of the considered SS is the combination of low permittivity ($\varepsilon_{33}^T/\varepsilon_0 \approx$ 105–125) and high electromechanical coupling coefficient ($K_p \approx$ 0.2–0.3). This results in high g_{31}, which characterizes material sensitivity to mechanical stress. Such materials are known to be effective in accelerometers, flaw detectors, and diagnostic medical devices [8, 9]. Moreover, low permittivity of materials is favorable for their application in high-frequency transducers [10]. The parameters of such compositions are presented in the table in order of increasing g_{31}.

Some compositions of the system are characterized by enhanced anisotropy of the electromechanical coupling coefficients ($K_t/K_p \geq 3$), which makes them suitable for selectively sensitive accelerometers. In addition, high Curie temperatures ($T_c \geq 300$°C) enable the extension of the SS operating temperature range. Finally, like most niobates [9], the considered SS offer a high velocity of sound, which simplifies the production of rf transducers and ensures good matching with external circuits, and low density, which permits their use in devices where weight is a key issue.

CONCLUSION

A precision X-ray diffraction study of the solid solutions made it possible to refine the data for phase transitions in the (Na, Li, $Sr_{0.5}$)NbO_3 ternary system. The relationship between the structural and electrical properties of the solid solutions was determined in wide range of component concentrations. The electrical features of these solutions were interpreted in more detail. Compositions combining low permittivity and high sensitivity to mechanical stress were obtained. They are promising for applications in highly sensitive high-frequency transducers.

ACKNOWLEDGMENTS

This work was supported in part by the Russian Foundation for Basic Research, project no. 99-02-17575.

REFERENCES

1. L. S. Ivanova, L. A. Reznichenko, O. N. Razumovskaya, and L. A. Shilkina, Izv. Akad. Nauk SSSR, Neorg. Mater. **23**, 525 (1987).
2. E. G. Fesenko, V. S. Filip'ev, and M. F. Kupriyanov, Fiz. Tverd. Tela (Leningrad) **11**, 466 (1969) [Sov. Phys. Solid State **11**, 366 (1969)].
3. V. J. Tennery, J. Am. Ceram. Soc. **49** (7), 376 (1996).

4. L. A. Shilkina, L. A. Reznichenko, M. F. Kupriyanov, and E. G. Fesenko, Zh. Tekh. Fiz. **47**, 2173 (1977) [Sov. Phys. Tech. Phys. **22**, 1262 (1977)].
5. L. A. Shilkina, I. V. Pozdnyakova, S. I. Dudkina, *et al.*, in *Abstracts of 8th International Symposium on Physics of Ferroelectric Semiconductors (IMFS-8), Rostov-on-Don, 1998*, p. 190.
6. L. A. Reznichenko, O. N. Razumovskaya, A. Ya. Dantsiger, *et al.*, in *Abstracts of International Scientific and Practical Conference "Piezotechnology-97," Obninsk, 1997*, p. 197.
7. S. Nimura and K. Uchino, Ferroelectrics **41** (1), 117 (1982).
8. E. G. Fesenko, A. Ya. Dantsiger, and O. N. Razumovskaya, *Novel Piezoelectric Ceramic Materials* (Rostov. Gos. Univ., Rostov-on-Don, 1983).
9. A. Ya. Dantsiger, O. N. Razumovskaya, L. A. Reznichenko, and S. I. Dudkina, *High-Efficiency Piezoelectric Ceramic Materials: Optimization of the Search* (Paĭk, Rostov-on-Don, 1995).
10. E. G. Fesenko, A. Ya. Dantsiger, L. A. Reznichenko, *et al.*, Zh. Tekh. Fiz. **52**, 2262 (1982) [Sov. Phys. Tech. Phys. **27**, 1389 (1982)].

Translated by A. Sidorova-Biryukova

Technical Physics, Vol. 45, No. 11, 2000, pp. 1437–1440. Translated from Zhurnal Tekhnicheskoĭ Fiziki, Vol. 70, No. 11, 2000, pp. 63–66.

SOLIDS

Ferroelectric Elastance of Sodium Niobate–Lithium Niobate Solid Solutions in Relation to *A*–O Bond Covalence

L. A. Reznichenko, A. Ya. Dantsiger, O. N. Razumovskaya, S. I. Dudkina, L. A. Shilkina, I. V. Pozdnyakova, and V. A. Servuli

Research Institute of Physics, Rostov State University, pr. Stachki 194, Rostov-on-Don, 344090 Russia

E-mail: larisa@riphys.rnd.su

Received October 19, 1999

Abstract—The ferroelectric elastance of (Na, Li, $A'_{0.5}$)NbO_3 solid solutions was found to vary directly with the total electronegativity of elements *A* ($EN_{\Sigma A}$), that is, with the *A*–O bond covalence at *B* = const. Using $EN_{\Sigma A}$ values and the position on the phase diagram, one can determine the solid solution parameters optimum for use in high-frequency (*A*' = Sr, Pb), medium-frequency (*A*' = Cd), and elevated-temperature (*A*' = Cd) devices.

INTRODUCTION

In this paper, we summarize the results of investigating solid solutions (SS) in $x NaNbO_3$–$yLiNbO_3$–$z A'_{0.5} NbO_3$ ternary systems, where *A*' stands for Sr, Pb, Cd [hereafter, systems (1)]. Their phase diagrams and electrical properties are outlined in [1–3]. From six to seven *z* sections with compositions varying between (2–5) and (20–45) mol % of $A'_{0.5} NbO_3$ at 2.5–5 mol % intervals were studied for each system. In each section, compositions with the $LiNbO_3$ content from 1–2.5 to 15–25 mol % were synthesized (*y* sections). Two-stage solid-phase reactions were used for SS synthesis; and hot pressing, for their sintering. Synthesis and sintering conditions are presented in [1–3]. This study is aimed at generalizing data obtained for systems (1).

RESULTS AND DISCUSSION

The parts of the phase diagram that are adjacent to $NaNbO_3$ are presented in [1–3]. Refined diagrams for these systems are shown in Figs. 1–3. They contain both monophase regions, namely, monoclinic (M_1, M_2, and M_4), rhombohedral (*Rh*), tetragonal (*T*), and cubic (K_2), and morphotropic regions (MRs) of various widths where the phases coexist. Near the MRs, the electrical parameters exhibit extrema correlating with changes in the structural parameters (for more detailed properties of various ferroelectrics, see [4, 5]). As was pointed out above, systems (1) differ by their third element *A*'(Sr, Pb, or Cd), i.e., by type of *A*–O bond.

Electronegativity (EN) is known to indicate the state of a chemical bond. Together with other factors, EN to a large extent defines most physical and physicochemical properties [6]. The chemical bond type is judged by the difference in the ENs of the components: the less the difference, the higher the bond covalence [6, 7]. As to the *A*–O bond, its covalence increases with increasing EN of the *A* element, since the gap between the ENs of the *A* element and O narrows in this case (the EN of oxygen is always higher than that of the *A* element in the corresponding valence states). In other words, the EN of the *A* element is indicative of the *A*–O bond covalence. The ENs of the *A* components in system (1) and covalence of the *A*–O bond are listed in Table 1 in increasing order.

In our previous studies of $Pb(Ti, Zr)O_3$–$\sum_{n=1}^{3} (PbB'_{1-\alpha}B''_{\alpha}O_3)_n$ (PZT) solid solutions [4, 5], we found that their ferroelectric elastance varies directly with the EN of the *B*" element in the corre-

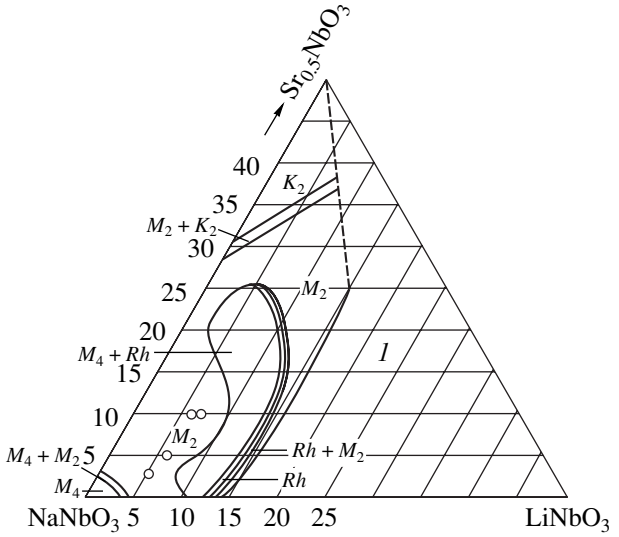

Fig. 1. Phase diagram of the ternary (Na, Li, $Sr_{0.5}$)NbO_3 system (*1*, heterogeneous region).

1063-7842/00/4511-1437$20.00 © 2000 MAIK "Nauka/Interperiodica"

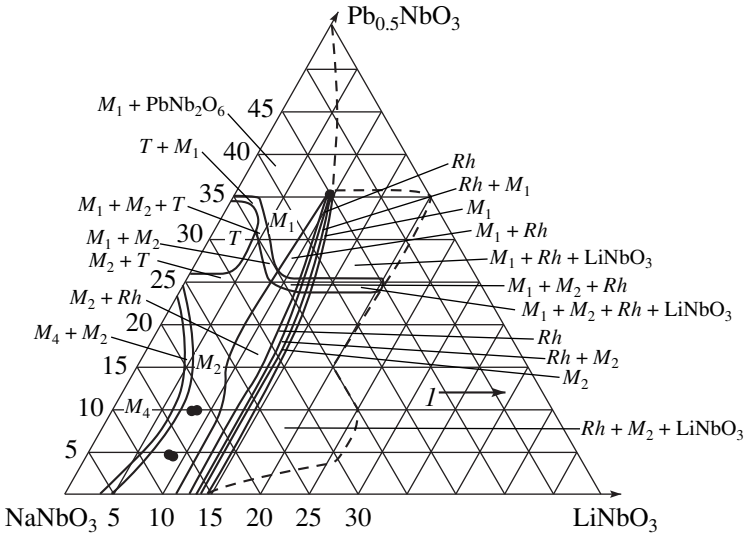

Fig. 2. Phase diagram of the ternary (Na, Li, $Pb_{0.5}$)NbO_3 system (*1*, the same as in Fig. 1).

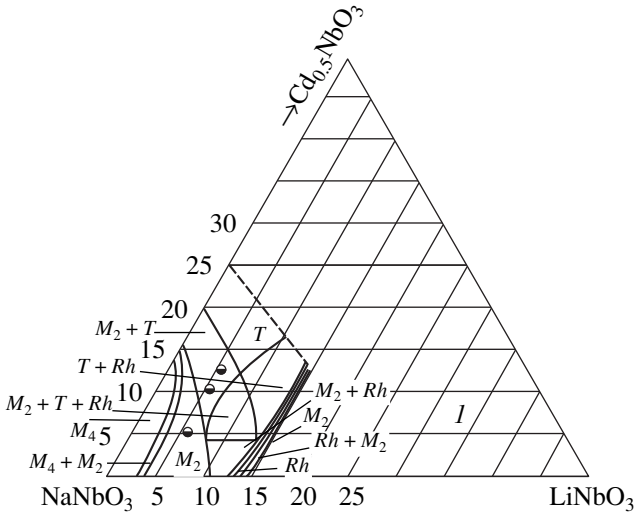

Fig. 3. Phase diagram of the ternary (Na, Li, $Cd_{0.5}$)NbO_3 system (*1*, the same as in Fig. 1).

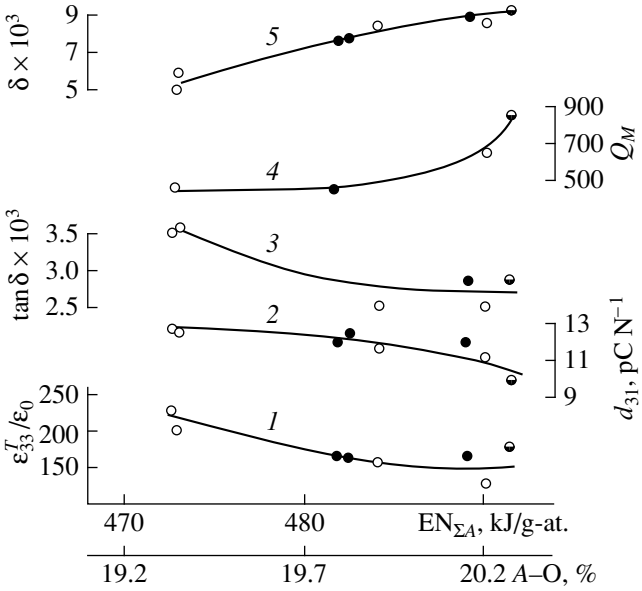

Fig. 4. Dependences of (*1*) $\varepsilon_{33}^T/\varepsilon_0$, (*2*) d_{31}, (*3*) tanδ, (*4*) Q_M, and (*5*) δ on the total EN of the *A* elements and *A*–O bond covalence for the (Na_x, Li_y, $A'_{0.5z}$)MbO_3 solid solutions belonging to the M_2 phase.

sponding oxidation state and, hence, with the *B*"–O bond covalence at *A* = const. This is supported by EN dependences of the electrical parameters: an increase in the EN leads to a decrease in $\varepsilon_{33}^T/\varepsilon_0$, $\tan\delta$, K_p, and d_{31} and an increase in V_R, Q_M, and δ.[1] These data were obtained for compositions with the optimum characteristics within the tetragonal region near the MR boundary. In addition, the component concentrations were roughly equal.

In the niobate SS of system (1), the element *A* varies, whereas *B* = const. In contrast to the PZT systems, the niobate systems have much more complex phase diagrams. As was mentioned above, they have a large number of phases and MRs and their characteristics are irregular. Because of this, correct relationships between the SS parameters and EN of the SS components must include the total EN of all the *A* components with regard to their concentrations. Moreover, the SS to be compared should be of the same phase and away from MR boundaries in order to eliminate their influence.

[1] $\varepsilon_{33}^T/\varepsilon_0$ is the relative permittivity, tanδ is the dielectric loss tangent, K_p is the electromechanical coupling coefficient, d_{31} is the piezoelectric modulus, V_R is the sound velocity, Q_M is the mechanical *Q*-factor, and δ is the homogeneous strain parameter [8].

Figure 4 shows the dependences of $\varepsilon_{33}^T/\varepsilon_0$, d_{31}, tanδ, Q_M, and δ on the total EN of the *A* elements ($EN_{\Sigma A}$) with account of their concentrations in the (Na_x, Li_y, $A'_{0.5z}$)NbO_3 SS and on the *A*–O bond covalence. Empty, filled, and half-filled circles mark the SS containing Sr, Pb, and Cd, respectively. These SS lie in the M_2 region, appearing in all the (Na, Li, $A'_{0.5}$)NbO_3 systems. In Figs. 1–3, these SS are marked with the corresponding circles. The selected SS compositions, related $EN_{\Sigma A}$'s, and *A*–O bond covalences are presented in Table 2.

The dependences shown in Fig. 4 are qualitatively the same as those for the SS in the PZT system. They indicate that the ferroelectric elastance of the niobate SS grows with $EN_{\Sigma A}$ and, hence, with *A*–O bond covalence.

Figure 5 shows the dependences of $\varepsilon_{33}^T/\varepsilon_0$, d_{31}, K_p, Q_M, and δ on $EN_{\Sigma A}$ and *A*–O bond covalence for the (Na_x, Li_y, $Cd_{0.5z}$)NbO_3 SS belonging to the region of coexistence of the M_2 and *T* phases (half-filled circles in Fig. 3). Note the particular complexity of this phase diagram and the small size of the M_2 phase region, from which only one SS can be presented in Fig. 4. Data in Fig. 5 also support a direct proportion between the SS ferroelectric elastance and *A*–O bond covalence.

Let us now trace how the crystallochemical parameter EN influences the areas of niobate SS application. Niobates are known [9] to have a set of unique parameters (low $\varepsilon_{33}^T/\varepsilon_0$, low density ρ, and high V_R), which makes them promising for high-frequency and microwave devices. Some of the parameters of system (1) can be judged by data presented in Fig. 4. It suggests that the location of the $Sr_{0.5}$- and $Pb_{0.5}$-containing SS in the phase diagram (within the M_2 phase), along with the $EN_{\Sigma A}$ values, strongly affects the parameters of these SS: they approach each other at close $EN_{\Sigma A}$'s. When $EN_{\Sigma A}$ = 482–490 kJ/g-at., these SS exhibit low $\varepsilon_{33}^T/\varepsilon_0$ (125–170) but comparatively high piezoelectric parameters; hence, high g_{31} [>10 (mV m)N]. Therefore, these materials are of potential use in high-frequency accelerometers, flaw detectors, and diagnostic medical devices.

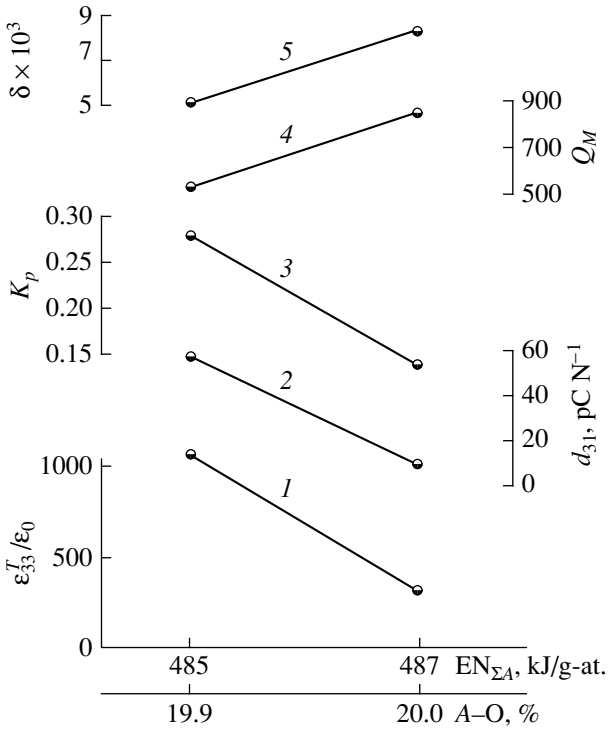

Fig. 5. Dependences of (*1*) $\varepsilon_{33}^T/\varepsilon_0$, (*2*) d_{31}, (*3*) K_p, (*4*) Q_M, and (*5*) δ on the total EN of the *A* elements and *A*–O bond covalence for the (Na_x, Li_y, $Cd_{0.5}$)NbO_3 solid solutions belonging to the morphotropic region M_2 + *T*.

The $Cd_{0.5}$-containing SS provide a somewhat different combination of parameters, as follows from Fig. 5. Here, two compositions in the region where the M_2 and *T* phases coexist have significantly differing parameters. Along with the SS having properties approaching those represented in Fig. 4, there is another SS with considerably higher $\varepsilon_{33}^T/\varepsilon_0$ (>1000), d_{31}, and K_p. This composition is located in the region of extreme parameters within the MR (M_2 +*T*). Moreover, this SS has an elevated Curie temperature T_c = 400°C (in the $Sr_{0.5}$- and $Pb_{0.5}$-containing systems, such MRs and corresponding properties are absent). The $Cd_{0.5}$-containing system includes several additional SS with high T_c (400–430°C)

Table 1. EN of the (Na, Li, $A'_{0.5}$)NbO_3 solid solutions and *A*–O bond covalence

Elements	Valence	EN, kJ/g-at.	*A*–O bond covalence, %
Na	1+	494	~22.4
Li	1+	523	~22.1
Sr	2+	523	~22.1
Pb	2+	712	~33.7
Cd	2+	816	~40.3

Table 2. Compositions of the selected $(Na_x, Li_y, A'_{0.5z})NbO_3$ solid solutions, $EN_{\Sigma A}$, and *A*–O bond covalence

A'	Composition			$EN_{\Sigma A}$, kJ/g-at.	*A*–O bond covalence, %
	z	*y*	*x*		
Sr	0.025	0.055	0.92	490.0	~20.2
	0.05	0.06	0.89	484.0	~19.8
	0.1	0.06	0.84	472.7	~19.3
	0.1	0.07	0.83	473.0	~19.3
Pb	0.05	0.075	0.875	489.0	~20.1
	0.1	0.075	0.825	481.7	~19.7
	0.1	0.08	0.82	482.4	~19.8
Cd	0.05	0.06	0.89	491.4	~20.2

and $\varepsilon_{33}^T/\varepsilon_0 = 300–700$. These combinations permit the use of these SS in high-temperature transducers operating at high and medium frequencies.

CONCLUSION

The ferroelectric elastance of the sodium niobate–lithium niobate solid solutions depends on the *A*–O bond covalence. The latter can be expressed in terms of the total electronegativity of the elements in the *A* sublattice ($EN_{\Sigma A}$), since these values are directly proportional to each other. The position of the solid solution in the phase diagram and its total electronegativity specify parameter combinations optimum for the use in various transducers (flaw detectors, accelerometers, and high-temperature sensors).

ACKNOWLEDGMENTS

This study was supported in part by the Russian Foundation for Basic Research, project no. 99-02-17575.

REFERENCES

1. L. S. Ivanova, L. A. Reznichenko, O. N. Razumovskaya, *et al.*, Izv. Akad. Nauk SSSR, Neorg. Mater. **23**, 525 (1987).
2. L. A. Reznichenko, O. N. Razumovskaya, A. Ya. Dantsiger, *et al.*, in *Proceedings of the International Conference "Piezotechnology-97," Obninsk, 1997*, p. 197.
3. E. G. Fesenko, L. A. Reznichenko, L. S. Ivanova, *et al.*, Zh. Tekh. Fiz. **55**, 601 (1985) [Sov. Phys. Tech. Phys. **30**, 354 (1985)].
4. E. G. Fesenko, A. Ya. Dantsiger, and O. N. Razumovskaya, *Novel Piezoelectric Ceramic Materials* (Rostov. Gos. Univ., Rostov-on-Don, 1983).
5. A. Ya. Dantsiger, O. N. Razumovskaya, L. A. Reznichenko, and S. I. Dudkina, *High-Efficiency Piezoceramic Materials: Optimization of the Search* (Paĭk, Rostov-on-Don, 1995).
6. A. S. Povarennykh, in *West-Ukrainian Division of All-Union Mineralogical Society* (Akad. Nauk Ukr. SSR, Kiev, 1962), pp. 3–27.
7. M. Kh. Karapet'yants and S. I. Drakin, *Structure of Materials* (Vysshaya Shkola, Moscow, 1967).
8. E. G. Fesenko, V. S. Filip'ev, and M. F. Kupriyanov, Fiz. Tverd. Tela (Leningrad) **11**, 466 (1969) [Sov. Phys. Solid State **11**, 366 (1969)].
9. E. G. Fesenko, A. Ya. Dantsiger, L. A. Reznichenko, *et al.*, Zh. Tekh. Fiz. **52**, 2262 (1982) [Sov. Phys. Tech. Phys. **27**, 1389 (1982)].

Translated by A. Sidorova-Biryukova

Technical Physics, Vol. 45, No. 11, 2000, pp. 1441–1446. Translated from Zhurnal Tekhnicheskoĭ Fiziki, Vol. 70, No. 11, 2000, pp. 67–73.

SOLIDS

On One Mechanism of Magnetization Reversal in Crystals with Combined Anisotropy

R. M. Vakhitov and V. E. Kucherov

Bashkortostan State University, ul. Frunze 32, Ufa, 450074 Bashkortostan, Russia

E-mail: NakhitovRM@bsu.bashedu.ru

Received December 22, 1999

Abstract—The effect of a magnetic field on the stability of null domain walls is considered in terms of a variational model. The walls are localized near defects in a (001)-oriented plate. The critical fields at which the inhomogeneities exist are found, and their role in magnetization processes taking place in the crystals under study is considered. © *2000 MAIK "Nauka/Interperiodica".*

INTRODUCTION

It is known that structure defects result in the nonuniformity of crystal parameters and strongly affect its static and dynamic properties. In particular, defects serve as pinning centers for magnetic inhomogeneities, which, as a rule, have a nontrivial configuration [1, 2]. They play an essential role in the formation and rearrangement of the domain structure and influence crystal magnetization processes [3]. Therefore, the study of the structure and properties of magnetic inhomogeneities localized on defects in applied materials seems to be topical.

MODEL OF NULL DOMAIN WALL

A number of materials, such as garnet ferrite films, feature the presence of two anisotropies of different natures: induced uniaxial anisotropy (IUA) and natural cubic anisotropy (NCA). In these materials, specific magnetic inhomogeneities [null domain walls (DWs), or static solitons (SS)] may exist [4]. These are magnetic inhomogeneities that separate two domains with the same magnetization orientation **M**. Different types of null DWs are known. Their structure and properties depend on the IUA (K_u) and NCA (K_1) constants, as well as on the film surface orientation. To be specific, consider a (001)-oriented plate where the IUA easy axis is aligned with the normal **n** to its surface, **n** ∥ *OZ* ∥ [001]. Then, within the model that includes exchange interaction, combined anisotropy, and demagnetizing fields of space charges localized on DWs [5], the energy of the magnetic inhomogeneities can be written in the form

$$\begin{aligned} E = \int\{&A[(\partial\Theta/\partial y)^2 + \sin^2\Theta(\partial\varphi/\partial y)^2] \\ &+ K_u\sin^2\Theta + K_1[\sin^4\Theta\sin^2(\varphi-\varphi_0) \\ &\times\cos^2(\varphi-\varphi_0) + \sin^2\Theta\cos^2\Theta] \\ &+ 2\pi M_s^2(\sin\Theta\sin\varphi - \sin\Theta_m\sin\varphi_m)^2\}dV, \end{aligned} \quad (1)$$

where A is an exchange parameter, M_s is the saturation magnetization, Θ and φ are, respectively, polar and azimuth angles of the vector **M**, φ_0 is the angle between the [100] direction and the $0X$-axis that lies in the DW plane, Θ_m and φ_m are angles that define the magnetization orientation in the domains, y is the coordinate along which the magnet is inhomogeneous, and V is the plate volume.

We assume that the plate thickness D is large and the contribution from the demagnetizing fields of nonuniformly distributed surface charges to energy (1) can be neglected (idealized model).

From the phase portrait of Lagrange–Euler equations minimizing (1), it follows that, at $\kappa > 1$ (where $\kappa = K_1/K_u$), there may exist solutions that correspond to a null Bloch wall ($\varphi = 0, \pi$) and have the form

$$\begin{aligned} &\tan\Theta = \pm a\cosh\xi, \quad \varphi_0 = \pi n/2, \quad n \in Z, \\ &a = (\kappa-1)^{-1/2}, \quad b = (\kappa-1)^{1/2}, \quad \xi = by/\Delta_0, \end{aligned} \quad (2)$$

where $\Delta_0 = \sqrt{A/K_u}$ is the DW width in a uniaxial crystal.

From (2), such solutions are associated with solitons of four types. They differ by sense of spin rotation in the transition polarization layer and deviation of the vector **M** from the (001) plane (up- or downward). The solitons are characterized by an energy E_s, effective width Δ_s, and maximum angle Θ_s (amplitude) of deviation of the vector **M** from the uniform state. The last two parameters define the soliton size and are given by

$$\begin{aligned} \Delta_s &= 2\Delta_0\{[\pi - 2\arctan\sqrt{1+2a^2}]\sqrt{1+a^2} \\ &+ \ln[(\sqrt{1+a^2} + \sqrt{1+2a^2})/2]\}/b, \\ \Theta_s &= |\pi/2 - \arctan(a)|. \end{aligned} \quad (3)$$

1063-7842/00/4511-1441$20.00

Stability analysis applied to solution (2) (the check that the condition $\delta^2 E_c > 0$ is fulfilled [4]) shows that an SS is an unstable formation.

In [6], conditions for the generation of null DWs in a (001) plate with combined anisotropy and the properties of null walls were considered. Specifically, it was shown that the inclusion of the factors that locally change the values of the K_1 and K_u constants (demagnetizing fields of the sample and the presence of defects) makes the SS stable. The profile of a "defect" was simulated as

$$K_1(y) = \begin{cases} K_1 - \Delta K_1 & \text{for} \quad |y| < l/2 \\ K_1 & \text{for} \quad |y| > l/2, \end{cases}$$
$$K_u(y) = \begin{cases} K_u + \Delta K_u & \text{for} \quad |y| < l/2 \\ K_u & \text{for} \quad |y| > l/2, \end{cases} \tag{4}$$

where l is the width of the defect and the contribution from the demagnetizing fields to energy (1) is described by the term

$$E_{ms} = M_s^2 L_x \int_{-\infty}^{\infty}\int_{-\infty}^{\infty} \cos\Theta(y)\cos\Theta(y') \times \ln(1 + D^2/(y-y')^2)\,dy\,dy', \tag{5}$$

where L_x is the plate size in the $0X$ direction.

As follows from the calculations, SS are stable only if existing defects make a negative contribution to the energy and the material parameters vary in a certain range. The upper stability limit (if any) means soliton diffusion and was predicted even in the idealized model [4]. However, this model gives ranges of SS stability (for example, in terms of the parameter κ) that differ markedly from our results. The lower stability limit is associated with SS collapse and specifies the least defect energy necessary for soliton generation. The lower limit arises mainly because of the competition between SS–defect interaction forces and magnetostatic forces. It was not discovered earlier.

THE EFFECT OF A MAGNETIC FIELD ON SURFACE SOLITON STABILITY

To study magnetization reversal in plates with defects like (4), it is necessary to take into account the interaction of the magnetization with an external magnetic field **H**. The contribution from this interaction to the total SS energy is given by the term

$$E_h = -\int_V \mathbf{H}\mathbf{M}\,dV, \tag{6}$$

which is the Zeeman energy of interaction.

It is clear that the effect of Zeeman interaction on the structure and stable states of SS depends on the field orientation relative to the crystallographic axes. Therefore, we will consider two typical directions of the field **H**: **H** || [100] and **H** || [001].

(1) **H** || [100]. In this case, the range of SS stability is found by the variational method where magnetization distribution (2) is taken as the trial function and the parameters a and b are treated as variational parameters. Such an approach is valid, because, within the idealized model including Zeeman interaction (6) (for **H** || [100]), the phase portrait of the associated Lagrange–Euler equations gives a magnetization trajectory in the form of closed loops (Fig. 1a, curve *1*). To these loops, there correspond magnetic inhomogeneities like SS with a distribution of the vector **M** in the form of (2).

This variational problem is solved by numerically minimizing energy (1) in terms of a and b with regard for (4)–(6). Calculations show that, if **H** || [100], SS with different polarizations become nonequivalent; that is, the polarization degeneracy of SS is removed. A soliton with $\varphi = \pi$ (the range of negative h's in Fig. 2) is energetically more favorable than that with $\varphi = 0$ (positive h's in Fig. 2). The size of a null DW with $\varphi = \pi$ grows with increasing h ($h = HM_s/2K_u$) but decreases for solitons of the other types. This can be explained by the fact that the magnetic field tends to align the spins of a null wall with $\varphi = \pi$ with the field, which increases its size. The spins of an SS with $\varphi = 0$ also tend to be aligned with the field. However, since the angle between them and the field is less than $\pi/2$, the size of these solitons will decrease. Such a consideration agrees well with experiments on magnetization reversal in imperfect magnetic films [7, 8].

It should be noted that, at a certain critical field H_c, solitons of both types become collapse-unstable and, at $H > H_c$, disappear. However, their critical (collapse) fields depend on the quality factor Q ($Q = K_u/2\pi M_s^2$) of the material in a different way: As Q increases, the collapse field of a null DW with $\varphi = 0$ increases and that of an SS with $\varphi = \pi$ diminishes (Fig. 2). This is explained by the reduced effect of the demagnetizing fields ($Q \longrightarrow \infty$) on magnetization reversal.

The dependence of the collapse fields of a null DW on the defect width l (Fig. 3) has an interesting feature. When l increases, the collapse field for an SS with $\varphi = 0$ grows and that for an SS with $\varphi = \pi$ drops. The reason is that, as l grows, the effect of NCA on magnetization reversal becomes more pronounced [9]; conversely, IUA begins to play a minor role (for $\Delta\kappa_u = -1$). Hence, the magnetic phases with **M** || [100] become more stable.

(2) **H** || [001]. In this case, the variational model of SS is somewhat more complicated, because homogeneous magnetic states with **M** || [100] are lacking in the field of the given orientation [9]. Their presence is the necessary condition for solutions in the form of (2) to exist. The Lagrange–Euler equations for energy (1)

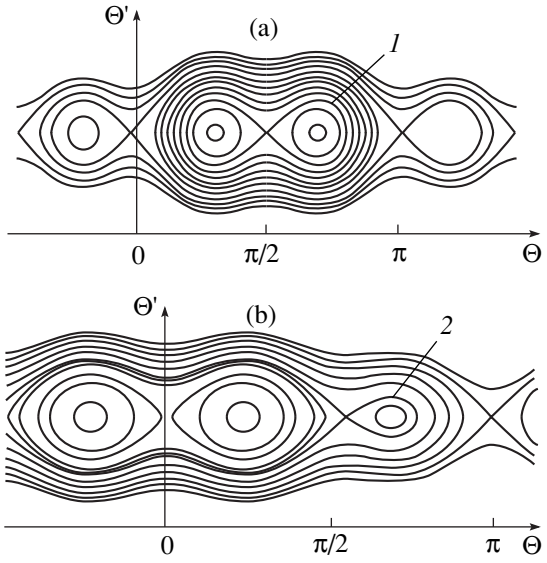

Fig. 1. Phase portrait of Lagrange–Euler equations. (a) **H** ∥ [100] and (b) **H** ∥ [001].

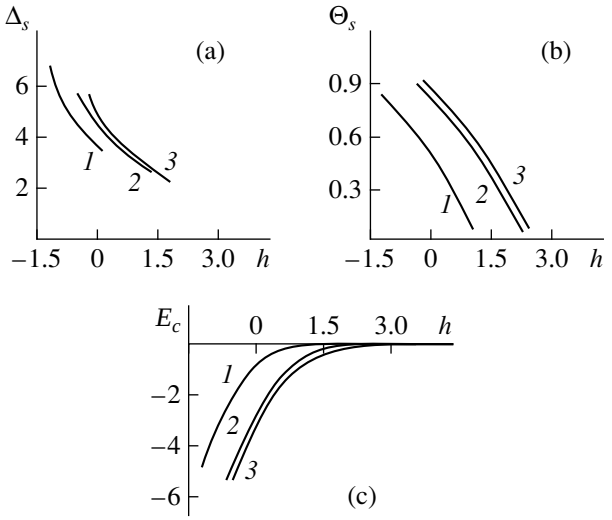

Fig. 2. (a) Width Δ_s, (b) amplitude Θ_s, and (c) energy E_c vs. h for $\kappa = 2$, $\Delta_0 = 0.15$, $D = 12$, $l = 3.4$, $\Delta\kappa_1 = 2.7$, $\Delta\kappa_u = -1$. Q = (*1*) 1, (*2*) 10, and (*3*) 30. $\Delta\kappa_u = \Delta K_u/K_u$; $\Delta\kappa_1 = \Delta K_1/K_u$.

with regard for Zeeman interaction (6) at $\varphi = 0, \pi$ have a first integral in the form of

$$(\Theta')^2 - V(\Theta) = \text{const}, \qquad (7)$$

where $V(\Theta) = \Delta_0^{-2}[(1 - 1/Q)\sin^2\Theta + \kappa\sin^2\Theta\cos^2\Theta - h\cos\Theta]$.

The phase portrait of Eq. (7) is shown in Fig. 1b (curve *2*). It is seen that soliton solutions exist in the form of separatrixes of closed loops, which intersect at the point $\Theta = \Theta_m$ near $\pi/2$. The point Θ_m corresponds to the polar angle of the equilibrium direction of **M** in the domains and is found from the minimum condition for energy density $E_0 = AV(\Theta)$ of a uniformly magnetized plate. The found values of Θ_m can be treated as boundary conditions for the soliton solutions of Eq. (7); i.e., at $y \longrightarrow \pm\infty$, $\Theta'(y) \longrightarrow 0$, and $\Theta \longrightarrow \Theta_m$. However, with these boundary conditions, the solutions cannot be found in known functions. Therefore, we approximate them by a trial function in the form

$$\tan\Theta = \frac{\cosh\zeta}{c\cosh\xi - a}, \quad c = \cot\Theta_m. \qquad (8)$$

The SS sizes for the given magnetization distribution in the transition layer are given by

$$\Delta_s = 2\frac{\Delta_0}{b}\left[\xi_p + k\left(\arctan\frac{1}{c} - \arctan\frac{\cosh\xi_p}{c\cosh(\xi_p - a)}\right)\right],$$

$$\Theta_s = \frac{\pi}{2} - \arctan\frac{1}{c + a}, \qquad (9)$$

$$k = \frac{(c^2 + 1)\cosh^2\xi_p + 2ac\cosh\xi_p + a^2}{a\sinh\xi_p}.$$

Here, $\xi_p = \ln(t + \sqrt{t^2 + 1})$ and t is found from a solution of the reduced cubic equation

$$t^3 + pt + q = 0, \quad p = -(2c^2 + 2 + a^2)/(c^2 + 1),$$
$$q = -2ac/(c^2 + 1). \qquad (10)$$

Note that, if the constant of integration in (7) is taken to be zero (which is the case at $h = 0$), magnetization distribution (8) in the transition layer is transformed into (2). This indicates the validity of the selected SS model.

The related variational problem for the magnetization distribution (8) is solved as in the previous case. As follows from the calculations, SS differing by the deviation of **M** from the uniform state become nonequiva-

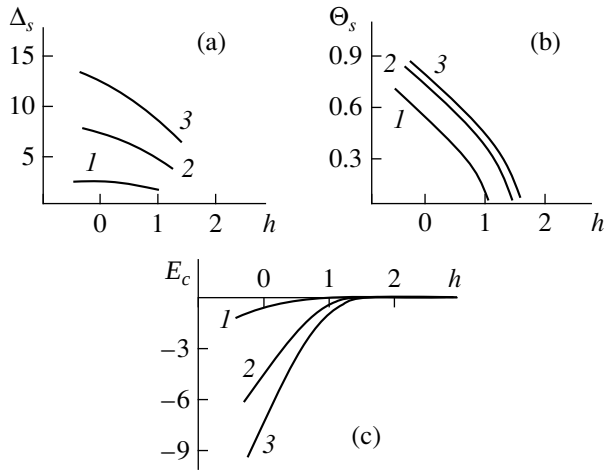

Fig. 3. SS parameters vs. external field h. $\kappa = 1.7$, $\Delta_0 = 0.15$, $D = 12$, $Q = 3$, $\Delta\kappa_1 = 2.7$, $\Delta\kappa_u = -1$. l = (*1*) 1, (*2*) 5, and (*3*) 10.

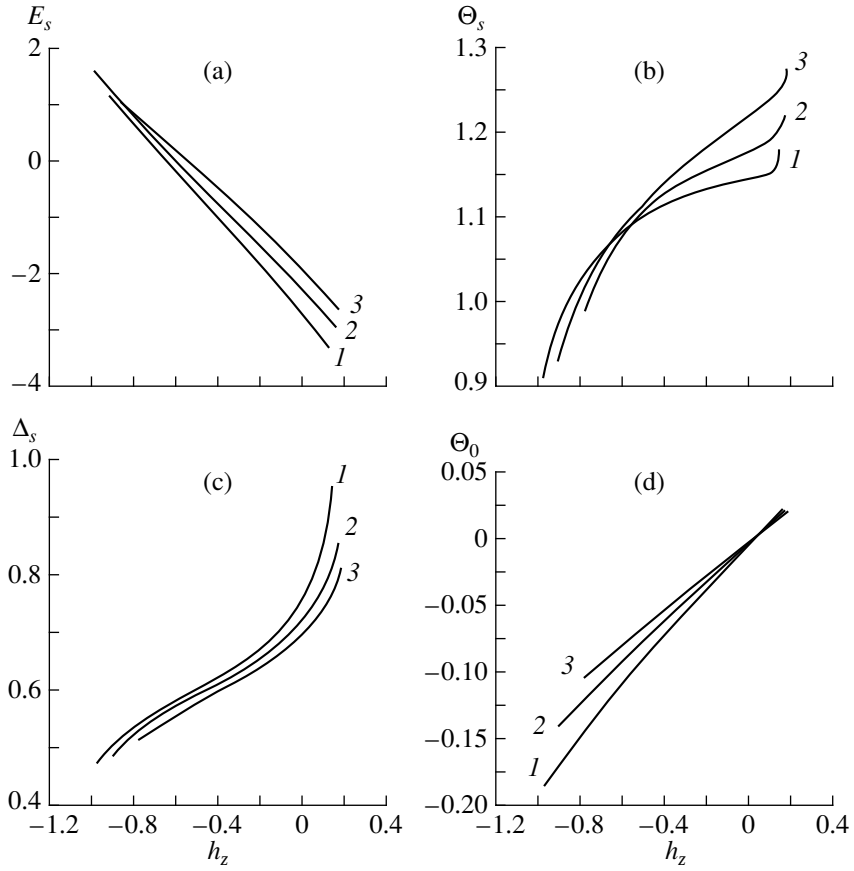

Fig. 4. (a) Energy, (b) amplitude, (c) width, and (d) angle Θ_0 vs. external field $h \parallel [001]$. $\Delta_0 = 0.15$, $D = 12$, $Q = 5$, $\Delta\kappa_1 = 5.7$, $\Delta\kappa_u = 1$, $\xi = 0$, and $l = 0.4$. κ = (*1*) 3.7, (*2*) 4.2, and (*3*) 4.7.

lent when the field is applied (Fig. 4). SS in which the magnetization deviates from the (001) plane toward the field (SS of the first kind) are energetically more favorable than those where the magnetization deviates in the opposite direction (SS of the second kind). The latter, which are of two types differing by polarization, are essentially reversed domains and represent their simplest model.

In Fig. 4, the deviation of the magnetization vector from the (001) plane increases with the field in the homogeneous state. The deviation is defined by the angle $\Theta_0 = \pi/2 - \Theta_\infty$. Because of this, the soliton amplitude also grows. With increasing h_z, the SS spins tend to be aligned with the field, causing the SS of the first kind to extend. When a critical value of h_z is attained, the first-kind SS begin to diffuse. In this case, $\Delta_s \longrightarrow \infty$ and $\Theta_s \longrightarrow \pi/2$, which means complete magnetization reversal with respect to the field. At the same time, the width and amplitude of the second-kind SS decrease as h grows. At some value of h, they collapse. However, at the collapse values of h, the SS energy becomes positive (i.e., the SS become metastable); hence, SS of this kind may collapse or transform into another localized state somewhat earlier, for example, when $E > 0$.

It is worth noting that the demagnetizing fields of the plate variously affect the stability range of the SS. Since magnetostatic energy (5) adds to the total energy of magnetic inhomogeneities, taking into consideration the magnetostatic interaction between charges uniformly distributed over the plate surface shrinks the SS stability range. The application of the magnetic field somewhat extends the stability range for the SS aligned with the field and narrows this range for those oriented oppositely. As Q decreases [the contribution of the demagnetizing fields to energy (1) grows], the collapse fields rise for the SS of the first kind (Fig. 5) and decline for the SS of the second kind. This results from the fact that the demagnetizing fields and the external magnetic field variously influence the spins in different SS regions. In the central part of the second-kind SS, these fields add up and the total field tends to align the spins, which here make an obtuse angle with the **H** field, with the [100] direction. Other spins of these SS (and also those of the SS of the first kind), which make an acute angle with **H**, are subjected to the oppositely acting fields. Consequently, as Q decreases, the critical field for the first-kind SS rises and that for the SS of the second kind drops. At the critical values of h, the SS of the first kind diffuse and those of the second kind collapse.

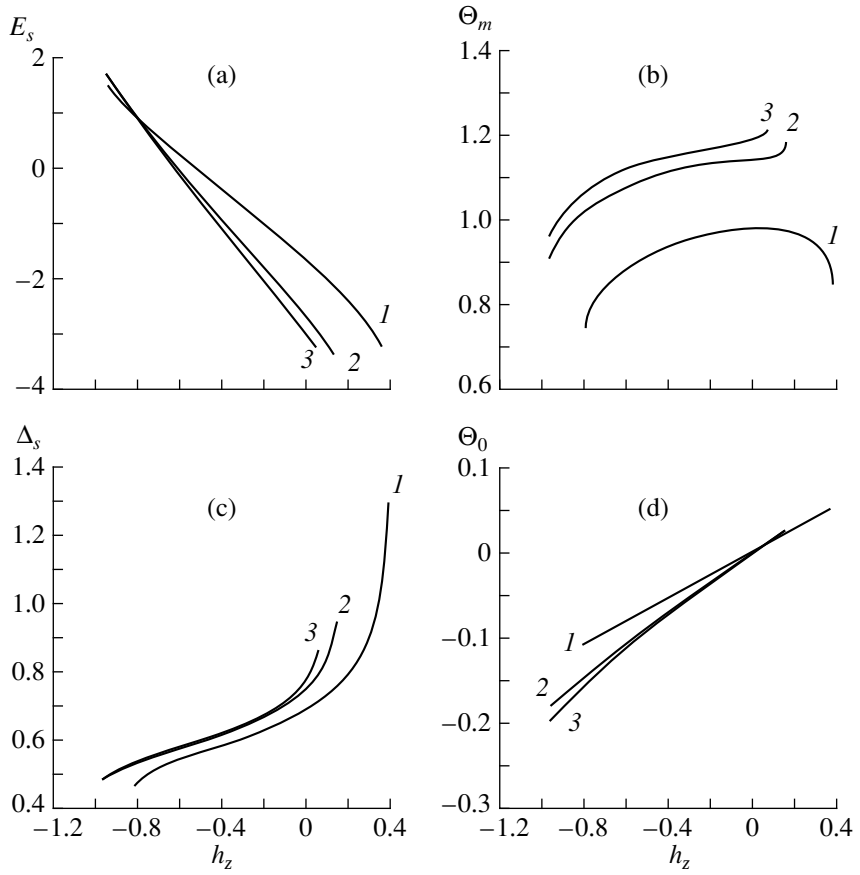

Fig. 5. SS parameters vs. field for the same material parameters as in Fig. 4. Q = (*1*) 1, (*2*) 5, and (*3*) 30.

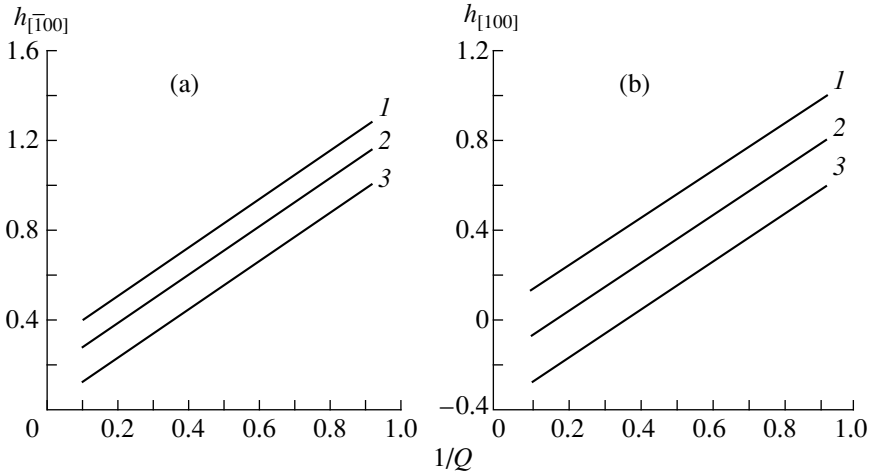

Fig. 6. SS nucleation field vs. Q^{-1} for $\Delta_0 = 0.15$, $D = 12$, $\xi = 0$, $\Delta\kappa_u = -1$. (a) $\Delta\kappa_1 = 2.7$ and l = (*1*) 1.0, (*2*) 1.3, and (*3*) 3.4; (b) $l = 3.4$ and $\Delta\kappa_1$ = (*1*) 2.7, (*2*) 2.8, and (*3*) 2.9.

In both cases, the magnet passes to the homogeneous state with **M** making an angle $\Theta = \pi/2 - \Theta_0$ with the field.

DISCUSSION

Based on the obtained results, we can conclude that magnetic inhomogeneities with various polarizations or deviations of the vector **M** from the (001) plane behave in a different manner when the external field is applied. In this sense, they can be thought of as nuclei of magnetization reversal [10], which correspond to various magnetization distributions near a defect with respect to the magnetic field. Static solitons, all spins of which (or the spins in their central region) make an

obtuse angle with the **H** direction, represent reversed domains originating at defects [11] when the field diminishes from the saturation state.

The critical (collapse or diffusion) fields of SS correspond to the fields of nucleation of reversed domains in our case. This is readily illustrated in Fig. 6, where the plots constructed for various values of the material parameters are straight lines. Analytically, they can be represented as

$$h_c = \alpha + \beta/Q, \tag{11}$$

where α and β are constants related to the material parameters.

With regard for the field sense and using the explicit form for h, one can rewrite expression (11) as

$$H_c = -\left(\alpha\frac{2K_u}{M_s} + 4\pi\beta M_s\right). \tag{12}$$

Thus, we have obtained the empirical formula for critical fields that coincides with the expression for coercive force obtained in [11]. It should be noted that a similar expression for coercive force was derived within the linear theory [12] that includes nucleation at defects. Specifically, it follows from this theory that the coefficient α varies in direct proportion with ΔK_u and ΔK_1 and is inversely proportional to the defect width. This is consistent with the results shown in Fig. 6. The empirical coefficient α decreases with increasing l (Fig. 6a) and grows with $\Delta\kappa_1$ (Fig. 6b). Also, the coefficient β is virtually independent of the material parameters and defect characteristics, being also equal to $\approx$1.1. It was noted [12] that empirical expression (12) for H_c can to some extent resolve "Brown's paradox" [11], since α can be arbitrarily small. Using appropriate averaging over defect sizes, ΔK_u, and ΔK_1, one can obtain coercive force values that agree with experimental data.

In this respect, [12, 13], where nucleation fields in uniaxial ferromagnets are studied in terms of the linear theory, are of interest works. The adopted model considers solitary magnetic inhomogeneities localized on defects. Their magnetization distribution coincides with that in null DWs. The relationships for H_c obtained in these articles correlate with ours and agree well with experimental data for Ni–Fe–B and Sm–Co uniaxial ferromagnets. Although these materials are magnetically hard ($K_u \gg 2\pi M_s^2$), the model of [12, 13] does not include the demagnetizing fields. In this respect, it differs substantially from the model in [14] and our model.

CONCLUSION

Magnetic inhomogeneities originating at defects are responsible for the magnetization of real crystals to the greatest extent. Their properties essentially depend on the material parameters, defect properties, and the strength and direction of the magnetic field. Our variational model, while somewhat limited, shows that SS whose spins (or some of the spins) make an obtuse angle with the field may be thought of as reversed domains. The critical (collapse or diffusion) fields of these SS define the coercive force of magnetic materials. This parameter specifies the magnetic performance of magnets and is very important for applications.

REFERENCES

1. A. B. Dichenko and V. V. Nikolayev, J. Magn. Magn. Mater. **53**, 71 (1985).
2. V. V. Fedotova, A. P. Ges', and T. A. Gorbachevskaya, Fiz. Tverd. Tela (St. Petersburg) **37**, 2835 (1995) [Phys. Solid State **37**, 1563 (1995)].
3. V. K. Vlasko-Vlasov, L. M. Dedukh, M. V. Indenbom, and V. I. Nikitenko, Zh. Éksp. Teor. Fiz. **84**, 277 (1983) [Sov. Phys. JETP **57**, 159 (1983)].
4. R. M. Sabitov and R. M. Vakhitov, Izv. Vyssh. Uchebn. Zaved., Fiz. **31**, 51 (1988).
5. A. Hubert, *Theorie der Domanenwande in geordneten Medien* (Springer, Berlin, 1974; Mir, Moscow, 1977).
6. R. M. Vakhitov and V. E. Kucherov, Fiz. Tverd. Tela (St. Petersburg) **40**, 1498 (1998) [Phys. Solid State **40**, 1360 (1998)].
7. V. V. Randoshkin and A. Ya. Chervonenkis, *Applied Magneto-optics* (Énergoatomizdat, Moscow, 1990).
8. E. Bruce, Bernacki, Te-ho Wu, and M. Mansuripur, J. Appl. Phys. **73**, 6838 (1993).
9. R. M. Vakhitov and V. Ye. Kucherov, in *Abstracts of Moscow International Symposium on Magnetism, Moscow, 1999*, p. 172.
10. I. A. Privorotskiĭ, Usp. Fiz. Nauk **108** (1), 43 (1972).
11. W. F. Brown, *Micromagnetics* (Interscience, New York, 1963; Nauka, Moscow, 1979).
12. H. Kronmüller, Phys. Status Solidi B **144**, 385 (1987).
13. A. Sakuma, S. Tanigawa, and M. Tokunaga, J. Magn. Magn. Mater. **84**, 52 (1990).
14. A. Sakuma, J. Magn. Magn. Mater. **88**, 369 (1990).

Translated by V. Isaakyan

Technical Physics, Vol. 45, No. 11, 2000, pp. 1447–1451. Translated from Zhurnal Tekhnicheskoĭ Fiziki, Vol. 70, No. 11, 2000, pp. 74–79.

SOLIDS

Pressure-Induced Increase in the Ionic Conductivity of Li, Na, and K Zeolites of Type A

R. A. Secco*, M. Rütter*, and Y. Huang**

** Department of Earth Sciences, University of Western Ontario, London, Ontario, N 6A 5B7 Canada*
E-mail: secco@julian.uwo.ca
*** Department of Chemistry, University of Western Ontario, London, Ontario, N 6A 5B7 Canada*
E-mail: yhuang@julian.uwo.ca

Received January 26, 2000

Abstract—The effect of pressure on the ionic conductivity of hydrated A-zeolites containing Li, Na, and K cations was investigated. Room-temperature experiments at pressures to 4.8 GPa show an increase in the conductivity, which attains its maximum value in the range of 1.7–1.8 GPa for the three zeolites. Further compression leads to a drastic decrease in the conductivity at 2.5–3.5 GPa. The decrease in the conductivity is associated with the pressure-induced transition to the amorphous state, as follows from previously reported IR spectroscopy data. It is believed that the increase in the conductivity with pressure and the subsequent transition to the amorphous state follow one or several of the following mechanisms: (1) cation conductivity involving hydroxyls, (2) hydroxyl–proton conductivity, and (3) enhanced cation mobility due to pressure-induced change in the degree of hydration. With decreasing pressure, the conductivity does not follow the compression curve. For pressure-cycled samples, the low-pressure conductivity during decompression is two orders of magnitude higher than its value at the same pressure during compression. Compression provides a new way for conductivity optimization in hydrated A-zeolites. © *2000 MAIK "Nauka/Interperiodica".*

INTRODUCTION

Zeolites belong to the class of framework aluminosilicates with the structure composed of TO_4 (T = Si, Al) units [1]. The TO_4 units form a three-dimensional spatial network consisting of interconnected channels and cavities. Such a structure with open channels and cavities allow zeolites to be used in the industry as ion exchangers, molecular sieves, and catalysts. The Al tetrahedra have negative charge, and cations provide the electroneutrality of the structure. The ability of the cations to diffuse through the open zeolite structure makes possible the high conductivity of the material and its use as solid electrolytes in electrochemical devices. Much effort has been made in the past three decades to reveal factors that control ion transport in an external electric field [2]. The studies were concentrated mainly on the insulating properties of the material and the effect of temperature, water content, and cation nature on the conductivity and dielectric properties. However, little is known about the influence of high pressure on the zeolite structure and ion transport. Recently, we have investigated the conductivity of hydrated Na A-zeolite as a function of pressure [3] and showed evidence for its pressure-induced amorphization. In this work, the effect of pressure on the room-temperature ionic conductivity in hydrated A-zeolites containing Li^+, Na^+, and K^+ cations is reported.

EXPERIMENT

Na A-zeolite was prepared by hydrothermal synthesis from a $SiO_2 : Al_2O_3 : Na_2O : H_2O = 2 : 1 : 5 : 15$ mixture at 80°C for 3.5 h. Li and K A-zeolites were obtained by the conventional ion exchange processes. The zeolites were thoroughly rinsed in distilled water to remove nonstoichiometric cation. The crystallinity and composition of the samples were confirmed by X-ray diffraction analysis (Philips PW1050 and Rigaku Geigerflex CN2029 diffractometers, Cu$K\alpha$ and Co$K\alpha$ radiations, respectively) and X-ray fluorescence analysis (Philips PW1450). In the obtained zeolites, the concentration ratio was M : Si : Al (M = Na, Li, or K) = 1 : 1 : 1. Prior to experiments, every zeolite powder was kept over a saturated NH_4Cl solution at room temperature for several days to provide complete hydration. High-pressure experiments were carried out in a 200-t cubic anvil–press [4], and pressure was calibrated using the known transition points of the Bi, Ti, and Ba standards. Each compacted powder sample was contained in a cylindrical boron nitride container with platinum electrodes at each of the sample ends (the electrode diameter and thickness were 1 and 0.4 mm, respectively). The container was placed in a pyrophyllite cell. To eliminate surface conductivity, the samples were surrounded by a grounded platinum guard ring. The conductivity was measured at the frequency 1 kHz with an LCR meter (Stanford Research SR720). Diffraction analysis

1063-7842/00/4511-1447$20.00

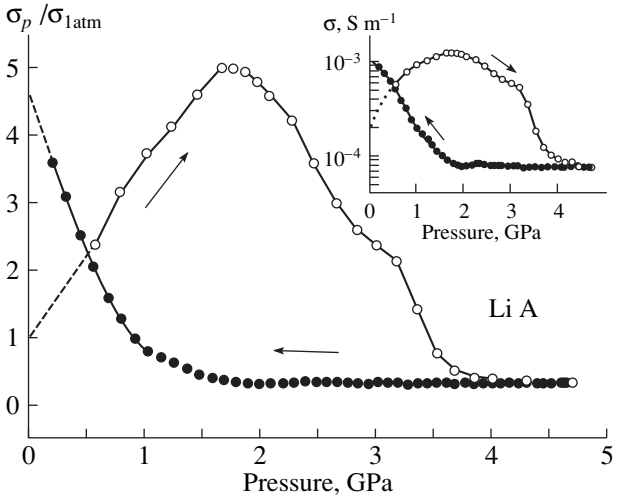

Fig. 1. Relative (normalized by the 1-atm value) ionic conductivity of the hydrated Li A-zeolite vs. pressure. The insert shows absolute conductivity.

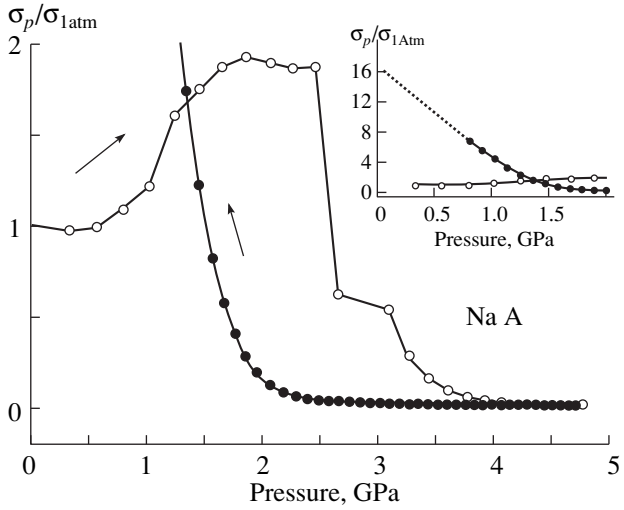

Fig. 2. The same as in Fig. 1 for the Na A-zeolite. The insert shows the low pressure range to illustrate that the conductivity increases when the pressure is reduced.

of samples exposed to high pressures was performed at a pressure of 1 atm and 22°C.

RESULTS AND DISCUSSION

Figures 1–3 demonstrate the pressure dependence of conductivity for the Li, Na, and K A-zeolites. The data are reduced to the conductivity value at 1 atm obtained by extrapolation. Since the aim of this work was to appreciate the effect of pressure on the structure (the very fact of this effect was confirmed macroscopically by *in situ* measurements of the conductivity), the samples were ground for X-ray diffraction analysis immediately after the high-pressure experiments. The conductivity of the samples at 1 atm was not measured. The insert in Fig. 1 shows the run of the initial conductivity value for the Li A-zeolites. The behavior of the curves is similar for all three zeolites. At low pressures, the conductivity grows with pressure, reaching the maximum. The peaks lie in the range of 1.7–1.8 GPa for all the curves, that for the Na A-zeolite being the broadest. At intermediate pressures, the conductivity declines and tends to a constant value at high pressures. When the pressure decreases, conductivity exhibits hysteresis; its value starts to recover roughly at the pressure of maximum conductivity. As the pressure drops further, the conductivity continues to grow and, at the least (initial) pressure, always exceeds its value at the beginning of the experiment. As follows from the conductivity values extrapolated to 1 atm, the samples subjected to high pressure improve their conductivity.

From the standpoint of simple models, using the concept of free volume, an increase in the conductivity of ionic conductors with pressure looks unusual. Conduction in zeolites is an ionic process and is associated primarily with the mobility of groups of exchangeable cations, which provide electroneutrality within structure cavities [2]. In A-zeolites, extra-framework cations are mobile; it was shown, however, that OH groups and protons produced by hydration add to the conductivity and decrease the energy of activation of conduction due to reduced cation–lattice attraction because of water–cation interaction [5]. It can be expected that the effect of pressure on the conductivity of ionic conductors is similar to its effect on volume. Many previous experiments showed that the conductivity drops with increasing pressure in many ionic conductors [6]. Therefore, it could be predicted that, in zeolites, applied pressure will decrease the volume and ionic mobility. As a result, the conductivity will be reduced due to the first-order effect. For hydrated zeolite samples, the second-order effects (pressure-induced conductivity changes such as in cation–lattice and cation–water bonding) may also be significant. The pressure of amorphization of the Li A-zeolite is observed at the same pressure of maximum conductivity. Therefore, an increase in the conductivity with pressure in hydrated Na A-zeolite was discussed with regard to the pressure-induced transition to the amorphous state of Li A-zeolite at 1.8 GPa [3, 7]. Although the water content after the high-pressure experiments was not checked, we do not suspect water losses during the experiments, relying on the conductivity behavior described below. In water-containing zeolites, conduction is positively correlated with water content (because of the reasons discussed above) and also to an additional contribution from hydroxyl and proton conduction [8]. We suggest that mechanisms underlying conductivity increase are one or several of the following: (1) increase in cation mobility due to OH conductance by the "vehicle" mechanism [8], (2) increase in hydroxyl–proton conductivity, and (3) enhanced mobility of hydrated cations due to pressure-induced change in the degree of hydration. In the

recent theoretical work [9], considering the molecular dynamics of hydrated Na A-zeolite with the flexible lattice, it was shown that, at 1 atm, a Na^+ ion is bonded to two or three water molecules on average. In general, applied pressure increases the coordination number of ions, which suggests a rise in the cation hydration with pressure. This leads to the formation of larger and possibly less mobile cation complexes (such as $[M(H_2O)_4]^+$), which can be compensated for by stronger screening between the cation M^+ and lattice. Conversely, a decrease in the cation hydration would result in smaller cation complexes (e.g., $[M(H_2O)]^+$) and enhanced cation–lattice interaction.

To verify such considerations, we performed two series of experiments. In the first, high-pressure cycling was applied to the K A-zeolite to see how repeat pressure cycles affect the conductivity. In Fig. 4a, a monotonous drop in the conductivity at the second compression cycle is the expected effect for the case when the free volume of ion transport is controllably changed in a material with unaffected crystal structure. That no sign of the pressure-induced transition to the amorphous state is seen at this stage means incomplete recovery of the crystal structure after the first return to 1 GPa. This interpretation is supported by IR spectra [7] and X-ray diffraction data for the samples subjected to high pressure. However, at the second decrease in pressure, the conductivity enhancement factor (CEF) attains ~90; in other words, the conductivity rises roughly by two orders of magnitude in comparison with the initial value. The higher CEF after the second cycle is also seen in Fig. 3. This may mean that the pressure-induced change in the cation hydration is irreversible. The retention of high-mobility species in the material that partially returned to the crystalline state with decreasing pressure locks in the high conductivity characteristics of the high-pressure preamorphous state. If the samples exposed to high pressure do retain high conductivity (which must be checked by measuring the conductivity at 1 atm), this means that compression opens a new way to optimize the conductivity of hydrated A-zeolites. This may be useful for applications.

In the other series of experiments, the maximum pressure of the first cycle was lower than that at the conductivity peak. The conductivity increases during the first compression and decreases more slowly when the pressure drops for the first time (Fig. 4b). At the second pressure rise, the conductivity continues to tend to its maximum, as was observed in the one-cycle experiments. At the second pressure drop, the conductivity also behaves as in the one-cycle experiments.

The fact that the pressure of maximum conductivity coincides with that of transition to the amorphous state poses the question as to whether water strengthens the zeolite network. In this context, it is of interest to consider the position of H_2O molecules that was determined by molecular dynamics simulation [9] for 1 atm.

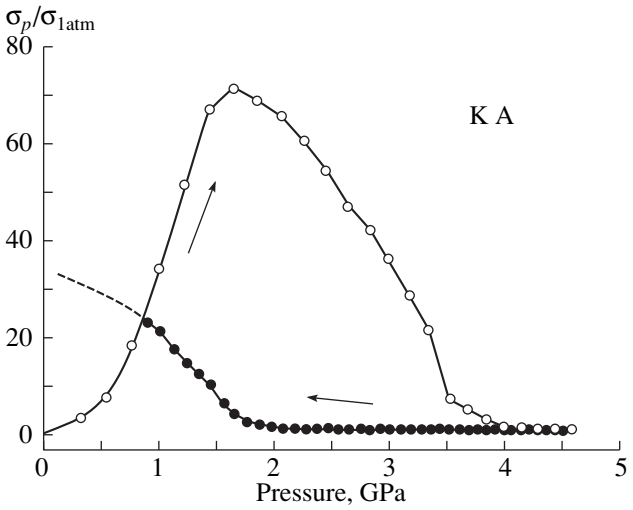

Fig. 3. The same as in Fig. 1 for the K A-zeolite.

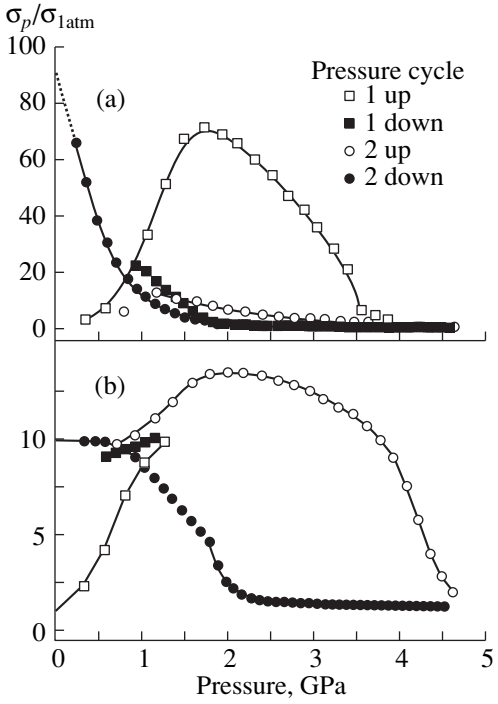

Fig. 4. The same as in Fig. 3 on pressure cycling K A-zeolite. The maximum pressure on the first cycle is (a) 4.6 and (b) 1.3 GPa.

Molecular water is contained in wide α cavities and can move inside and between them. α cavities of each unit cell contain more 20 water molecules. In [9], the mean population of water molecules per unit cell was estimated at 24.25, while in [10], the value obtained by X-ray diffraction analysis was found to be 22.9. Molecular dynamics simulation demonstrates that hydrogen atoms are, in general, closer to the cavity walls than oxygen atoms of the water. Water molecules can migrate not only between the α cavities but also

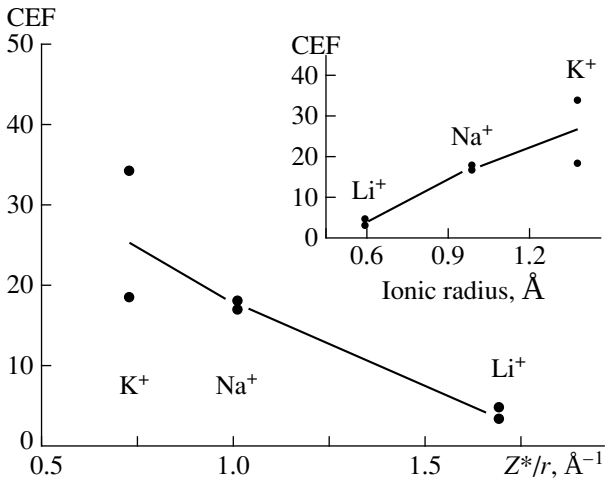

Fig. 5. Conductivity enhancement factor (CEF) vs. cation charge-to-radius ratio for the Li, Na, and K A-zeolites. The CEF values are obtained from the first cycle results (as for the data in Figs. 1–3, 5). The insert shows the CEF vs. cation radius dependence.

between characteristic regions within a cavity. The regions in which 90% of water molecules stay most of the time lie at a distance of 3 to 6 Å from the cavity center. Hence, within a cavity there exists an approximately spherical space of radius 3 Å where the water content is low. This means that water molecules in the α cavities are "arranged" in such a way that most of the oxygen atoms are close to the center of a cavity. Under low pressure, such an orientation (with a negative space charge present at the cavity center) results in electrostatic repulsion, which improves the resistance of the zeolite network to compression. A decrease in the volume with growing pressure causes stronger repulsion (the electrostatic repulsive force varies as the inverse square of distance). However, at high pressures, the cavity begins to shrink possibly because of the dynamic nature of water molecule arrangement and unstable (asymmetric) charge distribution. If this strengthening mechanism is valid, the networks of all the totally hydrated A-zeolites studied in this work must shrink at similar pressures [9], which is the case. This hypothesis will be verified further in experiments with water-free A-zeolites, and the simulation of molecular dynamics in high-density hydrated A-zeolite would provide a clear idea of the issue in question.

The conductivity gain at 1 atm vs. pressure is shown in Fig. 5 as the dependence of CEF on the cation charge-to-radius ratio and cation size. If the CEF depended on the ion size only, the CEF vs. ion radius curve would run inversely to that shown in the insert in Fig. 5. The observed dependence of CEF on ion radius in the series of isovalent cations can be explained only if cation–lattice interaction is taken into account. The larger K^+ cation interacts with the zeolite network more weakly than the smaller Li^+ cation because of the lower polarization energy of the former. This follows from the data in Fig. 5, which shows the expected change in the CEF slope with decreasing polarizability. This is consistent with the above assumption that applied pressure increases the degree of hydration. Further experiments with extra-framework cations Rb^+ and Cs^+ will have to answer the question as to whether higher values of CEF can be attained. The trend observed for the three cations studied in this work may however not be followed by Rb^+ and Cs^+ because of steric hindrances.

CONCLUSION

The effect of pressure on the ionic conductivity of hydrated zeolites that contain Li, K, and Na cations to conserve electroneutrality is complicated because of the presence of water. At pressures to ~1.7 GPa, the elevated conductivity may be associated with the hydroxyl-related cationic conductivity, hydroxyl–proton conductivity, and/or a change (possibly increase) in the cation hydration with the formation of more mobile species. At high pressures, the conductivity drops because of the pressure-induced transition to the amorphous state and, hence, the disappearance of cavities and channels where the cations can move. When the pressure is reduced, the conductivity trend on compression is not recovered. After several compression/decompression cycles, the low-pressure conductivity is two orders of magnitude higher than its initial value, as follows from the pressure cycling data. The obtained results indicate that the conductivity of hydrated A-zeolites can be optimized by applying pressure in the appropriate range. This can be useful for applications.

ACKNOWLEDGMENTS

We are grateful to R. Tucker for the preparation of high-pressure cells.

This work was supported by the grants of the Natural Sciences and Engineering Research Council of Canada to R.A. Sekko and YH.

R.A. Sekko gratefully acknowledges the Alexander von Humboldt Foundation for financial support in the form of fellowship and members of the Bayerisches Geoinstitut for their generous hospitally during the writing of the manuscript.

REFERENCES

1. *Introduction to Zeolites Science and Practice*, Ed. by H. van Bekkum, E. M. Flanigen, and J. C. Jansen (Elsevier, Amsterdam, 1991).
2. J. M. Kalogeras and A. Vassilikou-Dova, Cryst. Res. Technol. **31**, 693 (1996).
3. R. A. Secco and Y. Huang, J. Phys. Chem. Solids **60**, 999 (1999).
4. R. A. Secco, Can. J. Phys. **73**, 287 (1995).

5. D. N. Stamires, J. Chem. Phys. **35**, 3174 (1962); F. J. Jansen and R. A. Schoonheydt, in *Advances in Chemistry Series*, Ed. by W. M. Meier and J. B. Uytterhoeven (American Chemical Society, Washington, DC, 1973), Vol. 121, p. 96.
6. P. C. Allen and P. C. Lazarus, Phys. Rev. B **17**, 1913 (1978); G. A. Samara, Phys. Rev. B **23**, 575 (1981); R. A. Secco and E. A. Secco, J. Phys. Chem. Solids **53**, 749 (1992); K. M. Ault and R. A. Secco, Solid State Ionics **89**, 37 (1996); R. A. Secco and E. A. Secco, Phys. Rev. B **56**, 3099 (1997); R. A. Secco, E. A. Secco, and Q. Chen, Solid State Ionics **110**, 283 (1998).
7. Y. Huang, J. Mater. Chem. **8**, 1067 (1998).
8. E. Krogh Anderson, J. G. Krogh Anderson, and E. Skou, in *Chemistry of Solid State Materials*, Ed. by P. Colomban (Cambridge Univ. Press, Cambridge, 1992), Vol. 2.
9. D. A. Faux, W. Smith, and T. R. Forester, J. Phys. Chem. **101**, 1762 (1997).
10. V. Gramlich and W. M. Z. Meier, Z. Kristallogr. **133**, 134 (1971).

Translated by V. Isaakyan

Technical Physics, Vol. 45, No. 11, 2000, pp. 1452–1456. Translated from Zhurnal Tekhnicheskoĭ Fiziki, Vol. 70, No. 11, 2000, pp. 80–85.

SOLID-STATE ELECTRONICS

The Formation and Thermal Stability of Multilayer Ohmic Contacts to *n*-GaAs with TiB_x and Mo Diffusion Barriers

V. V. Milenin*, R. V. Konakova*, V. N. Ivanov, G. V. Beketov*, V. I. Poludin*, and I. B. Ermolovich***

** Institute of Semiconductor Physics, National Academy of Sciences of Ukraine, Kiev, 252028 Ukraine*

*** Orion State Research Institute, Kiev, Ukraine*

Received October 26, 1999

Abstract—Thermal degradation of Au/Mo/TiB_x/AuGe multilayer ohmic contacts with Mo and TiB_x diffusion barriers was studied. The contacts were employed in Gunn-effect diodes. Depth profiling of the components in the contacts was performed using Auger electron spectroscopy. The microrelief of the metal/semiconductor interface and contact surface morphology were examined with atomic force microscopy and scanning electron microscopy, respectively. The measurements were taken before and after argon annealing at T = 400, 600, or 800°C for 60 s. The resistance of the Gunn diode mesa was also measured. Annealing at 400°C is shown not to affect the sandwich structure of the contacts. Annealing at 600°C causes structure rearrangement in the layers up to cracking. It is found that the thermal threshold of degradation of the Au/Mo/TiB_x/AuGe/GaAs structure depends on the resistance of the TiB_x layer to thermal effects. Reasons for the degradation of Mo and TiB_x antidiffusion properties are discussed. *© 2000 MAIK "Nauka/Interperiodica".*

INTRODUCTION

It is well known that the performance of GaAs devices (frequency range, noise level, gain, etc.) depends essentially on the properties of ohmic contacts to the semiconductor (junction resistance as well as structure and phase homogeneity at the interfaces). Therefore, the effect of various process factors on the properties of ohmic contact systems on GaAs has been the subject of much investigation [1–6]. Yet, the production of low-resistance thermally stable ohmic contacts (OCs) to *n*-GaAs that offer linear current–voltage characteristic remains a challenge. Reasons for the structural inhomogeneity and, hence, thermal degradation of OCs are as follows: (1) The formation of high-resistivity (often unstable) intermetallic compounds at the interface, (2) diffusion mixing of contact materials at the interface, which causes the extension of the transition layer and compensation of the near-contact GaAs region, and (3) the formation of extended (on the order of the active layer thickness) alloying regions (irregular protrusions) at the metal/semiconductor (M/S) interface [7].

The first and partly third reasons can be eliminated by using transition metals and their high-temperature alloys for the metallization layers. The validity of such an approach was indicated in [8]. Mo/Ge, Ta/Ge, and TiW/Ge contact structures were found to retain their composition and microstructure at annealing temperatures of up to 350°C. Ge/Mo/Ge/W multilayer compositions subjected to special heat treatment in the InAs vapors offer still higher thermal stability [9].

However, the disadvantage of the above metallization systems is metal–arsenic solid-phase reactions, which reduce the thermal stability of the contacts (reasons 1 and 2). Reason 2 can be avoided if an additional layer of a thermally stable inactive compound is introduced into the metallization. As such layers, films of transition metal borides can be employed. Along with antidiffusion properties, they have a low resistivity [10], which is essential for OC metallization.

The aim of this work is to study the thermal degradation of multilayer OC metallizations with a TiB_x diffusion barrier.

EXPERIMENTAL TECHNIQUE

Ge, Au, TiB_x, and Mo were successively magnetron-sputtered in argon (5×10^{-3} torr) to form (1800 Å)Au/(200 Å)Ge/(1000 Å)TiB_x/(200 Å)Mo/(3000 Å)Au OCs. Prior to sputtering, the GaAs surface was subjected to photon cleaning. To make the contacts ohmic, the metal structure was annealed at 500°C in a hydrogen flow. To study the thermal stability of the contacts, they were subjected to additional short-term (60 s) heat treatment at 400, 600, or 800°C.

Processes taking place during the formation and thermal degradation of the contacts were analyzed with layer-by-layer Auger electron spectroscopy (AES), scanning electron microscopy (SEM), and atomic force microscopy (AFM) [11, 12].

1063-7842/00/4511-1452$20.00 © 2000 MAIK "Nauka/Interperiodica"

RESULTS AND DISCUSSION

The table lists the measured resistances of the Gunn-effect diode mesa having contacts prepared according to the above technique at various temperatures and times of hydrogen annealing.

It is seen that the contacts form at temperatures near 500°C and annealing times ≥30 s. Electron microscopy studies of the contact cross sections showed that OCs formed under these conditions have a continuous and relatively uniform alloying front at a depth of ≅2000 Å.

Figure 1 shows profiles of the contact components before and after the heat treatments. Since profile "distortions" depend on the character of interlayer interaction, we can separate factors that govern the OC behavior upon varying heat treatment conditions.

At annealing temperatures ≤400°C, the layered structure of the contacts is retained. No marked redistribution of the contact components and formation of intermetallic compounds at the interfaces are observed. The properties of the contacts depend largely on the completeness of the reaction between Au–Ge and GaAs, which is due to short-term annealing at ~500°C for 60 s.

With regard for the fact that the weight percentages of Au and Ge were taken in such a way as to prevent eutectic formation, metal–semiconductor interaction is limited by interdiffusion of the GaAs constituents and gold. At the annealing temperature, the contact metallization melts in areas where the Au–Ga(As) composition is eutectic. Upon cooling, Au–Ga, Au–Ge, and Au–GaAs phases precipitate in the transition layer of the contact [3, 6] and the interface attains granular structure (Fig. 2). The amounts and structures of the precipitated phases depend on annealing temperature, cooling rate, and contact preparation conditions [3, 4].

The selective absorption of Ga by the metallization makes possible its substitution by Ge atoms in the GaAs near-surface region. In this case, an n^+-layer formed on the GaAs surface provides low contact resistance.

During subsequent annealing (400°C) of the contact thus formed, the reactions at the interface with the semiconductor are completed and Au and Ge penetrate deeper into the GaAs lattice. The layered structure of the contact is retained, and the M/S interface morphology is further modified due to melting of the contact metallization in microareas where the reactions have not come to an end after short-term annealing (Fig. 2).

The persisting surface roughness (Fig. 2) substantiates this supposition. Annealing at 600°C does not result in the breakdown of the layered structure of the contact, but the antidiffusion properties of Mo and TiB_x are adversely affected. As a result, the Au atoms from the metallization reach the M/S interface and the Ga and As atoms penetrate deeply into the metallization. However, the electrical parameters of the contacts change insignificantly (see table). With the resistance

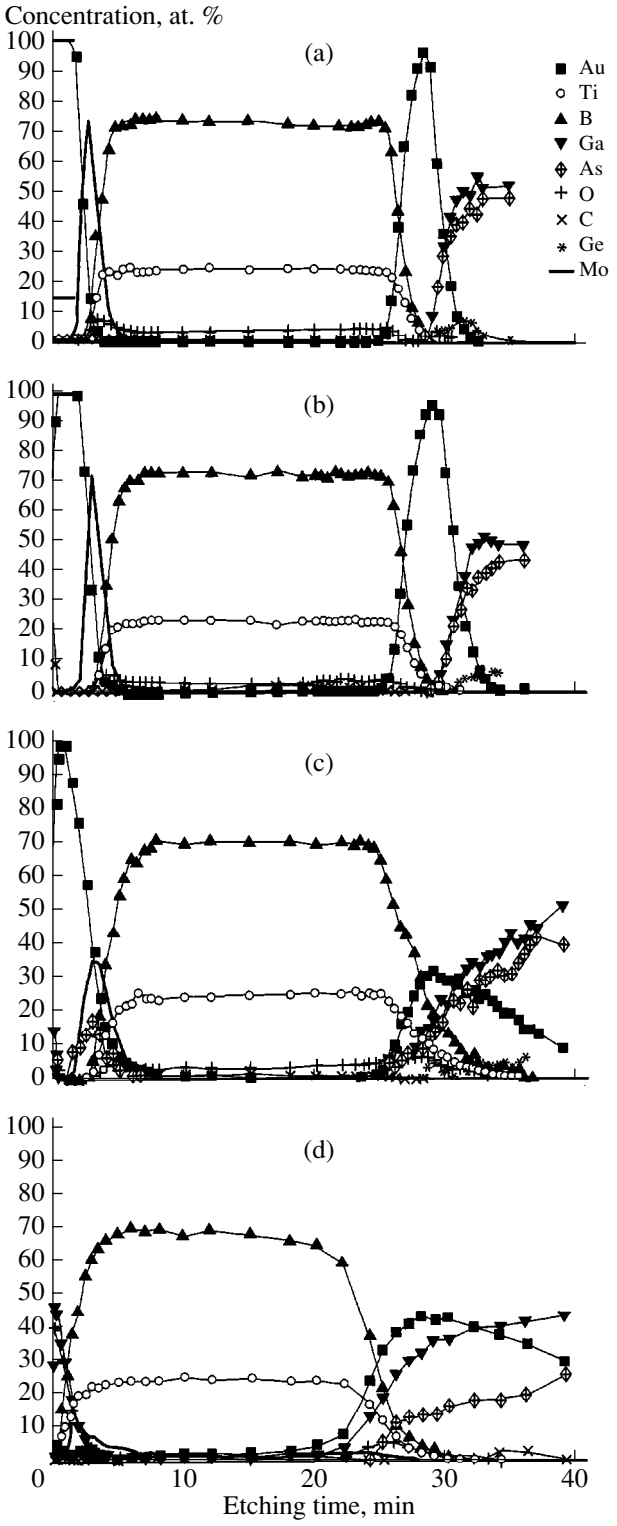

Fig. 1. Component profiles in the Au/Mo/TiB_x/Au–Ge/GaAs structure: (a) initial and (b) after annealing at 400, (c) 600, and (d) 800°C in argon for 60 s.

of the contacts remained unchanged and general layered structure being retained, such redistributions of the Au, Ga, and As atoms can be associated with local rear-

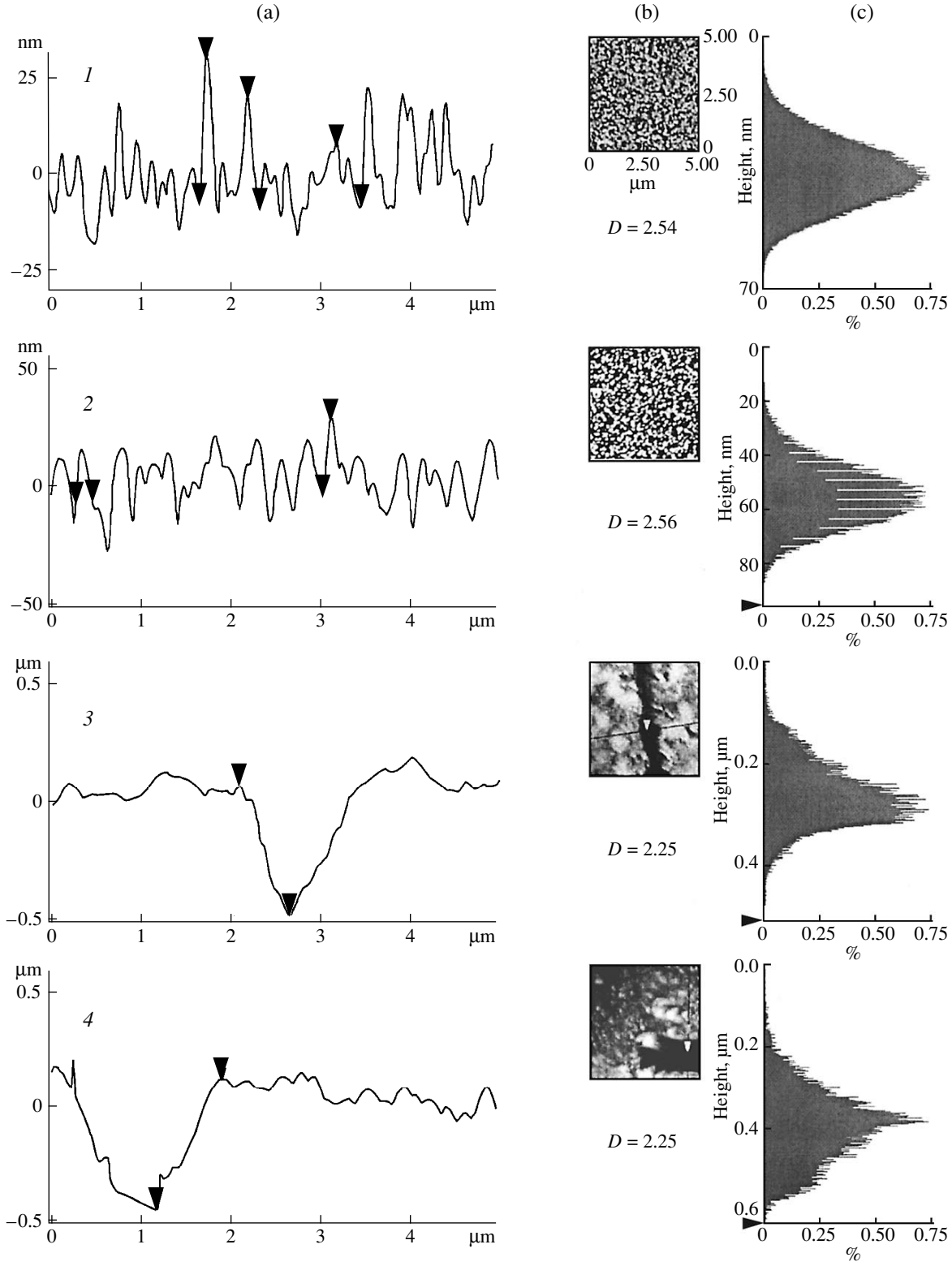

Fig. 2. Microrelief of the M/S interface (the metal is etched off) for various annealing conditions (see the caption to Fig. 1). (a) Surface roughness along the line shown in (b) and (c) roughness histogram. *D* is the fractal dimension.

rangements in the contact structure. Indeed, SEM data shown in Fig. 3 imply that the contact structure undergoes marked modifications after annealing at 600°C. The basic feature of this structure rearrangement is local cracking of the metal overlayers. As a result, channels arise in the film coating, and the GaAs constit-

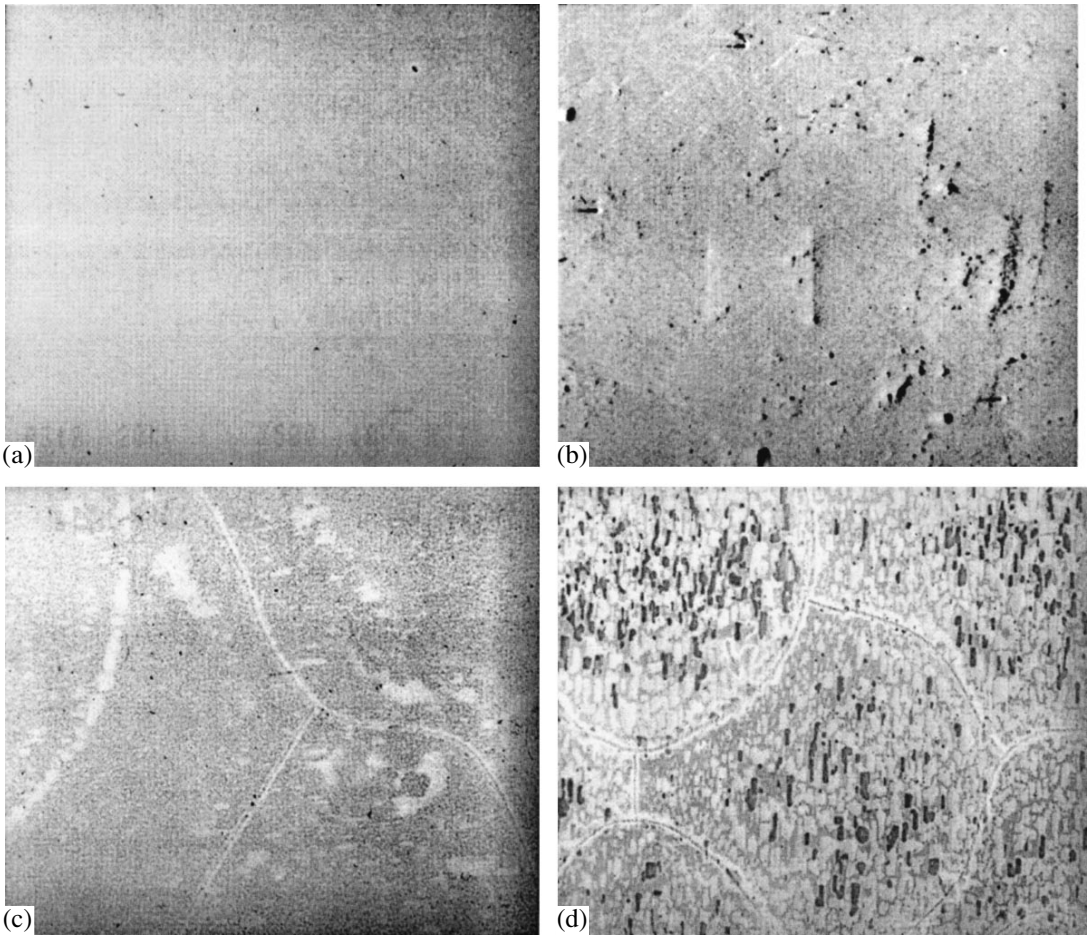

Fig. 3. SEM image of the Au/Mo/TiB_x/AuGe/GaAs contact structure (×500 magnification) for various annealing conditions (see the caption to Fig. 1).

uents can penetrate deeply into the metallization (Fig. 1). The thermal decomposition of GaAs favors this process. Intense interaction of Ga with the Au atoms, as well as the buffer properties of the molybdenum film, slows down the migration of the Au atoms toward the interface.

Annealing at 800°C causes dramatic transformation of the layered structure of the contacts. In this case, as follows from Fig. 1, the TiB_x layer totally loses its barrier properties, and the concentration of gold coming to the M/S interface sharply increases. This, in turn, enhances phase formation in the contacts. The dominant phases here may be Au_2Ga, Au_7Ga_2 [3], and possibly stable Ga, Ti, and B oxides [13]. Resulting crystallization microdefects make the interface rough and irregular, as evident from Fig. 2. The topographic inhomogeneity of the surface does not obey the Gaussian distribution. This means that activation processes at the interfaces play an essential role. Under such conditions, chemical reactions between the contact components and thermal decomposition of the semiconductor substrate are responsible for the interface microrelief.

The presence of various phases and resulting interface roughness adversely affect the electrophysical properties of the contacts. The reasons are increasing doping inhomogeneity of the semiconductor surface and the extended layer of complex composition that forms between the contact layers. In addition, AES data did not detect Ge atoms in both the metallization and near-contact region of the semiconductor. Sinks responsible for Ge atom localization have remained unclear. All the above factors cause the contact resistance to grow sharply (see table).

Thus, the thermal threshold of OC degradation depends on the TiB_x resistance to temperature effects. A low activation energy of Ga diffusion (≤0.3 eV) that was calculated with experimental data in Fig. 1 also favors the mechanism of contact degradation. As was mentioned (Fig. 3), contact degradation starts locally and appears as pores and cracks. We will note three sources of TiB_x local breakdown.

(1) Microcracks in the contact metallization due to structure relaxation during annealing. It is known that magnetron-sputtered films possess high internal compression stresses [14]. Nanometer grains and the disor-

The effect of temperature and annealing time on the diode resistance

T°, C (60 s)	R, Ω	Time, s (T = 500°C)	R, Ω
460	47	6	19.6
500	2.3	30	2.8
550	2.6	60	2.8
600	2.8	120	2.8
650	7.3	1800	2.8

dered atomic structure of the intergranular space, which is much larger than the grain volume, may substantially change the elastic properties of a material and structure relaxation mechanisms. Currently available information on the mechanical properties of TiB_x layers and the effect process factors have on them is scarce and contradictory. Therefore, there is no consensus of opinion regarding structure relaxation mechanisms in the objects under study. Only a qualitative correlation between the microstructure and strained state of the film has been found.

(2) Reactions between the contact metals and TiB_x. These may proceed primarily on disordered grain boundaries. Locally proceeding elevated-temperature reactions may promote pore formation in the TiB_x films, thus initiating cracking.

(3) A decrease in the corrosion resistance of the layers with increasing annealing temperatures. At moderate temperatures, amorphous films of titanium boride react with oxygen to form TiO_2 and B_2O_3 [15]. The former compound is volatile and leaves the contact. The formation of the heterogeneous $TiB_x + TiO_2$ composition violates the continuity of the film.

By varying conditions for TiB_x preparation, one can greatly suppress the effect of these sources and obtain contacts with enhanced thermal stability.

In conclusion, note one more interesting feature of the contacts. The case in point is the interface geometry in the structures subjected to various heat treatments. AFM data show that the M/S interface is a fractal [16] with the dimension D = 2.54. The surface roughness and irregularity does not change after annealing at 400°C (D = 2.56). After heat treatment at 600°C, D sharply drops to 2.25 and remains the same after annealing at 800°C. We failed to relate this parameter to physicochemical processes. Yet, it is noteworthy that the jump of fractal dimension coincides with the onset of contact degradation.

CONCLUSIONS

It was shown that TiB_x layers incorporated into the contact structure make the contacts more resistant to thermal effects. Physicochemical reasons responsible for the degradation of the OCs to GaAs during high-temperature annealings were analyzed. The degradation model for the contacts with TiB_x as a diffusion barrier was suggested.

ACKNOWLEDGMENTS

This work was supported by the Research Center of Ukraine (project no. 464).

REFERENCES

1. V. I. Strikha, G. D. Popova, and E. V. Buzaneva, Poluprovodn. Tekh. Mikroélektron. **20**, 20 (1975).
2. N. Braslau, Thin Solid Films **104**, 391 (1983).
3. B. A. Lapshinov, A. V. Kamlev, L. N. Kravchenko, and V. L. Oplesnin, Zarubezh. Élektron. Tekh., No. 5, 58 (1987).
4. *Ion Implantation and Beam Processing*, Ed. by J. S. Williams and J. M. Poate (Academic, New York, 1984; Naukova Dumka, Kiev, 1988).
5. É. B. Kaganovich and S. V. Svechnikov, Optoélektron. Poluprovodn. Tekh. **22**, 3 (1991).
6. Yu. A. Gol'dberg, Fiz. Tekh. Poluprovodn. (St. Petersburg) **28**, 1681 (1994) [Semiconductors **28**, 935 (1994)].
7. V. N. Ivanov, L. E. Kovalenko, T. S. Sumskaya, *et al.*, Élekton. Tekh., Ser. 2: Poluprovodn. Prib. **4** (195), 49 (1988).
8. W. T. Anderson *et al.*, IEEE Trans. Ind. Electron. **ID-29** (2), 149 (1982).
9. M. Murakami, W. H. Price, Y.-C. Shih, *et al.*, J. Appl. Phys. **62**, 3288 (1987).
10. R. A. Andrievskiĭ, Usp. Khim. **66** (1), 57 (1997).
11. V. T. Cherepin and M. A. Vasil'ev, *Methods and Devices for Analyzing Material Surfaces* (Naukova Dumka, Kiev, 1982).
12. G. Binning, C. F. Quata, and C. Gerber, Phys. Rev. Lett. **54**, 930 (1986).
13. T. A. Bryantseva, A. I. Volkov, and G. G. Dvoryankina, Élektron. Tekh., Ser. 2: Poluprovodn. Prib. **3** (119), 40 (1977).
14. J. Chen and S. A. Barnard, Mater. Sci. Eng. A **191**, 233 (1995).
15. D. K. Sood, S. Mukherjee, G. Katselis, *et al.*, Surf. Coat. Technol. **103–104**, 304 (1998).
16. J. Feder, *Fractals* (Plenum, New York, 1988; Mir, Moscow, 1991).

Translated by V. Isaakyan

Technical Physics, Vol. 45, No. 11, 2000, pp. 1457–1461. Translated from Zhurnal Tekhnicheskoĭ Fiziki, Vol. 70, No. 11, 2000, pp. 86–90.

OPTICS, QUANTUM ELECTRONICS

Self-reflection in a Naive Model of Nonlinear Media

K. D. Lyakhomskaya and P. I. Khadzhi

Pridnestrovsk State University, Tiraspol, 278000 Moldova

Received October 13, 1999

Abstract—The optical self-reflection in a naive model of a semi-infinite nonlinear medium is studied theoretically. It is demonstrated that a Fabry–Perot resonator is induced by a propagating wave in the medium if the incident intensity exceeds a critical value. Hysteresis dependences of the reflectivity and the resonator length on the incident intensity are predicted. © *2000 MAIK "Nauka/Interperiodica".*

In passing through a nonlinear medium, laser radiation may considerably change its propagation condition. Recent studies on nonlinear optics have predicted a new phenomenon, namely, self-reflection in a dense medium with saturable absorption under the action of laser radiation, the medium being modeled by a homogeneous system of two-level atoms [1–6]. The spatial distributions of a propagating wave, the refractive index, and the absorption coefficient were numerically analyzed in relation to the incident amplitude and a detuning parameter [1]. It was demonstrated for a semiinfinite medium that a self-reflected wave arises in the region where the nonlinear refractive index exhibits sharp nonuniformity. In [3], the multivalued nature of the reflectivity was predicted. As regards experiments, self-reflection was first observed in a ZnSe crystal [7].

The conventional theory of a stationary self-reflection effect rests on solving the wave equation in which the complex-valued nonlinear permittivity is determined by constitutive relations. The problem is that the slowly-varying-envelope approximation (SVEA) cannot reveal self-reflection, as highlighted in [1–6]. To see this, look at a semiinfinite absorbing nonlinear medium and assume that a forward and a backward wave propagate in it. With the SVEA, the wave equation yields an integral of motion for the wave amplitudes and this integral directly implies that one of the waves must be zero. The forward wave must exist, since it represents the excitation of the medium. Thus, the zero wave is the backward wave, which relates to self-reflection. On the other hand, the nonlinear wave equation defies analytical treatment beyond the SVEA [1–6]. Fundamental difficulties with the second-order nonlinear equation for a complex field amplitude are aggravated by conditions on the crystal front face [1–7]. For this reason, it is wise to consider a nonlinear model of the medium that would both allow for an analytical solution and include self-reflection. In the simplest case, optical properties of the medium are assumed to be step functions of the wave amplitude. This naive practice has been followed using bright and dark solitons [8–11] and surface nonlinear waves [12, 13]. The approach was substantiated for the excitonic spectral region at high excitation levels [14].

Let us investigate self-reflection in terms of the naive model of a semiinfinite nonlinear medium, the complex permittivity being defined as

$$\varepsilon(E) = \begin{cases} \varepsilon_1' + i\varepsilon_1'', & |E| < E_s (I < I_s) \\ \varepsilon_2' + i\varepsilon_2'', & |E| > E_s (I > I_s), \end{cases} \quad (1)$$

where ε_i' and ε_i'' are the real and the imaginary part of ε_i (i = 1, 2), respectively, and $E_s(I_s)$ is the amplitude (intensity) of a propagating wave at which the permittivity switches from one value to the other.

Let a monochromatic electromagnetic wave of amplitude E_0 and frequency ω be normally incident on a plane boundary between a vacuum and the medium. The wave penetrates the medium and propagates there along the x-axis, being partly reflected from the boundary. In the medium, the amplitude distribution $E(x)$ obeys the wave equation

$$\frac{d^2E}{dx^2} + \frac{\omega^2}{c^2}\varepsilon(E)E = 0. \quad (2)$$

Let $E_{0c}(I_{0c})$ denote a critical incident amplitude (intensity) that corresponds to $E(z = 0) = E_s$ $I(z = 0) = I_s$ in the medium. If $E_0 > E_{0c}$ ($I_0 < I_{0c}$), the solution of (2) includes only a forward wave. No backward wave exists because $E(x \longrightarrow \infty) \longrightarrow 0$, the medium being absorbing and semi-infinite. The amplitude of a reflected wave can be found from the condition that the tangential field components are continuous at $z = 0$. Accordingly, the respective intensities of the waves at $E_0 < E_{0c}$ are expressed as

$$I(z) = t_1^2 I_0 \exp(-2q_1 z), \quad I_r = r_1^2 I_0, \quad (3), (4)$$

1063-7842/00/4511-1457$20.00

where

$$t_1 = \frac{2}{\sqrt{(p_1+1)^2+q_1^2}}, \quad r_1 = \sqrt{\frac{(p_1-1)^2+q_1^2}{(p_1+1)^2+q_1^2}},$$

$$p_1 = a_1\cos\left(\frac{\alpha_1}{2}\right), \quad q_1 = a_1\sin\left(\frac{\alpha_1}{2}\right), \tag{5}$$

$$a_1 = (\varepsilon_1'^2+\varepsilon_1''^2)^{1/4},$$

$$\alpha_1 = \arctan\left(\frac{\varepsilon_1''}{\varepsilon_1'}\right), \quad z = \frac{\omega}{c}x.$$

Formula (3) shows that the intensity decreases exponentially in the medium and that the real and the imaginary field components are oscillating functions of the coordinate and have exponentially falling envelopes and a spatial frequency p_1.

Note that, if $0 < I_0 < I_{0c}$, then the reflectivity $R = r_1^2$ is independent of the incident intensity I_0 and is governed by ε_1' and ε_1''. Thus, we deal with the Fresnel reflection from the surface.

As the excitation grows, so does the wave amplitude in the medium. If $I_0 = I_{0c}$, we have $I = I_s$ for $z = 0$. Together with (3), this yields

$$I_{0c} = I_s t_1^{-2}. \tag{6}$$

It follows from (6) and (5) that I_{0c} depends solely on I_s, ε_1', and ε_1''.

If $I_0 \geq I_{0c}$, a region with $I \geq I_s$ forms in the medium. Consequently, $\varepsilon = \varepsilon_2' + i\varepsilon_2''$ throughout the region, whereas the other part of the medium still has $\varepsilon = \varepsilon_1' + i\varepsilon_1''$. The region extends from $z = 0$ to $z = z_s$, where z_s is the point at which $I = I_s$, the value of z_s rising with I_0. Thus, an originally uniform medium takes on a domain that is adjacent to the surface and differs from the other part in optical properties. The domain-interface position $z = z_s$ varies with the excitation level. Both a forward and a backward wave exist in the domain, having stationary field distributions, but only a forward wave exists for $z \geq z_s$. On the other hand, the domain can be regarded as an optically induced Fabry–Perot (FP) resonator with an externally controlled length z_s.

Let us solve equation (2) for the regions $0 \leq z \leq z_s$ and $z \geq z_s$ subject to the condition of tangential-component continuity at $z = z_s$. We thus obtain expressions

$$I(z) = \frac{I_s}{t_{21}^2}\Big\{[\exp(q_2(z_s-z)) + r_{21}\exp(-q_2(z_s-z))]^2 - 4r_{21}\sin^2\left(p_2(z_s-z)+\frac{\Theta_{21}-\Psi_{21}}{2}\right)\Big\}, \quad 0 \leq z \leq z_s, \tag{7}$$

$$I(z) = I_s\exp(-2q_1(z-z_s)), \quad z \geq z_s, \tag{8}$$

for the spatial distribution of the field intensity in the medium.

The reflected intensity is expressed as

$$I_r = \frac{I_s}{t_2^2 t_{21}^2}\Big\{[r_2\exp(q_2 z_s) - r_{21}\exp(-q_2 z_s)]^2 + 4r_2 r_{21}\sin^2\left(p_2 z_s + \frac{\Theta_{21}-\Theta_2+\Psi_2-\Psi_{21}}{2}\right)\Big\}, \tag{9}$$

$$I_0 \geq I_{0c},$$

$$I_r = r_1^2 I_0, \quad I_0 \leq I_{0c}. \tag{10}$$

For z_s at $I_0 \geq I_{0c}$, we have a transcendental equation depending on the excitation level and the parameters of the medium:

$$t_2^2 t_{21}^2 \frac{I_0}{I_s} = [\exp(q_2 z_s) - r_2 r_{21}(-q_2 z_s)]^2 + 4r_2 r_{21}\sin^2\left(p_2 z_s + \frac{\Phi_2+\Phi_{21}}{2}\right), \tag{11}$$

where

$$\Phi_2 = \frac{1}{2}(\Theta_2 - \Psi_2), \quad \Phi_{21} = \frac{1}{2}(\Theta_{21} - \Psi_{21}) \tag{12}$$

are the respective phase steps of the amplitude reflectivities ρ_2 and ρ_{21} for the two interfaces of the domain. Furthermore,

$$\Theta_2 = \arctan\left(\frac{q_2}{p_2-1}\right), \quad \Theta_{21} = \arctan\left(\frac{q_2-q_1}{p_2-p_1}\right),$$

$$\Psi_2 = \arctan\left(\frac{q_2}{p_2+1}\right), \quad \Psi_{21} = \arctan\left(\frac{q_2+q_1}{p_2+p_1}\right),$$

$$p_2 = a_2\cos\left(\frac{\alpha_2}{2}\right), \quad q_2 = a_2\sin\left(\frac{\alpha_2}{2}\right),$$

$$a_2 = (\varepsilon_2'^2+\varepsilon_2''^2)^{1/4}, \quad \alpha_2 = \arctan\left(\frac{\varepsilon_2''}{\varepsilon_2'}\right), \tag{13}$$

$$r_2 = \sqrt{\frac{(p_2-1)^2+q_2^2}{(p_2+1)^2+q_2^2}}, \quad r_{21} = \sqrt{\frac{(p_2-p_1)^2+(q_2-q_1)^2}{(p_2+p_1)^2+(q_2+q_1)^2}},$$

$$t_2 = \frac{2}{\sqrt{(p_2+1)^2+q_2^2}},$$

$$t_{21} = 2\sqrt{\frac{p_2^2+q_2^2}{(p_2+p_1)^2+(q_2+q_1)^2}}.$$

Expressions (7)–(13) constitute an analytical solution to the self-reflection problem.

Let us discuss the above results. Figure 1 shows the dependence of z_s on I_0/I_s, when $I_0 \geq I_{0c}$. In the absorption limit ($\varepsilon''_{1,2} > \varepsilon'_{1,2}$) z_s rises monotonically with I_0. By contrast, in the dispersion limit ($\varepsilon''_{1,2} < \varepsilon'_{1,2}$), z_s increases in an oscillatory fashion and $z_s(I_0)$ may be a multivalued function in certain regions. In other words, $z_s(I_0)$ may be bistable and even multistable so that z_s changes abruptly at certain values of I_0. This indicates radical restructuring of the field distribution in the medium: constructive nonlinear interference of the forward and the backward wave alternates with destructive interference as the length of the induced FP resonator is varied. A change in the excitation level leads to a new field distribution corresponding to a new resonator length. It can also be seen that the multistability in $z_s(I_0)$ is more noticeable and the hysteresis loops are wider for low intensities (near I_{0c}) at fixed $\varepsilon'_{1,2}$ and $\varepsilon''_{1,2}$. If $I_0 \gg I_{0c}$, absorption outweighs dispersion so that the multistability gradually disappears and the resonator length begins increasing monotonically. If I_0 goes down, monotonic decrease in $z_s(I_0)$ alternates with steps. At the final stage of its changes, z_s monotonically decreases and, starting from $I_0 = I_{0c}$, the resonator length is identically zero (Fig. 1a). Compared with increasing I_0, the steps lie at other values of I_0.

Figure 1 depicts $z_s(I_0)$ for $r_1 > r_2$. It is seen that $z_s(I_0)$ may change abruptly just as $I_0 \geq I_{0c}$. Still more interesting is the fact that the last step is at $I_0 < I_{0c}$, when I_0 decreases. This is because the reflectivity phase $\Phi_1 + \Phi_2$ is almost $\pi/2$, so that an induced FP resonator of an appreciable length arises at once if I_0 is as low as I_{0c}. The phenomenon is pronounced with infinitesimal absorption ($\varepsilon''_{1,2} \ll \varepsilon'_{1,2}$). In that case, the third sum term in (9) is proportional to $(\varepsilon'_2 - \varepsilon'_1)\sin^2(\sqrt{\varepsilon'_2} z_s)$, so that the reflection phase step is zero if $\varepsilon'_2 > \varepsilon'_1$ and is π if $\varepsilon'_2 < \varepsilon'_1$, resulting in an anomalous behavior of $z_s(I_0)$ near I_{0c}. Thus, the reflectivity phases play a very important role in the formation of the field distribution and the interface in the medium. As I_0 decreases, z_s first decreases monotonically, then changes abruptly, and finally the induced FP resonator abruptly disappears at $I_0 \leq I_{0c}$. Thus, if $r_1 > r_2$, the resonator is created at $I_0 = I_{0c}$ (as I_0 increases) and disappears at $I_0 < I_{0c}$ (as I_0 decreases). The latter can be seen from Fig. 1b.

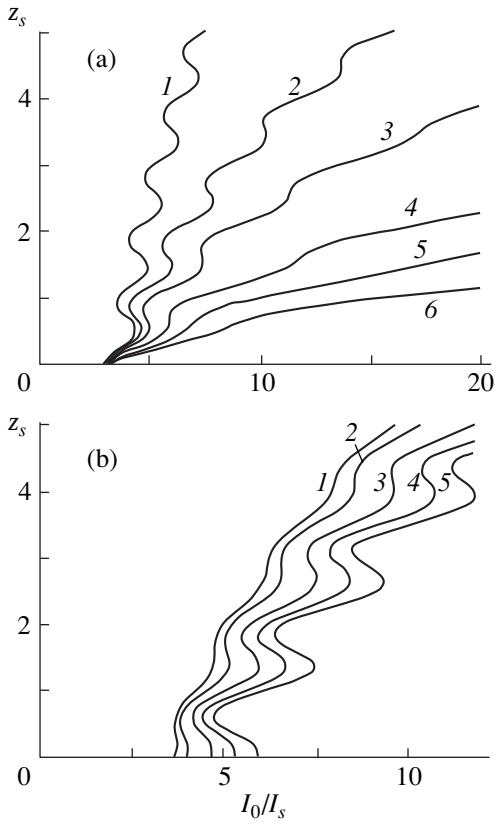

Fig. 1. Length of an optically induced FP resonator vs. normalized incident intensity. Panel (a) is computed for $r_1 < r_2$; $\varepsilon'_1 = 6$; $\varepsilon''_1 = 0.7$; $\varepsilon'_2 = 11$; and $\varepsilon''_2 =$ (*1*) 0.5, (*2*) 1, (*3*) 1.5, (*4*) 2.5, (*5*) 3.5, or (*6*) 5. Panel (b) is computed for $r_1 > r_2$; $\varepsilon'_1 = 11$; $\varepsilon''_1 = 0.7$; $\varepsilon''_2 = 0.5$; and $\varepsilon'_2 =$ (*1*) 8, (*2*) 9, (*3*) 11, (*4*) 13, or (*5*) 15.

The above-investigated dynamics of the domain interface essentially indicates that its position may change at an unsteady rate even if the excitation level is varied steadily. Remarkably, this result is obtained by qualitative reasoning in the context of a rudimentary model of the nonlinearity. In experiments, the motion of the domain interface can be examined with the help of the Doppler effect, following pioneering work [7]. This may provide more detailed information on the self-reflection dynamics in optically uniform media.

Since I_r depends on z_s (although in a complicated manner), the behavior of $z_s(I_0)$ governs that of $I_r(I_0)$. Figure 2 shows the reflectivity $R = I_r/I_0$ as a function of I_0 for different values of the permittivity parameters. It is seen that, for $I_0 < I_{0c}$, linear (Fresnel) reflection occurs with $R = r_1^2$, whereas, for $I_0 > I_{0c}$, the reflection becomes substantially nonlinear and even multistable. The multistability of $R(I_0)$ is pronounced in the disper-

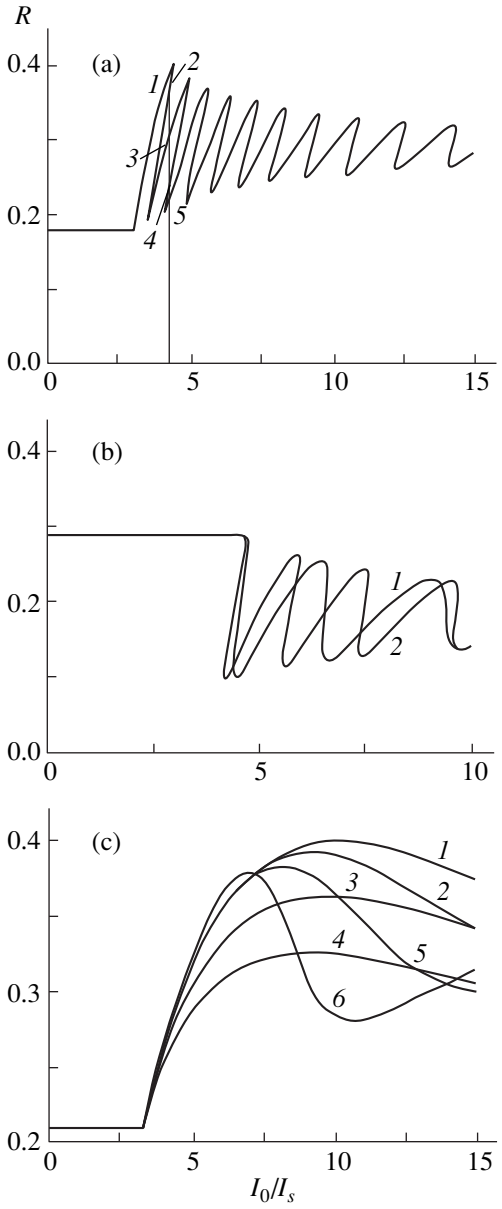

Fig. 2. Reflectivity vs. normalized incident intensity. Panel (a) is computed for $\varepsilon'_1 = 6$, $\varepsilon''_1 = 0.7$, $\varepsilon'_2 = 11$, and $\varepsilon''_2 = 0.5$. Panel (b) is computed for $\varepsilon'_1 = 11$, $\varepsilon'_2 = 6$, $\varepsilon''_1 = 0.7$, and $\varepsilon''_2 = (1)$ 0.5 or (2) 0.7. Panel (c) is computed for $\varepsilon'_1 = 6$; $\varepsilon''_1 = 3$; $\varepsilon'_2 = (1, 4–6)$ 11, (2) 9, or (3) 7; and $\varepsilon''_2 = (1–3)$ 10, (4) 8, (5) 6, or (6) 4.

sion limit, where $z_s(I_0)$ is a multivalued function. At higher excitation levels, $R(I_0)$ becomes smoother and the multistability gradually gives way to oscillatory behavior. If $I_0 \gg I_{0c}$, then $R(I_0)$ tends to r_2^2 asymptotically. The suppression of the multistability at $I_0 \gg I_{0c}$ stems from the fact that the domain interface goes deep into the medium, so that a significantly attenuated backward wave comes to the surface and cannot produce adequate constructive interference with the forward wave.

Figure 2a presents the dependence $R(I_0)$ for $r_2 > r_1$ in the dispersion limit ($\varepsilon''_{1,2} \ll \varepsilon'_{1,2}$). It is seen that once I_0 has crossed the critical level I_{0c}, the reflectivity rapidly and continuously grows to a maximum value 2–3 times larger than r_1^2 or r_2^2. A further increase in I_0 leads to multistability in $R(I_0)$. Specifically, we see the transition from a five- to a three-value region and then I_0 enters a single-value region, where $R(I_0)$ varies in a nonlinear (oscillatory) fashion and asymptotically approaches r_2^2 for $I_0 \gg I_{0c}$. The envelopes tend to the same level. Note that the oscillation rate of $R(I_0)$ is governed by p_2, whereas the number of spatial periods is limited by q_2. Figure 2 shows that decreasing ε''_2, the other permittivity parameters being fixed, reduces the oscillation amplitude of R and the limit value $R = r_2^2$.

Figure 2b depicts $R(I_0)$ for two values of ε''_2. Notice the high sensitivity to this parameter: as ε''_2 goes up, the multistability quickly disappears and the number of spatial periods markedly decreases. The reason is that increasing ε''_2 is equivalent to increasing the absorption coefficient and q_2, which ultimately suppresses the effect of the backward wave on the nonlinear interference. The graphs in Fig. 2b are plotted for $r_1 > r_2$. It is seen that, once I_0 has crossed the critical level I_{0c}, the reflectivity falls abruptly, which is equivalent to the formation of an induced FP resonator with a nonzero length.

Figure 2c displays the behavior of $R(I_0)$ in the strong absorption limit. The reflectivity now rises (or falls) monotonically, with no oscillation, due to the rapid decay of the backward wave and the consequent absence of interference.

The multivalued nature of $R(I_0)$ manifests itself in $I(z)$. The intensity distribution can easily be constructed from (7), (8), and the five computed values of $R(I_0)$ for $I_0/I_s = 4.24$ (see points *1–5* in Fig. 2a), the results being shown in Fig. 3. It turns out that $I(z)$ and its derivatives are multivalued on the surface, eventually determining different values of the reflectivity for the same I_0. The field distributions also differ in the number of spatial periods and in z_s. Thus, if $I_0 \geq I_{0c}$, then $I(z)$ is an oscillating function with an exponentially decreasing envelope for $0 \leq z \leq z_s$ and is an exponentially decaying function for $z > z_s$. Note that (7) is a self-similar solution: variations in I_0 and z_s result in nothing more than shifts of the origin.

In summary, we have investigated the self-reflection effect in the context of a naive model of a medium with a steplike dependence of the permittivity on the wave intensity. The extreme simplicity of the model allowed

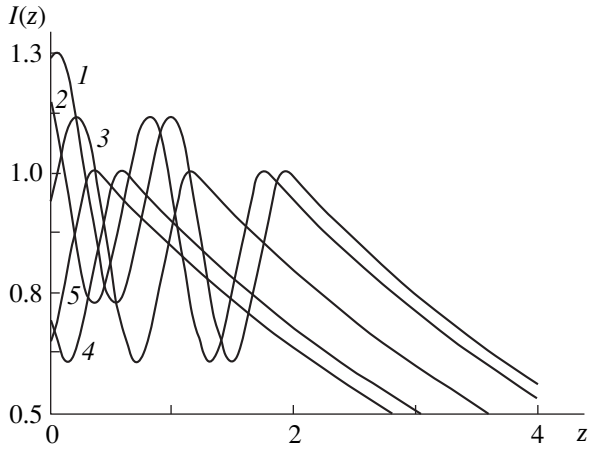

Fig. 3. Intensity distributions in the medium at $I_0/I_s = 4.24$ for R = (*1*) 0.383, (*2*) 0.359, (*3*) 0.3, (*4*) 0.23, and (*5*) 0.21. The curves are labeled as the corresponding points in Fig. 2a.

us to obtain exact analytical solutions and to elucidate their physical meaning. It has been demonstrated for an optically uniform nonlinear medium exposed to radiation that an induced FP resonator arises in the medium if the incident intensity exceeds a critical value, the resonator length being determined by the incident intensity. Hysteresis has been found in the behavior of surface reflectivity and resonator length as functions of the incident intensity. Intensity distributions in the medium have been computed.

We strongly believe that the properties of optical self-reflection predicted in this paper will show up in more realistic models of nonlinear media in which the permittivity function is derived from solutions of constitutive relations with regard for specific quantum transitions. On the other hand, sophisticated models allow for no analytical solutions that give an intricate picture of self-reflection. In the case of two light beams, the results would be difficult to explain even in qualitative terms. For these reasons, the complete analysis of the naive model performed in this study seems to be most useful. We think that our approach will yield many valuable insights.

REFERENCES

1. L. Roso-Franco, Phys. Rev. Lett. **55**, 2149 (1985); J. Opt. Soc. Am. B **4**, 1878 (1987).
2. L. Roso-Franco and M. L. Pons, J. Mod. Opt. **37**, 1645 (1990).
3. V. Malyshev and E. C. Jarque, J. Opt. Soc. Am. B **12**, 1868 (1995).
4. V. A. Malyshev and E. C. Jarque, Opt. Spektrosk. **82**, 630 (1997) [Opt. Spectrosc. **82**, 582 (1997)].
5. E. C. Jarque and V. Malyshev, Opt. Commun. **142**, 66 (1997).
6. W. Forysiak, R. G. Flesch, J. V. Moloney, and E. M. Wright, Phys. Rev. Lett. **76**, 3695 (1996).
7. A. Schulzgen, N. Peyghambarian, and S. Hughes, Phys. Status Solidi B **206**, 125 (1998).
8. A. E. Kaplan, Phys. Rev. Lett. **55**, 1291 (1985); IEEE J. Quantum Electron. **21**, 1538 (1985).
9. R. H. Enns, S. S. Rangnekar, and A. E. Kaplan, Phys. Rev. A **35**, 466 (1987); Phys. Rev. A **36**, 1270 (1987).
10. R. H. Enns and S. S. Rangnekar, Opt. Lett. **12**, 108 (1987); IEEE J. Quantum Electron. **23**, 1199 (1987).
11. L. J. Mulder and R. H. Enns, IEEE J. Quantum Electron. **25**, 2205 (1989).
12. P. I. Khadzhi and L. V. Fedorov, Zh. Tekh. Fiz. **61** (5), 110 (1991) [Sov. Phys. Tech. Phys. **36**, 564 (1991)].
13. N. N. Beletskiĭ and E. A. Gasan, Fiz. Tverd. Tela (St. Petersburg) **36**, 647 (1994) [Phys. Solid State **36**, 357 (1994)]; Ukr. Fiz. Zh. **38**, 1657 (1993).
14. P. I. Khadzhi, G. D. Shibarshina, and A. Kh. Rotaru, *Optical Bistability in a System of Coherent Excitons and Biexcitons in Semiconductors* (Shtiintsa, Chisinau, 1988).

Translated by A. Sharshakov

Technical Physics, Vol. 45, No. 11, 2000, pp. 1462–1469. Translated from Zhurnal Tekhnicheskoĭ Fiziki, Vol. 70, No. 11, 2000, pp. 91–98.

Theoretical Study of Thermoelectronic Laser Energy Conversion

I. V. Alekseeva*, A. P. Budnik*, P. P. D'yachenko*, V. A. Zherebtsov*, A. V. Zrodnikov*, and S. T. Surzhikov**

** Leipunskii Institute of Physics and Power Engineering, State Research Center of Russian Federation, Obninsk, 249020 Russia*

*** Institute of Problems of Mechanics, Russian Academy of Sciences, Moscow, 117526 Russia*

E-mail: budnik@ippe.rssi.ru

Received October 25, 1999; in final form, February 29, 2000

Abstract—The structure of the distribution of plasma parameters over the interelectrode space of a thermoelectronic converter of laser energy into electrical energy was analyzed. Processes occurring in the near-electrode discharge regions were studied. Equations describing the equilibrium core of a continuous optical discharge were derived, and boundary conditions were imposed on these equations. A method of numerical solution and a software package for simulating the energy converter operation were developed. *© 2000 MAIK "Nauka/Interperiodica".*

INTRODUCTION

Power beaming is a promising technology for power transmission [1–6]. It is based on the conversion of energy produced by a primary energy source into energy of electromagnetic radiation. This energy is transmitted by a microwave or laser beam and converted into electrical or other forms of energy for further use. One of the main advantages of laser power beaming is that it allows the size of transmitting and receiving devices to be reduced by several orders of magnitude. The conversion of laser energy into electrical energy is one of the most important stages of laser power beaming. There are several approaches to the implementation of this stage of power beaming. These approaches are based on various methods of direct energy conversion. Thermoelectronic conversion of laser energy into electrical energy [7] holds much promise for high-power space-qualified hardware with limited weight and dimensions. This method does not impose strict requirements on the wavelength and monochromaticity of laser radiation. Thermoelectronic laser energy converters (TELEC) are used for converting high-intensity laser beams ($\sim 10^4$–10^5 V cm^{-2}) at high temperatures of the cooler (more than 1 kK). This provides effective dissipation of unused energy in a vacuum. High upper temperature of the energy conversion cycle (15–20 kK) allows the energy converter efficiency to be significantly increased.

The method of thermoelectronic conversion of laser energy into electrical energy was put forward in [7]. The method is based on the conversion of energy of hot electrons produced by RF-discharge into direct current energy [8]. Although the fundamental principles of this method are relatively simple, a number of experimental attempts at its implementation failed [9, 10]. Presumably, these failures slowed the development of the theory of the method. As a result, an adequate theory of thermoelectronic laser energy conversion has not yet been accomplished. At present, theoretical studies of thermoelectronic laser energy conversion are encouraged by the results of experimental studies of the first TELEC [11].

In this work, thermoelectronic laser energy conversion and physical processes determining its efficiency were subjected to theoretical study. Particular emphasis was placed on the study of continuous optical discharge (COD) in the interelectrode space of the energy converter. Continuous optical discharge of this type is characterized by a small cross section (~1 mm), direct contact of the electrodes with the high-temperature (≈10 kK) regions of the discharge, and an electric current through the discharge. In conventional COD-based devices [12, 13], the processes occurring in the COD regions adjacent to the wall are often of subordinate importance. In this case, a rough description of these processes is quite sufficient. In TELEC, however, the processes occurring in the near-electrode discharge regions are of primary importance [8]. That is why particular emphasis in this work was placed on the near-electrode regions. Equations describing the equilibrium core of COD were derived, and boundary conditions were imposed on these equations.

BASIC EQUATIONS

A thermoelectronic laser energy converter is implemented as a gas-filled diode with a hot electron emitter and a relatively cold collector. Continuous optical dis-

1063-7842/00/4511-1462$20.00

charge in the interelectrode space of the diode is maintained by laser radiation. Plasma in the interelectrode space is dense and for the most part strongly ionized [11]. Thus, it can be described using equations of three-fluid hydrodynamics [14, 15]. In this work, we restrict our consideration to the steady-state case:

$$\nabla \mathbf{J} = \Gamma_i; \quad \nabla \mathbf{j}_i = \Gamma_i; \quad \nabla \mathbf{j}_a = -\Gamma_i;$$
$$\nabla P_e = en\nabla\varphi + \mathbf{R}_{ea} + \mathbf{R}_{ei}; \tag{1}$$
$$\nabla P_i = -en\nabla\varphi + \mathbf{R}_{ia} - \mathbf{R}_{ei};$$

$$\nabla P_a = -\mathbf{R}_{ea} - \mathbf{R}_{ia};$$
$$\nabla \mathbf{S}_e = -\Gamma_i(E_i + e\varphi) - \Delta S_{ei} - \Delta S_{ea} + \Delta S_{\text{rad}}; \tag{2}$$

$$\nabla \mathbf{S}_H = \Delta S_{ei} + \Delta S_{ea} - e\mathbf{j}_i\nabla\varphi. \tag{3}$$

Equations (1) are the continuity equations; Eqs. (2) are the motion equations for electrons, ions, and atoms, respectively; Eqs. (3) are the equations of energy conservation for electrons and heavy components of plasma (HCP), respectively; $\mathbf{J}$, $\mathbf{j}_i$, and $\mathbf{j}_a$ are the electron, ion, and atom flux densities, respectively; $\Gamma_i = n\bar{v}_e\sigma_i n_a[1 - (n_{aeq}/n_a)(n/n_{eq})^2]$ is the ion production rate in plasma; n and n_a are the electron (ion) and atom concentrations, respectively; $\bar{v}_e = \sqrt{8T_e/(\pi m)}$ is the thermal velocity of electrons; σ_i is the effective cross section of atom ionization by electrons; n_{eq} and $n_{aeq} = [P - n_{eq}(T_e + T)]/T$ are the equilibrium (quasi-equilibrium) electron (ion) and atom concentrations, respectively; T_e and T are the electron and atom (ion) temperatures, respectively; P_e, P_i, P_a, and P are the electron, ion, atom, and total plasma pressures, respectively; e is the elementary charge; φ is the electric potential; $\mathbf{R}_{ei} + \mathbf{R}_{ea} = -e\mathbf{J}/u_e - k_e^{(T)} n\nabla T_e$ and $\mathbf{R}_{ia} = -(e/u_i)[\mathbf{j}_i - (n/n_a)\mathbf{j}_a] - k_i^{(T)} n\nabla T$ are the forces of electron friction on ions and atoms (at $J \gg j_i$ and $J \gg (n/n_a)j_a$, which is usually true for interelectrode plasma in TELEC) and the friction force between ions and atoms, respectively; u_e, u_i, $k_e^{(T)}$, and $k_i^{(T)}$ are the electron and ion mobilities and thermal diffusion ratios, respectively;

$$\mathbf{S}_e = \mathbf{J}(\beta_e T_e - e\varphi) - \lambda_e\nabla T_e, \quad \mathbf{S}_H = -\lambda_H\nabla T \tag{4}$$

are the total electron energy flux and the heat energy flux for HCP (ions and atoms), respectively; $\beta_e = 5/2 + k_e^{(T)}$; λ_e and λ_H are the thermal conductivity coefficients for electrons and HCP, respectively; E_i is the atom ionization potential; $\Delta S_{ei} = (3m/M)m(T_e - T)/\tau_{ei}$ and $\Delta S_{ea} = (3m/M)n(T_e - T)/\tau_{ea}$ are the electron gas energy losses caused by electron–ion and electron–atom collisions, respectively; m and M are the electronic and ionic (atomic) masses, respectively; τ_{ei} and τ_{ea} are the electron–ion and electron–atom intercollision times; and ΔS_{rad} is the specific power of radiation contribution to the plasma electron energy. The transfer coefficients that are not given in this work can be found in [14, 15]. Equations for ΔS_{rad} are given below.

The set of simultaneous Eqs. (1)–(4) is subject to boundary conditions at the interface between quasi-neutral plasma and near-electrode space charge regions [14, 15]. The solution of this set of simultaneous equations (taking into account equations for ΔS_{rad}) allows the distribution of plasma parameters over the interelectrode space and the converter characteristics to be determined. However, this method of solving is too cumbersome. The analysis of the distribution of plasma parameters over the interelectrode space of TELEC facilitates solving of the problem and allows the methods used for studying COD in gases and slow combustion modes [16, 17] to be applied to TELEC.

Analysis of typical TELEC [11] showed that the plasma temperature at the center (core) of the optical discharge (i.e., at the site where the greatest part of the laser radiation energy is absorbed) is rather high ($T \approx T_e$). Plasma in the discharge core is strongly ionized and virtually equilibrium ($n \approx n_{eq}$). However, outside the core, there is a trend toward a decrease in the plasma temperature and density: at a distance $L_T = \{[M/(3m)]\lambda_H\tau_{eH}/n\}^{1/2}$ from the electrodes, the temperature T becomes lower than T_e (τ_{eH} is the electron-HCP intercollision time); at a distance $L_i = \sqrt{D_a/(n_a\sigma_i\bar{v}_e)}$ from the electrodes, the density n becomes lower than n_{eq} (D_a is the ambipolar diffusion coefficient).

If the electron temperature in the near-electrode plasma regions is about 10 kK (which is typical of TELEC), L_T far exceeds L_i, but these two values are considerably smaller than the interelectrode distance L. This allows the description of plasma in TELEC to be simplified in a manner similar to the description of plasma in the thermionic converter of heat energy into electrical energy (TIC) at strong currents through a diode [14]. Let the interelectrode space be divided into seven regions: (1) equilibrium core of the optical discharge, where all plasma components have equilibrium concentrations and virtually identical temperatures; the greatest part of the laser radiation energy is absorbed in this region; (2) two regions of quasi-equilibrium plasma at the COD periphery, where $T < T_e$, but electron, ion, and atom concentrations are related by the Saha equation at the electron temperature $n = n_{eq}(T_e)$; (3) two regions of nonequilibrium plasma adjacent to the quasi-equilibrium regions on the electrode sides, where $T < T_e$ and $n < n_{eq}(T_e)$; in these regions, most of the ions transferred to the electrodes are produced; and (4) near-electrode space charge regions (Langmuir layers), where particles move almost without collisions.

Assuming that in the COD core $T_e = T$ and $n = n_{eq}$, we obtain on rearrangement the following set of simul-

taneous equations describing the COD core plasma in TELEC without a gas flow ($P = P_0$):

$$-\nabla[\lambda\nabla T] = \Delta S_{\text{rad}} + \frac{eJ^2}{nu_e} - \mathbf{J}\left[\frac{3}{2}\nabla T + T\nabla k_e^{(T)} - T\nabla(\ln n)\right], \quad (5)$$

$$\nabla\mathbf{J} = 0,$$
$$e\nabla\varphi = \frac{e\mathbf{J}}{nu_e} + T\nabla(\ln n) + (1 + k_e^{(T)})\nabla T. \quad (6)$$

The atom concentrations and the atom and ion flux densities are determined by the following equations:

$$n_a = \frac{P_0}{T} - 2n, \quad \mathbf{j}_a = -\mathbf{j}_i, \quad (7)$$

$$\mathbf{j}_i = \frac{D_i n_a}{n + n_a} \times\left\{\frac{1}{T}[-en\nabla\varphi - \mathbf{R}_{ei} - (1 + k_i^{(T)})n\nabla T] - \nabla n\right\}, \quad (8)$$

where $n = n_{eq} = N(\sqrt{1 + (P_0/T)(1/N)} - 1)$; $N = (g_i/g_a)2(2\pi mT/h^2)^{3/2}\exp(-E_i/T)$; P_0 is the gas pressure in the converter chamber; g_i and g_a are the statistical ionic and atomic weights, respectively; h is the Planck constant; $\lambda = \lambda_H + \lambda_e$ is the heat conductivity of plasma; and D_i is the ionic diffusion coefficient. Equation (5) describes the energy balance of the COD core plasma with respect to the electric current through the converter. The physical meaning of the other equations is obvious.

Equations (5)–(8) were derived under the assumption that the ion production rate in plasma Γ_i was zero ($n \approx n_{eq}$). To make an estimate of the ion production rate, $\mathbf{j}_i$ should be calculated in the zeroth-order approximation using Eq. (8); then, Γ_i can be determined from the obtained value of $\mathbf{j}_i$ using the continuity Eq. (1) for ions.

Consider radiation processes in the COD core: interaction between laser radiation and plasma and radiative heat exchange induced by intrinsic plasma radiation. The specific power of the radiation contribution to the plasma energy was found to be $\Delta S_{\text{rad}} = W_L - Q$, where W_L is the specific power of the energy release in plasma caused by laser radiation absorption and Q is the specific power loss due to intrinsic radiation of plasma. Special boundary conditions are imposed on the obtained set of simultaneous equations to take into account radiation processes at the electrodes and in the near-electrode discharge regions.

Consider a weakly focused laser beam propagating in the positive direction z. In the quasi-optical approximation [18–20], its interaction with plasma can be described by the equation

$$2ik\frac{\partial E}{\partial z} = \frac{\partial^2 E}{\partial x^2} + \frac{\partial^2 E}{\partial y^2} + k^2\varepsilon_\delta E, \quad (9)$$

where $E(\mathbf{r})$ is the complex amplitude of laser radiation field intensity; $\varepsilon_\delta = (\varepsilon - \varepsilon_0)/\varepsilon_0$; $\varepsilon = \varepsilon_R + i\varepsilon_{Im}$ is the complex permittivity of the equilibrium plasma at the pressure P and temperature T; ε_0 is the real part of complex permittivity at the pressure P and temperature $T_0 = (T_E + T_C)/2$; T_E and T_C are the emitter and collector temperatures, respectively; $k = \omega\sqrt{\varepsilon_0}/c$ is the wave number; ω is the circular frequency of laser radiation; and c is the velocity of light in vacuum. If $\omega \gg \omega_p$ ($\omega_p = \sqrt{4\pi ne^2/m}$ is the plasma frequency), the permittivity can be determined using the following equations:

$$\varepsilon_R(T, P) = 1 + (\varepsilon_0 - 1)(T_0/T) - \omega_p^2/\omega^2, \quad \varepsilon_{Im} = \mu/k, \quad (10)$$

where μ is the laser radiation absorption coefficient (see, e.g., [19]).

The specific power of the energy release in plasma caused by laser radiation absorption is related to the complex amplitude $E(\mathbf{r})$ by the equation

$$W_L(\mathbf{r}) = \mu(\mathbf{r})c|E(\mathbf{r})|^2/(8\pi). \quad (11)$$

The intrinsic plasma radiation transfer in the discharge core is described by the equation

$$\mathbf{\Omega}\text{grad}J_\nu(\mathbf{r}, \mathbf{\Omega}) + k_\nu(T)J_\nu(\mathbf{r}, \mathbf{\Omega}) = k_\nu(T)J_{b\nu}(T), \quad (12)$$

where $J_\nu(\mathbf{r}, \mathbf{\Omega})$ is the spectral intensity of radiation in the direction $\mathbf{\Omega}$; $J_{b\nu}(T)$ is the spectral intensity of blackbody radiation at the temperature T; and $k_\nu(T)$ is the coefficient of absorption of optical radiation at the frequency ν by plasma at the temperature T. Spectral density of radiant energy U_ν is

$$U_\nu(\mathbf{r}) = \int_\Omega J_\nu(\mathbf{r}, \mathbf{\Omega})d\mathbf{\Omega}. \quad (13)$$

Mathematical simulation of COD in the slow combustion mode [12, 13] showed that the equation for intrinsic plasma radiation transfer in the discharge core can be solved in the multigroup diffusion approximation or even in the multigroup bulk-luminescence approximation. For this purpose, let us divide the spec-

tral range of heat radiation into S unequal subranges. Averaging over the sth subrange, we obtain

$$U_s = \int_{\nu_s}^{\nu_{s+1}} U_\nu d\nu; \quad U_{bs} = \int_{\nu_s}^{\nu_{s+1}} U_{b\nu} d\nu;$$
$$k_s = \int_{\nu_s}^{\nu_{s+1}} [k_\nu/(\nu_{s+1} - \nu_s)] d\nu, \tag{14}$$

where U_s are the group densities of radiation energy; $U_{b\nu}$ is the spectral density of the blackbody radiation energy; and k_s are the group spectral coefficients of radiation absorption (these coefficients can be calculated using the MONSTR system [13]). In the multigroup diffusion approximation, the radiation transfer equation takes the form

$$\nabla\{[1/(3k_s)\nabla U_s]\} = k_s(U_{bs} - U_s), \quad s = 1, 2, \ldots, S. \tag{15}$$

In the multigroup diffusion approximation, the specific power loss due to intrinsic plasma radiation is determined by the equation

$$Q = c\int_\nu k_\nu(U_{b\nu} - U_\nu)d\nu = c\sum_{s=1}^{S} k_s(U_{bs} - U_s). \tag{16}$$

In the multigroup bulk-luminescence approximation, radiation reabsorption is disregarded. Thus, we obtain

$$Q = c\sum_{s=1}^{S} k_s U_{bs}. \tag{17}$$

If necessary, the transfer Eq. (12) can be solved using other methods, such as the method of quadrupole moments [13] or higher approximations of the method of spherical harmonics.

NEAR-ELECTRODE REGIONS AND BOUNDARY CONDITIONS

Consider now the near-electrode nonequilibrium and quasi-equilibrium regions in order to obtain the boundary conditions for Eqs. (5) and (6). The analysis of the near-electrode regions is based on the fact that the values of L_i and L_T are small. Under standard conditions of TELEC operation, L_T is higher than L_i. Therefore, let us assume that, for both the emitter and collector, $L_i \ll L_T$. In the case under consideration, both L_T and L_i are considerably smaller than the interelectrode distance and the characteristic size of the electrodes. Therefore, the near-electrode regions can be considered as planar. Only the flux components normal to the electrode surface are considered in further discussion.

If the electron emission currents from the emitter are not too high, potential jumps across the Langmuir layers retard electron transfer from plasma. Under these conditions, nonequilibrium near-electrode regions of TELEC behave in the same manner as nonequilibrium near-electrode regions of TIC at high current densities, in which plasma is transformed into the quasi-equilibrium state throughout the majority of the interelectrode space. These TIC regions and boundary conditions at the interface between nonequilibrium and quasi-equilibrium plasma are given in [14]. The electron flux at the near-emitter interface between these regions is [14]

$$J_{i1} = J_E - (n_{i1}v_{el}/4)\exp(-e\Delta\varphi_{i1}/T_{e1}) - (j_i)_1, \tag{18}$$

where the quantities at the interface are denoted by the subscript $i1$. The total electron energy flux is

$$(S_e)_{i1} = 2T_E J_E - 2T_{e1}\frac{1}{4}n_{i1}\bar{v}_{e1}\exp(-e\Delta\varphi_{i1}/T_{e1}) + (j_i)_1(E_i + e\Delta\varphi_{i1}) - \delta(\Delta S_{ei} + \Delta S_{ea}), \tag{19}$$

where J_E is the emitted electron flux density; $\Delta\varphi_{i1}$ is the potential jump between the interface of the nonequilibrium and quasi-equilibrium regions and the emitter surface; T_{e1} is the electron temperature in the nonequilibrium region (this temperature is assumed to be invariable along the direction perpendicular to the electrode surface); $\bar{v}_{e1} = \bar{v}_e(T_{e1})$; and $\delta(\Delta S_{ei} + \Delta S_{ea})$ is the energy transferred by electrons to HCP in the nonequilibrium region;

$$(j_i)_1 = -2[n_{i1}D_{a1}/(\sqrt{2}L_{i1})]\{[\eta_1^2 - \eta_1(1 + T_E/T_{e1}) + T_E/T_{e1}]\eta_1^2\ln(1 - 1/\eta_1) + \eta_1^3 - \eta_1^2(1 + 2T_E/T_{e1})/2 - \eta_1(1 - 3T_E/T_{e1})/6 + (1 + T_E/T_{e1})/6\}^{1/2}, \tag{20}$$

where $(j_i)_1$ is the ion flux produced in the nonequilibrium region and transferred to the emitter; $\eta_1 = P_0/(n_{i1}T_{e1})$; and $L_{i1} = \sqrt{D_{a1}/[na_{a1}(\sigma_i)_1\bar{v}_{e1}]}$, D_{a1}, n_{a1}, and $(\sigma_i)_1$ are the ionization length, ambipolar diffusion coefficient, atomic concentration, and cross section of atom ionization by electrons in the near-emitter plasma, respectively. In the case of weakly ionized plasma in the nonequilibrium region ($1/\eta \ll 1$), the following equation is valid:

$$(j_i)_1 = -D_{a1}n_{i1}/(\sqrt{2}L_{i1}).$$

Equations (18)–(20) were obtained under the assumption that the HCP temperature in the nonequilibrium region is constant and equal to the electrode temperature, whereas the ionization length far exceeds the ion–atom intercollision mean free path ($L_{i1} \gg L_{ea}$). Therefore, plasma at the near-electrode interface is assumed to be weakly ionized.

Consider now the near-emitter quasi-equilibrium region. This region is small in width. Therefore, taking into account the high heat conduction of electron gas, the electron temperature variations along the direction perpendicular to the electrode surface can be neglected. The electron temperature is taken to be equal to the plasma temperature T_{T1} at the interface between the equilibrium and quasi-equilibrium regions (parameters relevant to this interface are denoted by the subscript T_1). Ion production in this region is also negligible, because atom ionization is virtually completely compensated by ion recombination. According to our estimations, in the cases of practical interest (i.e., if $eJ < 10^3$ A/cm^3), the contribution of friction forces (see the motion equations for electrons (2)) to the potential variation in the quasi-equilibrium region is less than $10^{-1}T_{T1}/e$. This contribution can be neglected. Thus, the electron concentration distribution over the region under consideration takes the Boltzmann form:

$$n = n_{i1}\exp[e(\varphi - \varphi_{i1})/T_{T1}]. \quad (21)$$

Taking into account that J is maintained at an invariable level within the quasi-equilibrium region and $T_{e1} = T_{T1}$, Eq. (18) is recast as

$$J_{T1} = J_E - (n_{T1}\nabla_{e1}/4)\exp(-e\Delta\varphi_{T1}/T_{T1}) - (j_i)_1, \quad (22)$$

where $\Delta\varphi_{T1}$ is the potential jump between the interface between equilibrium and quasi-equilibrium regions and the emitter surface.

Disregarding weak heating of ions by ion current, and taking into account that electron–ion collisions are the main cause of the energy transfer from electrons to HCP, we obtain the following equation for the ion and atom temperature T:

$$\frac{d}{dx}\left(\lambda_H\frac{dT}{dx}\right) = -\frac{3m}{M}\frac{n^2(T_{T1}-T)}{(\tau_{eiT1}n_{T1})}. \quad (23)$$

This equation is subject to the following boundary conditions:

$$T_{i1} = T_E \quad \text{and} \quad T|_{x\to\infty} = T_{T1}(L_{T1} \ll L), \quad (24)$$

where the x-axis is normal to the emitter surface. The HCP thermal conductivity can be approximated using equation [20]

$$\lambda_H = \frac{\lambda_a}{1 + (n\sigma_{ai}^{(2)})/(n_a\sigma_{aa}^{(2)})} + \frac{\lambda_i}{1 + (n_a\sigma_{ia}^{(2)})/(n_a\sigma_{ii}^{(2)})}, \quad (25)$$

where λ_a and λ_i are the temperature-dependent thermal conductivities of atoms and ions, respectively, and $\sigma_{aa}^{(2)}$, $\sigma_{ii}^{(2)}$, $\sigma_{ai}^{(2)}$, and $\sigma_{ia}^{(2)}$ are the effective scattering cross-sections.

Quasi-equilibrium electron (ion) concentration is determined by the equation

$$n = n_{eq} = \frac{N_{T1}(1 + T_{T1}/T)}{2} \times\left(\sqrt{1 + \frac{P_0}{T}\frac{4}{N_{T1}(1 + T_{T1}/T)^2}} - 1\right), \quad (26)$$

where $N_{T1} = (g_i/g_a)2(2\pi mT_{T1}/h^2)^{3/2}\exp(-E_i/T_{T1})$. At given P_0 and T_{T1}, the concentrations n and n_a and, therefore, the thermal conductivity λ_H, depend only on T in the quasi-equilibrium region. Therefore, Eq. (23) is a second-order nonlinear equation with coefficients. The right-hand side of the equation depends only on T. The first integral is equal to

$$\frac{dT}{dx} = \frac{1}{\lambda_H}\left[2\frac{3m}{M}\frac{1}{\tau_{eiT1}n_{T1}}\int_T^{T_{T1}}\lambda_H n^2(T_{T1}-T)dT\right]^{1/2}. \quad (27)$$

The HCP-transferred heat energy flux at the interface between quasi-equilibrium and nonequilibrium regions is determined by Eqs. (27) and (4):

$$(S_H)_{i1} = -\lambda_{HT1}\frac{\sqrt{2}T_{T1}}{L_{T1}}\left[\int_{T_E}^{T_{T1}}\frac{\lambda_H}{\lambda_{HT1}}\left(\frac{n}{n_{T1}}\right)^2 \times\left(1 - \frac{T}{T_{T1}}\right)d\left(\frac{T}{T_{T1}}\right)\right]^{1/2}, \quad (28)$$

where $L_{T1} = \{[M/(3m)]\lambda_{HT1}(\tau_{eiT1}n_{T1})/n_{T1}^2\}^{1/2}$.

If plasma in the quasi-equilibrium region is weakly ionized ($nT_{T1} \ll P_0$), the main contribution to the HCP heat conduction is made by atoms. However, atom scattering by ions may also be of considerable importance. In this case, both the numerator and denominator of the first term of Eq. (25) vary slightly with temperature (approximately, as $\sqrt{T}$). Disregarding the weak dependence of λ_H on T, we obtain from Eq. (28)

$$(S_H)_{i1} = -\lambda_{HT1}(\sqrt{2}T_{T1}/L_{T1})[\ln(T_{T1}/T_E) - (1 - T_E/T_{T1})]^{1/2}. \quad (29)$$

An equation for the flux of the total electron energy and HCP heat energy at the interface between quasi-equilibrium and nonequilibrium regions is obtained by the summation of Eqs. (19) and (28): $S_{i1} = (S_e)_{i1} + (S_H)_{i1}$. Taking into account that $L_{i1} \ll L_{T1}$, the term $\delta(\Delta S_{ei} + \Delta S_{ea})$ in the equation for S_{i1} is found to be negligible as compared to $(S_H)_{i1}$. As shown above, ion production in the quasi-equilibrium region, as well as the heating of ions by ion current and variations in the electron gas energy due to absorption and emission can also be disregarded. Thus, on summing Eqs. (3), we find that

the total energy flux variation in the quasi-equilibrium region is zero, i.e.,

$$S_{T1} = S_{i1} = (S_e)_{i1} + (S_H)_{i1}. \quad (30)$$

The plasma energy balance at the near-emitter boundary of the equilibrium COD core is obtained by summing Eqs. (4), assuming that the right-hand side of the obtained equation at the interface between the equilibrium and quasi-equilibrium regions is equal to the right-hand side of Eq. (30), and taking into account Eq. (21):

$$-\lambda_{T1}\left(\frac{dT}{dx}\right)\Big|_{T1} = -2(T_{T1} - T_E)J_E + S_{Hi1} + \left(E_i + 2T_{T1} + e\Delta\varphi_{T1} - T_{T1}\ln\frac{n_{T1}}{n_{i1}}\right)(j_i)_1 - J_{T1}\left[\left(\frac{1}{2} + k_{eT1}^{(T)}\right)T_{T1} - e\Delta\varphi_{T1}\right], \quad (31)$$

where $(S_H)_{i1}$ is determined by Eqs. (28) and (29); $(j_i)_1$, by Eq. (20); and n_{i1}, by Eq. (26). The potential jump $\Delta\varphi_{T1}$ is determined by Eq. (22):

$$\Delta\varphi_{T1} = \frac{T_{T1}}{e}\ln\frac{n_{T1}\nabla_{eT1}/4}{J_E - J_{T1} - (j_i)_1}. \quad (32)$$

The plasma energy balance at the near-collector boundary of the equilibrium COD core is described by a similar equation. The physical meaning of Eq. (31) is clear. The left-hand side of this equation is the energy flux through the boundary caused by heat transfer in the plasma. The first term on the right-hand side is the energy expended for heating emitted electrons from the emitter temperature T_E to the temperature T_{T1}. The second term is the energy transferred to the emitter in the process of heat transfer by ions and atoms. The third term is the energy expended for producing ions in the nonequilibrium region (these ions are then transferred to the emitter). The last term is the energy transferred from the boundary by the electron current.

The set of simultaneous equations for the COD core plasma (5) and (6) subject to the boundary conditions (31), (32), and similar conditions at the near-collector boundary of the core can be relatively easily solved in the one-dimensional (planar and cylindrically symmetrical) case if ΔS_{rad} depends explicitly only on the plasma temperature T, which is usually the case. Specifying the electron flux density near, for example, the emitter, we can derive the distribution of $\mathbf{J}$ over the interelectrode space from the equation $\nabla\mathbf{J} = 0$. Substituting the expression obtained into Eq. (5), we obtain the equation for temperature T. The coefficients of the equation obtained depend only on T and the coordinate normal to the electrodes. Solving this equation as subject to the boundary condition (31) and a similar condition at the near-collector boundary of the discharge core, we obtain T. Then, the distributions of n, n_a, φ, j_i, and $\mathbf{j}_a$ over the interelectrode space and the total potential drop in the interelectrode gap

$$V = \Delta\varphi_{T1} + (\varphi_{T2} - \varphi_{T1}) + \Delta\varphi_{T2}, \quad (33)$$

are calculated from Eqs. (6)–(8). Thus, we actually obtain the voltage–current characteristic of TELEC. The same approach can be applied to the case of a discharge that is slightly nonuniform along the direction of laser beam propagation. This case is of particular importance for TELEC.

The distribution of the incident laser beam intensity and the conditions for radiation reflection from the electrodes are imposed as boundary conditions on Eq. (9) of laser radiation propagation through the interelectrode space of TELEC. The equation of intrinsic plasma radiation propagation is subject to the boundary conditions for radiation reflection from the electrodes. These conditions are specified below in the discussion of the calculation results.

Equations (5) and (6) subject to the given boundary conditions are valid in the majority of the interelectrode space of TELEC. It should be noted, however, that in the frontal regions of COD, in which the plasma temperature decreases, while the distances L_i and L_T increase and at a certain temperature become comparable to the interelectrode distance L, the distinction between the equilibrium plasma region and near-electrode regions loses its meaning. However, the volume of the frontal regions of COD is small in comparison with the total volume of COD in the interelectrode space of TELEC, so that the frontal regions have little effect on the process of laser energy conversion into electrical energy. Therefore, a rough description of the frontal regions of COD without regard for deviations from equilibrium is quite sufficient. Equations (5) and (6) are used for this purpose. At the electrodes and laser beam input windows, the plasma temperature is assumed to be equal to the temperature of these surfaces.

METHOD OF NUMERICAL SOLUTION AND RESULTS OF CALCULATIONS

The method of solution is similar to that used for mathematical simulation of steady-state motion of an optical discharge along the CO_2 laser beam in the slow combustion mode. The method was developed in [16, 17]. The steady-state solution of the set of simultaneous Eqs. (5), (6), (9), and (12) was sought. For this purpose, the time derivative of the plasma temperature T was added to the left-hand side of Eq. (5). The iterative solution of the problem consisted of two stages. At the first stage, the laser radiation field and group spectral densities of radiant energy at a given instant of time were determined on the basis of a given temperature field. The values of Q and W_L were calculated. These values were then used for solving the evolutionary problem of the temperature T calculation.

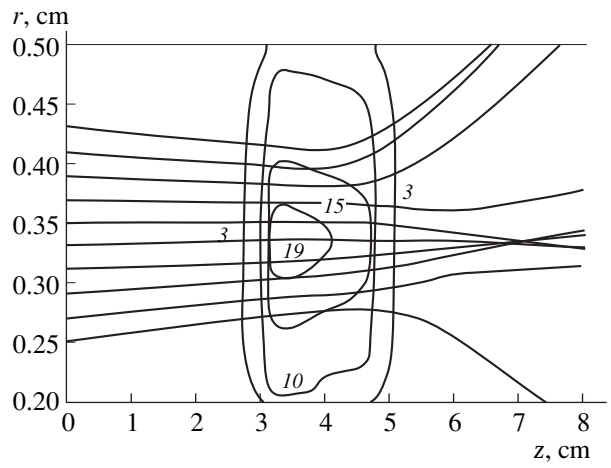

Fig. 1. Isotherms and laser beam paths through the COD core plasma in the interelectrode space of TELEC under no-load conditions: x_1 = 0.2 cm; r_2 = 0.5 cm; laser radiation power, 100 kW; T_E = 2000 K; T_C = 1000 K; J_E = 500 A/cm^2; P = 1 atm; and F = 15 cm. The temperature values (kK) are given near isotherms.

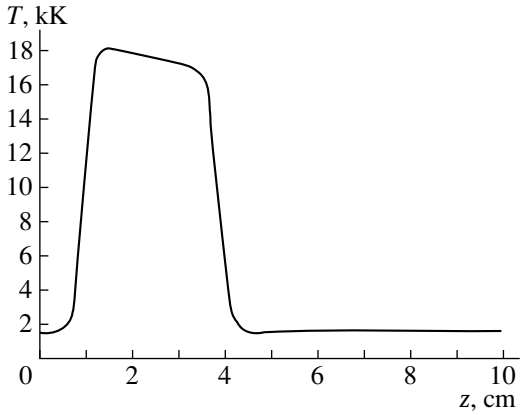

Fig. 3. Plasma temperature distribution along the z-axis under no-load conditions: r_1 = 0.2 cm; r_2 = 0.5 cm; laser radiation power, 169 kW; T_E = 2000 K; T_C = 1000 K; J_E = 500 A/cm^2; P = 0.5 atm; and F = 15 cm.

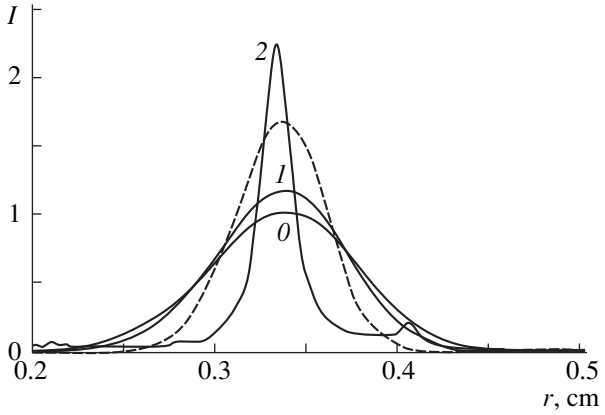

Fig. 2. Radial distribution of laser radiation intensity (relative units) under the same conditions as in Fig. 1: (*0*) z = 0 cm; (*1*) z = 2 cm; and (*2*) z = 6 cm.

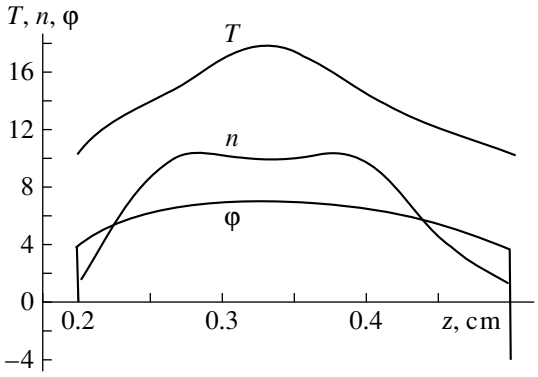

Fig. 4. Radial distribution of the plasma temperature (in kK), electron concentration (normalized to 10^{16} cm^{-3}), and the electric field potential (in V) under the same conditions as in Fig. 3.

Then, the laser and heat radiation fields were recalculated and the evolutionary equation for T was solved again. This process was iterated until a steady-state solution was obtained. The iterative method is described in more detail in [21].

The electrode temperature for argon-filled TELEC was ~10^3 K at argon pressure $P \sim 1$ atm. A tubular laser beam (wavelength 5.3 μm) directed along the z-axis was focused on a ring in the middle of the emitter–collector gap at a distance F from the TELEC input (z = 0). Both emitter and collector were implemented as two coaxial cylinders of radius r_1 and r_2, respectively. The axially symmetrical geometry was selected to make the mathematical simulation of TELEC less sophisticated. Besides, it was taken into account that the emitter area should far exceed the collector area to provide effective operation of TELEC. The laser beam was assumed to be totally reflected from the electrodes, whereas the plasma radiation was assumed to be totally absorbed by the electrodes. The value of eJ_E was taken to be sufficiently high (hundreds of A/cm^2) to attain a high efficiency of TELEC operation. Such values of J_E can be achieved using a packed tungsten emitter consisting of a great number of small tungsten wires. It is necessary to provide diffusion of cesium vapors through the emitter [11]. According to the experimental data [11], the electron emission current density increased with increasing temperature T_R of the cesium tank incorporated in the emitter. At T_E = 2000 K and T_R = 693 K, the electron emission current density exceeded 200 A/cm^2. It should be noted, however, that the operation of packed emitters is as yet imperfectly understood. Experimental studies [11] showed that the injection of small amounts of cesium (≈10^3 Pa) into the interelectrode space had no effect on the COD characteristics. Thus, emitters based on refractory metals with equilibrium films of adsorbed cesium seem to be appropriate for TELEC (such emitters are commonly used in TIC).

Typical distribution of the COD core plasma temperature over the interelectrode space of TELEC is shown in Fig. 1. The longitudinal (along the *z*-axis) size of the high-temperature region of COD is approximately 2 cm, which far exceeds the interelectrode distance (0.3 cm). The plasma temperature in the middle of the interelectrode gap reaches 20 kK; near the interface between the discharge core and nonequilibrium near-electrode regions, the plasma temperature is about 10 kK. Thus, the electron temperature in the nonequilibrium near-electrode regions is rather high (the TELEC output voltage depends on this temperature [8]). The laser beam trajectories calculated in the geometrical optics approximation are shown in Fig. 1. Refraction and absorption of laser radiation causes significant variations in the laser radiation intensity distribution over the beam cross section (Fig. 2). The laser radiation intensity distribution at a distance $z = 6$ cm, calculated without regard for the laser beam interaction with the plasma, is shown in Fig. 2 for comparison (dashed-line curve). It is seen that despite the absorption of laser radiation by plasma, its intensity can exceed that of laser radiation not interacting with plasma due to the laser beam self-focusing. The plasma temperature distribution along the *z*-axis at $P = 0.5$ atm is shown in Fig. 3. The discharge length increases with decreasing pressure, while the discharge becomes more uniform along the *z*-axis. A decrease in the pressure also causes a decrease in the density of the energy flux transferred from the discharge to the electrodes by intrinsic plasma radiation. Radial distributions of the plasma temperature, electron concentration, and electric field potential in the middle cross section of the discharge ($z = 2.5$ cm) are shown in Fig. 4. A significant temperature drop across thin ($\sim 10^{-3}$–10^{-2} cm) near-electrode regions causes a considerable heat energy flux ($\sim 10^2$–10^3 W/cm^2) transferred by HCP from the discharge core to the electrodes. A great deal of energy is spent producing ions in the nonequilibrium regions because of the high temperature of the near-electrode plasma. The main energy losses, however, are due to intrinsic plasma radiation (10^3–10^4 W/cm^2). In the middle of the interelectrode gap, plasma is almost fully ionized and slightly overheated (a slight minimum of the electron concentration *n* in the middle of the gap), whereas the near-electrode plasma is weakly ionized. The electric field potential distribution over the interelectrode space exhibits a significant jump (~10 V) near the electrodes and a relatively small drop across the discharge core (~1 V).

Thus, a set of simultaneous equations describing the equilibrium COD core in TELEC, as well as the boundary conditions for the set and a method for its numerical solution were developed in this work. The solution of this set of simultaneous equations allows the distribution of plasma parameters over the interelectrode space and the energy characteristics of the converter to be determined. The results of mathematical simulation will be considered in detail in a separate work.

ACKNOWLEDGMENTS

This work was supported by the Russian Foundation for Basic Research, project no. 97-02-17583.

REFERENCES

1. P. E. Glaser, J. Energy **1** (2), 75 (1977).
2. V. A. Vanke, V. M. Lopukhin, and V. L. Savin, Usp. Fiz. Nauk **123**, 633 (1977) [Sov. Phys. Usp. **20**, 989 (1977)].
3. V. A. Grilikhes, *Solar Power-Generating Plants in Space* (Nauka, Leningrad, 1986).
4. M. Nagatomo, S. Sasaki, Y. Naruo, and V. A. Vanke, Usp. Fiz. Nauk **164**, 631 (1994).
5. R. J. Lipinski and D. A. McArthur, in *Proceedings of the Conference "Arzamas-16," Russian Federal Nuclear Center, Institute of Experimental Physics, 1995*, p. 44.
6. *Space Technology and Applications International Forum*, Ed. M. S. El-Genk, (American Institute of Physics, Woodbury, 1998), Part 3, p. 1073; p. 1212.
7. N. S. Rasor, in *Laser-Energy Conversion Symposium* (NASA Ames Research Center, 1973), NASA TM X-62, pp. 51–62.
8. J. F. Waymouth, J. Inst. Electr. Eng. **8** (8), 380 (1962).
9. E. J. Britt, in *Radiation Energy Conversion in Space: Technical Papers of the 3rd NASA Conference, New York, 1978*, p. 421.
10. D. L. Alger, E. J. Manista, and R. W. Thompson, in *Radiation Energy Conversion in Space: Technical Papers of the 3rd NASA Conference, New York, 1978*, p. 437.
11. N. P. Kozlov, A. V. Pekshev, Yu. S. Protasov, and V. I. Suslov, in *Radiation Plasmodynamics* (Énergoatomizdat, Moscow, 1991), Vol. 1, pp. 462–498.
12. Yu. P. Raizer and S. T. Surzhikov, in *Proceedings of the 26th AIAA Plasmadynamics and Laser Conference, San Diego, 1995*, AIAA Paper 95–1999.
13. S. T. Surzhikov, *Computational Experiment in the Construction of Models for Radiating Gas Mechanics* (Nauka, Moscow, 1992).
14. F. G. Baksht, G. A. Dyuzhev, A. M. Martsinovskiĭ, *et al.*, *Thermionic Converters and Low-Temperature Plasma* (Nauka, Moscow, 1973).
15. I. P. Stakhanov, A. S. Stepanov, V. P. Pashchenko, and Yu. K. Gus'kov, *Plasma Thermionic Conversion of Energy* (Atomizdat, Moscow, 1968).
16. S. T. Surzhikov, Mat. Model. **7** (8), 3 (1995).
17. A. P. Budnik, A. S. Vakulovskiĭ, A. G. Popov, and S. T. Surzhikov, Mat. Model. **8** (5), 3 (1996).
18. S. M. Rytov, Yu. A. Kravtsov, and V. I. Tatarskiĭ, in *Introduction to Statistical Radio Physics* (Nauka, Moscow, 1978), Part 2.
19. Yu. P. Raizer, *Laser-Induced Discharge Phenomena* (Nauka, Moscow, 1974; Consultants Bureau, New York, 1977).
20. A. G. Shashkov and T. N. Abramenko, *Heat Conduction of Gaseous Mixtures* (Énergiya, Moscow, 1970).
21. I. V. Alekseeva, A. P. Budnik, V. A. Zherebtsov, and S. T. Surzhikov, Preprint No. 2679, FÉI (Institute of Physics and Power Engineering, Obninsk, 1998).

Translated by K. Chamorovskiĭ

Technical Physics, Vol. 45, No. 11, 2000, pp. 1470–1474. Translated from Zhurnal Tekhnicheskoĭ Fiziki, Vol. 70, No. 11, 2000, pp. 99–104.

The Sensitivity of Thermal-Lens and Phase-Shift (Interferometric) Techniques in Photothermal Spectroscopy: A Comparative Study

A. Yu. Luk'yanov and M. A. Novikov

Institute of Physics of Microstructures, Russian Academy of Sciences, Nizhni Novgorod, 603600 Russia
E-mail: luk@ipm.sci-nnov.ru

Received January 10, 2000

Abstract—The thermal-lens and phase-shift (interferometric) techniques of photothermal spectroscopy are studied theoretically for the coaxial and mutually orthogonal propagations of probing and pumping beams. Respective expressions for the amplitude of detected signals are derived for the case of the volume absorption of pumping radiation. The sensitivities of the two techniques are numerically analyzed for different parameter values. It is demonstrated that the phase technique offers higher sensitivity especially if the size of the region with a perturbed temperature field is much larger than the probing beam radius. © *2000 MAIK "Nauka/Interperiodica".*

During the last decade, methods of photothermal (thermal wave) spectroscopy have gained acceptance in microscopy, nondestructive testing characterization of thermal properties of objects and media, impurity or contamination control, etc. Focus is placed on optical methods, since they are contactless and offer high sensitivity and spatial resolution. The photothermal deflection technique (PDT) and the thermal-lens technique (TLT) remain the most popular in this field, owing to their simplicity. The principal features of the two approaches are well understood, especially in the ray-optics approximation [1, 2]. Less frequently used and hence less explored is the interferometric (or phase-shift) technique (IT). Too little effort, however, has been put into comparing the capabilities of the PDT, TLT, and IT. One could cite only a few studies on this subject. For example, [3] presents a comparative ray-optics analysis of the ultimate sensitivity for the three techniques in certain limiting cases of volume optical absorption in the test object, whereas [4] compares photothermal signals for the PDT and IT in the case of surface absorption.

This study analyzes photothermal signals detected with the IT and TLT in the case of volume absorption. We compute them according to the approach suggested in [4]. It consists in solving a diffraction problem and amounts to computing the Fresnel–Kirchhoff integral. Thus, it works beyond the ray-optics approximation.

We start with the coaxial-beam configuration (Fig. 1). The temperature distribution is cylindrically symmetric, so that we can write the heat diffusion equation in cylindrical coordinates. Consider sinusoidally modulated continuous pumping with a Gaussian intensity distribution. Consequently, the heat equation reads as

$$\frac{1}{r}\frac{\partial}{\partial r}\left(r\frac{\partial T}{\partial r}\right)+\frac{\partial^2 T}{\partial z^2}-\frac{1}{\chi}\frac{\partial T}{\partial t}=-\frac{Q(r,\varphi,z,t)}{K}, \qquad (1)$$

where

$$Q(r,\varphi,z,t)=\alpha\frac{P_{\text{pump}}}{\pi r_{\text{pump}}^2}\exp\left(-\frac{2r^2}{r_{\text{pump}}^2}\right)\cos\Omega t, \qquad (2)$$

r_{pump} is the pumping beam radius; P_{pump} is the average pump power; K is the thermal conductivity; $\chi = K/(\rho c)$ is the thermal diffusivity; and ρ and c are the density and heat capacity, respectively.

Neglecting heat transfer along the z axis, we express temperature oscillation at a pump-modulation angular frequency Ω as

$$T_\Omega(r, z=0, \varphi, t)=\text{Re}\left\{\int_0^\infty \xi d\xi J_0(r\xi)\right.$$
$$\left.\times\left(\frac{\alpha}{K}\frac{P_{\text{pump}}}{2\pi}e^{-\xi^2 r_{\text{pump}}^2/8}\right)\frac{e^{i\Omega t}}{\xi^2+i\Omega/\chi}\right\}. \qquad (3)$$

Let l denote the length of the heated region. Having passed through it, a probing light wave of wavelength λ_{probe} acquires an additional phase shift. If the thermal lens is thin, the phase shift is

$$\Phi(r,\varphi,t)=\frac{2\pi}{\lambda_{\text{probe}}}\frac{\partial n}{\partial T}\int_{-1/2}^{1/2} T(r,z,\varphi,t)dz$$
$$=\frac{2\pi}{\lambda_{\text{probe}}}\frac{\partial n}{\partial T}lT_\Omega(r,z=0,\varphi,t). \qquad (4)$$

1063-7842/00/4511-1470$20.00

Now, let us find the amplitude distribution of the probing beam in the far-field zone, where a photodetector is situated. In the cylindrical coordinates, the Fresnel–Kirchhoff integral has the form

$$U(r', \varphi', t) = \frac{i}{\lambda_{\text{probe}} L}\int d\varphi \int r dr U(r, z = 0, \varphi, t) \times \exp\left\{-\frac{ik}{2L}[r^2 + r'^2 - 2rr'\cos(\varphi - \varphi')]\right\}, \quad (5)$$

where L is the distance from the heated region to the photodetector, k is the probing beam wavenumber, and $U(r, z = 0, \varphi)$ is the probing beam amplitude in the heated region.

We are interested in thermal perturbations small enough to satisfy the approximation

$$U(r, z = 0, \varphi, t) = U_0(r, z = 0, \varphi)e^{i\Phi(t)} \approx U_0(r, \varphi)(1 - i\Phi(t)). \quad (6)$$

Here, U_0 is the probing beam amplitude in the absence of the thermal perturbations. Following [5], we adopt a Gaussian distribution for the amplitude:

$$U(r, z = 0, \varphi, t) = E_0\frac{\omega_0}{\omega(z_1)}\exp\left[-r^2\left(\frac{1}{\omega^2(z_1)} + \frac{ik}{2R(z_1)}\right)\right],$$

$$\omega^2(z) = \omega^2(1 + z^2/z_0^2), \quad R(z) = z(1 + z_0^2/z^2),$$

$$z_0 = \pi\omega^2 n/\lambda_{\text{probe}}.$$

Consequently, the intensity distribution of the probing beam in the far-field zone has the form

$$I(r', \varphi', t) = |U(r', \varphi', t)|^2 = I_0(r', \varphi') + U_0^*(r', \varphi') \times \Delta U(r', \varphi', t)U_0(r', \varphi')\Delta U^*(r', \varphi', t). \quad (7)$$

Here, $I_0(r', \varphi')$ is the unperturbed intensity distribution and

$$\Delta U(r', \varphi', t) = -\frac{1}{\lambda_{\text{probe}} L} \times \int d\varphi \int r dr U_0(r', \varphi', t)\Phi(r, \varphi, z, t) \times \exp\left\{-\frac{ik}{2L}[r^2 + r'^2 - 2rr'\cos(\varphi - \varphi')]\right\}. \quad (8)$$

With the TLT, thermal perturbations are usually sensed by a photodetector with a circular diaphragm placed in front of it. Then the TLT signal is proportional

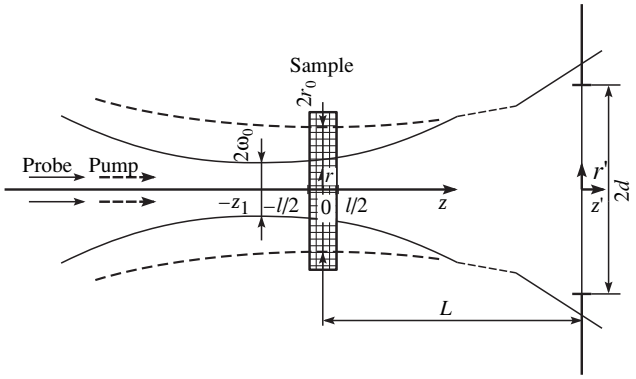

Fig. 1. Coaxial-beam configuration. The length of the test sample is shorter than that of the pumping beam waist.

to a change in the probing beam intensity after the diaphragm, ΔI_{T1}, which is expressed as

$$\Delta I_{T1}(t) = \eta\int_0^d r' dr' \int_{-\pi}^{\pi} d\varphi [U_0^*(r', \varphi')\Delta U(r', \varphi', t) + U_0(r', \varphi')\Delta U^*(r', \varphi', t)], \quad (9)$$

where η is the quantum yield of the photodetector and d is the diaphragm radius.

Inserting (8) into (9), we obtain

$$\Delta I_{T1}(t) = -\eta\iint r dr d\varphi |U_0|^2 \Phi(r, \varphi, t) \times \mathrm{Im}\left\langle \omega_0^2\left(1 + i\frac{z_1}{z_0}\right)\exp\left\{\frac{r^2}{\omega_0^2(1 + iz_1/z_0)}\right\} \times \int_0^{kd/L} \exp\left\{-\frac{\xi^2}{4}\omega_0^2\left(1 + i\frac{z_1}{z_0}\right)\right\} J_0(\xi r)\xi d\xi\right\rangle, \quad (10)$$

where $J_0(\xi r)$ is the Bessel function of the first kind.

Inserting the expression for $\Phi(r, \varphi, t)$ into (10), we finally arrive at the formula for the TLT signal amplitude normalized to the probing beam intensity:

$$\mathrm{TlSignal}_{\parallel} = \frac{\pi\omega_0^4}{\lambda}\frac{\partial n}{\partial T}\frac{\alpha l}{K}P_{\text{pump}}\mathrm{Abs}\left(\int_0^{kd/L} \xi d\xi \exp\left\{-\frac{\xi^2\omega_0^2}{2}\right\} \times \int_0^{\infty} \frac{\lambda d\lambda}{\lambda^2 + i\Omega/\chi}\mathrm{Im}\left[I_0\left\{\frac{\lambda\xi}{2}\omega_0^2\left(1 - i\frac{z_1}{z_0}\right)\right\} \times \exp\left\{-\frac{\lambda^2}{4}\left[\frac{r_{\text{pump}}^2}{2} + \omega_0^2\left(1 - \frac{z_1}{z_0}i\right)\right]\right\}\right]\right), \quad (11)$$

where $I_0(\xi r)$ is the modified Bessel function of the first kind.

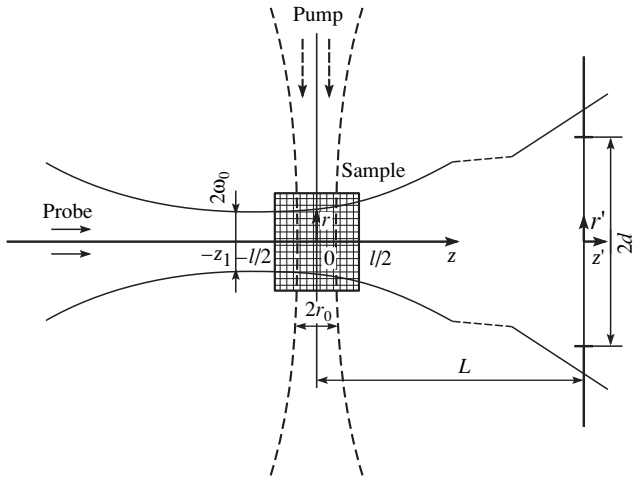

Fig. 2. Orthogonal-beam configuration. The two beams intersect inside the test sample.

Formula (11) describes the TLT signal in general terms. To maximize the amplitude, one should find the optimal values of kd/L and z_1.

Now, let us proceed to IT detection. According to this technique, the additional phase shift of the probing light wave is detected with an interferometer: one of its beams passes through the heated region, whereas the other beam goes outside it. Several types of optical interferometer can detect thermal waves [6–8]. We prefer polarization interferometers [9]. They enjoy high stability, high sensitivity, and small overall dimensions [10]. Moreover, they are free from optical loss. In the IT, the intensity distribution at the photodetector aperture is given by

$$\begin{aligned} I(r', \varphi', t) &= \left|U(r', \varphi', t) + U_{\text{ref}}(r', \varphi', t)^2\right| \\ &= \left|U_0(r', \varphi')^2\right| \cos^2\frac{\delta}{2} + \frac{1}{2}\cos\frac{\delta}{2} \\ &\times (U_0'(r', \varphi')\Delta U'^*(r', \varphi', t)e^{i\delta/2} \\ &+ \Delta U(r', \varphi', t)U_0'^*(r', \varphi')e^{i\delta/2}), \end{aligned} \tag{12}$$

where δ is the constant phase difference between the interferometer beams,

$$U_{\text{ref}}'(r', \varphi) = U_0'(r', \varphi')e^{i\delta}, \tag{13}$$

$$U'(r', \varphi') = U_0'(r', \varphi') + \Delta U'(r', \varphi', t). \tag{14}$$

Integrating the last term in (14) over the primed variables, we obtain the magnitude of the photothermal signal:

$$\Delta I_{\text{phsh}}(t) = \eta \sin\delta \int_{-\pi}^{\pi} d\varphi \int_0^{\infty} dr r |U_0(r, \varphi)|^2 \Phi(r, \varphi, t). \tag{15}$$

As one would expect, the signal is maximum if $\delta = \pi/2$. In what follows, we assume δ to equal this value.

Inserting the expression for $\Phi(r, \varphi, t)$ into (15), we arrive at the formula for the IT signal amplitude normalized to the probing beam intensity:

$$\begin{aligned} \text{IntSignal}_{\parallel} &= \frac{\omega_0^2}{8\lambda_{\text{probe}}}\frac{\partial n}{\partial T}\frac{\alpha l}{K}P_{\text{pump}} \\ &\times \text{Abs}\left[Ei\left(-\frac{i\Omega}{\chi}\frac{r_{\text{pump}}^2 + \omega_0^2}{8}\right)\right], \end{aligned} \tag{16}$$

where

$$E_i(x) = \int_{-\infty}^{x} \frac{e^t}{t} dt$$

is the exponential integral.

Now, let us look at the orthogonal configuration (Fig. 2). The corresponding temperature distribution at the angular frequency Ω is

$$\begin{aligned} T_{\Omega}(x, y, z, t) &= \text{Re}\int_0^{\infty} \xi d\xi \frac{\alpha}{K}\frac{P_{\text{pump}}}{2\pi} J_0(\xi\sqrt{y^2 + z^2}) \\ &\times e^{-\frac{\xi^2 r_{\text{pump}}^2}{8}} \frac{e^{i\Omega t}}{\xi^2 + i\Omega/\chi}, \end{aligned} \tag{17}$$

where x, y, and z are the Cartesian coordinates.

Assuming the length of the cell to be much larger than the size of the region with the perturbed temperature distribution, we express the probing beam phase as

$$\Phi_{\Omega}(x, y, t) = \frac{2\pi}{\lambda_{\text{probe}}}\frac{\partial n}{\partial T}\int_{-\infty}^{\infty} dz T(x, y, z, t). \tag{18}$$

Applying the above computing procedure, we obtain expressions for the IT and TLT signal amplitudes normalized to the probing beam intensity:

$$\begin{aligned} \text{IntSignal}_{\perp} &= \frac{\pi^2}{2}\sqrt{\frac{\chi}{\Omega}}\frac{\omega_0^2}{\lambda_{\text{probe}}}\frac{\partial n}{\partial T}\frac{\alpha l}{K}P_{\text{pump}} \\ &\times \text{Abs}\left[\text{Erfc}\left(\sqrt{\frac{\Omega}{\chi}\frac{r_{\text{pump}}^2 + \omega_0^2}{8}e^{i\pi/4}}\right)\right], \end{aligned} \tag{19}$$

$$\begin{aligned} \text{TlSignal}_{\perp} &= 2\pi\frac{\omega_0^4}{\lambda_{\text{probe}}}\frac{\partial n}{\partial T}\frac{\alpha l}{K}P_{\text{pump}}\text{Abs}\left(\int_0^{kd/L} dt\right. \\ &\times \exp\left\{-\frac{t^2\omega_0^2}{2}\right\} t\int_0^{\infty}\frac{dx}{x^2 + i\Omega/\chi}\text{Im}\left[I_0\left\{\frac{tx}{2}\omega_0^2\left(1 - i\frac{z}{z_0}\right)\right\}\right. \\ &\left.\left.\times \exp\left\{-\frac{x^2}{4}\left[\frac{r_0^2}{2} + \omega_0^2\left(1 - \frac{z}{z_0}i\right)\right]\right\}\right]\right). \end{aligned} \tag{20}$$

To compare the sensitivities of the two techniques, let us evaluate the sensitivity ratio

$$\left(\frac{\text{IntSigmal}}{\text{IntNoise}}\right)/\left(\frac{\text{TlSignal}}{\text{TlNoise}}\right).$$

We will take into account only probing beam shot noise. Then,

$$\left(\frac{\text{IntSignal}}{\text{IntNoise}}\right)/\left(\frac{\text{TlSignal}}{\text{TlNoise}}\right) = \frac{\text{IntSignal}}{\text{TlSignal}}\left(1-\exp\left(-\frac{\omega_0^2 k^2 d^2}{2L^2}\right)\right)^{1/2}. \quad (21)$$

For the two configurations, the sensitivity ratios behave similarly except that the slope of the curves is somewhat larger for the orthogonal configuration. We therefore restrict our investigation to the dependences of

$$\left(\frac{\text{IntSignal}}{\text{IntNoise}}\right)/\left(\frac{\text{TlSignal}}{\text{TlNoise}}\right)$$

on $f = 2\pi\Omega$ and r_{pump} for the coaxial configuration and on K and probing beam radius for the orthogonal configuration.

Figure 3 shows the sensitivity ratio plotted against r_{pump} for three values of f. If r_{pump} is so small that the thermal diffusion length is much greater than r_0, the sensitivity ratio is independent of r_0, since the heat source can be considered as a point. If the thermal diffusion length is much less than r_0, the sensitivity ratio rises steeply and is no longer dependent on Ω, since the shape of the thermal perturbation approaches that of the pumping beam.

Figure 4 shows the sensitivity ratio plotted against the modulation frequency for three values of the probing beam radius w_0. It is seen that the IT signal grows faster than the TLT signal as the frequency decreases, especially at small $w_{0,s}$. Qualitatively, this stems from the fact that a decrease in f leads to the expansion of the heated region, so that the absolute values of the temperature rise faster than its coordinate derivatives governing the generation of the TLT signal.

The above explanation also applies to the faster growth of the IT signal as a function of K for the orthogonal configuration (Fig. 5).

Figure 6 displays the sensitivity ratio versus the probing beam radius at three values of f for the orthogonal configuration. Notice that the IT signal increases faster as the radius decreases. In qualitative terms, this is due to the facts that the edge of the thermal lens, like that of any other lens, has a stronger effect and that the

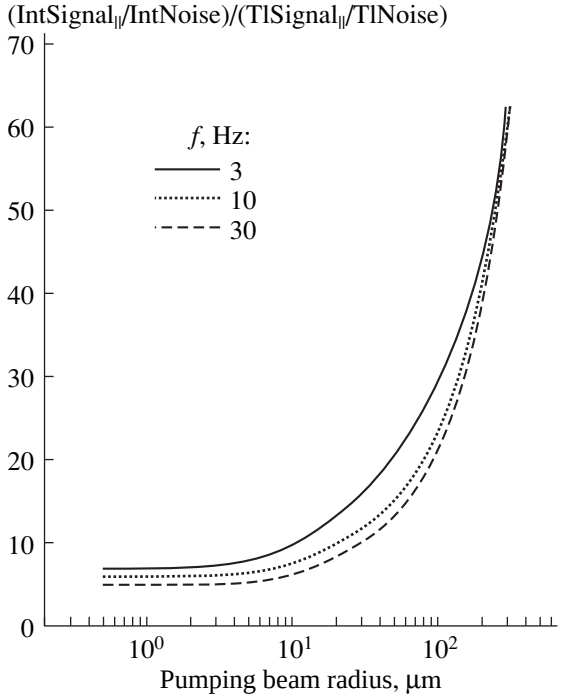

Fig. 3. Coaxial-beam configuration: the sensitivity ratio vs. the pumping beam radius for three values of the modulation frequency at $K = 1.5 \times 10^{-3}$ W/(cm deg), $\rho = 0.9$ g/cm^3, $c = 2$ J/(g deg), and $w_0 = 3$ μm.

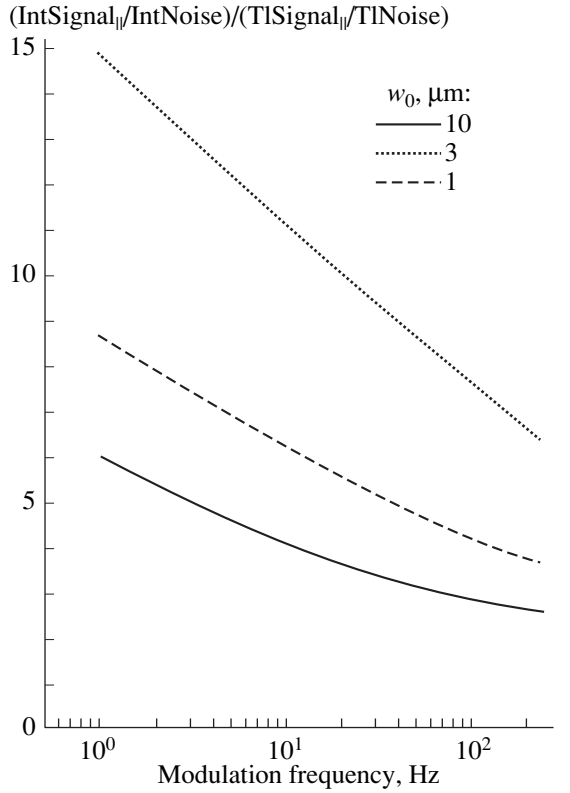

Fig. 4. Coaxial-beam configuration: the sensitivity ratio vs. the modulation frequency for three values of the probing beam radius at $K = 0.32$ W/(cm deg), $\rho = 0.9$ g/cm^3, $c = 2$ J/(g deg), and $r_0 = 10$ μm.

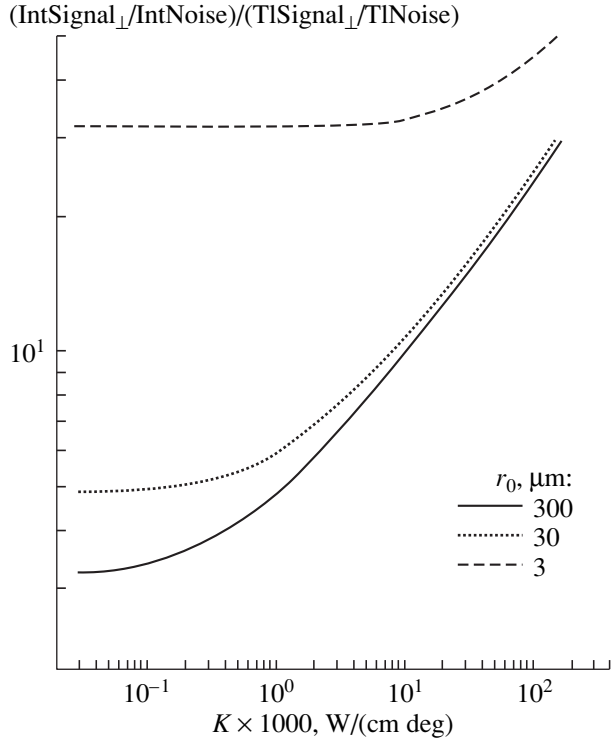

Fig. 5. Orthogonal-beam configuration: the sensitivity ratio vs. the thermal conductivity at $\rho = 0.9$ g/cm^3, $c = 2$ J/(g deg), $\omega_0 = 3$ μm, and $f = 10$ Hz.

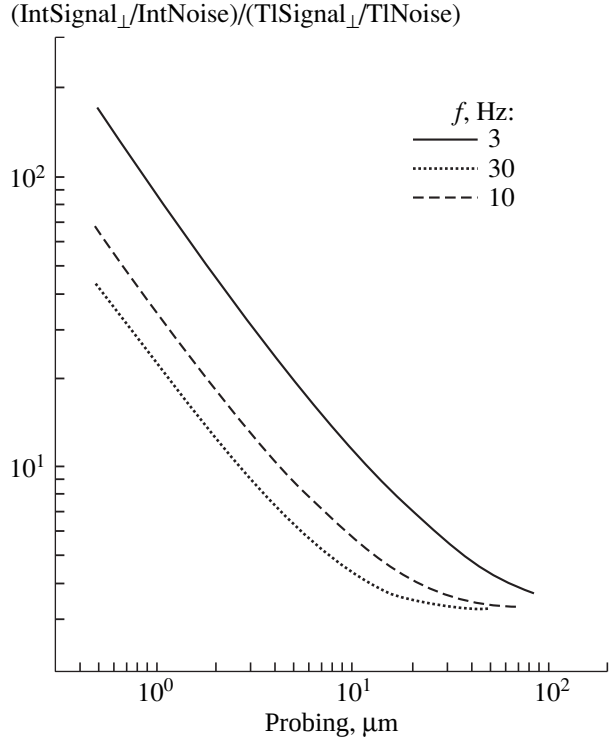

Fig. 6. Orthogonal-beam configuration: the sensitivity ratio vs. the probing beam radius at $K = 1.5 \times 10^{-3}$ W/(cm deg), $\rho = 0.9$ g/cm^3, $c = 2$ J/(g deg), and $r_0 = 10$ μm.

phase shift of the probing light is maximum at the center of the heated region.

If technical noise, whose magnitude is proportional to the probing light intensity, dominates, then the ratio

$$\left(\frac{\text{IntSignal}}{\text{IntNoise}}\right)/\left(\frac{\text{TlSignal}}{\text{TlNoise}}\right) = \frac{\text{IntSignal}}{\text{TlSignal}}\left(1 - \exp\left(-\frac{\omega_0^2 k^2 d^2}{2L^2}\right)\right)$$

and the associated dependences are basically the same as in the above.

In summary, the interferometric approach has been found to offer higher sensitivity than the thermal-lens one in all of the cases concerned, especially if the size of the perturbed-temperature region is larger than the probing beam radius.

REFERENCES

1. *Photoacoustic and Photothermal Phenomena III*, Ed. by D. Bićanić, (Springer, Berlin, 1992).
2. A. Mandelis, *Principles & Perspectives of Photothermal and Photoacoustic Phenomena* (Elsevier, New York, 1992).
3. P. K. Brazhnik and M. A. Novikov, Opt. Spektrosk. **70**, 453 (1991) [Opt. Spectrosc. **70**, 264 (1991)].
4. A. L. Glazov and K. L. Muratikov, Zh. Tekh. Fiz. **61** (11), 187 (1991) [Sov. Phys. Tech. Phys. **36**, 1302 (1991)].
5. A. Yariv, *Quantum Electronics*, 3rd ed. (Sov. Radio, Moscow, 1980; Wiley, New York, 1989).
6. A. L. Glasov and K. L. Muratikov, Int. J. Optoelectron. **4**, 589 (1989).
7. P. K. Brazhnik, M. A. Novikov, and A. A. Pushkin, Opt. Spektrosk. **68**, 631 (1990) [Opt. Spectrosc. **68**, 368 (1990)].
8. W. Faubel, B. S. Seidel, and H. J. Ache, Opt. Eng. **35**, 3555 (1996).
9. A. Yu. Luk'yanov, G. B. Vladykin, A. A. Aratskova, *et al.*, Zh. Fiz. Khim. **71**, 1497 (1997).
10. M. Francon and S. Mallick, *Polarization Interferometers: Application in Microscopy and Macroscopy* (Academic, New York, 1971).

Translated by A. Sharshakov

Technical Physics, Vol. 45, No. 11, 2000, pp. 1475–1477. Translated from Zhurnal Tekhnicheskoĭ Fiziki, Vol. 70, No. 11, 2000, pp. 105–107.

RADIOPHYSICS

Energy Extraction from an Oversized Cavity through a Package of Interference Switches with Summation of the Output Signals

S. N. Artemenko, V. A. Avgustinovich, P. Yu. Chumerin, and Yu. G. Yushkov

Research Institute of Nuclear Physics, Tomsk Polytechnical University, Tomsk, 634050 Russia

Received December 30, 1999

Abstract—It was shown experimentally that the pulse power output of a resonant microwave compressor with an oversized cavity and an interference switch used for energy extraction could be increased using a package of interference switches with summation of the output signals instead of a single switch. The use of two switches for energy extraction provided an almost twofold increase in the output signal power and a corresponding (almost twofold) decrease in the signal duration. It is shown that energy extraction through four switches with signal summation is possible. *© 2000 MAIK "Nauka/Interperiodica".*

1. It is well known [1] that the density of electromagnetic wave power flux through waveguide transmission lines with gas insulation can reach 1–5 MW/cm^2. Therefore, the traveling wave power in oversized cavities with gas insulation and a cross section of ~10^2–10^3 cm^2 can reach 0.1–1 GW. The use of such cavities in resonant microwave compressors holds much promise. In addition to the high power of the traveling wave in the oversized cavity, resonant microwave compressors have advantages such as simple design, rather low weight, small dimensions, and the possibility of operation at a pulse repetition rate exceeding 1 kHz [2].

However, the lack of effective methods and devices for rapid energy extraction from a capacious energy storage is one of the main obstacles to the development of compressors on the basis of oversized cavities. The best known device for energy extraction (an interference switch based on rectangular waveguide tees [3]) does not provide sufficiently rapid energy extraction because of rather loose coupling between the tees and a capacious energy storage. So far, the search for more effective methods and devices for energy extraction has not met with any considerable success [4, 5].

The results of the well-known parallel compression experiment should be noted in this context [6]. In this experiment, energy was extracted from two synchronously excited resonant microwave compressors. Then, the output signals from the two compressors were summed up. The results of this experiment thus provide hope that the problem of rapid energy extraction from oversized cavities can be solved through the use of several identical switches for synchronous extraction of energy. It can be easily shown that the total peak power P of the output signal is determined in this case by the equation

$$P = nP_1 = n\beta_1 P_2/M_0^2, \quad (1)$$

while the signal duration τ is

$$\tau = \tau_1/n \approx TM_0^2/\beta_1 n, \quad (2)$$

where n is the number of switches; P_1 and τ_1 are the peak power and duration of the output signal for a single switch, respectively; β_1 is the switch–cavity coupling factor for a single switch; and P_2 and M_0^2 are the traveling wave power and power gain provided by the cavity, respectively.

As seen from Eq. (2), the number of switches providing maximum rate of energy extraction (i.e., extraction within the time interval comparable to the cavity round-trip time T) is determined by the expression

$$n \approx M_0^2/\beta_1. \quad (3)$$

The typical power gain M_0^2 provided by oversized resonators is approximately 10^3, whereas the attainable switch–cavity coupling factor β_1 is about 10^2. Thus, approximately ten switches are required to provide the maximum rate of energy extraction. According to Eq. (1), the total output signal power P is comparable in this case to the power of the traveling wave in the cavity.

The goal of this work was to describe the results of experimental study of synchronous energy extraction from an oversized 3-cm-range cavity through two and four switches with further summation of the output signals.

1063-7842/00/4511-1475$20.00

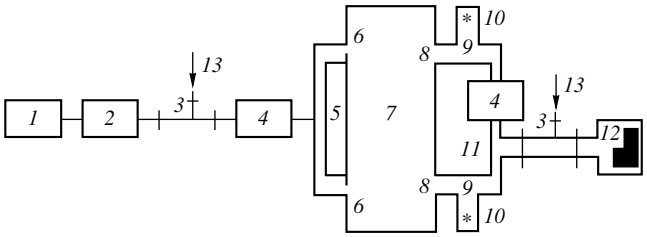

Fig. 1. Diagram of the experimental setup used for studying synchronous energy extraction from an oversized cavity through two interference switches.

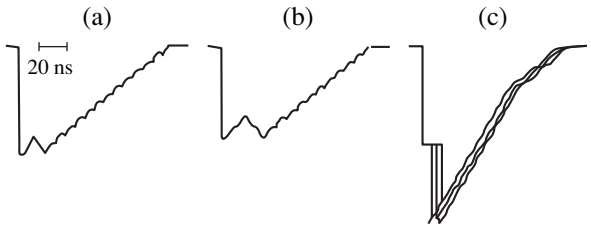

Fig. 2. Output pulse envelopes in the cases of (a, b) separate energy extraction through each of the switches, and (c) synchronous energy extraction through the two switches with further summation of the output signals.

2. A cylindrical cavity 90 mm in diameter and 200 mm in length was used in the experiment. A cavity operating at a frequency of 9.28 GHz was tuned to the $H_{01(11)}$ oscillation mode. To decrease the effect of intermodal interference at the coupling windows, the cavity was excited through two windows in one of the cavity lids. The windows were arranged on the same diameter at a half-radius distance from the center of the lid. The power from a microwave generator was delivered to the cavity through rectangular waveguides via a matched *E*-tee (Fig. 1). The intrinsic *Q*-factor of the cavity without switches was about 10^5.

The connection of two more waveguide switches to the other lid of the cavity through coupling windows with diameters of 10 mm (these windows were also arranged on the same diameter at a half-radius distance from the center of the lid) reduced the *Q*-factor of the system. The reduction in the *Q*-factor depended on the mutual arrangement of the input and output windows and the reach of the arm of the switches. To minimize the reduction in the *Q*-factor, the optimum reach of the arm was selected, and the windows were placed in the same longitudinal cross section of the cavity. Thus, a *Q*-factor value of $\sim 7 \times 10^4$ was attained. Optimization of the reach of the arm also provided the identical action of the separately opened switches and additive action of the switches during their synchronous opening. In tuning the system with two switches, the basic challenge was to select an optimum reach of the input arm and ensure equal field intensities in the switches. To assess the accuracy of the field intensity equalization, the signals at the output of switches with known coupling losses were compared in the amplitude accumulation mode. It was found that the field intensities in the switches were equal to each other with an accuracy of ~25%.

3. In the high-power operation mode, the system was powered by a magnetron generator with an output pulse power of ~60 kW and a pulse duration of ~1 μs. The diagram of the experimental setup used for studying synchronous energy extraction through two switches with further summation of the output signals is shown in Fig. 1: (*1*) microwave generator, (*2*) circulator, (*3*) directional couplers, (*4*) phase shifters, (*5*) matched waveguide *E*-tee, (*6*) input coupling windows, (*7*) oversized storage cavity, (*8*) output coupling windows, (*9*) interference switches, (*10*) spark gaps, (*11*) summing waveguide *H*-tee, (*12*) matched load, and (*13*) detector heads.

Synchronous operation of the switches was provided by applying high-voltage pulses from the same source to the gas-filled spark gaps of the switches. This induced microwave breakdowns in the switches. The output signals were summed up using the waveguide *H*-tee.

Oscillograms of the output pulse envelopes, obtained in the cases of separate energy extraction through each switch and synchronous energy extraction through the two switches with summation of the output signals, are shown in Figs. 2a–2c, respectively. As seen from Fig. 2, the output pulse duration in the case of energy extraction through one of the switches, the other one being turned off, was 60 and 80 ns for the first and second switches, respectively; in the case of synchronous energy extraction through two switches with further summation, the output pulse duration was ~35 ns, while the time spread of the signals to be summed up did not exceed 10 ns. The gain in the cases under consideration was 8, 7, and 10 ± 1 dB, respectively. Thus, synchronous extraction of energy provided almost a twofold decrease in the output pulse duration and a corresponding (almost twofold) increase in the summed up signal power.

4. The results of experimental study of energy extraction from the cavity through a package of four switches are similar to those considered above. As in the case of two switches, tuning of the system with four switches consisted in selecting an optimum reach of the arm, equalizing the field intensities in the switches, and determining optimum mutual arrangement of the input and output windows. In the cases with both two and four switches, the optimum reach of the arm was found to be approximately a quarter-wavelength. The output windows were arranged on two mutually orthogonal diameters at angles of 45° with respect to the diameter parallel to the line passing through the centers of the input windows. Upon tuning, the intrinsic *Q*-factor of the system with four switches was $\sim 6 \times 10^4$.

It should be noted that synchronous energy extraction through four switches with a further summation of signals could be performed even in the case of a considerable (two- to threefold) difference between the field intensities in the switches. In this case, however, an increase in the time spread of the summed up pulses was observed, while the amplitude and duration of pulses at the output of the switch with minimum field intensity varied with time. This was due to the fact that this switch came into action last, when the majority of energy had already been extracted through the other switches. Summation was performed separately for two pairs of the switches. The fact that the signal duration at the output of a given switch decreased as the other switches were sequentially turned on was used for monitoring the extraction synchronism.

It should also be noted that the process of energy extraction from the compressor through four switches was not completely additive. The signal amplitudes at the output of synchronously operating switches differed from the output signal amplitudes obtained in the case of the isolated operation of the switches. Presumably, this was caused by the switching-induced disturbance of the field in the cavity and corresponding changes in the switch–cavity coupling factor. Therefore, in contrast to energy extraction systems with a single switch [7], the optimum reach of the arm for systems with energy extraction through a package of switches is a quarter-wavelength. In this case, the symmetric arrangement of the switches about the cavity axis allows strong intermodal interference near the coupling windows to be compensated, whereas the invariability of the field structure in the cavity in changing from the storage mode to the extraction mode provides stability of the switch–cavity coupling.

5. Thus, it was shown that synchronous energy extraction from an oversized cavity through a package of interference switches allowed the energy extraction rate to be increased. Synchronous energy extraction with further summation of the output signals provided an increase in the total output signal power proportional to the number of switches, whereas the total output signal duration was found to be inversely proportional to the number of switches. In our opinion, this method for increasing the extraction rate can be used not only in conventional microwave compressors, but also in self-excited oscillators with pulse compression in the oscillatory system. These oscillators have relatively low Q-factors. Therefore, to provide effective operation of an oscillator in the compression mode, the extraction time should be comparable to the oscillatory-system round-trip time. It is also our opinion that compressors with energy extraction through a package of switches can be used in phased arrays.

ACKNOWLEDGMENTS

We are grateful to V. L. Kaminskiĭ for expert assistance. This work was supported by the Russian Foundation for Basic Research, project no. 97-02-16461.

REFERENCES

1. A. L. Fel'dshteĭn, L. R. Yavich, and V. P. Smirnov, *Handbook on Components of Waveguide Technology* (GÉI, Moscow, 1963).
2. V. L. Kaminskiĭ, S. A. Novikov, and S. V. Razin, Prib. Tekh. Éksp., No. 3, 103 (1999).
3. A. N. Didenko and Yu. G. Yushkov, *High-Power Nanosecond Microwave Pulses* (Énergoatomizdat, Moscow, 1984).
4. S. N. Artemenko, V. L. Kaminskiĭ, and Yu. G. Yushkov, Zh. Tekh. Fiz. **63** (2), 105 (1993) [Tech. Phys. **38**, 111 (1993)].
5. A. L. Vikharev, N. F. Kovalev, and M. I. Petelin, Pis'ma Zh. Tekh. Fiz. **22** (19), 41 (1996) [Tech. Phys. Lett. **22**, 795 (1996)].
6. S. A. Novikov, S. V. Razin, P. Yu. Chumerin, and Yu. G. Yushkov, Pis'ma Zh. Tekh. Fiz. **16** (20), 46 (1990) [Sov. Tech. Phys. Lett. **16**, 784 (1990)].
7. S. I. Artemenko, V. A. Avgustinovich, V. L. Kaminskiĭ, *et al.*, Radiotekh. Élektron. (Moscow) **42**, 1011 (1997).

Translated by K. Chamorovskiĭ

Technical Physics, Vol. 45, No. 11, 2000, pp. 1478–1488. Translated from Zhurnal Tekhnicheskoĭ Fiziki, Vol. 70, No. 11, 2000, pp. 108–117.

ELECTRON AND ION BEAMS, ACCELERATORS

Theoretical Investigation of Unstable Axial Mass-Selective Extraction of Ions from a Nonlinear Trap

M. Yu. Sudakov

Esenin State Pedagogical University, ul. Svobody 46, Ryazan, 390000 Russia

E-mail: Sudakov@qms.sotkom.ru

Received December 30, 1999

Abstract—The unstable axial mass-selective extraction of ions from a three-dimensional quadrupole ion trap is studied theoretically. A method for mapping the ion coordinates over the period of the RF power-supply voltage is developed with allowance for nonlinear distortions of the quadrupole potential. Equations for the envelope of ion oscillations are derived in the form of the equation of motion of a material point in the field of effective forces. The effect of the "delayed extraction" of ions in the presence of negative even field harmonics is explained. The positive even harmonics of the distorted quadrupole potential are shown to be favorable for ion extraction. The dynamics of the extracted ions is investigated. © *2000 MAIK "Nauka/Interperiodica".*

INTRODUCTION

The operation of Paul three-dimensional quadrupole ion traps in modern-day commercial mass spectrometers is based on the method of displacing the working point out of the stability domain. In the literature, this method is known as unstable axial mass-selective extraction (UAMSE) [1]. Investigation of the UAMSE revealed that, in a three-dimensional trap with hyperbolically shaped electrodes (Fig. 1a), the ion extraction is delayed; as a result, the neighboring spectral lines (emitted by ions with the closest masses) overlap and the mass resolution of the device worsens [2]. This effect stems from the fact that the quadrupole potential in a Paul trap is inevitably distorted because of the finite dimensions of the hyperbolic electrodes [3].

Numerical calculations [2] showed that, in the presence of positive even field harmonics, there is no delay of ion extraction. For this reason, the quadrupole field in actual mass spectrometers is nonlinearly distorted on purpose. One of the ways of distorting the quadrupole field in the desired manner is to increase the distance between the end electrodes and the center of the trap (Fig. 1b) up to $z_0 = r_0/\sqrt{2}$, in which case the electrode surfaces are equipotential surfaces of the quadrupole field. This method of "extending" the electrode system of a three-dimensional trap was implemented for the first time by the Finigan MAT Company in fabricating an ITD™–700 apparatus and was a company secret for a long time, until it was disclosed in [4]. Another method, specifically that of decreasing the asymptotic angle Θ of the electrode system (Fig. 1c), was implemented by the Bruker–Franzen Analytic GMbH Company in fabricating an ESQUIRE™ apparatus [5]. In both cases, the relative distortion of the geometry of the electrode system ($\Delta z_0/z_0$ or $2\Delta\Theta_0/\Theta_0$) amounted to approximately 10%. This gives rise to distortions of the quadrupole field in the form of even harmonics with positive amplitudes. Devices with such electrode systems are referred to as nonlinear ion traps [3].

Our study is aimed at constructing an analytic theory of the mass-selective extraction of ions from a nonlinear trap. For this purpose, we develop a method for mapping the ion coordinates over the period of the RF field. This new method makes it possible to thoroughly investigate ion motion during the UAMSE and to study the effect of nonlinear distortions of the quadrupole field.

EQUATIONS OF ION MOTION IN A NONLINEAR TRAP

In an axisymmetric ion trap, the electric field potential can be expanded in the field harmonics [3]

$$\varphi(\rho, \Theta, z, t) = V(t)\sum_{k>1} A_k P_k(\cos\Theta)\frac{\rho^k}{r_0^k}, \qquad (1)$$

where (ρ, Θ, z) are cylindrical coordinates, r_0 is the inner radius of a ring electrode (the "field radius"), P_k is the kth order Legendre polynomial, A_k are the amplitudes of the field harmonic, and the time-dependent periodic function $V(t + T) = V(t)$ describes the supply voltage.

In actual traps, the end electrodes are usually grounded and the supply voltage is applied to the ring electrode. Consequently, the function $-2V(t)$ is equal to the potential of the ring electrode with respect to the

1063-7842/00/4511-1478$20.00

end electrodes. Let the origin of the coordinates be at the point at which the potential is minimum. Then, we have $A_1 = 0$ and the remaining harmonics can be written as

$$k = 2: \rho^2 P_2(\cos\Theta) = -\frac{1}{2}(2z^2 - r^2) \quad \text{(quadrupole harmonic)}, \tag{2}$$

$$k = 3: \rho^3 P_3(\cos\Theta) = -\frac{1}{2}(2z^3 - 3zr^2) \quad \text{(hexapole harmonic)}, \tag{3}$$

$$k = 4: \rho^4 P_4(\cos\Theta) = -\frac{1}{8}(8z^4 - 24z^2r^2 + 3r^4) \quad \text{(octopole harmonic)}, \tag{4}$$

$$k = 5: \rho^5 P_5(\cos\Theta) = -\frac{1}{8}(8z^5 - 40z^3r^2 + 15zr^4) \quad \text{(decapole harmonic)}, \tag{5}$$

$$k = 6: \rho^6 P_6(\cos\Theta) = -\frac{1}{16}(16z^6 - 120z^4r^2 + 90z^2r^4 - 5r^6) \quad \text{(dodecapole harmonic)}. \tag{6}$$

For a trap with an ideal hyperbolic electrode system, we have $A_2 = 2$, and the higher field harmonics vanish. However, in real traps, the amplitude A_2 is somewhat different from 2 and the higher harmonics in potential (1) are nonzero. The motion of an ion with mass number M and positive charge e along the z-axis is described by the equation

$$M\frac{d^2z}{dt^2} + 2e\frac{A_2}{r_0^2}V(t)z = -eV(t)\frac{\partial}{\partial z}\sum_{k>2}A_kP_k(\cos\Theta)\frac{\rho^k}{r_0^k}.$$

In studies of the UAMSE, the ion motion in directions perpendicular to the axis of the trap is usually neglected [2] because, in industrial-scale devices, the ions move in a light buffer gas (helium at a pressure of 10^{-3} torr [1]). Collisions between ions and molecules of a buffer gas force ion oscillations in both the transverse and axial directions to damp. However, we cannot ignore ion oscillations in the axial direction, because, despite collisional damping, they grow and become unstable during the axial extraction. Under these assumptions, the above equation of motion reduces to the following equation describing ion motion in the axial direction:

$$\frac{d^2z}{dt^2} + 2\frac{e}{M}\frac{A_2}{r_0^2}V(t)z = -\frac{e}{M}V(t)\sum_{k>2}kA_k\frac{z^{k-1}}{r_0^k}. \tag{7}$$

If the supply voltage varies harmonically in time, $V(t) = U + V\cos(\omega_0 t)$, it is convenient to introduce the

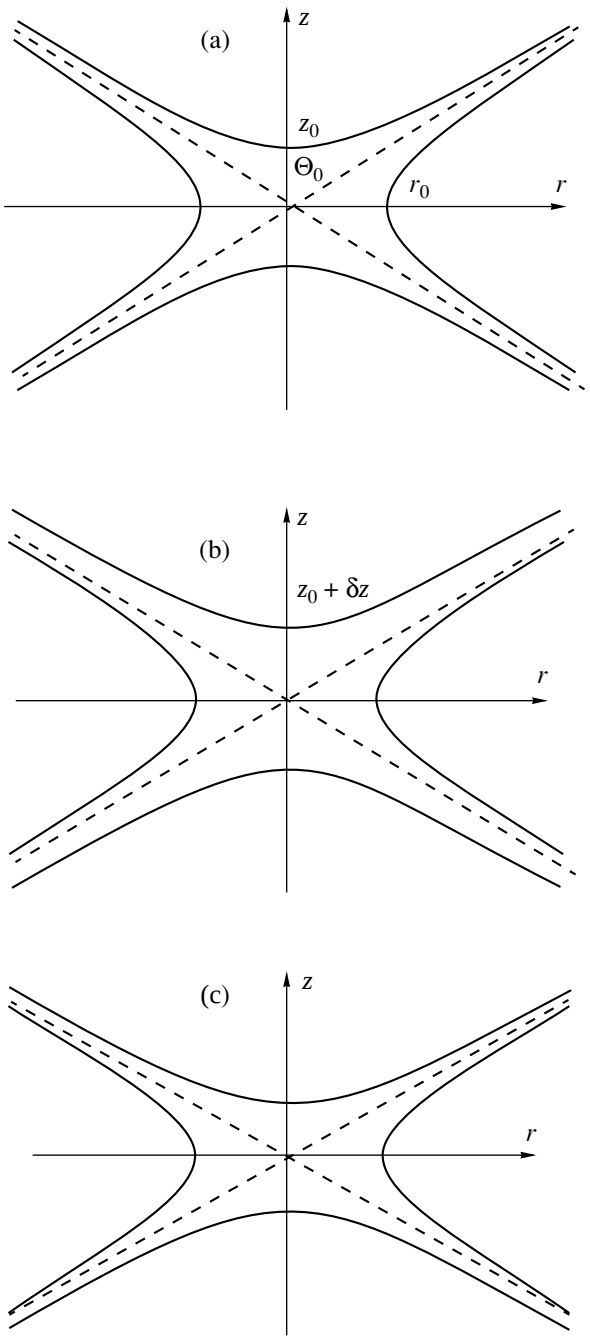

Fig. 1. Cross sections along the axis of rotation of the electrode system of the three most widely used three-dimensional traps. (a) A Paul trap in which the surfaces of all of the three electrodes—two end (caplike) electrodes and a ring electrode—are equipotential surfaces (hyperboloids of revolution) of the quadrupole field. The equipotential surfaces have a common asymptotic in the form of a cylindrical surface with an opening angle $\Theta_0 = 54.37°$ ($\tan\Theta_0 = \sqrt{2}$). The dashed lines show the cross section of this cylindrical surface. The distance $2z_0$ between the apexes of the end electrodes is related to the inner radius r_0 of the ring electrode by $z_0/r_0 = 1/\sqrt{2}$. (b) The trap fabricated by the Finigan MAT Company. (c) The trap fabricated by the Bruker–Franzen Analytic GMbH Company.

following dimensionless Mathieu parameters:

$$\xi = \frac{\omega_0 t}{2}, \quad a = \frac{8eA_2U}{Mr_0^2\omega_0^2}, \quad q = \frac{4eA_2V}{Mr_0^2\omega_0^2}, \qquad z_0 = \frac{r_0}{\sqrt{A_2}}, \tag{8}$$

where U is a constant potential difference between the end and ring electrodes, V is the amplitude of the harmonic part of the supply voltage, and z_0 is the distance from the center of the trap to the end electrodes (under the assumption that the electric field deviates from being quadrupole only slightly). Below, we will express the coordinates of an ion in units of z_0; in other words, in Eq. (7), we make the replacement $z(t) \longrightarrow z(\xi)z_0$. Also, the ion velocity will be expressed in units of $\omega_0 z_0/2$, which corresponds to the replacement $dz/dt \longrightarrow z'(\omega_0 z_0/2)$. Thus, the basic dimensionless equation of ion motion in the axial direction has the form

$$z'' + [a + 2q\cos(2\xi)]z = -\frac{1}{2}[a + 2q\cos(2\xi)]\sum_{k>2} k\alpha_k z^{k-1}, \tag{9}$$

where $\alpha_k = A_k/\sqrt{A_2^{k-2}}$ is the ratio of the amplitudes of the nonlinear field harmonics to the amplitude of the quadrupole harmonic.

METHOD OF MATRIX MAPPINGS

In the absence of nonlinear distortions, Eq. (9) reduces to the Mathieu equation, which is widely used in the theory of parametric resonances and whose properties have been studied very well [6]. In the (a, q) plane, we can plot the boundaries of the regions corresponding to the parametric resonance of ion oscillations (unstable ion motion). The ions with nonresonant values of a and q can be trapped in the quadrupole potential. As a result, we arrive at the stability diagram [6] of axial ion motion in the quadrupole field (Fig. 2). In the RF field regime ($a = 0$), the first stability domain lies between zero and $q_0 = 0.908047$. It is this domain that is used in the UAMSE method. For a prescribed initial amplitude V_{ini} of the supply voltage, the ions with masses larger than $M_b = 4eA_2V_{\text{ini}}/q_0 r_0^2 \omega^2$ are trapped in the quadrupole potential. As the voltage amplitude is gradually increased, the ions from each group with the same mass M leave the first stability domain (and, accordingly, the working volume of the trap) in increasing order of their masses (because the parameter q is inversely proportional to the ion mass). The escaping ions move toward the end electrodes and enter the detector system after passing through the holes in the end electrodes.

To describe the UAMSE theoretically requires a mathematical apparatus that would allow us to solve the Mathieu equation with the slowly varying parameters a and q and with nonlinear distortions (which strongly affect the ion extraction process) on the right-hand side. To do this, we develop the method of nonlinear mappings, which is based on the properties of nonlinear equations with periodically varying coefficients.

In the absence of nonlinear distortions and at constant values of a and q, the solution can be written as

$$z(n\pi + \tau) = x_n u_1(\tau) + v_n u_2(\tau), \tag{10a}$$

$$z'(n\pi + \tau) + x_n u_1'(\tau) + v_n u_2'(\tau), \quad 0 < \tau < \pi, \tag{10b}$$

where x_n and v_n are the coordinate and velocity of an ion at the beginning of the nth period of the RF field, the phase τ is assumed to be zero at the beginning of each period, and u_1 and u_2 are two solutions to the linear Mathieu equation with the initial conditions

$$u_1(0) = 1, \quad u_1'(0) = 0, \quad u_2(0) = 0, \quad u_2'(0) = 1. \tag{11}$$

We write Eqs. (10) at the end of a period of the RF field ($\tau = \pi$) in matrix form:

$$\begin{pmatrix} x_{n+1} \\ v_{n+1} \end{pmatrix} = U(\pi)\begin{pmatrix} x_n \\ v_n \end{pmatrix},$$

with

$$U(\tau) = \begin{bmatrix} u_1(\tau) & u_2(\tau) \\ u_1'(\tau) & u_2'(\tau) \end{bmatrix}. \tag{12}$$

Here, $x_{n+1} = z(\pi)$ and $v_{n+1} = z^0(\pi)$ are the coordinate and velocity of an ion (the ion state vector) at the beginning of the next period. Under the above assumption that the phase τ vanishes at the beginning of each period, the periodicity properties of the problem imply that the solutions u_1 and u_2 of the linear equation do not differ between the periods. This allows us to write the relationship between the state vectors at the beginning and at the end of each period in the form of (12), with the same matrix $U(\pi)$. We continue to proceed in this manner in order to arrive at the following relationship between the state vectors at the beginning of every two successive periods:

$$\begin{pmatrix} x \\ v \end{pmatrix}_{n+1} = M\begin{pmatrix} x \\ v \end{pmatrix}_n, \qquad \text{with} \quad M \equiv U(\pi) = \begin{bmatrix} m_{11} & m_{12} \\ m_{21} & m_{22} \end{bmatrix}. \tag{13}$$

In [7–9], the matrix approach to describing ion motion in a quadrupole field was developed through an analysis of mapping (13). The main results obtained in this way can be summarized as follows.

1. An analysis of the matrix mapping (13) makes it possible to find the condition for the ion motion to be stable: $|m_{11} + m_{22}| < 2$ [10]. Geometrically, this condition determines the stability diagram of ion motion in the plane of the parameters a and q of the supply voltage (Fig. 2).

2. The matrix approach makes it possible to solve Eqs. (13) for arbitrary initial state vectors:

$$\begin{pmatrix} x \\ v \end{pmatrix}_n = \begin{bmatrix} \cos(n\pi\beta) + A\sin(n\pi\beta) & B\sin(n\pi\beta) \\ -\Gamma\sin(n\pi\beta) & \cos(n\pi\beta) - A\sin(n\pi\beta) \end{bmatrix} \begin{pmatrix} x \\ v \end{pmatrix}_0, \quad (14)$$

where

$$\cos(\pi\beta) = \frac{m_{11} + m_{22}}{2}, \quad A = \frac{m_{11} - m_{22}}{\sin(\pi\beta)},$$

$$B = \frac{m_{12}}{\sin(\pi\beta)}, \quad \Gamma = \frac{-m_{21}}{\sin(\pi\beta)}.$$

3. An analysis of solution (14) shows that, in the phase plane (z, z'), the coordinates of the state vectors of stable ion trajectories lie on the "trapping ellipses"

$$Ax^2 + 2\Gamma xv + Bv^2 = \Sigma. \quad (15)$$

The area Σ of the trapping ellipse is determined by the initial conditions (x_0, v_0) and is conserved by virtue of the Liouville theorem.

4. Relationships (10), together with solution (14), make it possible to calculate the ion trajectory $x(\xi)$ at each instant $\xi = nT = \tau$. To construct an exact complete solution to the problem, it is sufficient to obtain a pair of solutions $u_1(\tau)$ and $u_2(\tau)$ over one period. This can be done by applying approximate methods for solving differential equations or, for a harmonically varying supply voltage, by turning to the analytic methods used in the theory of Mathieu equations.

The essence of the proposed method of nonlinear mappings consists in constructing and studying a matrix mapping in the form of (13) for an inhomogeneous Mathieu (Hill) equation whose right-hand side should incorporate nonlinear distortions of the quadrupole field, as is done, e.g., in (9). Note that this method of mappings is widely used in the theory of nonlinear periodic oscillations and self-oscillatory processes [11]. Here, we apply these methods to study parametric ion oscillations in a nonlinearly distorted quadrupole field near the marginal stability for ion motion.

MATHEMATICAL APPARATUS FOR THE METHOD OF NONLINEAR MAPPINGS

Let us construct a nonlinear mapping for Eq. (9). In the stability diagram, we choose a reference point (a_0, q_0) at which we obtain a pair of solutions (u_1, u_2) to the Mathieu equation with the initial conditions (11). We describe the supply voltage at the reference and current points by the functions

$$f_0(\xi) = a_0 + 2q_0\cos(2\xi),$$
$$f(\xi) = a + 2q\cos(2\xi). \quad (16)$$

The reference point should be sufficiently close to the current point (a, q) in order for the difference $f_0 - f$ to be small in comparison with f_0. We rewrite Eq. (9) as

$$z'' + f_0(\xi)z = [f_0(\xi) - f(\xi)]z - \frac{1}{2}f(\xi)\sum_{k>2} k\alpha_k z^{k-1}. \quad (17)$$

In this equation, we move all of the terms that describe nonlinear distortions to the right-hand side. The characteristic solutions (u_1, u_2) satisfy the homogeneous equation (17). Consequently, over each period

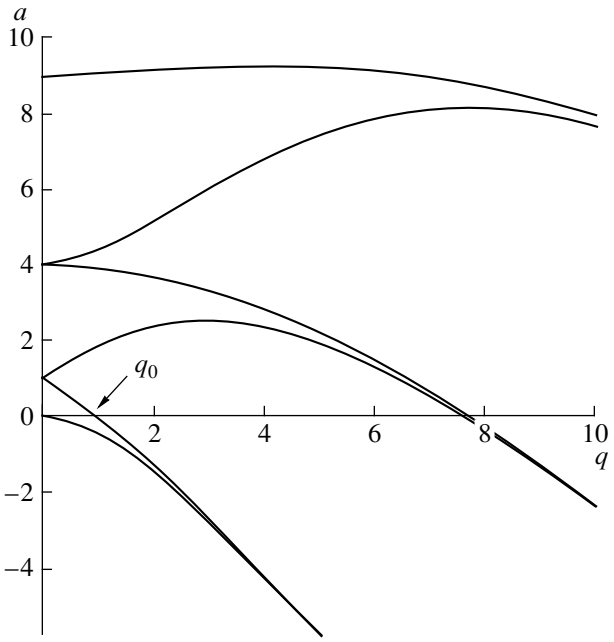

Fig. 2. Stability diagram of the axial ion motion. The parameter a is proportional to the constant potential difference U between the electrodes in the trap, and the parameter q is a measure of the amplitude V of the alternating voltage. For ions with different masses, the parameters a and q lie on the same line, which passes through the origin of the coordinates of the diagram and has a slope angle such that $\tan\alpha = 2U/V$.

$[n\pi, (n+1)\pi]$, the inhomogeneous equation (17) can be solved by the method of unknown Lagrange multipliers:

$$z(n\pi + \tau) = c_1(\tau)u_1(\tau) + c_2(\tau)u_2(\tau), \tag{18a}$$

$$z(n\pi + \tau) = c_1(\tau)u_1'(\tau) + c_2(\tau)u_2'(\tau), \quad 0 < \tau < \pi. \tag{18b}$$

These formulas give the first equation relating the functions $c_1(\tau)$ and $c_2(\tau)$,

$$c_1'(\tau)u_1(\tau) + c_2'(\tau)u_2(\tau) = 0. \tag{19a}$$

The second equation follows from Eq. (17):

$$c_1'(\tau)u_1'(\tau) + c_2'(\tau)u_2'(\tau) = (f_0 - f)(c_1u_1 + c_2u_2) - \frac{1}{2}f\sum_{k>2} k\alpha_k(c_1u_1 + c_2u_2)^{k-1}. \tag{19b}$$

In resolving Eqs. (19) with respect to the derivatives of $c_1(\tau)$ and $c_2(\tau)$, we must keep in mind that the Wronskian for the linear homogeneous equation is equal to unity: $u_1(\tau)u_2'(\tau) - u_2(\tau)u_1'(\tau) = 1$, so that we obtain

$$\begin{pmatrix} c_1' \\ c_2' \end{pmatrix} = \left(f_0 - f - \frac{1}{2}\sum_{k>2} k\alpha_k(c_1u_1 + c_2u_2)^{k-2} \right) \times \begin{bmatrix} -u_2u_1 & -u_2^2 \\ u_1^2 & u_1u_2 \end{bmatrix} \begin{pmatrix} c_1 \\ c_2 \end{pmatrix}. \tag{20}$$

According to formulas (18), the initial conditions for the matrix equation (20) are the coordinates of the state vector at the beginning of each period:

$$c_1(0) = x_n, \quad c_2(0) = v_n. \tag{21}$$

Solving Eqs. (20) over the period $0 < \tau < \pi$, we use formulas (18) to construct the following mapping with a time-varying mapping matrix:

$$\begin{pmatrix} x \\ v \end{pmatrix}_{n+1} = \begin{bmatrix} m_{11}^{(n)} & m_{12}^{(n)} \\ m_{21}^{(n)} & m_{22}^{(2)} \end{bmatrix} \begin{pmatrix} x \\ v \end{pmatrix}_n = M_n \begin{pmatrix} x \\ v \end{pmatrix}_n. \tag{22}$$

The matrix equation (22) describes the desired mapping between the state vectors of an ion over every two successive periods of the supply voltage. This equation is generally nonlinear, because, in the presence of nonlinear distortions of the quadrupole potential, the matrix M_n depends on the state vector at the beginning of each period.

Let us transform mapping (22) to the equation for an integer-valued variable. We apply this mapping to the state vector two times and eliminate the variable v_n to arrive at the following recurrence relation for x_n:

$$\begin{aligned} x_{n+1} &= m_{11}^{(n)}x_n + m_{12}^{(n)}v_n = m_{11}^{(n)}x_n + m_{12}^{(n)} \\ &\quad \times [m_{21}^{(n-1)}x_{n-1} + m_{22}^{(n-1)}v_{n-1}] \\ &= m_{11}^{(n)}x_n + m_{12}^{(n)}m_{21}^{(n-1)}x_{n-1} + m_{12}^{(n)} \\ &\quad \times \frac{m_{22}^{(n-1)}}{m_{12}^{(n-1)}}[x_n - m_{11}^{(n-1)}x_{n-1}]. \end{aligned} \tag{23}$$

According to the Liouville theorem, the determinant of Eq. (17) should satisfy the condition $\det(M_n) = 1$. With this condition, we obtain

$$m_{12}^{n-1}x_{n+1} + m_{12}^{n}x_{n-1} = [m_{11}^{n}m_{12}^{n-1} + m_{22}^{n-1}m_{12}^{n}]x_n. \tag{24}$$

Generally, it might be more convenient to analyze Eq. (24) rather than Eq. (22).

The exact mapping matrix M_n is impossible to calculate analytically [this is equivalent to solving the basic Eq. (9) exactly]. However, the nonlinear distortions, which strongly affect oscillatory ion motion over many oscillation periods, perturb the ion trajectories over one oscillation period only slightly. This circumstance allows us to determine the mapping matrix over each oscillation period by approximate analytic methods and to employ the exact mapping (22) for an adequate description of the ion motion. Solving the recurrence relation (22) or (24), we obtain the state vectors of an ion at the same fixed times in each period of the RF field. The ion trajectory between the points determined by the state vectors found in such a manner can be traced using relationships (10), or, more precisely, formulas (18). We thus can follow the entire ion trajectory, even though Eqs. (22) are discrete in character. Moreover, we can also choose the initial phase of the RF voltage so that the ion oscillation amplitude is maximum at the fixed times at which the state vectors were calculated. This choice ensures that the difference Eq. (24) describes the envelope of ion oscillations, thereby substantially simplifying the theoretical analysis of the ion motion.

In the next section, we will apply this method to describe ion motion during the UAMSE.

ION MOTION DURING THE SCANNING OF THE MASS SPECTRUM

Near the marginal stability for the axial ion motion in a trap supplied by applying an RF voltage, the working point ($a = 0$, q) for ions with a given mass crosses the boundary of the first stability domain at the point ($a_0 = 0$, $q_0 = 0.90804671$). It is this point that will be used as a reference, in which case the solutions $u_1(\tau)$ and $u_2(\tau)$ are Mathieu functions of integer order. The plots of these solutions are shown in Fig. 3. By virtue of the symmetry of the harmonically varying supply

voltage, we have $\beta_z = 1$ at the boundary of the stability domain and, accordingly, we obtain $u_1(\pi) = u_2'(\pi) = -1$, $u_2(\pi) = D = 5.59366$, and $u_1'(\pi) = 0$, the solution $u_1(\xi)$ being an even periodic function.

In the Appendix, we calculate the mapping matrix using an approximate method that is valid under the condition that corrections to the undistorted solution are small over a period of the RF field. This condition can be written as

$$q_0 \gg |q(n) - q_0|, \quad \alpha_3 A, \quad \alpha_4 A^2, \ldots, \tag{25}$$

where $q(n)$ is the current position of the working point. The characteristic dimensionless amplitude A of the ion oscillations in the working volume over the period at hand should be smaller than unity. We consider the ion motion near marginal stability under the condition that the difference $q - q_0$ is smaller than 0.01, in which case the amplitude α_0 of the relative nonlinear distortions does not exceed 2%. Hence, conditions (25) are satisfied with a high accuracy.

We assume that, during the scanning of the mass spectrum, the current working point $q(n)$ for ions with a given mass crosses the boundary of the first stability domain. As the working point approaches this boundary, the envelope of ion oscillations changes at a progressively slower rate. Consequently, in the case at hand, Eq. (24) contains a small parameter—the rate of change of the function $|x_n|$. This enables us to transform the difference Eq. (24) into differential form.

For definiteness, we assume that the derivative $d(\ln|x_n|)/dn$ is on the order of $\varepsilon \ll 1$. Since the diagonal elements of the matrix M_n are close to unity, the quantity x_n is an alternating-sign function, so that, to within terms on the order of ε^2, we obtain

$$\begin{aligned} x_n &= (-1)^n X(n), \\ x_{n\pm1} &\approx (-1)^{n\pm1}\left[X \pm \frac{dX}{dn} - \frac{1}{2}\frac{d^2X}{dn^2}\right], \end{aligned} \tag{26}$$

where $X(n)$ is a continuous function of time expressed in terms of the period of the RF field: $n = t/T$.

Under the assumption that the quantities $q_0 - q(n)$, $\alpha_3 x_n$, and $\alpha_4 x_n^2$ are on the order of ε^2, we can also assume that $m_{12}^{n-1} \approx m_{12}^n$ and $m_{22}^{n-1} \approx m_{22}^n$, in which case the recurrence relation (24) reduces to the following differential equation for the function $X(n)$:

$$\frac{d^2X}{dn^2} + [2 + \mathrm{Spur}(M_n)]X = 0. \tag{27}$$

The trace of the matrix M_n, $\mathrm{Spur}(M_n)$, is calculated in the Appendix:

$$\begin{aligned} \mathrm{Spur}(M_n) &= -2 + 2[q_0 - q(n)]DQ_{20} \\ &\quad - Dq(n)\sum_{k>2} k\alpha_k P_{k-2}(x_n, v_n), \end{aligned} \tag{28}$$

where P_k is a polynomial of degree k and

$$Q_{20} = \int_0^\pi \cos(2\xi)u_1^2(\xi)d\xi = 0.77396.$$

For further analysis, we must determine the velocity v_n. In approximation (26), the first equation in (22) gives

$$v_n = \frac{(-1)^{n+1}}{D}\frac{dX}{dn}. \tag{29}$$

Since the derived function $X(n)$ is on the order of ε, we can treat Eq. (27) with $v_n = 0$, in which case we obtain

$$\begin{aligned} \mathrm{Spur}(M_n) &= -2 + 2[q_0 - q(n)]DQ_{20} \\ &\quad - Dq(n)\sum_{k>2} k\alpha_k X^{k-2} Q_{k0}, \end{aligned} \tag{30}$$

where

$$Q_{k0} = \int_0^\pi \cos(2\xi)u_1^k(\xi)d\xi. \tag{31}$$

Note that the function $u_1(\xi)\cos(2\xi)$ is an odd function with respect to the point $\xi = \pi/2$. Consequently, for odd values of k, we have $Q_{k0} = 0$, so that, in this approximation, the odd harmonics of the distorted quadrupole

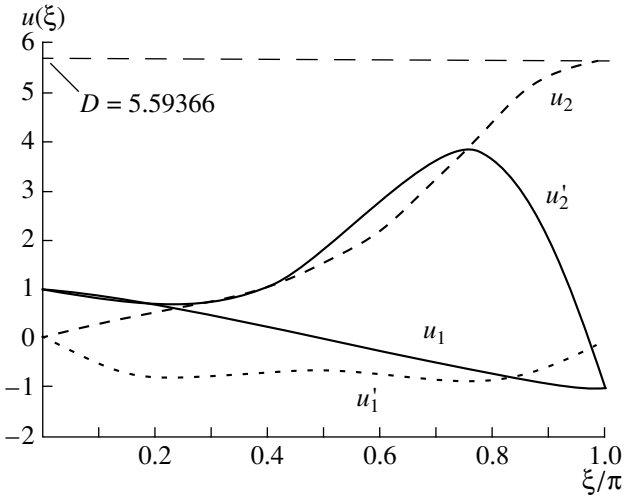

Fig. 3. Plots of the solutions to the Mathieu equation with the initial conditions (11).

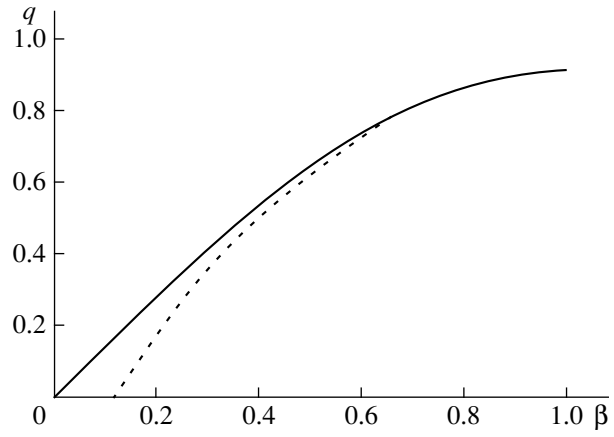

Fig. 4. Dependence $q(\beta)$ along the line $a = 0$, characterizing the RF field regime. The solid curve is obtained by directly solving the Mathieu equation on a grid with 2000 mesh points on the RF field period. The dotted curve is obtained from formula (34), which approximates the exact dependence.

potential do not contribute to Eq. (27), which thus reduces to

$$\frac{1}{D}\frac{d^2X}{dn^2} + 2Q_{20}[q_0 - q(n)]X - q(n)4\alpha_4 Q_{40}X^3 - q(n)6\alpha_6 Q_{60}X^5 - \ldots = 0. \quad (32)$$

In the linear approximation ($\alpha_k = 0$), Eq. (32) with $q(n) = \text{const}$ describes harmonic oscillations with the frequency

$$\Omega = \sqrt{2DQ_{20}(q_0 - q)}. \quad (33)$$

Since the function $X(n)$ is the envelope of high-frequency ion oscillations, expression (33) is obviously nothing more than the ion bounce frequency. On the other hand, the period T_b of the ion bounces is determined by the stability parameter β_z [6]: $T_b = 1/(1 - \beta_z) = \pi/\Omega$ (in units of the period of the RF field). This yields the following relationship between the stability parameter β_z and the parameter q near the marginal stability:

$$q(\beta) = q_0 - \frac{\pi^2}{2DQ_{20}}(1 - \beta)^2 = 0.908047 - 1.139869(1 - \beta)^2. \quad (34)$$

In Fig. 4, we show the results of the exact calculation of the dependence $q(\beta)$ by integrating the Mathieu equation along the line $a = 0$. For comparison, we also plot the approximate dependence (34). In accordance with Fig. 4, formula (34) is an expansion of the exact dependence $q(\beta)$ in powers of $(1 - \beta)$ correct to second-order terms. For $|q - q_0| < 0.01$, formula (34) is accurate to within an error of less than 0.2%. For this reason, ion motion near the marginal stability is very accurately described by Eq. (32).

Now, we turn to the analysis of Eq. (32) with the nonlinear distortions of the quadrupole field. At fixed $q(n) = \text{const}$, Eq. (32) is the equation of motion of a material point with an effective mass D^{-1} in the force field described by the potential

$$U_{\text{eff}}(X) = (q_0 - q)Q_{20}X^2 - qQ_{40}\alpha_4 X^4 - qQ_{60}\alpha_6 X^6 - \ldots. \quad (35)$$

Analyzing the ion motion in this potential promotes a deeper understanding of the effect of the nonlinear distortions of the quadrupole field. Figure 5a shows the distorted potential (35) with a negative relative amplitude α_4 of the octopole harmonic for different values of $q_0 - q$. If this difference is positive (the working point is inside the stability domain), then the effective electric field provides a potential well with infinitely high slopes (Fig. 5a, curve *1*), in which case Eq. (32) describes nonlinear oscillations with an amplitude-dependent frequency. Small-amplitude oscillations are almost harmonic with the frequency

$$\Omega(q, A) = \sqrt{2DQ_{20}(q_0 - q)} - \frac{3DQ_{40}\alpha_4}{\sqrt{2DQ_{20}(q_0 - q)}}\frac{A^2}{2}. \quad (36)$$

The oscillation amplitude A can be assumed to be small if the second term in expression (36) is negligible compared to the first term, $3Q_{40}\alpha_4 A^2 \ll 4Q_{40}(q_0 - q)$.

According to the linear Mathieu equation, the bounce frequency tends to zero when the working point approaches the boundary of the first stability domain. According to expression (36), the bounce frequency increases with oscillation amplitude. Consequently, an increase in the amplitude of the ion bounces in a distorted electric field with negative even harmonics forces the working point to displace deeper into the stability domain and prevents the energy transfer from the field to the ions. The amplitude of the parametric oscillations of the ions in the z-direction stops increasing because of the nonlinear processes; as a result, the ions experience nonlinear bounces near the marginal stability. These considerations explain the effect of the delayed ion extraction in a Paul trap with finite-sized electrodes [2]. Qualitatively, the delayed extraction effect is described by Eq. (32), which implies that the potential well should also exist outside the first stability domain. For a working point lying outside this domain, we have $q_0 - q < 0$, in which case the effective electric field provides a potential well with two dips (Fig. 5a, curve *3*). Since Eq. (32) describes a conservative system, the total effective energy of the ion bounces is conserved:

$$E_{\text{eff}} = \frac{1}{D}\left(\frac{dX}{dn}\right)^2 + U_{\text{eff}}(X). \quad (37)$$

For $E_{\text{eff}} < 0$, the ions oscillate around one of the equilibrium positions:

$$X_m = \pm\sqrt{\frac{(q-q_0)Q_{20}}{2q\alpha_4 Q_{40}}}. \quad (38)$$

For $E_{\text{eff}} > 0$, the ion oscillations are symmetric. For $\alpha_4 < 0$, the ion oscillations are on the whole stable (of course, provided that the oscillation amplitude is smaller than the sizes of the trap).

Due to the presence of a potential well outside the stability domain, some of the ions experience stable motion inside the working volume of the trap even when the working point lies outside the stability domain. As a result, we can see that the negative even harmonics of the distorted quadrupole potential act to delay the UAMSE of the ions in a Paul trap with finite-size electrodes.

The situation is radically different in industrial-scale nonlinear traps, which satisfy the condition $\alpha_4 > 0$. In the stability domain $q_0 - q > 0$, the effective potential $U_{\text{eff}}(X)$ provides a well with slopes of finite height (Fig. 5b, curve *1*). The half-width of the potential well can be deduced from formula (38), and the well depth is equal to

$$U_m = (q_0 - q)Q_{20}\frac{X_m^2}{2}. \quad (39)$$

Small-amplitude oscillations of an ion around the center of the trap are anharmonic. According to expression (36), the frequency of small anharmonic oscillations decreases as their amplitude increases, in which case the working point is displaced toward the boundary of the stability domain. If the oscillation amplitude becomes larger than the width of the potential well, then the oscillations become absolutely unstable, because the oscillation energy E_{eff} exceeds the well depth U_m.

As the working point approaches the stability boundary, the phase difference decreases and, accordingly, the width and depth of the potential well both become smaller. As a result, the ion trapping region is reduced. In the stability domain $q_0 - q < 0$, the effective potential provides a hump (Fig. 5b, curve *3*), in which case the motion of the ions is unstable regardless of their initial positions. This indicates the onset of the "explosive ejection" of ions [2]: the flow of ions with a given mass becomes progressively more intense and is rapidly damped when the ions cross the boundary of the stability domain.

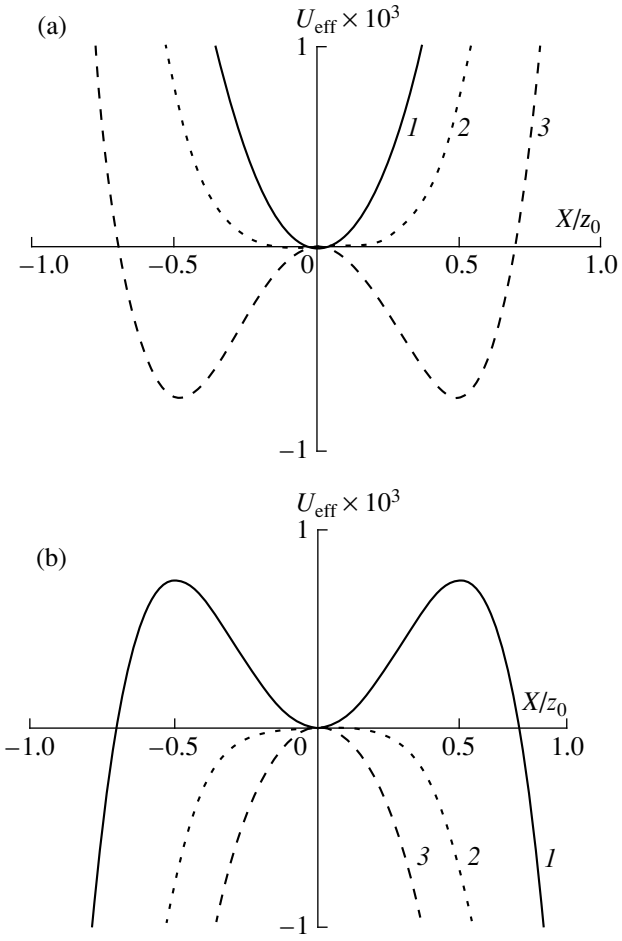

Fig. 5. Profiles of the effective potential (35) in which the ions experience a bounce motion for α_4 = (a) –0.02 and (b) +0.02 at $q = q_0 - 0.008$ (inside the stability domain), (*2*) q_0 (at the marginal stability), and (*3*) $q_0 + 0.008$ (outside the stability domain).

DISCUSSION OF THE RESULTS

The results obtained in the previous section show that the method of nonlinear mappings is very efficient in describing ion motion near the marginal stability. The proposed method is capable of explaining the effect of delayed ion extraction in the presence of negative even harmonics of the distorted quadrupole potential as well as the effect of the explosive ejection of ions in the presence of positive even harmonics. Both of these effects, which were analyzed numerically by Franzen [2], can be described analytically by introducing the notion of the effective potential.

Let us discuss a number of factors that were neglected for simplicity but may nevertheless play an important role. First, Eq. (7) and, accordingly, Eq. (32) contain no terms describing collisional damping. In collisions between ions and molecules of a light buffer gas, the direction of the ion velocity remains essentially unchanged and the ion kinetic energy decreases by an amount governed by the molecule-to-ion mass ratio. As a result, the oscillatory ion motion is damped and the conservative oscillations described by Eq. (32) become dissipative. Ion oscillations around the equilibrium position (the bottom of the potential well) are damped on a sufficiently long time scale. However, the conclu-

sions of the previous section apply also to nonlinear traps with damped ion oscillations. In the presence of a negative octopole harmonic of the distorted quadrupole field, the delay of ion extraction becomes even more appreciable due to the damping of ion bounces near the bottom of the potential well. In the presence of a positive octopole harmonic, the potential well exists only in the stability domain and disappears when away from the stability boundary.

Second, in analyzing Eq. (32), we assumed that the parameter $q(n)$ is constant. However, this parameter increases during the scanning of the mass spectrum. The standard scanning speed in industrial-scale devices [1] is $dM/dt = 5555$ u/s. From (8), we obtain

$$\frac{dq}{dt} = -\frac{q_0}{M}\frac{dM}{dt}. \quad (40)$$

For the supply voltage frequency $\omega_0/2\pi = 1$ MHz and the mass $M = 500$ u, the rate at which the parameter q changes over a period of the RF field is 10^{-5}. Consequently, we are justified in assuming that, during ion extraction, the working point is displaced in a quasistatic fashion, the more so because, in Eq. (32), we restrict ourselves to considering $q(n)$ values for which the difference $q(n) - q_0$ is a small quantity on the order of the amplitude of the nonlinear distortions or even smaller. A faster scanning of the spectrum may necessitate the inclusion of the change in the parameter $q(n)$, which is inevitably accompanied by a degradation of the spatial resolution. In contrast, scanning the mass spectra at a lower speed (0.025 u/s) makes it possible to achieve a mass resolution of 3.1×10^{-7} in each scanning cycle [1].

And finally, in Eq. (32), we neglected nonlinear distortions described by the odd field harmonics. The reason for this is as follows. Near the marginal stability, the ion oscillations have the form of beatings during which the ion coordinate runs through negative and positive values in the entire range determined by the current amplitude. In this case, nonlinear distortions are averaged and, in the first approximation, the contribution of odd harmonics vanish. However, in practice, odd harmonics make a nonvanishing contribution, which can be incorporated into the proposed method by using the second-order perturbation theory. It is well known [2] that the contribution of odd harmonics is analogous to the contribution of negative even harmonics and is unfavorable for the axial mass-selective ion extraction. This is likely the reason for substantial (up to 10%) distortions of the geometry of nonlinear Paul traps in industrial-scale devices. Such distortions stem from the necessity of producing positive even field harmonics in order to suppress the effect of odd harmonics.

CONCLUSION

We have constructed a nonlinear mapping for the equation of ion motion along the axis of the trap for parameters of the supply voltage that are near the marginal stability ($\beta_z = 1$) for the axial motion. This mapping can be reduced to the difference equation for the envelope of the ion oscillations. With allowance for the change in the parameters a and q during the scanning of the mass spectrum, this difference equation can in turn be reduced to a differential equation with a nonlinear right-hand side. This differential equation makes it possible to interpret ion oscillations as the motion of a material point in a force field whose effective potential contains nonzero even harmonics.

Depending on the sign of the amplitude of the octopole harmonic, we can distinguish between two possible cases. For $\alpha_4 < 0$, the bounce frequency near the marginal stability increases with the bounce amplitude due to the nonlinear distortions, or, equivalently, the working point is displaced deeper into the stability domain. In terms of the effective potential, this can be explained by the fact that, for $\alpha_4 < 0$, the potential well is outside the stability domain. Such distortions, which are typical of a Paul trap, are responsible for the delay in ion extraction.

For $\alpha_4 > 0$, the effective potential provides a well with finite-height slopes inside the stability domain, whereas, outside the stability domain, the potential well is absent. As a result, ions with a given mass are extracted from the working volume when passing through the stability boundary. Thus, a regime of ion selection occurs.

The results obtained imply that it is expedient to develop an electrode system capable of creating a quadrupole field with the desired odd harmonics in the trapping region and to use the UAMSE method in designing and fabricating present-day compact high-resolution spectrometers.

ACKNOWLEDGMENTS

I am grateful to N.V. Konenkov for his interest in this work and fruitful discussions.

APPENDIX

Calculation of the Mapping Matrix

In order to construct the matrix mapping, it is necessary to find an approximate solution to the exact set of Eqs. (20). For this purpose, we can apply an approximate method in which the functions on the right-hand sides of Eqs. (20) are assumed to be constant. We are justified in applying this approach because we only need to solve Eqs. (20) for one period $0 < \xi < \pi$ of the RF field rather than to look for asymptotic solutions on long time scales, on which the approximate method fails.

Treating the quantities c_1 and c_2 on the right-hand side of the matrix Eq. (20) as constants equal to their

values at the beginning of the period of the RF field, we obtain the solution of (20) in the form

$$\begin{bmatrix} c_1(\pi) \\ c_2(\pi) \end{bmatrix} = \left\{ 1 + \int_0^{\pi} \left(f_0 - f\frac{f}{2} \sum_{k>2} k\alpha_k (x_n u_1 + v_n u_2)^{k-2} \right) \times \begin{bmatrix} -u_2 u_1 & -u_2^2 \\ u_1^2 & u_1 u_2 \end{bmatrix} d\xi \right\} \begin{pmatrix} x_n \\ v_n \end{pmatrix}. \tag{A.1}$$

For $\xi = \pi$, Eqs. (18) generate the matrix mapping

$$\begin{pmatrix} x \\ v \end{pmatrix}_{n+1} = \begin{bmatrix} m_{11}^{(n)} & m_{12}^{(n)} \\ m_{21}^{(n)} & m_{22}^{(n)} \end{bmatrix} \begin{pmatrix} x \\ v \end{pmatrix}_n = M_n \begin{pmatrix} x \\ v \end{pmatrix}, \tag{A.2}$$

$$M_n = L_n + G_n, \tag{A.3}$$

where

$$L_n = U(\pi) \left[1 + \int_0^{\pi} (f_0 - f) W(\xi) d\xi \right], \tag{A.4}$$

$$G_n = -\frac{1}{2} U(\pi) \int_0^{\pi} f(\xi) \times \sum_{k>2} k\alpha_k [x_n u_1(\xi) + v_n u_2(\xi)]^{k-2} W(\xi) d\xi, \tag{A.5}$$

$$U(\pi) = \begin{bmatrix} u_1(\pi) & u_2(\pi) \\ u_1'(\pi) & u_2'(\pi) \end{bmatrix} = \begin{bmatrix} -1 & D \\ 0 & -1 \end{bmatrix}, \quad W(\xi) = \begin{bmatrix} -u_1 u_2 & -u_2^2 \\ u_1^2 & u_1 u_2 \end{bmatrix}. \tag{A.6}$$

We calculate the nonlinear part of the mapping matrix (24) to obtain

$$L_n = \begin{bmatrix} -1 + 2[q_0 - q(n)](Q_{11} + DQ_{20}) & D + 2[q_0 - q(n)](Q_{02} + DQ_{11}) \\ -2[q_0 - q(n)]Q_{20} & -1 - 2[q_0 - q(n)]Q_{11} \end{bmatrix}, \tag{A.7}$$

where $D = u_2(\pi) = 5.59366$ and

$$Q_{pq} = \int_0^{\pi} \cos(2\xi) u_1^p u_2^q d\xi. \tag{A.8}$$

Calculating the nonlinear part of the mapping matrix yields

$$G_n^{(3)} = -3\alpha_3 q_n \times \left\{ x_n \begin{bmatrix} Q_{21} + DQ_{30} & Q_{12} + DQ_{21} \\ -Q_{30} & -Q_{21} \end{bmatrix} + v_n \begin{bmatrix} Q_{12} + DQ_{21} & Q_{03} + DQ_{12} \\ -Q_{21} & -Q_{12} \end{bmatrix} \right\}, \tag{A.9}$$

for the hexapole distortions ($k = 3$) and

$$G_n^{(4)} = -4\alpha_4 q_n \times \left\{ x_n^2 \begin{bmatrix} Q_{31} + DQ_{40} & Q_{22} + DQ_{31} \\ -Q_{40} & -Q_{31} \end{bmatrix} + 2x_n v_n \begin{bmatrix} Q_{22} + DQ_{31} & Q_{13} + DQ_{22} \\ -Q_{31} & -Q_{22} \end{bmatrix} + v_n^2 \begin{bmatrix} Q_{13} + DQ_{22} & Q_{04} + DQ_{13} \\ -Q_{22} & -Q_{13} \end{bmatrix} \right\}, \tag{A.10}$$

for the octopole distortions ($k = 4$).

The nonlinear parts of the mapping matrix for higher order distortions can be evaluated in a similar way.

In order to examine the recurrence relation (24), we need to calculate the trace of the mapping matrix:

$$\begin{aligned} \mathrm{Spur}(L_n) &= -2 + 2[q_0 - q(n)]DQ_{20}, \\ \mathrm{Spur}(G_n^{(3)}) &= -3\alpha_3 Dq(n)[x_n Q_{30} + v_n Q_{21}], \\ \mathrm{Spur}(G_n^{(4)}) &= -4\alpha_4 Dq(n)[x_n^2 Q_{40} + 2x_n v_n Q_{31} + v_n^2 Q_{22}]. \end{aligned} \tag{A.11}$$

For the solutions u_1 and u_2 at the marginal stability, the constants in the above formulas are calculated to be $Q_{20} = 0.77396$, $Q_{30} = 0$, $Q_{21} = 2.23778$, $Q_{40} = 0.707862$, $Q_{31} = 1.97977$, and $Q_{22} = 11.9614$.

REFERENCES

1. R. E. March, in *Advances in Mass Spectrometry* (Elsevier, Amsterdam, 1998), Vol. 14, Chap. II, p. 241.
2. J. Franzen, Int. J. Mass Spectrom. Ion Processes **125**, 165 (1993).
3. Y. Wang and J. Franzen, Int. J. Mass Spectrom. Ion Processes **132**, 155 (1994).

4. J. Louris, J. Schwartz, G. Stafford, *et al.*, in *Proceedings of the 40th ASMS Conference on Mass Spectrometry and Allied Topics, Washington, DC, 1992*, p. 1003.
5. J. Wang and J. Franzen, Int. J. Mass Spectrom. Ion Processes **112**, 167 (1992).
6. N. W. McLachlan, *Theory and Application of Mathieu Functions* (Clarendon Press, Oxford, 1947; Inostrannaya Literatura, Moscow, 1963).
7. A. Pipes Louis, J. Appl. Phys. **24**, 902 (1953).
8. P. H. Dawson, *Quadrupole Mass Spectrometry and Its Applications* (Elsevier, Amsterdam, 1976), Chap. IV, p. 79.
9. R. M. Waldren and J. F. J. Todd, in *Dynamic Mass Spectrometry* (Heyden, London, 1978), Vol. 5, Chap. 2, p. 14.
10. M. Yu. Sudakov, Zh. Tekh. Fiz. **64**, 170 (1994) [Tech. Phys. **39** (1), 96 (1994)].
11. I. V. Butenin, Yu. I. Neĭmark, and N. A. Fufaev, *Introduction to the Theory of Nonlinear Oscillations* (Nauka, Moscow, 1987).

Translated by O. Khadin

Technical Physics, Vol. 45, No. 11, 2000, pp. 1489–1495. Translated from Zhurnal Tekhnicheskoĭ Fiziki, Vol. 70, No. 11, 2000, pp. 118–125.

EXPERIMENTAL INSTRUMENTS AND TECHNIQUES

Cluster Structure of Fullerene-Containing Soot and C_{60} Fullerene Powder

O. P. Gorelik*, G. A. Dyuzhev, D. V. Novikov***, V. M. Oĭchenko***, and G. N. Furseĭ*****

** FOMA Company, Houston, USA*

*** Ioffe Physicotechnical Institute, RAN, St. Petersburg, 194021 Russia*

E-mail: dgan@hm.csa.ru

**** Bonch-Bruevich State University of Telecommunications, St. Petersburg, 191065 Russia*

Received July 8, 1999

Abstract—Electron microscopy and electron diffraction methods were employed in a study of the structure of a fullerene-containing soot produced in gas discharge and of a C_{60} fullerene powder. The data obtained were analyzed with the use of fractal geometry concepts. It has been shown that, in the structure of the objects studied, several spatial scales can be identified. The effective radius of the structure's "elementary particles" calculated using scaling relationships is equal to 6 Å for the soot and 4.5 Å for the C_{60} fullerene. The "elementary particles" combine into associates. The number of particles in an associate in both the soot and the C_{60} powder is not large (about 10). The associates form fractal nanoclusters 30-80 nm in size having a fractal dimension of 1.60 ± 0.05 in the soot and of 1.8 ± 0.05 in the C_{60} fullerene. The structure of the soot nanocluster is unstable and can be significantly modified by externally applied factors (e.g., as a result of treatment with toluene). The nanoclusters combine into aggregates having the form of branching cross-linked filaments. Eventually, these aggregates combine to form macroparticles of soot. © *2000 MAIK "Nauka/Interperiodica".*

The "exponential" growth of scientific interest in fullerenes, which persisted until recently and culminated in the award of the Nobel Prize in 1996, is now gradually subsiding because the unrestrained optimism regarding the spread of fullerenes as a new material in various fields of technology has not so far been justified. In our view, one of the main reasons is that fullerenes are not readily available because of their high cost in the world market.

At present the only method of preparing fullerene-containing soot in commercial quantities is the Huffman-Kretschmer method [1] by which the soot is produced in an electric arc with graphite electrodes in an atmosphere of helium gas. A mixture of fullerenes is extracted from the soot with organic solvents and pure fullerenes are separated using liquid chromatography. The greatest cost of fullerene products is introduced by the fullerene-containing soot. However, it is obvious that the present scale of experimental studies, which could have contributed to the improvement of the soot production and, consequently, to the reduction of fullerene production costs, is still insufficient [1–6].

The purpose of this work is to study the structure of fullerene-containing soot and C_{60} fullerene powder using electron microscopy and electron diffraction.

EXPERIMENTAL

The fullerene-containing soot was prepared in pilot plants equipped with cylindrical plasma reactors. The arc discharge was fired between a movable cylindrical cathode 8 mm in diameter and a fixed anode of a square cross-section of an area 9×9 mm. The arc current was 180 Å, the distance between electrodes 6 mm, and helium pressure 70 torr. The percentage of fullerenes in the soot produced was typically $\alpha \sim 10$–12%. The soot collected in the reactor was ground and thoroughly mixed in a mechanical mixer. Fullerenes were extracted from the soot with 0-xylene. The solvent was then filtered and evaporated. Separation of the fullerenes into fractions was carried out in chromatographic columns with toluene as the eluent. After chromatography, C_{60} fullerene powder was extracted from the solution by vacuum evaporation of the solvent at a temperature of 200°C.

The morphology of soot particles was studied in a EMV-100L electron microscope at an accelerating voltage of 75 kV and a magnification of 10^5. Samples for the electron microscopy were prepared by dispersing the soot ultrasonically in collodion. The thin dispersion film formed on the water was placed on supporting netting and examined under the electron microscope.

Electron diffraction patterns of the samples were obtained in a microdiffraction regime with an accelerating voltage of 75 kV. Computer processing of the micrographs was done at 3×10^6 magnification with the use of a cluster–lattice model [7] following a method [8] proposed for the analysis of network topology of polymer surfaces. The scanned area of the image was about 5×10^3 nm.

1063-7842/00/4511-1489$20.00 © 2000 MAIK "Nauka/Interperiodica"

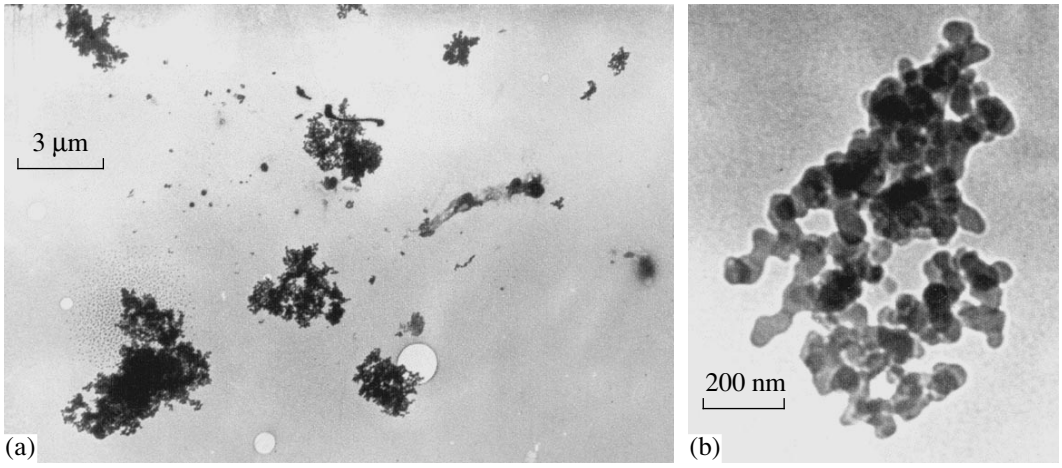

Fig. 1. Electron micrographs of the fullerene-containing soot.

OBTAINED RESULTS AND THEIR PROCESSING

Analysis of numerous micrographs has shown that the outward appearance and structure of fullerene-containing soot and C_{60} powder depend markedly on the magnification value chosen. At low magnifications (Fig. 1a), the fullerene-containing soot looks like an ordinary soot produced by the thermal evaporation of graphite [9]. As a result of ultrasonic dispersion, soot particles disintegrate into aggregates having the form of branching cross-linked filaments (Fig. 1b). The cross-linking elements of these aggregates are nanoclusters with an average diameter of 30–80 nm and a near-spherical form. Photographs of isolated nanoclusters of fullerene-containing soot could not be obtained (Fig. 2) as they were used in the dispersed powder of C_{60} (Fig. 3). The purpose of this work was to study the nanocluster structure in both the soot and the C_{60} powder.

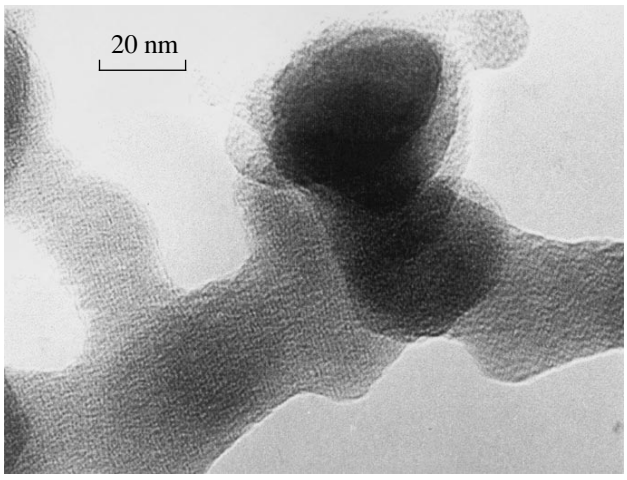

Fig. 2. Nanoclusters of the fullerene-containing soot.

A nanocluster is obviously a spatial structure that has to be reconstructed using its plane projections. In principle, such a procedure can be accomplished with the use of stereographic methods [10], although these methods are rather complicated.

As seen in Figs. 2 and 3, the nanoclusters of fullerene-containing soot and C_{60} powder have a non-uniform density. Regions of higher density form a spatial network and represent associates of elementary structural units which, in particular, include fullerene molecules.

In the analysis of the spatial distribution of the elements constituting a nanocluster, the following procedure was used. On the picture of a nanocluster, a planar square lattice was superimposed with the distance between sites being $r = 0.8$–1 nm, and the sites topologically corresponding to the regions of higher density in the image were marked. The spatial distribution of the density was described by a radial distribution function $g(R)$ of the marked lattice sites

$$g(R) = \rho(R, \delta)/\bar{\rho}, \quad (1)$$

where $\rho(R, \delta)$ is the density distribution of marked sites in a layer of thickness δ at a distance R from an arbitrarily chosen site and $\bar{\rho}$ is the density of marked sites averaged over the entire image. In order to eliminate the effect on the form of function $g(R)$ of the periodicity of the lattice itself, the value of δ was taken as $2r$ [11]. The function $g(R)$ was obtained by averaging over 2000 or more centers. The standard error of function values did not exceed 0.5%.

Figure 4 shows the form of the correlation function $g(R)$ for density distributions in the nanoclusters of fullerene-containing soot and C_{60} powder. The distance between function maxima determines the period L of the spatial alternation of the associates in a nanocluster. The position of the first function minimum corresponds to the associate correlation radius ξ [12]. L and ξ values are given in the table.

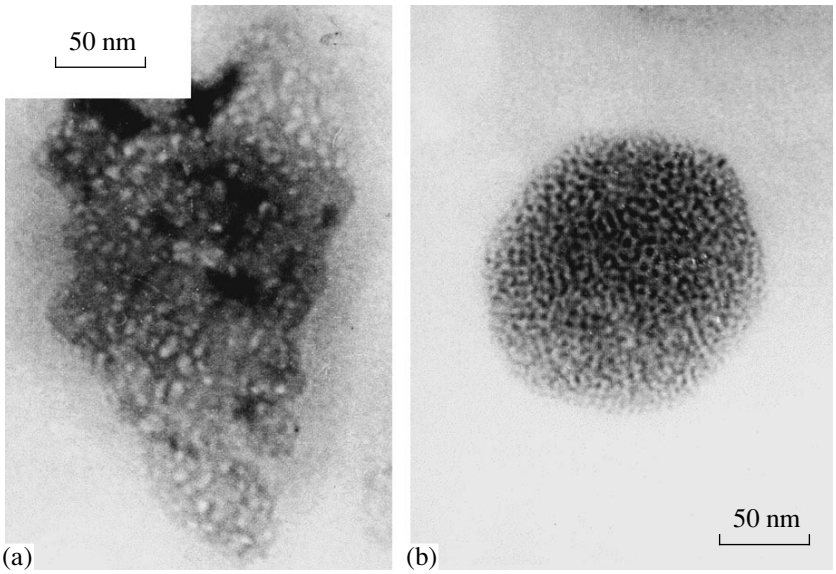

Fig. 3. Nanoclusters of the C_{60} powder.

The lattice density of nanoclusters ρ_Π corresponding to the fraction of regions of higher density was determined from the formula

$$\rho_\Pi = \rho/\rho', \tag{2}$$

where ρ' is the specified density of lattice sites equal to $1/r^2$.

To characterize the spatial structure of a nanocluster, an average lattice density $\rho_\Pi(R)$ of the marked lattice sites over radius R [7] was used

$$\rho_\Pi(R) = \rho(R)/\rho', \tag{3}$$

where $\rho(R) = (1 + 2\pi\rho\int_o^R g(R)RdR)/\pi R^2$.

Figure 5 shows in logarithmic coordinates the dependence of the average lattice density $\rho_\Pi(R)$ of the nanocluster samples studied on the radius R. It is seen that at $R < R^*$ these dependences are straight lines, i.e., the density decreases as

$$\rho_\Pi(R) \sim R^{D-2}, \tag{4}$$

where D is the fractal dimension of a nanocluster. The values of D are given in table.

Assuming self-similarity of the nanocluster structure at $R < R^*$ and self-similarity of the internal structure of its elements at $R < \xi$, with the use of scaling relationships, some conclusions concerning the nature of the nanocluster elements can be attempted. It is evident that for the C_{60} powder these elements should represent associates of C_{60} molecules. For the number s of particles in an associate, relationships given in [7] hold:

$$s = \omega(\xi/R_0)^D, \tag{5}$$

where R_0 is the radius of "elementary" particles comprising the associate, ω is the degree of filling of the associate with the "elementary" particles

$$s = \Omega\langle S\rangle, \tag{6}$$

where $\langle S\rangle$ is an average area of the associate projection and Ω its average density. Quantities ω and Ω are related by formula $\omega/\Omega = \pi R_0^2$. For randomly packed hard spheres we have $\omega = 0.637$ [13].

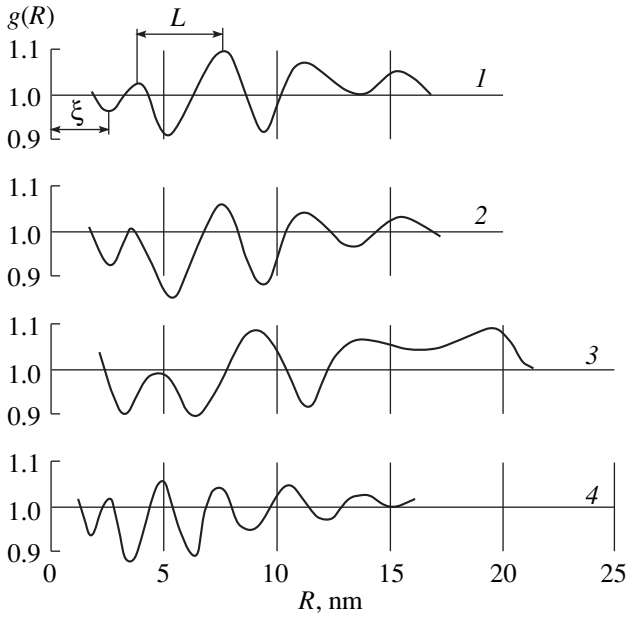

Fig. 4. Correlation functions for different samples: (*1*) C_{60} nanoclusters of porous structure; (*2*) C_{60} nanoclusters of usual structure; (*3*) fullerene-containing soot; (*4*) fullerene-containing soot briefly treated with toluene.

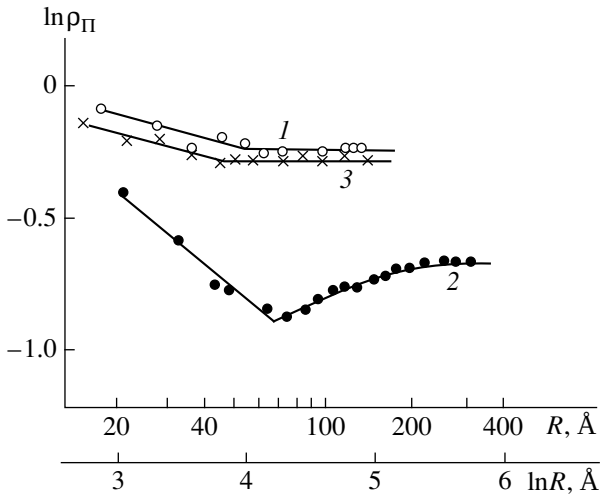

Fig. 5. Dependence of the average lattice density ρ_Π on the scaling radius R. (*1*) C_{60} nanoclusters; (*2*) fullerene-containing soot; (*3*) fullerene-containing soot briefly treated with toluene.

The area $\langle S \rangle$ of a projection is given by the relationship [14]

$$\langle S \rangle = 2\rho_\Pi \xi L. \quad (7)$$

It follows from (5), (6), and (7) that

$$R_0 = (2/\pi\rho_\Pi L \xi^{1-D})^{1/(2-D)}. \quad (8)$$

Expression (8) was derived for a planar surface ($E = 2$). To obtain the R_0 value in the bulk ($E = 3$), the relationship $R_0(E = 3) = 4/\pi R_0(E = 2)$ should be used [10].

The number s of "elementary particles" in the associates and their radii R_0 are given in the table.

Figure 6 shows electron diffraction patterns of the samples of initial fullerene-containing soot as well as of the soot treated with toluene for 5 min and 24 h. The treatment with toluene consisted in placing the support net with the preparation in a glass filled with toluene for a preset time, and then the preparation was dried in air and analyzed.

DISCUSSION OF RESULTS

We would like to begin the discussion with the results obtained for samples of the C_{60} fullerene powder because it is a considerably simpler and more comprehensible object. It is known [15] that in the crystallization of pure fullerenes and, in particular, C_{60}, a perfect crystal lattice is rarely formed. Various distortions seen in X-ray diffraction patterns are usually explained as being due to crystallization defects.

In the C_{60} fullerene powders studied, two types of nanocluster structures were identified. Nanoclusters which could be considered as belonging to an amorphous type (type I) have a porous structure (Fig. 3a). The pores have a clearly discernible period of spatial alternation equal to ~3.5 nm (Fig. 4, curve *1*). The average pore size determined from the halfwidth of dips of the function $g(R)$ is equal to ~2 nm. It should be noted that this nanocluster type is very unstable. Under the impact of an electron beam in a microscope, the pores "overgrow" within a few seconds.

The structure of type II nanoclusters is formed by spatially ordered associates of rather high density. These nanoclusters often have a hexagonal habit (Fig. 3b). Analysis of the function $g(R)$ (Fig. 4, curve *2*) shows that associates with a correlation radius $\xi = 2.5 \pm 0.5$ nm have an alternation period $L = 3.5$ nm. It should be noted that the alternation periods of associates of C_{60} molecules in type II nanoclusters coincide with those in type I clusters.

Type II nanoclusters have a net-like fractal structure [7] because, as a result of increasing R, their average density decreases as $\rho_\Pi(R) \sim R^{D-2}$ and in logarithmic coordinates the function $\rho_\Pi(R)$ is a straight line (Fig. 5, curve *1*). The fractal dimension is $D = 1.80 \pm 0.05$.

The radius R_0 of "elementary" particles forming the associates in nanoclusters of the C_{60} powder calculated

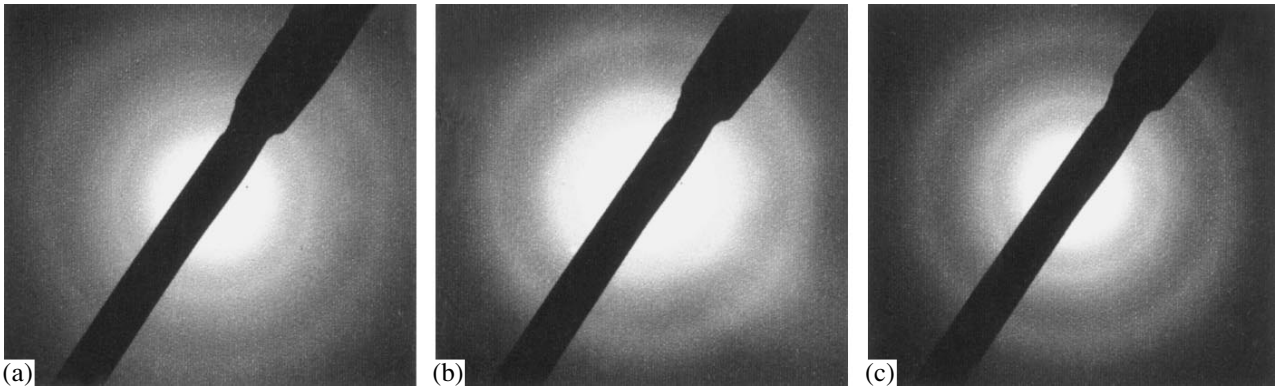

Fig. 6. Diffraction patterns of samples of fullerene-containing soot. (a) Starting soot sample; (b) brief treatment with toluene; and (c) prolonged treatment with toluene.

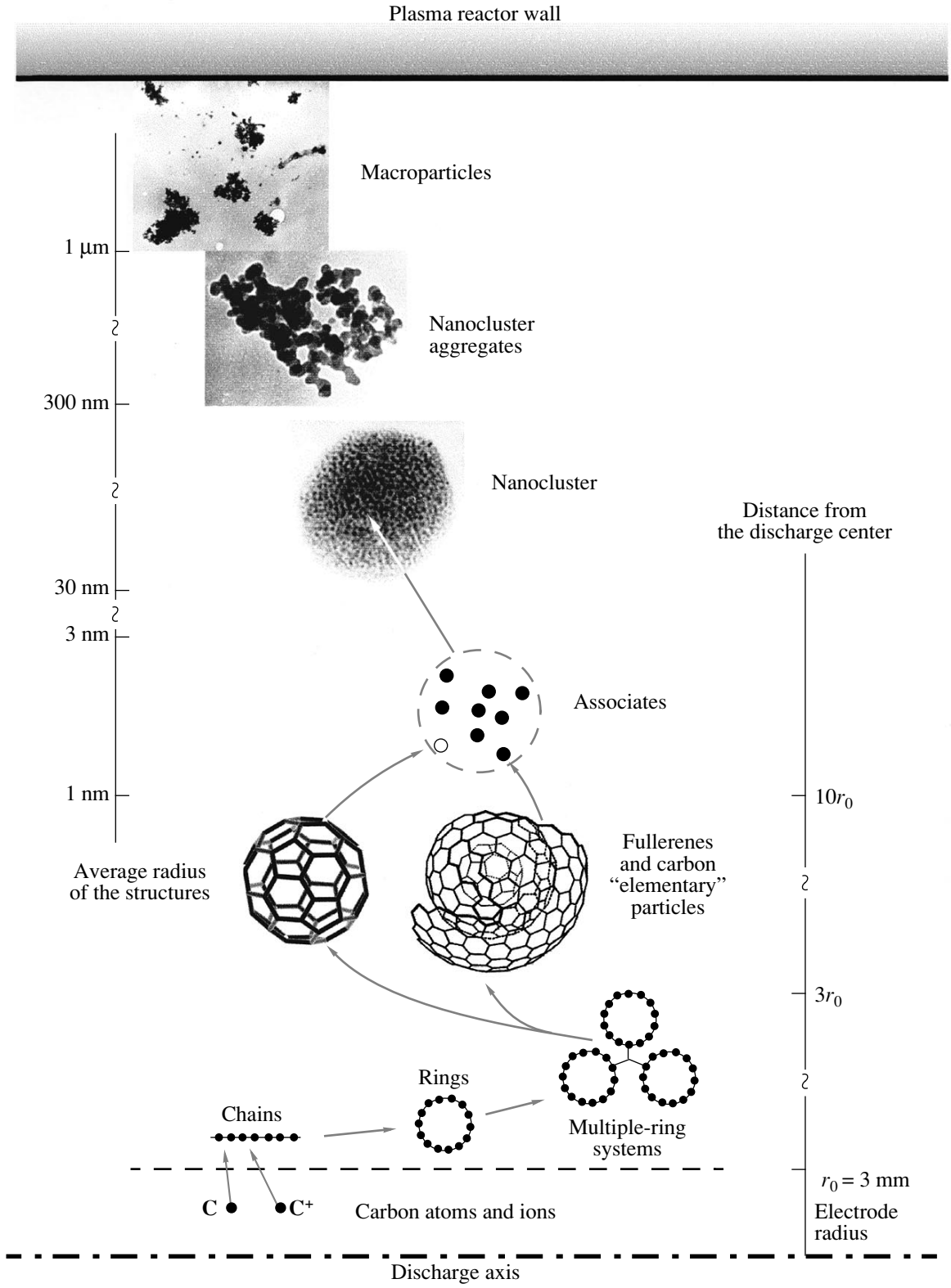

Fig. 7. Formation of the fullerene-containing soot.

Parameters of nanoclusters' structure

Sample	$\rho_\Pi(\xi) \pm 10\%$	ξ, nm $\pm 10\%$	L, nm $\pm 10\%$	$D \pm 10\%$	R_0, nm	s
Fullerene C_{60}	0.8	2.5	3.5	1.80	0.45	14
Fullerene-containing soot	0.55	3.0	4.5	1.60	0.6	8
Fullerene-containing soot briefly treated with toluene	0.8	1.5	2.5	1.80	–	–

by Eq. (8) is equal to 0.45 nm and the degree of aggregation $s = 14$. The results obtained appear quite reasonable since the radius of the C_{60} fullerene is 0.35 nm and the fullerene powder was produced using a supersaturated toluene solution in which associates of fullerene molecules with $s \sim 8$ [16] have been observed.

At $R > R^* = 5$ nm, the fractal dimension of the nanocluster changes from $D = 1.8$ to $D = 2$, and the network becomes continuous with both the correlation radius R^* and the period L_s of about 10 nm. Note that the maximum of $g(R)$ is most pronounced at $R = 8$ nm (Fig. 4, curve *2*). Spatial structures with $L_s = 2R^*$ are typical of hexagonal honeycomb-type networks [8].

Let us now analyze the experimental data on fullerene-containing soot. The function $g(R)$ for the soot nanoclusters (Fig. 4, curve *3*) corresponds to a correlation radius of associates equal to $\xi = 3$ nm. The alternation period of the associates L is about 4 nm. In the range $R < R^* = 7 \pm 0.5$ nm, the lattice density decreases according to the law described by formula (4) (Fig. 5, curve *2*) and the fractal dimension is $D = 1.60 \pm 0.05$.This value of D is more typical of the cluster-cluster than cluster-particle aggregation [17].

If scaling relationships are used for the nanoclusters as well, then the radius of "elementary" particles comprising an associate, as calculated by Eq. (8), is $R_0 \sim 0.6$ nm and the degree of aggregation $s \sim 8$. In the case of soot, the associates will naturally contain, apart from fullerenes, carbon particles that failed to incorporate into the fullerenes during the growth process because of some "architectural" error. The size of such carbon particles is close to that of the fullerene.

The small number of "elementary" particles in the associate ($s \sim 8$) explains the effect of aging of the fullerene soot first observed in [18]. This effect is observed in soot with high fullerene content ($\alpha > 12\%$), in which the value of α drops after a few days of storage to $\alpha \sim 8\%$ and then remains without change for a long time. The following explanation can be suggested: if α is large and there are associates containing at least two fullerene molecules, then dimers that are insoluble in organic solvents can be formed. On the other hand, the formation of dimers in associates containing just one fullerene molecule is unlikely.

At $R > R^*$ an unusual phenomenon is observed in the nanoclusters of fullerene-containing soot when the lattice density $\rho_\Pi(R)$ begins to rise. Only at $R > 25$ nm, i.e., when their radius becomes comparable to the size of a single nanocluster, does the transition to the continuous network of a percolation cluster with $\rho_\Pi(R) = \text{const} = 0.6$ occur. The reason for the growth of $\rho_\Pi(R)$ is not yet quite clear. Maybe the spatial structure of the soot nanoclusters is rather unstable and can be modified by some external factors.

Figure 6 shows electron diffraction patterns of three soot samples. It is seen that even after a brief treatment with toluene, which is too short for the fullerene molecules to pass into the solution, the width of diffraction maxima increases for the same interplanar distances $d_1 = 1.26$ Å and $d_2 = 2.2$ Å. Brief treatment with toluene significantly affects the correlation function $g(R)$ and the lattice density ρ_Π of the nanoclusters (Fig. 4, curve *4* and table), decreasing their correlation radius ξ and the alternation period L and increasing the fractal dimension D. After brief treatment with toluene, the structure of fullerene-containing soot becomes similar to that of the nanoclusters of C_{60} powder (Fig. 5, curve *3*).

Although not all the experimental facts have been interpreted yet, there is no doubt that the structure of nanoclusters in fullerene-contain soot is intrinsically unstable and can be changed by treatment not only in organic solvents but, apparently, in gases as well.

CONCLUSION

The experimental results obtained add up to a qualitative picture of fullerene soot formation in arc discharge. Of course, this picture will be in many respects disputable, but we think that it has a right to exist.

Soot formation is a multistage process, both spatially and as regards the particle size (Fig. 7).

In the active zone of discharge, where the electric current is flowing, the plasma temperature is so high that only carbon atoms and ions are present there [19].

Away from the discharge axis and towards the chamber walls, the plasma temperature decreases, and the formation of C_2 molecules occurs, followed by that of chains, rings and multiple-ring systems.

The transformation of the multiple-ring systems into fullerenes and soot particles is now being actively studied theoretically, but the picture is still far from

clear. Among the experimental results relating to this field, the determination in [20] of the spatial position of the fullerene formation zone and the exposure in [21] of the important role of charged particles in the fullerene formation process should be noted. At the next stage, the aggregation of fullerenes and small carbon particles into associates ("failed" fullerenes) takes place. As shown above, the number of particles in an associate is not large (less than 10). Limited associate size is possibly due to the fact that, in the particle formation zone, the plasma concentration is still appreciable and the electric charge residing on associates prevents their aggregation. The situation in this case is probably similar to the plasma crystal in a dust plasma [22].

It is to be noted that the above steps in the ladder of fullerene formation are spatially well defined, because they proceed within a zone of the fan plasma jet flowing out of the interelectrode gap. Subsequent steps take place in the zone of gas convection, so their spatial boundaries are apparently more diffuse.

Interaction between the associates gives rise to the fractal structure of the nanoclusters studied in this work. The nanoclusters combine into aggregates that also have a fractal structure [9]. And, finally, the aggregates stick together to form macroparticles one micron and larger in size. It is possible that the formation of macroparticles takes place not in the gas medium but on the reactor walls.

ACKNOWLEDGMENTS

This study was supported in part by the Russian Foundation for Basic Research, project no. 97-02-18340.

REFERENCES

1. W. Krätschmer, L. D. Lamb, K. Fostiropoulos, and D. R. Huffman, Nature (London) **347**, 354 (1990).
2. D. H. Parker, P. Wurz, K. Chatterjee, *et al.*, J. Am. Chem. Soc. **113**, 7499 (1991).
3. D. V. Afanas'ev, I. O. Blinov, A. A. Bogdanov, *et al.*, Zh. Tekh. Fiz. **64** (10), 76 (1994) [Tech. Phys. **39**, 1017 (1994)].
4. A. Huczko, H. Lange, P. Byszewski, *et al.*, J. Phys. Chem. **101**, 1267 (1997).
5. T. Belz, J. Find, D. Herein, *et al.*, Ber. Bunsenges. Phys. Chem. **101**, 712 (1997).
6. D. R. Huffman, Mol. Mater. **7**, 11 (1996).
7. J. Feder, *Fractals* (Plenum, New York, 1988; Mir, Moscow, 1991).
8. D. V. Novikov, A. N. Krasovskiĭ, A. I. Andreeva, and S. V. Basov, Kolloidn. Zh. **61**, 240 (1999).
9. E. F. Mikhaĭlov and S. S. Vlasenko, Usp. Fiz. Nauk **165** (3), 263 (1995).
10. E. R. Weibel, *Stereological Methods* (Academic, New York, 1979).
11. D. V. Novikov and A. V. Varlamov, Kolloidn. Zh. **59**, 355 (1997).
12. D. V. Novikov, T. E. Sukhanova, V. K. Lavrent'ev, and M. E. Vylegzhanina, Vysokomol. Soedin., Ser. A **41**, 1266 (1999).
13. J. M. Ziman, *Models of Disorder: the Theoretical Physics of Homogeneously Disordered Systems* (Cambridge Univ. Press, Cambridge, 1979; Mir, Moscow, 1982).
14. D. V. Novikov, A. V. Varlamov, and S. V. Veselova, Zh. Prikl. Khim. (St. Petersburg) **70**, 1180 (1997).
15. I. V. Arkhangel'skiĭ, E. V. Skokan, Yu. A. Velikodnyĭ, *et al.*, Dokl. Akad. Nauk **363**, 494 (1998).
16. V. N. Bezmel'nitsin, A. V. Eletskiĭ, and M. V. Okun', Usp. Fiz. Nauk **168**, 1195 (1998).
17. B. M. Smirnov, *Physics of Fractal Clusters* (Nauka, Moscow, 1991).
18. D. V. Afanas'ev, A. A. Bogdanov, G. A. Dyuzhev, *et al.*, Zh. Tekh. Fiz. **67** (2), 125 (1997) [Tech. Phys. **42**, 234 (1997)].
19. T. W. Ebbesen, J. Tabuchi, and K. Tanigaki, Chem. Phys. Lett. **191** (3–4), 336 (1992).
20. G. A. Dyuzhev and V. I. Karataev, Fiz. Tverd. Tela (St. Petersburg) **36**, 2795 (1994) [Phys. Solid State **36**, 1528 (1994)].
21. D. V. Afanas'ev, G. A. Dyuzhev, and V. I. Karataev, Pis'ma Zh. Tekh. Fiz. **25** (5), 35 (1999) [Tech. Phys. Lett. **25**, 182 (1999)].
22. V. N. Tsitovich, Usp. Fiz. Nauk **167** (1), 57 (1997).

Translated by B. Kalinin

Technical Physics, Vol. 45, No. 11, 2000, pp. 1496–1501. Translated from Zhurnal Tekhnicheskoĭ Fiziki, Vol. 70, No. 11, 2000, pp. 126–132.

EXPERIMENTAL INSTRUMENTS AND TECHNIQUES

A Gas-Discharge Ionizer for an Argon Ionization Detector

E. V. Krylov

Design and Technological Institute of Geophysical and Environment-Friendly Instrument Building, Siberian Division, Russian Academy of Sciences, Novosibirsk, 630090 Russia

E-mail: ekr@uiggm.nsc.ru

Received December 14, 1999

Abstract—The design of an ionizer for gas analyzers using the gas discharge instead of a radioactive source is considered. A high-frequency discharge between isolated electrodes is used as an ionizer in an argon ionization detector for gas chromatography. It is shown that the replacement of a radioactive source by the gas discharge improves the detector performance. An analytical model for the argon ionization detector is proposed. Model results are in good agreement with experiment. © *2000 MAIK "Nauka/Interperiodica".*

Most of modern gas analyzers convert the concentration of a substance to be analyzed into electric current. Thus, the process of ionization, i.e., the formation of charged particles in a gas, is of primary importance in gas analysis. Radioactive sources of β particles (^{63}Ni or ^{3}H) are most often used for the ionization of microimpurities in the gas. In spite of the well-known advantages of such ionizers (stability, long service time, and much operating experience), they have a common drawback: danger of radioactive environmental pollution. Therefore, designing a radiation-free ionizer is becoming more and more topical. Below, we shall discuss the application of an electric gas discharge as a source of charged particles in gas analysis.

GAS DISCHARGE

Gas discharges differ in a number of characteristics: plasma properties (equilibrium or nonequilibrium), the effect of near-cathode processes (electrode or electrodeless discharge), etc. [1]. Requirements imposed on the ionizer for gas analysis considerably restrict the number of acceptable types of gas discharge. Note first of all that an equilibrium plasma, i.e., the plasma with similar temperatures of electrons and gas molecules, cannot be used because of high gas temperatures and high energy needed to generate the plasma. The use of a dc discharge is also limited due to its instability. In this case, charged particles fast leave the discharge region by the action of the field. Thus, the field strength should be raised to sustain the discharge, which leads to instabilities due to ionization overheating [1]. As a result, the ion current also becomes unstable, and the use of the dc gas discharge (corona discharge) as an ionizer is made difficult.

One way of preventing the dc discharge instability is based on the fact that a finite time interval is required for the instability to reach the macrolevel. Therefore, if the energy is delivered to the discharge by short high-intensity pulses, the instability does not develop. However, a sufficiently dense plasma is formed in this case, since the ionization strongly depends on the pump energy. Once a pump pulse is switched off, dissipative processes suppress the development of the instability. If the pulse repetition period is comparable to the energy relaxation time in the plasma, its period-averaged parameters, including the degree of ionization, will be stable. Such a pulsed discharge can be used as an ionizer [2, 3].

However, an rf gas discharge seems to be the most promising in this respect. If its frequency is high enough, charged particles are lost only through neutralization and diffusion processes. Weaker fields insufficient for the development of the instability are required to generate and maintain the plasma in this case. If, however, the field strength is raised to increase the efficiency of ionization, the above reasoning concerning pulse energy delivery remains valid here, too.

An rf capacitive discharge between the isolated electrodes, in our opinion, is the best compromise for the contradictory requirements imposed on a source of charged particles in gas analyzers. In what follows, we shall consider physical and technological principles behind the use of a gas-discharge source in argon ionization detectors designed for an Ekho field gas chromatograph [4].

AN ARGON IONIZATION DETECTOR (AID)

Design

An AID version being considered (Fig. 1) consists of two, ionization and reaction, chambers. An ionizer (β source or gas-discharge ionizer) is placed in the ionization chamber. An active agent (metastable excited particles and/or electrons) is transported to the reaction chamber by means of a carrier gas and/or a constant electric field produced by an extra electrode. A high-voltage electrode (anode) is located near the gas inlet in the reaction chamber. The gas to be analyzed and active

1063-7842/00/4511-1496$20.00

particles coming from the ionization chamber interact in the reaction chamber in the presence of a high-intensity electric field, causing microimpurities to be ionized. The ion current, being the response of the detector, is measured with the cathode.

Processes in the Reaction Chamber

The following reactions proceeding in the reaction chamber, specify the AID response and should be taken into account in calculations.

Collision ionization of a carrier gas (K_a is the equilibrium constant of the reaction):

$$e(V) + G \longrightarrow G^+ + 2e_t,$$

where G is a gas particle, $e(V)$ is an electron whose energy (imparted by the field) is higher than the ionization energy of the particle, G^* is an ionized particle, and e_t is a thermalized electron.

Generation of excited particles G^* (K_e is the equilibrium constant):

$$e(V) + G \longrightarrow G^* + e_t,$$

where $e(V)$ is an electron whose energy (imparted by the field) is higher than that of an excited particle.

Collision ionization of an impurity molecule A (F_i is the equilibrium constant):

$$e(V) + G \longrightarrow G^+ + 2e_t.$$

Penning ionization of an impurity molecule A whose ionization energy is less than the energy of the excited particle G^* (K_p is the equilibrium constant):

$$A + G^* \longrightarrow A^+ + e_t.$$

The annihilation of excited particles may follow various paths and is characterized by the general reaction constant K_d.

AID Design

Let us write a system of charge balance equations

$$G_0^* + K_e n = G^*(K_d + K_p A),$$

$$A^+ = K_p A G^* + K_i n A, \quad G^+ = K_a n,$$

$$n = A^+ + G^+ + n_0.$$

The designations used correspond to those introduced above, but the letters now refer to the concentrations of the related particles normalized to the gas density N, n is the density of free electrons, and subscript 0 marks particles coming from the ionization chamber. The system has a solution relative to n:

$$n = \frac{\beta G_0^* + n_0}{1 - K_a - K_u A - \beta K_b}, \qquad \text{where} \quad \beta = \frac{A}{\gamma + A},$$

and $\gamma = K_d/K_p = 10^{-4}$–$10^{-5}$ [5]; the detector response, i.e., the current being measured, $I = eNn$ (e is the electron charge).

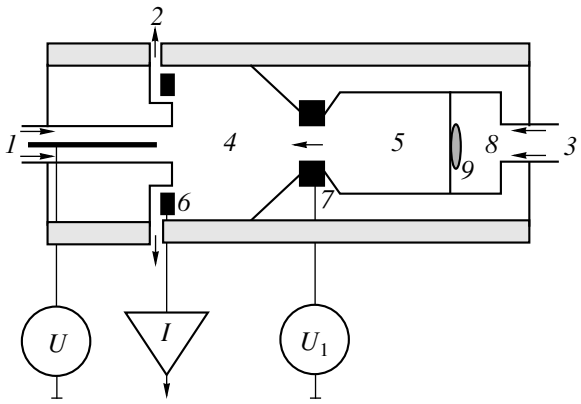

Fig. 1. Argon ionization detector with a gas-discharge ionizer: *U*, high-voltage power source; *I*, electrometric amplifier; U_1, constant voltage source applied to the additional electrode (β source can be used instead of the discharger and discharge initiator); *1*, inlet of gas to be analyzed Q_k; *2*, vent $Q_k - Q_n$, *3*, carrier gas Q_n; *4*, reaction chamber; *5*, ionization chamber; *6*, measuring electrode; *7*, additional electrode; *8*, discharger; and *9*, discharge initiator.

This formula describes the detector current as a function of the concentration of the material being analyzed, electric field strength, and characteristics of the detector. The concentration A enters into the formula through the coefficient β. The field dependence appears through the reaction constants K_i, K_e, and K_a, which essentially depend on the field. At the zero field, they are equal to zero; when the strength E grows to some value, the constants increase drastically. The parameters G_0^* and n_0, appearing in the formula, depend on the detector design.

Asymptotic Behavior

Let us analyze the formula for the limiting values of A and E.

(1) First, it should be mentioned that, as A increases, the coefficient β approaches 1 and the detector current approaches a constant value. The upper limit of the linear range lies at $A \sim \gamma \sim 10^{-4}$–$10^{-5}$. Therefore, there is no point in analyzing the system for $A > \gamma$, and the equation can be simplified by using the condition $A \ll \beta$ and neglecting the terms of the second order of smallness with respect to A:

$$n = \frac{\beta G_0^* + n_0}{1 - \beta K_e - K_a}.$$

(2) Range of small concentrations. In this case, $\beta \approx A/\gamma$, and

$$n = \frac{A G_0^* + n_0 \gamma}{\gamma(1 - K_a) - A K_e}.$$

Note the fundamental difference between the detectors considered. The linear range of an AID with a β source (free electrons as active particles) is limited

below by the value $I = eNn_0/(1 - K_a)$. This so-called background current is caused by the flow of electrons from the ionization chamber. The response of an AID with a capacitive discharge (excited atoms as active particles) is due to the flow of excited atoms from the ionization chamber and ideally can remain linear up to vanishingly small impurity concentrations. The condition $n_0 = 0$ can easily be realized in practice by applying a small blocking voltage to the extra electrode.

(3) Low fields. The reaction constants K_i, K_e, and K_a approach zero; hence,

$$e = \frac{AG_0^*}{\gamma + A} + e_0. \quad (1)$$

(4) High fields. For this case, the detector current is determined by the denominator. At some field, it approaches zero (the current tends to infinity), and the high-voltage electrode breaks down.

Calculations of the Reaction Constants

For further analysis, we must know the dependence of the reaction constants K_i, K_e, and K_a on the electric field strength E. The plasma processes characterized by these constants are of the same physical nature: they transfer energy from an electron accelerated by the field to a neutral particle. Thus, we can determine one constant and then obtain the others, substituting the corresponding initial data, namely, the energy and cross section of the interaction.

We will calculate the constant of some generalized reaction in argon. The dependence of the cross section of this process on the collision energy $\sigma(\varepsilon)$, as well as the distribution of electrons over velocity $f_0(u)$ and energy $n(\varepsilon)$, are assumed to be given [5, 6]. Then, a number of effective collisions ν is given by

$$\nu = \frac{N}{n}\int_{\varepsilon_0}^{\infty} n(\varepsilon)u\sigma(\varepsilon)d\varepsilon,$$

where ε_0 is the characteristic energy of the process and n is the electron concentration.

Due to the nonlocal character of the process, the spatial characteristic of ν, $\alpha = \nu/\mu E$, seems to describe the situation more adequately than the time characteristic. Here, μ is the electron mobility:

$$\mu = \frac{4\pi e}{3mn}\int_0^{\infty}\left(-\frac{\partial f_0}{\partial u}\right)\frac{u^3}{\nu_m}du,$$

where ν_m is the number of transport collisions [6].

Given $\alpha(E)$, one can write the differential equation for the number of ions (N_i) or excited atoms (N_e),

$$dN_i = \alpha_i N_i dr, \quad dN_e = \alpha_e dr.$$

Separating the variables and integrating, we obtain the formula for the number of particles generated by one electron when it moves from a point r_1 to the anode (point r_0):

$$N_i(r_1) = \exp\left\{\int_{r_0}^{r_1}\alpha_i(E(r))dr\right\},$$

$$N_e(r_1) = \int_{r_0}^{r_1}\alpha_e(E(r))dr.$$

Finally, integrating $N(r)$ over the volume of the dividing chamber and normalizing the result to the density of seed electrons $n(r)$, we obtain the reaction constant K:

$$K = \frac{\int_{\nu} N(r)n(r)dr}{\int_{\nu} n(r)dr}.$$

A rigorous calculation with the use of the above formulas faces a number of serious problems. The system of gas flows and electric fields causes the inhomogeneous distribution of the active particles inside the reaction chamber. The physical properties of the object being analyzed (electrons in the gas), which serve as the initial data, are known only from experiments, i.e., are given in the tabulated, rather than in the analytical, form. Therefore, the rigorous analysis of the system must use only numerical methods. However, from the above formulas, one can make several general conclusions. First, from the definition of the coefficient α, it follows that $\alpha_i/\alpha_e = \nu_i/\nu_e$. Second, the number of effective collisions depends on the number of electrons whose energy exceeds the characteristic energy of the process; hence, $\nu_i > \nu_e > \nu_a$.

After these remarks, we proceed to the AID design in simpler terms. Let us divide the reaction chamber into two areas with a sharp boundary between them. First comes the ionization area in the immediate vicinity of the anode, where electrons subjected to the electric field ionize neutral particles of the carrier gas. Its boundary is at a distance of d_a from the anode surface. Next is the excitation area, where excited particles are generated. Its boundary is at a distance of d_e from the anode surface. The electric field E and the corresponding coefficient α are assumed to be constant in either area. With increasing the anode voltage U, only the boundary position changes:

$$d = \sqrt{U/E} - r_0,$$

where r_0 is the anode radius.

Let us justify this assumption. First, the dependence $\alpha(E)$ is of a well-defined threshold character. This fact, together with the sharp spatial inhomogeneity of the

near-anode field, allows one to treat the boundary between the areas as a line on one side of which $\alpha = 0$ and $\alpha \neq 0$ on the other. Under this assumption, the AID response takes the simpler form

$$I = nN(K_a + 1)\frac{\beta G_0^* + e_0}{1 - \beta K_e}.$$

Since we consider the range of moderate fields, the boundaries lie close to the anode. This allows the linearization of the integrals with respect to the small parameter d:

$$K_a = \exp(\alpha_a(E_a)d_a) - 1, \quad K_e = \alpha_e(E_e)d_e.$$

To estimate the coefficient α, one can use the experimental dependence of the Townsend coefficient on the field strength $\alpha(E)$ [7]. The same dependence is suitable for the estimation of $\alpha_e = \alpha_e\nu_e/\nu_a$. The relationship between ν_a and ν_e is considered in the general case in [8].

EXPERIMENT

When an rf discharge between isolated electrodes is used for gas ionization, the physical processes and design concepts differ essentially from the conventional case [9]. The main distinction is that the ionizer must maintain the discharge in an open, rather than in a closed, space. This results in substantial electron losses; hence, the energy needed to initiate and maintain the discharge is high. The field strength can be increased by either increasing the voltage applied to the gap or decreasing the distance between the electrodes and insulator thickness. The first way complicates the design of a pump oscillator and deteriorates its weight–size and power characteristics. The second way also suffers from drawbacks. If the amplitude of electron oscillations becomes larger than the interelectrode distance, the discharge initiation voltage decreases in a much lesser degree with decreasing the distance. The tendency to decrease the insulator thickness also has the natural limit—breakdown of the insulator. Note that the application of a thin layer with high thermal and electric strength and a high permittivity on the electrode is considered to be a key problem in designing effective gas-discharge ionizers of such type. The best solution today is the use of a quartz capillary (outer diameter is 0.2 mm; inner, 0.1 mm) for electrode isolation. One electrode is placed inside the capillary, and the other, outside. The discharge develops over the electrode surface and in its immediate vicinity. Such a design [10] was used in all the experiments performed.

Even if the design of the gap is optimal, a high-frequency voltage with an amplitude of several hundred volts is required to initiate and maintain the discharge. It is easy to show that the reactive power in the megahertz frequency range will be tens of watts for a capacitive load of several tens of picofarad. This means that the design of a pump oscillator in the form of an amplifier combined with a step-up transformer is inappropriate because of its cost inefficiency. An acceptable way to reach the required parameters is to use a resonant oscillator with a capacitive load as a component of the output *LC*-circuit [11]. The best combination of service characteristics (high efficiency of ionization, stability, and cost efficiency) is attained when the pump energy is delivered to the discharge by pulses. Our version had the following characteristics: supply voltage 30–75 V, pulse repetition period 0.1–0.5 ms, pulse duration 20 μs, frequency 13.7 MHz, discharge maintenance voltage 430 V, discharge initiation voltage 630 V, and power consumption 0.12–1.2 W.

The amplitude of the AID signal depends linearly (with an accuracy of 7%) on the supply voltage of the discharge initiator. In our opinion, this is due to an increase in the flow of excited atoms with increasing pump energy. To correctly compare the AIDs with the rf discharge and the β source, the supply voltage was chosen such that the signals from both detectors were equal. A negative voltage of 20 V was applied to the additional electrode. This is sufficient to fully suppress the flow of charged particles from the discharge and to minimize the ion flow from the reaction chamber. The flow rate of the carrier gas was varied.

In the experiments with the AIDs having the β source, a foil of ^{63}Ni with an activity of 10 μCi replaced the gap in the ionization chamber. A positive voltage of 20 V was applied to the additional electrode (the carrier gas was not used, since the detector signal in this case depends only slightly on its flow rate).

RESULTS AND DISCUSSION

The AIDs with the rf discharge and those with the β source were tested as a part of the Ekho field gas chromatograph. Concentration dependences of the detector response (Fig. 2) were measured as a dependence of the chromatogram peak amplitude on the sample volume. The sample was introduce by a gas syringe that contained a certain amount of saturated toluene vapor. Knowing the concentration of the saturated vapor at room temperature, one can estimate the upper limit of the sample concentration (in the maximum of a chromatogram) from the ratio between the introduced and peak volumes. This estimation does not take into account material losses in the analytical path and input errors. Therefore, experimentally found characteristics of the detectors in the range of small concentrations are rough.

As one would expect, the linear range of the detector is limited from above by concentrations of about 100 ppm for both types of the ionizers. The lower limit is determined by the value and stability of the background current, i.e., the current in the absence of the chromatographic signal. The background peak for the AIDs with the β source is due to the electron flow from the ionization chamber and equals about 10^{-9} A. An impurity concentration of 0.1 ppm caused a valid signal

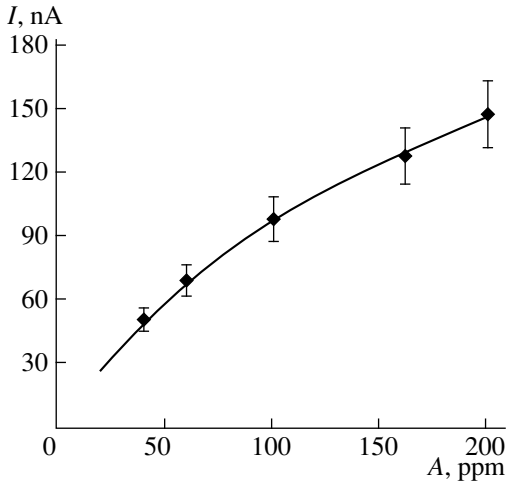

Fig. 2. Concentration dependence of the argon ionization detector.

of the same value (Fig. 3). Electrons are dragged out of the ionization chamber by the constant field, as follows from the diode-type shape of the current–voltage characteristic of the additional electrode.

For the AIDs with the capacitive gas discharge, the background current is almost 100 times less. One can suggest several reasons for its origin. It may result from the interaction between excited and neutral atoms of the carrier gas. The reaction may proceed by the Hornback–Molnar mechanism:

$$G + G^* \longrightarrow G_2^+ + e$$

or Büttner–Chadet mechanism:

$$G^* + G^* \longrightarrow G^+ + G + e.$$

However, it was shown [12] that the former reaction in argon has an insignificant effect. The latter reaction

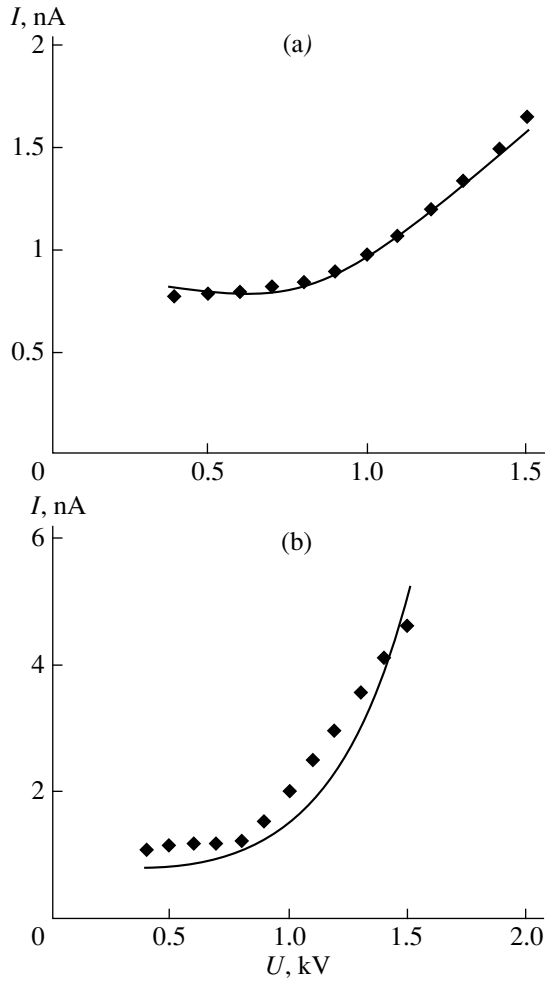

Fig. 3. Argon detector with a radioactive source. (a) Experimental voltage dependence of the background current (data points) and calculated dependence of the detector current on the anode voltage for an impurity concentration of 30 ppb (curve); (b) experimental voltage dependence of the peak amplitude (0.2 μ*l*) (data points) and calculated dependence of the detector current on the anode voltage for an impurity concentration of 4 ppm (curve).

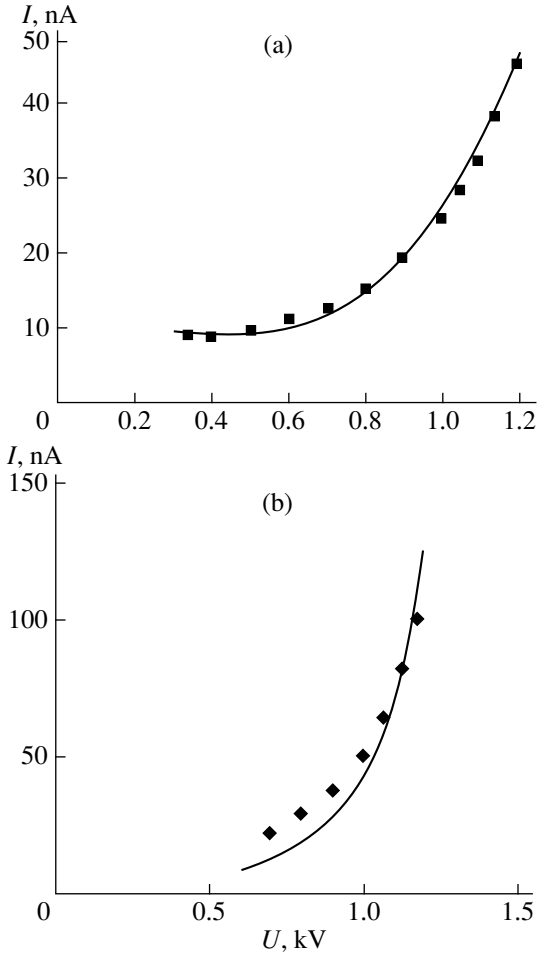

Fig. 4. Argon detector with the capacitive gas discharge. (a) Experimental voltage dependence of the background current (data points) and calculated dependence of the detector current on the anode voltage for an impurity concentration of 30 ppb (curve); (b) experimental voltage dependence of the peak amplitude (1 μ*l*) (data points) and calculated dependence of the detector current on the anode voltage for an impurity concentration of 20 ppm (curve).

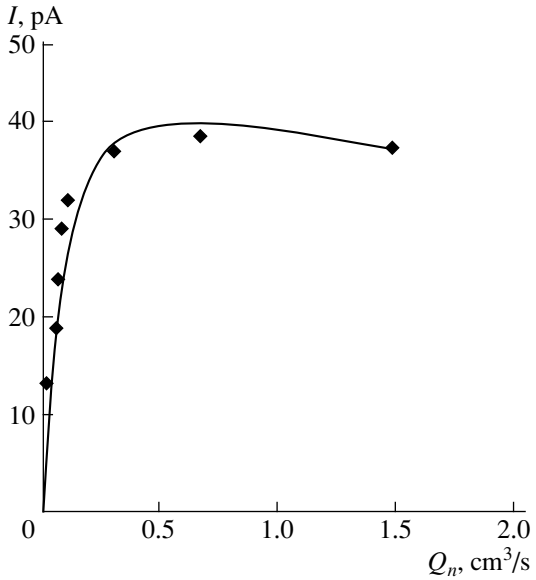

Fig. 5. Background current vs. carrier gas flow rate: data points, experiment; curve, calculation.

is essential only at high concentrations of excited particles. Moreover, this reaction implies a quadratic dependence of the detector response on the concentration of excited particles. This does not agree with the linear dependence of the background current on the voltage across the discharger.

Uncontrollable impurities in the carrier gas that have an ionization energy smaller than the excitation energy of an argon atom seems to be a more probable reason for the background current in the AIDs with the capacitive discharge. This impurity (contamination) ionizes by the Penning mechanism and gives the same AID response as the material being analyzed (in this case, background current would be more properly termed background signal). The impurity concentration extrapolated from the concentration dependence falls into the range of 10–100 ppb. The value 30 ppb, used in the calculations, gives the best agreement with the experiment (Fig. 4).

For the AIDs with the capacitive discharge, the active particles G_0^* are transferred into the reaction chamber by means of the carrier gas. Hence, the detector response depends on the carrier gas flow rate Q_n. This dependence can be estimated if it is assumed that the annihilation of the active particles (when they are transported from the ionization chamber to the reaction chamber within a time $t_{tr} \sim 1/Q_n$) follows an exponential law with a characteristic time τ. Moreover, one should take into account that the active particles are dragged out of the reaction chamber by the carrier gas. Then,

$$G_0^* \sim \frac{1}{1 + Q_n/Q}\exp\left(-\frac{t_{tr}}{\tau}\right),$$

where Q is the gas flow from the chromatographic column.

As we have shown, for small concentrations of the gas being analyzed, the detector response $I \sim G_0^*$. The constancy of the background signal allows one to check the proposed dependence of the concentration of excited particles on the carrier gas flow rate with a good accuracy (Fig. 5).

CONCLUSIONS

(1) The analytical model of an argon ionization detector with an additional high-voltage electrode is proposed. The model is in satisfactory agreement with the experiment.

(2) A laboratory prototype of the ionizer was tested as a part of the detector.

(3) The use of the rf capacitive discharge in the detector allows one to improve its characteristics in comparison with the β source detector.

ACKNOWLEDGMENTS

The author thanks A.T. Shishmarev and I.A. Buryakov for their assistance in the experiments.

REFERENCES

1. Yu. P. Raĭzer, *Modern Physics of Gas Discharge* (Nauka, Moscow, 1980).
2. Zhao Jianguo and D. M. Lubman, Anal. Chem. **65**, 866 (1993).
3. W. E. Wentworth, S. V. Vasnin, S. D. Stearns, and C. J. Meyer, Chromatographia **34** (5–8), 219 (1992).
4. Ékho-EW Field Portable Chromatograph (Model 2), Certificate No. 5517 (Registration No. 17712-98 in the State List of Measurements, 1998).
5. V. V. Brazhnikov, *Differential Detectors for Gas Chromatography* (Nauka, Moscow, 1974).
6. *Physical Quantities: Handbook* (Énergoatomizdat, Moscow, 1981).
7. S. C. Brown, *Basic Data of Plasma Physics* (MIT Press, Cambridge, 1959; Atomizdat, Moscow, 1961).
8. Yu. P. Raĭzer, *Laser-Induced Discharge Phenomena* (Nauka, Moscow, 1974; Consultants Bureau, New York, 1977).
9. Yu. P. Raĭzer, M. N. Shneĭder, and N. A. Yatsenko, *Radio-Frequency Capacitive Discharge* (Nauka, Moscow, 1995).
10. I. A. Buryakov and E. V. Krylov, RF Inventor's Certificate No. 2120626, GOIN 27/6, Byull. Izobret., No. 29 (1998).
11. E. V. Krylov, Prib. Tekh. Éksp., No. 5, 47 (1997).
12. J. Leonhardt, Dissertation (Math-Nath. Fakultat Karl-Marx-Univ., Leipzig, 1966).

Translated by M. Astrov

Technical Physics, Vol. 45, No. 11, 2000, pp. 1502–1504. Translated from Zhurnal Tekhnicheskoĭ Fiziki, Vol. 70, No. 11, 2000, pp. 133–135.

BRIEF COMMUNICATIONS

Self-Localization of Temperature Domains in Tunable Spectrum Semiconductors

Yu. V. Gudyma

Fed'kovich State University, Chernovtsy, 274012 Ukraine

Received October 4, 1999; in final form, January 31, 2000.

Abstract—It is shown that, in semiconductors with temperature-tunable optical absorption, a macroscopic self-localization of temperature domains is possible due to deformation-thermal interaction. This phenomenon can be considered as a large-scale analog of the well-known self-capture effects. © *2000 MAIK "Nauka/Interperiodica".*

(1) Under fairly strong electron–phonon interaction, self-localization of quasi-particles (electrons and phonons) occurs in crystals in regions having the size of the order of the lattice is constant. The quasi-particles in this case are variously called small-radius polarons, condensons, and polarizing or deforming excitons [1]. We show below that, on the surface of semiconductors with tunable electronic spectrums, a macroscopic self-localization of temperature domains is possible due to deformation-thermal interaction. This phenomenon, despite being quite unusual, represents a large-scale analog of the known self-capture effects.

This effect is closely related to the formation on the surfaces of solids of periodic structures as a result of irradiation with power laser light [2]. The periodic modulation of the surface relief is invariably produced when the intensity of the laser source exceeds a threshold value. Observed in experiments (on Si, Ge, GaAs, and InSb) were both irreversible lattices (persisting after the laser pulse time) and reversible lattices (existing only for the duration of the laser pulse). The formation in *p*-CdTe, *n*-CdS, and *p*-ZnTe of structures having a nonlinear conductivity dependence due to the generation of defects [3, 4] is possibly of a similar nature. The formation on a semiconductor surface of periodic defect structures under laser irradiation was studied in [5]. Under localized pulsed laser irradiation, angstrom-scale quasi-static deformation profiles were studied in [6].

(2) When fluctuations of temperature T about its average value modulate the semiconductor band gap

$$E_g^* = E_g(1 - bT), \tag{1}$$

where the coefficient

$$b = \frac{1}{E_g}\left|\frac{\partial E_g}{\partial T}\right|$$

characterizes the rate of these variations, the optical absorption coefficient is

$$\alpha = \alpha_0\left(\frac{\hbar\omega - E_g^*}{\hbar\omega - E_g}\right)^{1/2}. \tag{2}$$

Here, $\alpha = \alpha_0$ at $T = 0$. Under irradiation, the transverse fluctuations of temperature contribute additional forces to the equation of elastic medium vibrations on its surface (optical-acoustic effect):

$$\frac{\partial^2 u}{\partial t^2} = \nu^2\Delta u - \frac{K\beta}{\rho}\nabla T, \tag{3}$$

where u is the medium displacement vector; ν is the sound velocity in the medium; K is the uniform pressure modulus; β is the coefficient of volume expansion; ∇ and Δ are differential operators specified on the semiconductor surface.

Modulation of the optical absorption in the medium, in turn, causes additional modulation of the temperature T in accordance with the thermal conductivity equation

$$\chi\Delta T - \frac{K\beta}{\rho}\nabla u + \frac{1}{\rho c_p}\left(\alpha P - \frac{H}{l}(T - T_0)\right) = 0, \tag{4}$$

where χ is the temperature conductivity of the medium; ρ is the medium density; c_p is the thermal capacity of a material at constant pressure; P is the incident power density; H is the heat emission coefficient; l is the wafer thickness; and T_0 is a thermostat temperature.

The thermal conductivity equation is written assuming that the temperature distribution is maintained constant with a continuous laser heat source. A more easily tractable form of equation (4) is

$$\chi\Delta T - \frac{K\beta}{\rho}\nabla u + \frac{\alpha P}{\rho c_p} - \frac{T - T_0}{\tau} = 0, \tag{5}$$

where τ is the temperature relaxation time.

1063-7842/00/4511-1502$20.00

In dimensionless variables $r' = \alpha_0 r$, $t' = \alpha_0 \nu t$, $u' = \alpha_0 u$, and $T' = bT$, equations (3) and (5) take the respective forms

$$\frac{\partial^2 u'}{\partial t'^2} = \Delta u' - \frac{K\beta}{\nu^2 \rho b}\nabla T', \tag{6}$$

$$\Delta T' - \frac{K\beta}{\nu^2 b\rho}\nabla u' + \frac{\alpha b P}{\chi \rho c_p \alpha_0^2} - \frac{T' - T_0'}{\alpha_0^2 \tau \chi} = 0. \tag{7}$$

Below, the prime will be omitted from symbols for the sake of simplicity. Equations (6) and (7) describe an extremal action

$$S = \iint\left\{\frac{1}{2}\left(\frac{\partial u}{\partial t}\right)^2 - \frac{1}{2}(\nabla u)^2 - \frac{K\beta}{\nu^2 \rho b}u\nabla T + \frac{1}{2}(\nabla T)^2 - \frac{(T - T_0)^2}{2\alpha_0^2 \chi \tau} - \frac{2}{3}\frac{bP}{\alpha_0 \chi \rho c_p}\frac{(\hbar\omega - E_g + E_g T)^{3/2}}{E_g(\hbar\omega - E_g)^{1/2}}\right\} dr dt. \tag{8}$$

The Eulerian equation in dimensionless variables is obtained by minimizing $S = \iint F(T, u) dr dt$ with respect to T and u:

$$\frac{\partial}{\partial t}\left(\frac{\partial u}{\partial t}\right) - \Delta u + \frac{K\beta}{\nu^2 \rho b}\nabla T = 0, \tag{9}$$

$$\nabla j + \frac{bP}{\chi \rho c_p}\frac{\alpha}{\alpha_0^2} - \frac{1}{\alpha_0^2 \chi \tau}(T - T_0) = 0, \tag{10}$$

where

$$j = j_\tau + j_u = \nabla T - \frac{K\beta}{\nu^2 \rho b}u. \tag{11}$$

Taking account of the self-action in (10) makes the current functionally dependent on lattice vibrations and, as a result, the equation becomes nonlinear.

To be able to apply the field theory, we introduce a minimum time $\tau = it$ and consider the minimum action $S \longrightarrow iS$. The dimensionless density of the Lagrangian in this case has the form

$$L = \frac{1}{2}\int\left(\frac{\partial u}{\partial \tau}\right)^2 dr + \frac{1}{2}\int(\mathrm{div} u)^2 dr + \min_T \int\left\{\frac{K\beta}{\nu^2 \rho b}u\nabla T - \frac{1}{2}(\nabla T)^2 - \frac{(T - T_0)}{2\alpha_0^2 \chi \tau} + \frac{2}{3}\frac{bP}{\alpha_0 \chi \rho c_p}\frac{(h\omega - E_g + E_g T)^{3/2}}{E_g(\hbar\omega - E_g)^{1/2}}\right\} dr, \tag{12}$$

and the energy conservation law is

$$E = \frac{1}{2}\int\left(\frac{\partial u}{\partial \tau}\right)^2 dr + U(u, T). \tag{13}$$

The Lagrangian contains only quadratic and linear vibrational terms; therefore, the problem can be analytically solved with respect to vibrational modes and the corresponding variables eliminated. This reduces the problem to varying the action, which depends exclusively on $T(r, \tau)$ as is shown below.

(3) We are interested in those trajectories with energy $E = 0$ (on the localization line), which at $\tau = -\infty$ begin at the point $u = 0$ and at $\tau = 0$ terminate on the surface $U(u, T) = 0$. From the conservation of the energy $E = 0$, it follows that, at the trajectory end point, $\partial u/\partial \tau = 0$ (localized states). Thus, the macroscopic problem considered is formally analogous to that of penetration by tunneling of an autolocalized barrier in the quantum case [1]. Minimization of L with respect to u yields the Eulerian equation

$$\frac{\partial^2 u}{\partial \tau^2} + \Delta u - \frac{K\beta}{\nu^2 \rho b}\nabla T = 0, \tag{14}$$

which is to be solved under conditions

$$u|_{r = -\infty} = 0, \quad \left.\frac{du}{d\tau}\right|_{\tau = 0} = 0. \tag{15}$$

The solution meeting conditions (15) has the form

$$u = \nabla \int G(\tau - \tau', r - r')\frac{K\beta}{\nu^2 \rho b}T dr' d\tau', \tag{16}$$

where the Green's function is

$$G(r, \tau) = \int e^{i[\omega(\tau - \tau') - k(r - r')]}\frac{1}{k^2 + \omega^2}\frac{dk}{(2\pi)^3}\frac{d\omega}{2\pi}, \tag{17}$$

and the function $T(r, \tau)$ is extrapolated by parity to the region $\tau > 0$.

Substituting (16) into (12) and using the δ function, the density of the Lagrangian is obtained:

$$L = \frac{1}{2}\min_T \int\left\{\left(\frac{K\beta}{\nu^2 \rho b}\right)^2 \nabla T \nabla \int_{-\infty}^{+\infty} G(r - r', \tau - \tau') \times T(r', \tau') dr' d\tau' - (\nabla T)^2 - \frac{(T - T_0)^2}{\alpha_0^2 \chi \tau} + \frac{4}{3}\frac{bP}{\alpha_0 \chi \rho c_p}\frac{(\hbar\omega - E_g + E_g T)^{3/2}}{E_g(\hbar\omega - E_g)^{1/2}}\right\} dr. \tag{18}$$

From (18) follows the Eulerian equation for the temperature

$$-\Delta T + \frac{(T - T_0)}{\alpha_0^2 \chi \tau} - \frac{bP}{\alpha_0 \chi \rho c_p}\left(\frac{\hbar\omega - E_g + E_g T}{\hbar\omega - E_g}\right)^{1/2} = 0. \tag{19}$$

The minima corresponding to the free and self-localized states are separated by a self-localized barrier. Its height is determined by the position of a saddle point of the adiabatic potential surface [1], the role of which in this case is played by the Lagrangian (18). The normalized value of the self-localized barrier according to (18) is

$$W = \frac{K\beta}{\nu^2\rho b}. \quad (20)$$

The barrier transparency can be characterized by a quantity $D = \exp(-2W)$. An estimate made using parameter values typical of A^2B^6 semiconductor compounds (CdS, ZnS, and others), namely, $K = 10^{11}$ N/m^2, $\beta = 10^{-5}$ deg^{-1}, $\nu = 10^5$ m/s, $\rho = 5$ g/cm^3, and $b = 5 \times 10^{-3}$ deg^{-1}, yields $\log D \approx -4$.

4. The above calculation procedure reveals an analogy between the formation of domains with the subsequent spatial localization of the temperature at the surface of tunable electronic spectrum semiconductors heated by band-to-band absorption of light with quantum effects of self-localization. The calculation method used corresponds to penetration of the self-localization barrier by tunneling [1]. The dependence of the band width on temperature provides a mechanism of feedback between the equations of thermal conductivity and elastic medium vibrations. Moreover, temperature fluctuations produce additional forces causing vibrations of the elastic medium. The system becomes spatially nonhomogeneous. Thus, the process of development of deformation–thermal instability in the semiconductors in question has the character of a large-scale self-localization. Of course, states corresponding to the concerted propagation of a temperature domain and its accompanying diffusion are also possible.

As a function of the emergence of stable temperature nonuniformities, defect structures will form on the semiconductor surface. Moreover, on the actual surface there are always some roughness and inoculation defects present, which enhance the photoinduced destruction process. The technique and the problems of the experimental optical-acoustic spectroscopy of condensed matter have been described in detail in [7].

REFERENCES

1. S. V. Iordanskiĭ and É. I. Rashba, Zh. Éksp. Teor. Fiz. **74**, 1872 (1978) [Sov. Phys. JETP **47**, 975 (1978)].
2. V. I. Emel'yanov, Kvantovaya Élektron. (Moscow) **28** (1), 2 (1999).
3. D. I. Tsyutsyura and P. S. Shkumbatyuk, Pis'ma Zh. Tekh. Fiz. **19** (1), 12 (1993) [Tech. Phys. Lett. **19**, 4 (1993)].
4. P. S. Shkumbatyuk and D. I. Tsyutsyura, Zh. Tekh. Fiz. **65** (12), 136 (1995) [Tech. Phys. **40**, 1276 (1995)].
5. I. A. Dorofeev and M. N. Libenson, Zh. Tekh. Fiz. **65** (10), 111 (1995) [Tech. Phys. **40**, 1037 (1995)].
6. V. I. Emel'yanov and I. M. Panin, Fiz. Tverd. Tela (St. Petersburg) **39**, 2029 (1997) [Phys. Solid State **39**, 1815 (1997)].
7. V. P. Zharov and V. S. Lekhotov, *Laser Optico-Acoustic Spectroscopy* (Nauka, Moscow, 1984).

Translated by B. Kalinin

Technical Physics, Vol. 45, No. 11, 2000, pp. 1505–1508. Translated from Zhurnal Tekhnicheskoĭ Fiziki, Vol. 70, No. 11, 2000, pp. 136–139.

BRIEF COMMUNICATIONS

Nonlinear Optical Properties of Thin Films at a Low Light Intensity

A. V. Khomchenko

Institute of Applied Optics, Belarussian Academy of Sciences, Mogilev, 212793 Belarus

E-mail: ipo@physics.belpak.mogilev.bu

Received March 3, 2000

Abstract—Nonlinearity of optical parameters of semiconductor and dielectric films for a 0.63-nm-wavelength light with intensity lower than 100 mW/cm^2 is discovered and studied. © *2000 MAIK "Nauka/Interperiodica".*

Optical signal processors use materials whose refractive indices and absorption factors depend on light intensity. Semiconductors feature the greatest refractive index n_2. Therefore, researchers focus on developing and searching for semiconductor materials or structures with giant optical nonlinearity. The optical nonlinearity in semiconductor materials, regardless of the mechanism behind it, is usually observed at the light power density of no less than ~10–100 W/cm^2.

In this paper, we report that variations in the refractive index and absorption factor are observed at the incident light intensity of a few milliwatts with n_2 and nonlinear absorption factor k_2 reaching values as high as ~10^{-3} cm^2/W.

Properties of amorphous films of arsenic sulfide, gallium selenide, and tin dioxide (SnO_2), as well as those of polycrystalline zinc selenide (ZnSe) films, and of color and quartz glass films, are studied. The amorphous and polycrystalline films were produced by vacuum deposition. The substrate was made of fused quartz or K8 optical glass. The substrate temperature during the deposition process was no higher than 250°C. Spectral optical parameters of the film material (refractive index n and absorption factor k) were studied by the waveguide method at the wavelength of the He–Ne laser [1] and in the improper absorption spectral band of the semiconductor material. In the experiment, we recorded the Fourier spectrum of the light beam reflected from the base of a prism coupling element and processed it to determine the real h' and imaginary h'' parts of the propagation constant h of the waveguide mode. The nonlinear refractive index n_2 and the absorption factor k_2 were determined under the self-action conditions at a wavelength of 0.633 μm [2]. The intensity of the incident light ranged from 0.5 μW to 1.0 mW. The light beam radius at the prism base was within 150 μm.

When studying optical properties of thin vitreous arsenic sulfide films, we measured nonlinear optical constants n_2 and k_2 for the light intensity ranging from 10 to 100 W/cm^2 at 0.63 μm. Quartz glass was used as a substrate. Our result, $n_2 = 1.5 \times 10^{-5}$ cm^2/W, was in satisfactory agreement with results available in the literature [3]. However, we discovered a strong nonlinear dependence of the thin-film spectral optical parameters on the incident-light intensity in the range below 0.1 W/cm^2 [2]. The measured nonlinear constant was $n_2 = 2.65 \times 10^{-3}$ cm^2/W. Variations in the films optical parameters caused by a rise in its temperature due to light absorption were several orders of magnitude lower than the measured values [4], which testified to the fact that the origin of the observed optical nonlinearity is nonthermal.

This feature of arsenic sulfide films indicates that there exist several mechanisms of optical nonlinearity with different saturation energies. Similar measurements in polycrystalline zinc selenide films also revealed significant nonlinear variations in the spectral optical properties of thin films [5]. Figure 1 shows the increment $\Delta h'$ versus incident light power, where $\Delta h' = h' - h'_0$, and h'_0 is the value taken by h' at the minimal light intensity. The scatter in the obtained h' was significantly higher than the measurement error ($\delta h' = 5 \times 10^{-6}$), which required more thorough studies of zinc selenide film parameters versus light intensity. The dependencies obtained were nonmonotonic and had a serrated structure. The character of the nonlinear dependence and the values of n_2 of the deposited film material were determined by the crystalline quality of the deposited film. Curves *1–3* in Fig. 1 show $\Delta h'(I)$ for films deposited at substrate temperatures of 140, 180, and 250°C, respectively. The corresponding estimates of average crystallite dimensions in these films obtained from spectrophotometric measurements were 19, 7, and 12 nm.

1063-7842/00/4511-1505$20.00

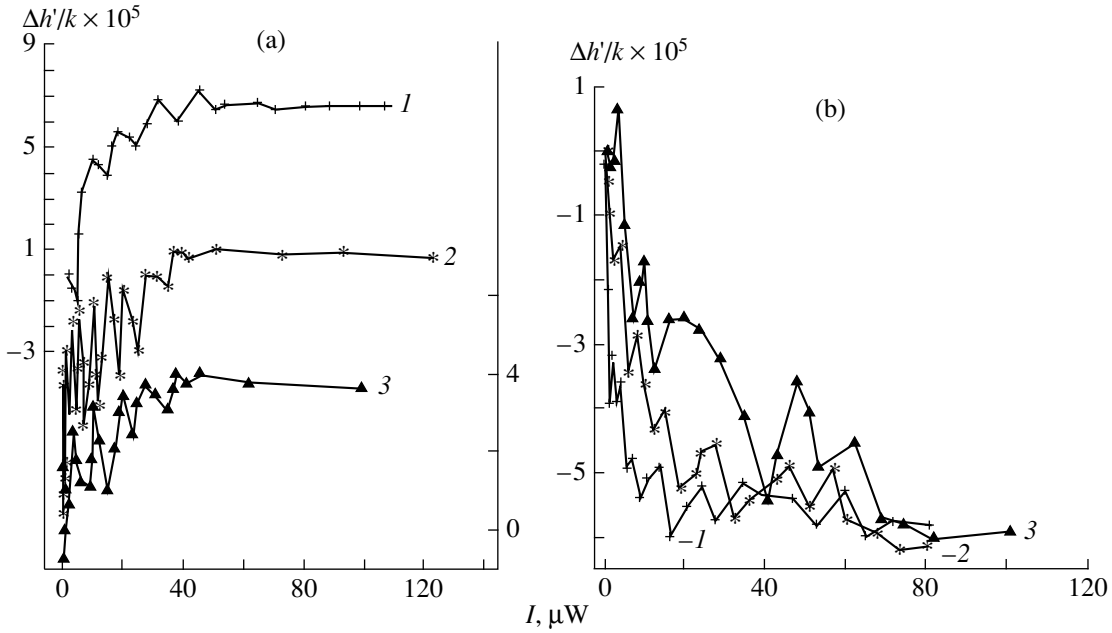

Fig. 1. $\Delta h'(I)$ (a) for ZnSe films deposited at the substrate temperature of (*1*) 140, (*2*) 180, and (*3*) 250°C; (b) for color-glass films deposited at the substrate temperature of (*1*) 140 and (*2*) 190°C (*1*) before and (*3*) after thermal annealing.

Similar variations in the spectral optical properties versus incident light intensity were also observed in GaSe, ZnO, SnO_2, $LiNb_2O_3$, and other films.

Thin-film structures in which size-quantization effects are observed are often produced from glass doped with semiconductors. Therefore, we studied nonlinear optical properties of thin-film structures fabricated by sputtering color glasses (OS12) and ceramic targets that contained SiO_2, ZnSe, or CdSe. In this case, a similar nonmonotonic dependence $h'(I)$ was observed. Properties of these films differed only in that, in contrast to polycrystalline ZnSe films, which exhibited a reduced absorption, the absorption factor of the films based on color glasses increased with light intensity. In these materials, the optical nonlinearity is governed by the size of semiconductor crystallites infused into the glass matrix [6]. The size of semiconductor crystallites can be changed through thermal annealing or by changing film deposition conditions. Figure 1b shows $h'(I)$ for OS12 glass films before and after thermal annealing at 400°C for 6 h. Increasing the substrate temperature in the course of the film deposition also changed the character of the nonmonotonic dependence $h(I)$ (Fig. 1b, curves *1* and *3*).

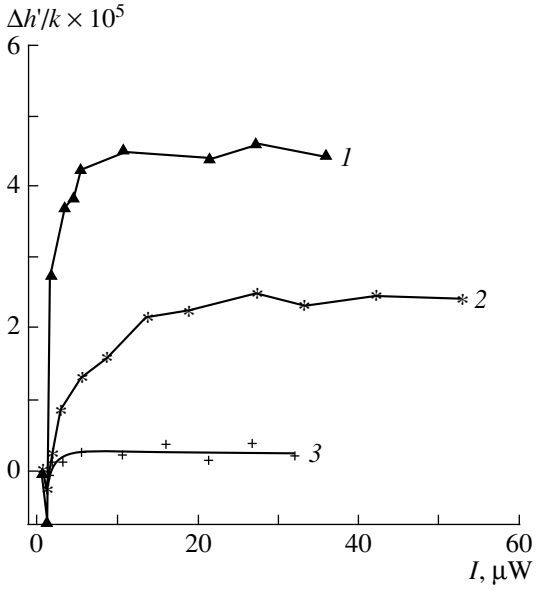

Fig. 2. h' versus incident light intensity for SiO_x films at the film material absorption factor of (*1*) 3×10^{-5}, (*2*) 9×10^{-6}, and (*3*) 3×10^{-6}.

It should be noted that optical nonlinearity at low light intensities was also observed in films produced by sputtering fused quartz. In this case, n_2 was $\sim 10^{-7}$ cm^2/W, which is lower than that for semiconductor films or for films produced from color glasses. The nonlinear behavior of the spectral optical parameters versus incident light intensity was reliably recorded in films with distorted stoichiometry. When the optical loss in the waveguiding film was ~2 dB/cm, the effect was almost absent (Fig. 2).

The experimental studies of nonlinear optical properties of thin-film structures in which size quantization effects are observed allow us to assume that the optical nonlinearity in these structures is caused by electron processes evolving on the semiconductor–dielectric interface. In this regard, we tried to create such a non-

linear medium by producing a mulilayer structure. It was fabricated by the alternate deposition of conducting material SnO_2 and dielectric SiO_2. This structure with ~10-nm-thick layers modeled a small-sized nonlinear medium. Figure 3 presents plots $h'(I)$ for a structure containing three layers of tin oxide separated by silicon dioxide layers. The conducting films were 12-, 24-, and 36-nm-thick. Three peaks of various widths are also clearly seen in the $h'(I)$ plot. In this kind of structure, the optical nonlinearity also depends on the optical quality of the dielectric layers. Figure 3 displays $h'(I)$ for three SnO_2 films fabricated in the course of a single deposition process on various substrates. Pure quartz glass was used as the substrate; the structure was a quartz glass–SiO_x film. The absorption factor for the SiO_x film was (curve *3*) 1.5×10^{-5} and (curve *4*) 5×10^{-6}, and the film thickness was 1 μm. The high values of n_2 and k_2 indicate that light can be controlled by light in these structures at an intensity of ~10 mW/cm^2.

As follows from the results presented above, the nonlinear properties are most pronounced in structures that use a defective SiO_x film as a substrate. This allows us to suppose that the surface state is the factor that governs the nonlinear behavior of the spectral optical parameters of thin films in this case. In the polycrystalline films and size-quantization structures based on glasses doped with semiconductors, the surface of individual semiconductor crystallites additionally contributes to the optical nonlinearity.

The analysis of the above results shows that processes that evolve in multilayer structures, polycrystalline films, and films of glasses doped with semiconductors and that cause nonmonotonic behavior of their optical properties versus light intensity are similar. Presumably, generation and recombination of charge carriers at the surface-state energy levels play a vital role here. Certainly, not all surface states take part in the recombination. For part of the states, only band–level transitions are feasible; then, the surface state is a trap. These states are more typical of semiconductor–dielectric interfaces.

In our experiments, the refractive index and absorption factor of the film material were independent of exposure, while an additional illumination by the second laser beam at $\lambda = 0.63$ nm also changed the spectral absorption factor of the film material. Figure 4 shows absorption spectra of the SnO_2 film before and in the process of additional illumination by a light beam at $\lambda = 0.63$ nm. The spectra were measured by the wave guide Fourier-spectroscopy technique. Curve *3* in Fig. 4 shows the absorption spectrum of this film in water vapor. The analysis of these results indicates that there also exist empty surface-state energy levels in the transmission band of the film material. Presumably, the existence of the surface states is the factor that determines the significant nonlinearity in spectral optical properties of thin films at low light intensities.

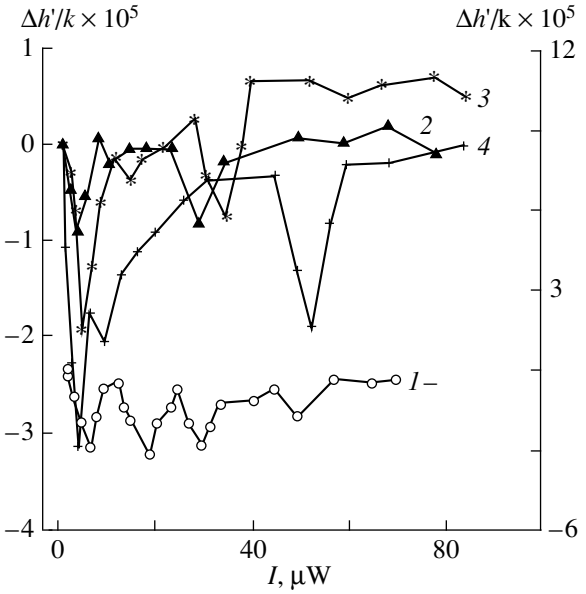

Fig. 3. $\Delta h'(I)$ for (*1*) a multilayer structure based on SnO_2 containing three conducting layers, (*2*) SnO_2–substrate structures, and SnO_2–SiO_x–substrate structures at the SiO_x absorption factor of (*3*) 1.5×10^{-5} and (*4*) 5×10^{-6}.

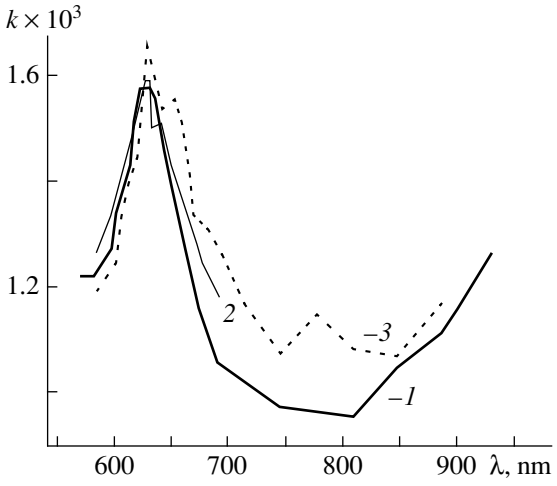

Fig. 4. Absorption spectrum of the SiO_2 film (*1*) before and (*2*) in the process of additional illumination with light at $\lambda = 0.63$ and (*3*) in water vapor.

A significant nonlinearity in optical properties of thin films illuminated by 0.63-nm-wavelength light with intensity below 100 mW/cm^2 was discovered. The nonlinear refractive index reached values as high as $n_2 \times 10^{-3}$ cm^2/W. Presumably, the thin-film optical nonlinearity is caused by the surface-state energy levels within the forbidden band. For small-sized structures, the character of the nonlinearity is determined by the quality of the semiconductor–dielectric matrix interface; for polycrystalline films, it is determined by the crystal quality of the film material and by the size of individual crystallites.

ACKNOWLEDGMENTS

The author is grateful to A.I. Voĭtenkov for fruitful discussion of the results.

REFERENCES

1. V. P. Red'ko, A. A. Romanenko, A. B. Sotskiĭ, and A. V. Khomchenko, Pis'ma Zh. Tekh. Fiz. **18** (3), 14 (1992) [Sov. Tech. Phys. Lett. **18**, 100 (1992)].
2. A. B. Sotskiĭ, A. V. Khomchenko, and L. I. Sotskaya, Pis'ma Zh. Tekh. Fiz. **20** (16), 49 (1994) [Tech. Phys. Lett. **20**, 667 (1994)].
3. A. Yu. Vinogradov, É. A. Smorgonskaya, and E. I. Shifrin, Pis'ma Zh. Tekh. Fiz. **14**, 642 (1988) [Sov. Tech. Phys. Lett. **14**, 287 (1988)].
4. A. B. Sotskiĭ, A. V. Khomchenko, and L. I. Sotskaya, Opt. Spektrosk. **78**, 502 (1995) [Opt. Spectrosc. **78**, 453 (1995)].
5. A. V. Khomchenko, Zh. Tekh. Fiz. **67** (9), 60 (1997) [Tech. Phys. **42**, 1038 (1997)].
6. S. Sh. Gevorkyan and N. V. Nikonorov, Pis'ma Zh. Tekh. Fiz. **16** (13), 32 (1990) [Sov. Tech. Phys. Lett. **16**, 494 (1990)].

Translated by A. Khzmalyan

Technical Physics, Vol. 45, No. 11, 2000, pp. 1509–1511. Translated from Zhurnal Tekhnicheskoĭ Fiziki, Vol. 70, No. 11, 2000, pp. 140–142.

BRIEF COMMUNICATIONS

Intensive Molecular Gas Evaporating from the Surface of a Spherical Particle into a Vacuum

I. A. Kuznetsova, A. A. Yushkanov, and Yu. I. Yalamov

Ushinskiĭ Yaroslavl State Pedagogical University, ul. Respublikanskaya 108, Yaroslavl, 150000 Russia

Moscow Pedagogical University, ul. Radio 10a, Moscow, 107005 Russia

E-mail: kuz@univ.uniyar.ac.ru

Received March 22, 2000

Abstract—The kinetic problem of intensive diatomic gas evaporation from the surface of a spherical particle in a vacuum is solved. The analytical expressions for the parameters of a vapor gas at the hydrodynamic evaporation boundary are obtained, and their dependences on the Knudsen number in the range $0 < \mathrm{Kn} \le 0.1$ are studied. © *2000 MAIK "Nauka/Interperiodica".*

Interest in the problem of intensive evaporation from the surface of a spherical particle in a vacuum is caused not only by its theoretical significance but also by its important practical applications [1–3]. The results of numerical simulations [2, 3] imply that, for $\mathrm{Kn} \ll 1$ ($\mathrm{Kn} = \lambda/r_0$, where λ is the mean free path of molecules close to the evaporation surface and r_0 is the particle radius), the size of the flow-forming region in the vicinity of a particle in the expanding gas flow is much greater than λ. This case ($\mathrm{Kn} \ll 1$) corresponds to the hydrodynamic flow in which the Navier–Stokes description corrected for the kinetic boundary conditions is valid. The relations between parameters of condensed and gas phases, i.e., the jumps of parameters in the Knudsen layer, can be found only in the framework of the kinetic theory.

In [4], it was shown that three regions of a steady flow may be distinguished in the case of gas flow from a point source for the Reynolds number $\mathrm{Re} \gg 1$ and the Prandtl number $\mathrm{Pr} = 3/4$. Far from the particle, there is a region of a nonviscous radial flow described by the Euler equations. As the source is approached, this region goes into a so-called intermediate region where the Mach number $M \sim 1$ corresponds to the crossing of the sonic point. As the Mach number decreases, i.e., as the source is neared, one more region is distinguished. In this internal region, the gas flow is considered to be planar and one-dimensional.

In [1] it is assumed that an evaporating surface is adjacent to a gas-dynamic region where the gas flow is planar and one-dimensional [4]. In [1], the hydrodynamic boundary conditions for evaporating mono- and diatomic gases in the limiting case $\mathrm{Kn} \longrightarrow 0$ are obtained.

In the aforementioned papers, except for [1], monatomic gases were considered. However, most gases are polyatomic, and, hence, the study of the aforementioned processes, as applied to molecular gases, is of considerable interest.

The aim of this paper is to describe the intensive molecular (diatomic) gas evaporation from a spherical surface in a vacuum at small Knudsen numbers ($0 < \mathrm{Kn} \le 0, 1$).

It is well known that, in a wide temperature range, the rotational degrees of freedom may be described semiclassically for most molecular gases [5, 6]. We assume that the parameters describing a particle are given: T_s is the temperature of the particle surface, and n_s is the density of the saturated vapor of the particle material at temperature T_s. We consider a spherically symmetric steady flow of evaporated substance. Taking into account the small value of the Knudsen number, we describe the velocity distribution function in the gas by the Chapman–Ensky function, which after linearization takes the form [5, 7]

$$f = f_0(1 + \Phi_\eta + \Phi_T),$$

$$\Phi_\eta = -\frac{4}{3}\eta\left(\frac{du}{dr} - \frac{u}{r}\right)\frac{1}{p}\frac{m}{2kT}\left[(v_r - u)^2 - \frac{v_\theta^2 + v_\varphi^2}{2}\right], \quad (1)$$

$$\Phi_T = \frac{\kappa}{c_p p}\frac{1}{T}\frac{dT}{dr}c_r\left(\frac{7}{2} - \frac{mc^2}{2kT} - \frac{J\omega^2}{2kT}\right),$$

$$f_0(\mathbf{v}, \omega) = \left(\frac{m}{2\pi kT}\right)^{3/2}\left(\frac{J}{kT}\right)\exp\left\{-\frac{m\mathbf{c}^2}{2kT} - \frac{J\omega^2}{2kT}\right\},$$

where Φ_η and Φ_T are the viscosity and heat-conduction; m and J, the mass and moment of inertia of the molecule; $\mathbf{v}$ and ω, the velocities of the translational and rotational motions of the molecule; $\mathbf{u}$ and $\mathbf{c} = \mathbf{v} - \mathbf{u}$, the mean and thermal velocities of molecules; k, the Boltzmann constant; p, n, and T, the pressure, density, and temperature of the gas; η and κ, the coefficients of vis-

1063-7842/00/4511-1509$20.00

cosity and heat conductivity; and c_p, the specific heat at p = const.

We represent the boundary condition on the surface $r = r_0$ under the assumption that the molecules leaving the surface constitute a Maxwellian distribution with the temperature equal to the surface temperature T_s. For the sake of simplicity, the coefficients of evaporation and energy accommodation are considered to be equal to unity:

$$f_s(\mathbf{v}, \omega) = n_s\left(\frac{m}{2\pi kT_s}\right)^{3/2}\left(\frac{J}{kT_s}\right)\exp\left\{-\frac{mv^2}{2kT_s}-\frac{J\omega^2}{2kT_s}\right\}, \quad v_r > 0. \tag{2}$$

The motion of evaporated substance in an expanding flow is described by the Navier–Stokes equations involving coefficients of viscosity η and thermal conductivity κ.

Far from the particle, in the region of nonviscous flow ($\eta = 0$, $\kappa = 0$), the Navier–Stokes equations go over to the Euler equations. The solution of the latter is well known and presented in [4]. In the intermediate region, close to the sonic point $r = r_1$, the solution of the Navier–Stokes equations is expressed in terms of modified Hankel functions [4].

In the internal region, which is adjacent to the evaporating surface [1], the hydrodynamic equations for Pr = 3/4 and Kn $\ll$ 1 are reduced to the following form [4]:

$$\frac{dw}{d\xi} = 2 - (k_1 a)^{2/3} - w - \frac{1}{w}, \tag{3}$$

$$\theta + \frac{\gamma-1}{2}w^2 - \frac{\gamma+1}{2} = 0, \tag{4}$$

where

$$\xi = \frac{x - x_1'}{a}, \quad x_1' = \frac{r_1}{r}, \quad a = \frac{8\gamma}{3(\gamma+1)}\eta\frac{r_1}{\dot m},$$

$$\beta = \frac{\gamma-1}{\gamma+1}, \quad x_1' = 1 + [1(1-\beta)]^{-1/3}a^{2/3}\xi_1,$$

$$k_1 = \left(\frac{4}{\gamma+1}\right)\xi_1^{3/2}.$$

Here, $w = u/c_1$; $\theta = T/T_1$; γ is the adiabatic exponent; $\dot m$, the mass flux from the particles ($\dot m$ = const); $c_1 = \sqrt{\gamma R_\mu T_1}$ and T_1, the mean values of speed u and temperature T at the sonic point $r = r_1$, respectively (i.e., $w = 1$ and $\theta = 1$ at $r = r_1$); a, a small quantity; and $a^{-1} \sim$ Re. The solution of equation (3) is given by

$$\frac{1}{R} = x_1' + k_1^{-1/3}a^{2/3}\left[\frac{1}{\arctan\{(k_a a)^{-1/3}(1-w)\}} - \frac{\pi}{2}\right] - \frac{a}{k_1}\log(1-w). \tag{5}$$

Here $R = 1/x = r/r_1$ is the dimensionless radius vector, and the quantity $\xi_1 = 2.3381$ is defined by asymptotically matching the solution of (3) with the solution in the intermediate region where $w \sim 1$. We use expressions (3)–(5) to find the gradients of the quantities dT/dr, du/dr, appearing in the distribution function (1). After performing the corresponding transformations, taking into account the relation $\eta = \lambda p_0(2m/\pi kT_0)^{1/2}$, the distribution function (1) takes the form:

$$f = f^0[b_0 + b_1 h_0^{1/2}v_r + b_2 h_0 v_r^2 + b_3 h_0^{3/2}v_r^3 + b_3 h_0^{3/2}v_r(v_\phi^2 + v_\theta^2) + b_4 h_0(v_\phi^2 + v_\theta^2)] + 2h_0^{1/2}z_0\tau(v_r - u_0)j\omega^2,$$

$$b_0 = 1 + z_0^4 d - (7 - 2z_0^2)z_0^2\tau,$$

$$b_1 = -2z_0^3 d + (7 - 6z_0^2)z_0\tau, \tag{6}$$

$$b_2 = z_0^2 d + 6z_0^2\tau, \quad b_3 = -2z_0^2\tau, \quad b_4 = -z_0^2 d + 2z_0^2\tau,$$

$$d = \frac{\gamma+1}{\gamma}\left\{\frac{1}{w_0}\left(\frac{dw}{d\xi}\right)_0 + R_0 a\right\}, \quad \tau = \frac{\gamma^2-1}{2\gamma}\frac{w_0}{\theta_0}\left(\frac{dw}{d\xi}\right)_0,$$

$$R_0 = \frac{r_0}{r_1}, \quad z_0 = \sqrt{\frac{\gamma}{2}M_0}, \quad w_0 = M_0\sqrt{\frac{\gamma+1}{2+(\gamma-1)M_0^2}},$$

$$a_0 = \frac{8\gamma}{3\sqrt{\pi}(\gamma+1)}\frac{\mathrm{Kn}}{z_0}\frac{1}{R_0}, \quad h_0 = \frac{m}{2kT_0}.$$

Here, the subscript 0 denotes the values of quantities at the hydrodynamic evaporation boundary. We will assume the Knudsen layer to be infinitesimally thin and consider it as a surface of gas-dynamic discontinuity where the conservation equations for fluxes of mass, momentum, and energy are valid, i.e., the quantities C_0, C_1, and C_2 are constant:

$$\int Q_i f d^3v\omega d\omega = C_i; \quad i = 1, 2, 3; \quad Q_1 = m, \quad Q_2 = mv_r, \quad Q_3 = mv^2/2 + J\omega^2/2. \tag{7}$$

These conditions make it possible to obtain the relationship between surface parameters T_s and n_s, on the one hand, and the vapor gas parameters T_0 and n_0, on the other hand, on the external surface of the Knudsen layer without solving the Boltzmann equation. The integration of (7), taking (6) into account, yields a set of three equations in four variables: M_0, Kn, T_0/T_s, and n_0/n_s. It is convenient to choose M_0 as a free parameter.

Then, the dimensionless temperature T_0/T_s and density n_0/n_s are defined by the following expressions:

$$\frac{T_0}{T_s} = \frac{3X_1}{X_3}, \quad \frac{n_0}{n_s} = \frac{T_s}{2X_2T_0}, \tag{8}$$

and the Knudsen number Kn is found from the solution of the equation

$$\frac{\sqrt{\pi}}{2\sqrt{3}}\frac{\sqrt{X_1}\sqrt{X_3}}{X_2} - 1 = 0. \tag{9}$$

The following notation is used above:

$$X_1 = b_0F_0 + b_1F_1 + b_2F_2 + b_2F_2 + b_3F_3 + b_4F_0 + b_3F_1,$$

$$X_2 = b_0F_1 + b_1F_2 + b_2F_3 + b_3F_4 + b_4F_1 + b_3F_2,$$

$$X_3 = b_0(2F_0 + F_2) + 2z_0^2\tau F_0 + b_1(2F_1 + F_3) - 2z_0\tau F_1 + b_2(2F_2 + F_4) + b_3(2F_3 + F_5) + b_4\left(\frac{5}{2}F_0 + F_2\right) + b_3\left(\frac{5}{2}F_1 + F_3\right),$$

$$F_0 = z_0y_1 + y_2, \quad F_1 = (1/2 + z_0^2)y_1 + z_0y_2,$$

$$F_2 = (3z_0/2 + z_0^3)y_1 + (1 + z_0^2)y_2,$$

$$F_3 = (3/4 + 3z_0^2 + z_0^4)y_1 + (5z_0/2 + z_0^3)y_2,$$

$$F_4 = (15z_0/4 + 5z_0^3 + z_0^5)y_1 + (2 + 9z_0^2/2 + z_0^4)y_2,$$

$$F_5 = \frac{1}{8}(15 + 90z_0^2 + 60z_0^4 + 8z_0^6)y_1 + \frac{1}{8}(66z_0 + 56z_0^3 + 8z_0^5)y_2,$$

$$y_1 = 1 + \mathrm{erf}(z_0), \quad y_2 = \frac{\exp(-z_0^2)}{\sqrt{\pi}},$$

$$\mathrm{erf}(z_0) = \frac{2}{\sqrt{\pi}}\int_0^{z_0}\exp(-x^2)dx.$$

The calculation results for the boundary values of the macroscopic parameters of a diatomic gas are listed in the table. For Kn $\longrightarrow$ 0, the Mach number M_0, temperature T_0/T_s, and density n_0/n_s tend to the limiting values that are in satisfactory agreement with the results of [1] for Kn $\longrightarrow$ 0: $M_0 = 0.415$, $T_0/T_s = 0.913$, and $n_0/n_s = 0.661$. The table shows that the Mach number M_0 increases with increasing Knudsen number Kn, whereas the limiting values of dimensionless temperature T_0/T_s and gas density n_0/n_s decrease, i.e., the temperature and density jumps increase in the Knudsen layer.

Table

Kn	M_0	w_0	T_0/T_s	n_0/n_s
Kn $\longrightarrow$ 0	0.404	0.436	0.942	0.663
0.0025	0.430	0.463	0.936	0.647
0.005	0.447	0.481	0.932	0.637
0.01	0.477	0.511	0.924	0.620
0.02	0.528	0.563	0.911	0.593
0.03	0.577	0.612	0.897	0.568
0.04	0.622	0.657	0.884	0.547
0.05	0.665	0.698	0.871	0.529
0.06	0.703	0.735	0.858	0.513
0.07	0.735	0.765	0.848	0.501
0.08	0.762	0.790	0.838	0.491
0.09	0.782	0.809	0.830	0.484
0.10	0.798	0.823	0.824	0.479

The comparison of the results with the data obtained by numerical simulations [2] for the case of monatomic gas makes it possible to conclude that, for small values of the Knudsen number, the inclusion of rotational degrees of freedom for a diatomic gas yields a decrease in temperature and density jumps in the Knudsen layer in comparison with those for a monatomic gas.

REFERENCES

1. R. H. Edwards and R. L. Collins, in *Proceedings of the International Symposium on Rarefied Gas Dynamics* (Academic, New York, 1969), Vol. 2, p. 1489.
2. Y. Sone and H. Sugimoto, Phys. Fluids A **5**, 1491 (1993).
3. N. M. Bulgakova, M. Yu. Plotnikov, and A. K. Rebrov, Izv. Akad. Nauk, Mekh. Zhidk. Gaza, No. 6, 137 (1997).
4. A. Sakurai, Q. J. Mech. Appl. Math. **11** (3), 274 (1958).
5. V. M. Zhdanov and M. Ya. Alievskiĭ, *Transfer and Relaxation Processes in Molecular Gases* (Nauka, Moscow, 1989).
6. L. D. Landau and E. M. Lifshitz, in *Statistical Physics* (Nauka, Moscow, 1976; Pergamon, Oxford, 1980), Part 1.
7. A. B. Poddoskin and A. A. Yushkanov, Izv. Akad. Nauk, Mekh. Zhidk. Gaza, No. 5, 182 (1998).

Translated by M. Fofanov